Alma Mater Studiorum

Università degli Studi di Bologna

DIPARTIMENTO DI FISICA E ASTRONOMIA

Dottorato di ricerca in Astronomia
Ciclo XXVIII

COSMIC-LAB: Unexpected Results from High-resolution Spectra of AGB Stars in Globular Clusters

Dottorando:
Emilio Lapenna

Relatore:
Chiar.mo Prof. Francesco R. Ferraro

Co-Relatori:
Dr. Alessio Mucciarelli
Dr. Livia Origlia
Chiar.ma Prof. Barbara Lanzoni

Coordinatore:
Chiar.mo Prof. Lauro Moscardini

Esame finale anno 2015

Settore Concorsuale: 02/C1 – Astronomia, Astrofisica, Fisica della Terra e dei Pianeti
Settore Scientifico-Disciplinare: FIS/05 – Astronomia e Astrofisica

arXiv:1601.04346v1 [astro-ph.SR] 17 Jan 2016

Alla Mia Famiglia

"L'astronomia costringe l'anima a guardare oltre e ci conduce da un mondo ad un altro."

Platone

Contents

Introduction **1**

1 Elemental Abundances and Chemical Evolution **5**

1.1 α and other light elements 6

1.2 Iron-peak elements 11

1.3 Neutron-capture elements 13

2 Globular Clusters: Evolutionary Sequences and Chemical Composition **15**

2.1 Evolutionary sequences 15

2.2 Overall chemistry 19

2.2.1 Metallicity distribution 19

2.2.2 Pre-enrichment 23

2.2.3 Star-to-star variations and signatures of self-enrichment 25

2.2.4 Open questions 31

3 Chemical abundances of AGB stars in globular clusters **35**

3.1 NLTE effects in AGB stars 36

3.2 The lack of SG AGB stars in GCs 37

3.3 AGB overconcentration in the core of 47Tuc 38

3.3.1 Blue straggler stars in GCs 39

3.4 A few words on the NLTE effect 40

4 Non Local Thermodynamic Equilibrium Effects on Asymptotic Giant Branch Stars in 47Tucanae **43**

4.1 Observations 43

4.2 Analysis 45

4.2.1 Radial velocities 45

4.2.2 Chemical analysis . . . 45
4.3 Iron abundance . . . 47
4.3.1 Sanity checks . . . 48
4.4 Discussion . . . 53
4.4.1 A possible signature of NLTE effects? . . . 53
4.4.2 Impact on traditional chemical analyses . . . 55
4.4.3 Searching for evolved BSSs among AGB stars: a new diagnostic? . . . 57
4.5 Summary . . . 59

5 The Origin of the Spurious Iron Spread in the Globular Cluster NGC3201 63
5.1 Observations . . . 63
5.2 Analysis . . . 64
5.2.1 Analysis with spectroscopic gravities . . . 65
5.2.2 Analysis with photometric gravities . . . 66
5.2.3 Uncertanties . . . 68
5.3 Discussion . . . 68
5.4 Conclusions . . . 72

6 A Chemical *Trompe-l'œil*: No Iron Spread in the Globular Cluster M22 77
6.1 Observations . . . 77
6.2 Iron abundance . . . 78
6.2.1 Method (1): spectroscopic T_{eff} and log g . . . 81
6.2.2 Method (2): spectroscopic T_{eff} and photometric log g . . . 82
6.2.3 Method (3): photometric T_{eff} and log g . . . 84
6.3 A sanity check: NGC6752 . . . 86
6.4 No iron spread in M22 . . . 86
6.5 The s-process elements abundance . . . 90
6.6 Discussion: re-thinking M22 . . . 91

7 Chemical Analysis of Asymptotic Giant Branch Stars in M62 101
7.1 Observations and spectral analysis . . . 101
7.1.1 Radial velocities . . . 102
7.1.2 Atmospheric parameters and stellar masses . . . 104
7.1.3 Chemical abundances . . . 104

7.2 Results . . . 106
7.2.1 Iron and titanium . . . 106
7.2.2 Oxygen, sodium, magnesium and aluminum . . . 111
7.3 Discussion and conclusions . . . 116

8 Weighing Stars: the Identification of an Evolved Blue Straggler Star in the Globular Cluster 47Tucanae 125
8.1 Observations and membership . . . 126
8.2 Chemical analysis . . . 128
8.2.1 Uncertanties . . . 131
8.3 Discussion . . . 133
8.4 Summary and conclusions . . . 136

Conclusions 141

Appendix 145

A Radial Velocities from VLT-KMOS Spectra of Giant Stars in the Globular Cluster NGC6388 145
A.1 Introduction . . . 146
A.2 Observations and data reduction . . . 148
A.3 Kinematic analysis . . . 152
A.3.1 Accuracy of the wavelength calibration . . . 153
A.3.2 Radial velocity measurements . . . 157
A.3.3 Line-of-sight rotation and velocity dispersion profiles . . . 159
A.4 Discussion and conclusions . . . 159

B Lines and Continuum Sky Emission in the Near Infrared: Observational Constraints from Deep High Spectral Resolution Spectra with GIANO-TNG 165
B.1 Introduction . . . 166
B.2 Observations and spectral analysis . . . 167
B.3 The sky lines and continuum emission . . . 170
B.3.1 OH lines and the hot-OH component . . . 170
B.3.2 O_2 and unidentified lines . . . 172
B.3.3 The sky continuum emission . . . 173

B.4 Discussion and conclusions 176

Introduction

Globular clusters (GCs) are among the most interesting stellar systems and have been targeted by several studies from the beginning of the astrophysical research. These systems are thought to be the first stellar aggregates formed in the very early epochs of the Galaxy formation.

For decades, the GCs have been thought to be the best example of simple stellar population (SSP). This terminology was suggested to highlight the overall property of a population in which stars show similar characteristics in terms of age and metallicity. In fact, a SSP is assumed to be originated in a single star formation episode from a cloud with an homogeneous chemical composition. In this way, all the stars share the same age, since they were born at the same time, and the same metallicity, since they were formed from the same material. Moreover, since GCs typically are older than $\sim$ 10 Gyr, they can be considered as living "relics" of the first stellar aggregates formed and they can be used as tracers of the chemical enrichment history of the host galaxies.

Today, the huge progress that has been accomplished thanks to the rising number of photometric and spectroscopic facilities demonstrated, however, that the SSP concept should be revised. In fact, important chemical anomalies have been detected in GCs, the main ones consisting in the so-called "anticorrelations" among light-elements and in peculiar behaviours observed for iron-peak and neutron-capture elements.

This observational evidence suggests that GCs are complex systems, which during their lifetimes undergo a series of processes able to deeply affect the global characteristics. In this sense, GCs can be considered, at least to a first approximation, as "closed" systems, which mainly suffered auto-enrichment processes with a negligible interaction with the Inter Galactic Medium. In this way, the chemical imprint of different polluters takes a fundamental role in defining the chemical characteristics of the descendants. The study of the chemical composition of stars in GCs is thus fundamental not only to test their chemical models and to unveil the nature of the polluters, but also to better constrain the nucleosyn-

thesis of the elements.

In this context, my thesis is focused on AGB stars, which have an important role in defining the characteristics of GCs for several reasons: (1) the AGB stars dominate the integrated light of stellar populations of intermediate ages ($t < 2$ Gyr), (2) they are an important nucleosynthesis site for the chemical element formed through $proton$- and $neutron$-capture chains and (3) they are thought to be the main polluters in the self-enrichment processes during GC lifetimes. However, due to their short evolutive timescales, AGB stars are numerically the smallest population in GCs, and nowadays only a few studies have investigated their chemical characteristics. Moreover, a few recent results (Ivans et al., 2001; Beccari et al., 2006; Campbell et al., 2013) have awoken the interest for these stars and highlighted the need of new and comprehensive characterizations.

This thesis is aimed at chemically clarifying this poorly studied evolutionary phase. The thesis presents the analysis of a large sample of high-resolution spectra of AGB stars in GCs acquired at the Very Large Telescope (ESO) and at the MPG-2.2m telescope (ESO). The results are quite unexpected and they are contributing to a new understanding of GC chemistry. The work is part of the project Cosmic-Lab, a five year research program funded by the European Research council.

The work is organized as follows: Chapter 1 presents an introduction to the nucleosynthesis sites and channels from which the main chemical elements form. Chapter 2 is focused on the main properties of GCs, their stellar populations and the main formation scenarios suggested so far. Chapter 3 is devoted to illustrate the known properties of AGB, in light of a few recent results from the literature. Chapter 4 reports on the spectroscopic analysis of a sample of 24 AGB stars belonging to the GC 47Tucanae ([Fe/H] = -0.7 dex) which has shown evidence of important non-local thermodynamic equilibrium (NLTE) effects. Chapter 5 and 6 present the discussion of the iron content of two GCs (namely NGC3201 and M22), demonstrating that (at odds with previous claims) they show no intrinsic metallicity spreads. Chapter 7 presents the high-resolution spectroscopic analysis of a sample of 19 giant stars in M62 which has revealed that the same NLTE mechanism discovered in 47Tucanae affects also the titanium lines. Chapter 8 describes how the ionization balance between chemical abundances derived from neutral and ionized elements can be used as a powerful weighing device and presents the discovery of an anomalously heavy (1.4 $M_{\odot}$) star in a sample of photometrically indistinguishable giants of 47Tucanae (this objects most likely is an evolved blue straggler star).

Finally in the Appendices A and B two side-product works are discussed. They deal with the characterization of the performances of two new-generation spectrographs: as GIANO and KMOS.

Chapter 1

Elemental Abundances and Chemical Evolution

The chemical enrichment history of galaxies is driven by the nucleosynthesis occurring in many generations of stars. Indeed, stars are the most important nucleosynthetic site in which the chemical elements heavier than He are build up with different processes on different timescales. The processes that form the elements are strictly linked to the physics of stellar interiors and their evolution over time.

Generally speaking, according to their mass, stars are able to synthesize different elements through different channels and to release a fraction of them (the so-called yields) at different epochs from the star formation onset, not only at the end of their lifetimes (e.g. as Supernovae) but also during their evolution (e.g. through wind activity from AGB stars, fast rotating massive stars and Wolf-Rayet stars). When these yields are released they are mixed in the Inter Stellar Medium (ISM), and subsequent stellar generations can form from this pre-enriched material. The total yield of a given element depends on the mass of the corresponding metal ejected by the stars and on the relative frequency of stars of different masses born in a stellar generation (the so-called Initial Mass Function, IMF). Another chemical evolution parameter is the star formation rate (SFR), which is commonly assumed to be proportional to the star formation efficiency and to some power of the normalized gas surface mass density.

Hence, chemical abundance ratios are powerful diagnostics of the IMF and SFR parameters of stellar systems, also flagging the timescales of chemical evolution. In particular, investigating the chemical composition of the oldest stars is especially important, because these are fossils of the earliest epoch of the galaxy chemical evolution history. The main elements that can be observed and studied in stars can be divided in three main families

based on their different formation processes and nucleosynthetic sites: α and other light elements, iron-peak elements, and neutron-capture elements. In the following sections we will briefly examine some of their characteristics and peculiarities.

1.1 α and other light elements

The name "α-elements" is due to the fact that these chemical species are formed through α-capture processes on seed nuclei. The α particle consists in a nucleus of Helium made of two protons and two neutrons. The main elements belonging to this family, i.e. **O, Ne, Mg, Si, S, Ca,** and **Ti** (see green boxes in Figure 1.1), are progressively built up starting from the burning of He and C (see Woosley & Weaver, 1995).

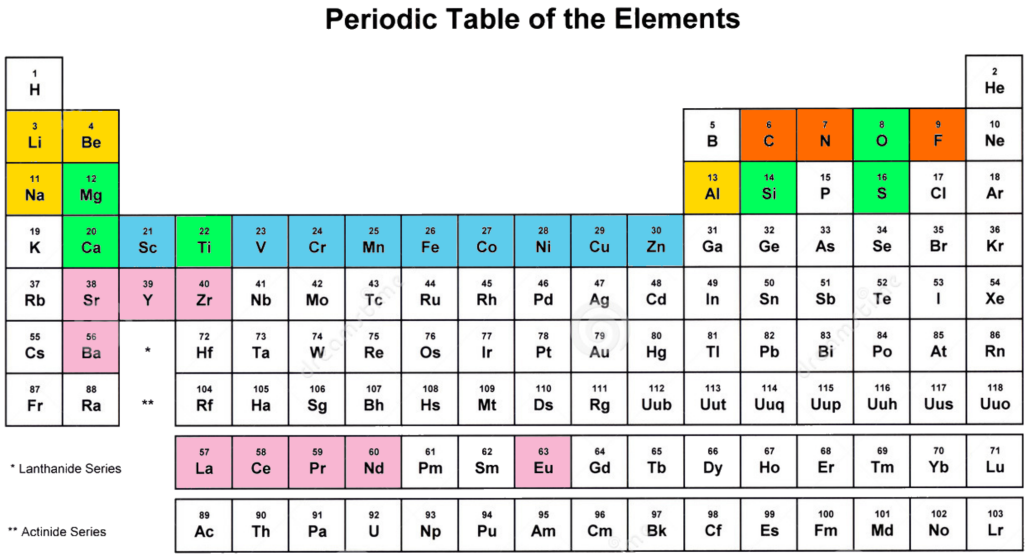

Figure 1.1 The periodic table of elements. The colors highlight the different classes: Green = α-elements, Yellow and Red = light-elements, Blue = Iron-Peak elements and Pink = s- and r-process elements. Only the main and well studied elements are highlighted.

The stellar evolution theory indicates that α-elements are mostly synthesized in massive stars. Indeed, thanks to the very high temperatures reached in the interior of such stars, the α-capture process is able to convert the seed nuclei into heavier elements, with a copious production of the other even-Z elements in between. The elements produced by such massive stars are released into the ISM at the end of the stellar life, during SN explosions. From the very early investigations of Aller & Greenstein (1960) and Wallerstein (1962) it was

found that in Galactic metal-poor stars the [α/Fe] abundance ratio is overabundant with respect to the solar value. The [α/Fe]-[Fe/H] trend in our Galaxy shows two different regimes (see Figure 1.2): for $-1.0 <$ [Fe/H] < 0.0 dex, the [α/Fe] ratio increases as the metallicity decreases, reaching a factor of 2-3 above solar (i.e., [α/Fe] $\simeq 0.3$ dex) at [Fe/H] $\simeq -1$ dex, while for [Fe/H] < -1 dex the [α/Fe] ratio remains almost constant.

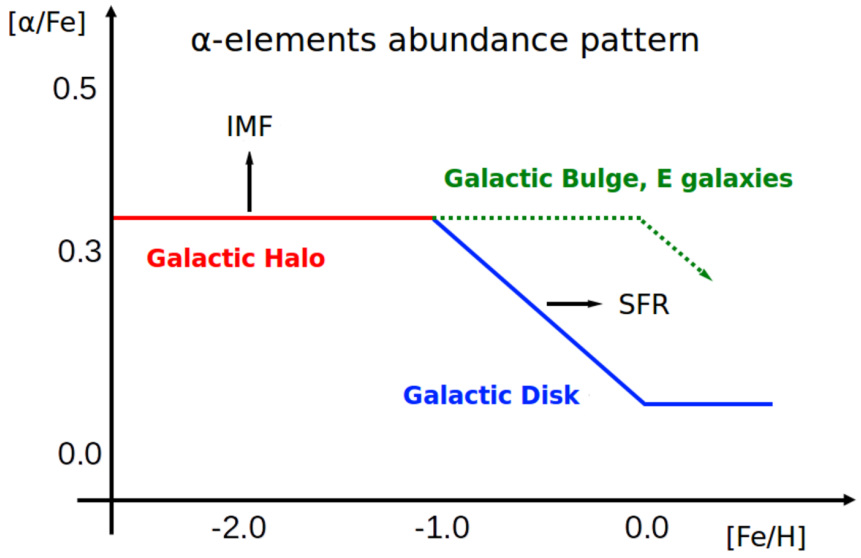

Figure 1.2 The effect of the change of both IMF and SFR on the α abundance pattern observed in our Galaxy.

Tinsley (1979) suggested that the [α/Fe] trend is due to the time delay between the explosions of Type II Supernovae (SNII), which produce α-elements and little amount of iron-peak elements (e.g. Arnett, 1978; Woosley & Weaver, 1995), and Type Ia Supernovae (SNIa), which provide mostly iron-peak elements and little α-elements (e.g. Nomoto et al., 1984; Thielemann et al., 1986). Thus, after the delay for the onset of SNIa, the [α/Fe] ratio decreases from the value set by the SNII ejecta. Accordingly, the position of the knee in the [α/Fe]-[Fe/H] trend flags the metallicity reached by the system at the epoch when SNIa start to dominate. In turn, this depends on the SFR: if it is high, then the gas reaches larger [Fe/H] before the ejecta of SNIa are fully mixed into ISM, and the position of the knee in the diagram will be at a higher [Fe/H] (see black arrow in Figure 1.2). On the other hand, a change of the IMF determines an increase or decrease of the number of high-mass stars formed, which explode as SNII; this corresponds to different amount of α elements produced and, therefore, to a different value of the "plateau" in the [α/Fe]-[Fe/H] diagram

(see black arrow in Figure 1.2). Hence, the study of the [α/Fe] trend (and of the chemical composition of stars, in general) in stellar populations is very important, since it traces the modes and timescales of the chemical enrichment process.

Other important light elements such as **He, Li, Be, C, N, F, Na, Al, P,** and **K** (yellow and red boxes in Figure 1.1) may have a fundamental role in defining the properties of stellar populations in specific evolutionary stages.

Helium is the most abundant among the few chemical elements produced directly during the primordial nucleosynthesis of the Big Bang (^{3}He and ^{4}He). The most recent determination of the primordial He mass fraction provides a value Y=0.254$\pm$0.003 (Izotov et al., 2013). Also, ^{4}He is produced in stars with masses larger than $\sim$0.08 $M_\odot$ through the hydrogen-burning chains.

Lithium is produced mainly during the Big Bang nucleosynthesis, in the form of ^{7}Li. In metal-poor ([Fe/H]$<$-1.5 dex) halo dwarf stars the surface abundance of lithium turns out to be constant regardless of the metallicity and the temperature, with a value A(Li)$\sim$2.2 (the so-called Spite-Plateau, Spite & Spite, 1982). Additionally, ^{7}Li can be produced in AGB stars (with mass between 5 and 8 $M_\odot$) through the Cameron-Fowler mechanism and perhaps in novae and SNII (see Romano et al., 2001).

The only stable isotope of beryllium, ^{9}Be, is a pure product of cosmic-ray spallation of heavy nuclei (mostly CNO) in the interstellar medium (Reeves, 1970) with negligible/null contribution from the Big Bang and stellar nucleosynthesis. Recently, the measurement of the Be abundance has been proposed as a "clock" to date the oldest stars (Pasquini et al., 2004).

Carbon and nitrogen, together with oxygen, are the most abundant metals in the Universe. During the Post main Sequence evolution, the stellar surface abundances of carbon and nitrogen can be significantly altered by the dredge-up of material processed by the CNO cycle, with a resulting [C/Fe] depletion and a corresponding [N/Fe] enhancement, while O abundance remains almost unaffected. Additional extra-mixing processes are also invoked to explain some extreme [C/Fe] depletions and [N/Fe] enhancements, although the precise physical mechanisms responsible for their occurrence are still unknown and/or debated. Such modifications of the *ab initio* C and N abundances induced by stellar evolution complicate the interpretation of the observed trends in different stellar populations and galactic environments.

From a nucleosynthetic perspective, fluorine is a very interesting element, and its cosmic

origin is still to be understood. Three main production mechanisms for ^{19}F, the only stable isotope of fluorine, have been proposed. 1) neutrino nucleosynthesis in SNII. The core collapse of a massive star, following a SNII explosion, leads to a prodigious neutrino flux. In spite of the small cross sections, the large amount of neutrinos gives rise to a significant spallation of ^{20}Ne to ^{19}F (Woosley & Haxton, 1988) in the overlying (neon-rich) shells of the core. 2) Thermal-pulsing asymptotic giant branch stars. The production of fluorine starts from ^{14}N burning (Forestini et al., 1992; Jorissen et al., 1992; Gallino et al., 2010; Abia et al., 2011; Kobayashi et al., 2011), then it is transported up to the surface by the third dredge-up. Fluorine production in AGB stars is expected to be accompanied by the slow neutron-capture nucleosynthesis (the s-process). It has been demonstrated observationally that AGB stars produce fluorine, see for example Jorissen et al. (1992) and Abia et al. (2011). 3) Wolf-Rayet stars. Meynet (1993) and Meynet & Arnould (1996, 2000) suggested that Wolf-Rayet (W-R) stars might contribute to the Galactic fluorine budget. ^{19}F is produced in the convective cores of W-R stars during the core He-burning phase. Using a semi-analytic multizone chemical evolution model, Renda et al. (2004) showed for the first time the impact of the AGB and W-R star contributions to the Galactic chemical evolution of fluorine. They showed that the production was dominant in the early Universe and that the contribution of AGB stars successively grows. Based on old yields and nonrotating models, they also showed that the contribution of W-R stars is significant for solar and supersolar metallicities, increasing the [F/O] ratio by a factor of two at solar metallicities. Their conclusion was that all three production sites are needed to explain the Galactic chemical evolution of fluorine for a range of metallicities. The abundance of fluorine in stars is difficult to measure because of a paucity of suitable spectral lines and a systematic, massive study of its abundance in different stellar populations and environment is still lacking. Highly ionized F V and F VI lines in the UV have been used by Werner et al. (2005) in extremely hot post-AGB stars, and a handful of F I lines between 6800-7800 Å have been used in extreme helium stars and R Coronae Borealis stars (Pandey, 2006; Pandey et al., 2008). All other studies have used the HF molecular lines in the K-band and mostly the HF line at 23358 Å.

Other important odd-Z elements are Na and Al, which have been studied in several astrophysical environments. Both in field and cluster stars the Na and Al abundances showed a clear star-to-star dispersion. From the analysis of a sample of field stars in the interval $-3 <$ [Fe/H] < -1 dex, Pilachowski et al. (1996) found a small deficiency of [Na/Fe] with values around $-0.2/-0.3$ dex. Reddy et al. (2006) found a hint for an increase of [Na/Fe]

with increasing [Fe/H] in the metallicity range $-1.0 <$ [Fe/H] < -0.6 dex, followed by a decrease towards solar values for $-0.6 <$ [Fe/H] < 0 dex. On the contrary, in globular cluster (GCs) stars a very high dispersion was observed with abundances spanning a range between slightly subsolar [Na/Fe] up to 1.0 dex. A similar behaviour was observed for Al in field stars, which show an increase of the [Al/Fe] abundances as [Fe/H] increases, the trend is not as strong for Na. However, at very low metallicities ([Fe/H] < -2.8 dex), the relation [Al/Fe] versus [Fe/H] seems to become rather flat (Andrievsky et al., 2008). On the contrary, in GCs the [Al/Fe] behaviour well resembles that of [Na/Fe], with abundances spanning up to 1.0 dex. So the Na and Al abundances in GCs appear to be correlated, and they are correlated with N enhancements and O depletions. These abundance patterns have been interpreted either as evidence of internal nucleosynthesis and mixing operating in individual stars or, alternatively, as characteristic of a dispersion in the composition of the material out of which the stars formed (see Kraft, 1994; Shetrone, 1996a,b; Kraft et al., 1997, and references therein for details). Currently, the formation channels of the Na and Al remain controversial. Na should likely form by means of hydrostatic carbon and hydrogen burning through the NeNa cycle, while Al should form by means of hydrostatic carbon and neon burning and during hydrogen burning through the MgAl chain. In the NeNa cycle the ^{20}Ne is progressively converted in ^{23}Na by several proton captures, while in the MgAl chains the ^{24}Mg is finally converted in ^{26}Al (Denisenkov & Denisenkova, 1989; Langer et al., 1993; Cavallo et al., 1996; Prantzos et al., 2007; Straniero et al., 2013). However, several other formation channels have been proposed so far, thus it is difficult to use Na and Al as probes of Galactic chemical evolution until their nucleosynthesis is better constrained.

Phosphorus has a single stable isotope ^{31}P, and its most likely sites of production are O and Ne burning shells in the late stages of the evolution of massive stars, which end up as SNII. The production mechanism probably occurs via neutron capture, as it is for the parent nuclei ^{29}Si and ^{30}Si. According to Woosley & Weaver (1995), there is no significant P production during the explosive phases. Recently, Caffau et al. (2011) analyzed the high excitation IR PI lines at 1051-1068 nm in a sample of twenty Galactic stars, finding a systematic increase of [P/Fe] for decreasing [Fe/H]; [P/Fe] is close to zero for solar metallicity stars. Cescutti et al. (2012) compared the observed results to a model of the chemical evolution of P in the Milky Way, adopting different sets of yields. They conclude that P is formed mainly in massive stars (core-collapse SNe) and that the yields of P available in the literature are all too low and have to be artificially increased by a factor of 3 to satisfactory

reproduce the observed data, including the solar photospheric P. From their best model they predict a "plateau" at [P/Fe] $\sim$ +0.5 dex in the metal poor metallicity range ($-3.0 <$ [Fe/H] < -1.0 dex), if normal yields from SNII are adopted, and at [P/Fe] = $+0.2$ to $+0.3$ dex if hypernova yields are assumed. However, previous chemical evolution models for P (Fenner et al., 2005; Kobayashi et al., 2006) suggested a flat trend in the range $-2.0 <$ [Fe/H] < 0.0 dex.

Potassium is mainly produced by a combination of hydrostatic oxygen shell burning and explosive oxygen burning in proportions that vary depending on the stellar mass. Measurements of [K/Fe] in the Milky Way suggest an enhanced value in metal-poor stars and a decrease toward the solar value for stars more metal-rich than -0.5 dex (Reddy et al., 2003; Zhang et al., 2006; Andrievsky et al., 2010).

1.2 Iron-peak elements

The elements with a nucleosythesis closely linked to that of iron are usually tagged as "iron-peak elements". This family includes **Sc, V, Cr, Mn, Fe, Co, Ni, Cu,** and **Zn** (blue boxes in Figure 1.1). These elements are mostly produced during the explosive nucleosynthesis associated to SNIa, but some contributions from the weak s-processes in massive stars (e.g. for Cu) and from SNII have been also proposed (e.g. for Fe, Cu and Zn).

Iron is probably the best known chemical element and it has been extensively studied in almost all astrophysical contexts. This is due to the huge number of available atomic transitions over the whole spectral range, and at all the metallicities, which normally allows one to obtain a very precise estimate of the iron abundance. Moreover, as the majority (but not all) of iron-peak elements, iron has only two main formation channels: SNII and SNIa. After the collapse of the core and the subsequent explosion, the SNII are able to release in the ISM a few tenths of solar masses of iron. Conversely, SNIa mainly release iron and other iron-peak elements. Thus, there are no nuclear reactions able to alter the iron abundance of a star. Because of this, all abundance ratios are usually expressed in terms of iron content.

Up to now, only few studies have investigated the behaviour of Scandium and Vanadium in our Galaxy. Although Zhao & Magain (1990a,b) have found that the [Sc/Fe] is slightly supersolar in metal-poor dwarfs, several other studies found no evidence for a deviation from [Sc/Fe] = 0.0 in field stars (Peterson et al., 1990; Gratton & Sneden, 1991; McWilliam et al., 1995b). The same applies for V for which abundances fully compatible with a solar

[V/Fe] $\sim$ 0.0 dex have been measured by Gratton & Sneden (1991).

The case of Manganese is quite different. From [Fe/H] = 0.0 to -1.0 dex, the [Mn/Fe] ratios are sub-solar in a manner that mirrors the α-element overabundances, and in the interval [Fe/H] = -1.0 to -2.5 dex, [Mn/Fe] remains roughly constant around -0.4 dex. Thus the trend of [Mn/Fe] with [Fe/H] is similar, but opposite, to that of [α/Fe]. Moreover, McWilliam et al. (1995a) discovered that below [Fe/H] $\sim$ -2.5 dex, the [Mn/Fe] ratio decreases steadily with decreasing [Fe/H], suggesting that Mn is among those elements whose yields depend on the metallicity of the parent stars. This is also supported by the results of McWilliam et al. (2003) who compared the [Mn/Fe] versus [Fe/H] relation in the Galactic bulge, in the solar neighbourhood and in the Sagittarius dwarf spheroidal galaxy concluding that the Mn is produced by both SNIa and SNII in a metallicity-dependent way. Very similar to that of [Mn/Fe] is the behaviour of [Cr/Fe], which is found to rise as the metallicity increase. Also for this element a metallicity-dependent yield by both SN types has been proposed although the main production should occur during incomplete explosive Si burning (Woosley & Weaver, 1995; Limongi & Chieffi, 2003).

[Ni/Fe] is usually found to be close to the solar value at different metallicities, suggesting that the origin of Ni is strictly linked to that of Fe from both SN types.

[Co/Fe] is found to increase as metallicity decreases, in particular, below [Fe/H] $\sim$ -2.5 dex McWilliam et al. (1995b) found a steep rise of [Co/Fe] up to 1 dex. This likely suggests that the main contribution in the production of Co comes from SNII. However, the explosion energies may have a big impact on the amount of Co produced as suggested by Umeda & Nomoto (2005).

Cu and Zn abundances are difficult to obtain due to the paucity of available atomic transitions. In our Galaxy Sneden & Crocker (1988) and Sneden et al. (1991) studied the abundances of Cu and Zn as a function of metallicity and discovered that [Cu/Fe] decreases linearly with declining metallicity, while Zn is roughly constant at [Zn/Fe] = 0.0 dex for all metallicities (see also Bensby et al., 2005; Nissen et al., 2007). However, [Zn/Fe] rises steeply to $\sim$ +0.5 at the lowest metallicities (Cayrel et al., 2004). Sneden et al. (1991) suggested that the nucleosynthesis of Cu may be predominantly due to "weak s-process" in the cores of massive stars, with a small contribution from explosive burning in SNII. The s-process is one of the possible channels through which the neutron-capture process occur (see the next section for details). However, Matteucci et al. (1993) suggested that the main production of Cu and Zn occurs in SNIa. A more recent comprehensive study by Romano

& Matteucci (2007) have shown that Cu should be mainly synthesized in massive stars, during core-helium and carbon-shell hydrostatic burnings, as well as in explosive complete Ne burning (e.g. Woosley & Weaver, 1995; Limongi & Chieffi, 2003).

1.3 Neutron-capture elements

The "neutron-capture" elements are characterized by a proton number Z larger than 30 (pink boxes in Figure 1.1) and form through subsequent neutron captures on a seed nucleus, in general an iron-peak element. These processes, if compared to the radiative decay timescales of the unstable nuclei, can be slower or faster, thus resulting in the slow (s-process) or rapid (r-process) neutron captures. The s-process occurs in two different branches: the $weak$-s process is responsible for the formation of nuclei with an atomic number $29 < Z < 40$ and the $main$-s process can produce heavier nuclei up to Z = 84. The s-process captures through the $weak$ channel mainly occur in massive stars ($M \gtrsim 13$ $M_{\odot}$) while the $main$ channel dominates the nucleosynthesis during the thermal pulse stage of low-mass (1-3 $M_{\odot}$) AGB stars at neutron densities of 10^7-10^9 cm^{-3} (e.g. see Busso et al., 1995; Lambert et al., 1995). Here the main source of neutrons is expected be the $^{13}C(\alpha, n)^{16}O$ reaction. The neutron capture process can also happen in a very fast way, thus resulting in the so called r-process. This makes use of the large number of neutrons available and occurs in unstable neutron-rich and very radioactive regions (Sneden & Cowan, 2003; Cowan & Thielemann, 2004; Arnould et al., 2007). The most plausible sites for this process are the core-collapse SNe during the explosion, in which a density of up to $\sim 10^{25}$ neutrons cm^{-3} can be achieved. The typical s-process elements observable in the stars are **Sr, Y, Zr, Ba,** and **La**, while the main chemical element produced through r-process is **Eu**. Generally speaking, the behaviour of such groups in the Galaxy can be considered roughly specular. At low metallicities the amount of r-elements in stars is clearly supersolar, reaching values up to $+1.5$ dex for [Eu/Fe] (see Barklem et al., 2005). With the increase of [Fe/H] these abundances decline reaching a [Eu/Fe] $\sim$ 0.0 dex at solar metallicity. This behaviour closely resembles that of α-elements thus suggesting that r-elements may have a common origin mainly due to the contribution of SNII. On the other hand, the production of s-elements may occur in a metallicity-dependent way, mainly due to neutron-captures processes during the thermal pulses of AGB stars. In fact, at low metallicities a large number of neutrons is available for a limited amount of seed nuclei, in general iron-peak elements.

This would result in a larger number of captures, thus favoring the production of s-elements belonging to the group of Ba and La (A $>$ 130). With the increase of metallicity, i.e. of the available seed nuclei, the number of neutron captures per atom decreases, thus favoring the formation of s-elements belonging to the group of Sr, Y, and Zr (A $\sim$ 90). In our Galaxy the [s/Fe] ratio generally increases with metallicity thanks to the rising contribution of AGB stars, and the proportion between heavy-s and light-s progressively changes. In any case, it is important to underline that it is difficult to tightly constrain the chemical evolution history of neutron capture elements for two main reasons: (1) for almost all of these elements a high dispersion of the abundances is observed, regardless of the metallicity (this makes difficult a clean detection of any possible trend able to constrain the evolution), and (2) "pure" s or r-element do not exist, in the sense that secondary channels have a non-negligible contribution to the formation of each of these elements (see Arlandini et al., 1999).

Chapter 2

Globular Clusters: Evolutionary Sequences and Chemical Composition

GCs are roughly spherical ensambles of stars, which are tightly bound by gravity. Their name comes from the Latin word *globulus* which means "small sphere". Our Galaxy hosts more than $\sim$ 150 GCs, spanning a wide range of metallicities (over $\sim$ 2 dex), but a small range of ages: they are mostly older than 10 Gyrs.

2.1 Evolutionary sequences

During their lifetimes, stars evolve through different stages characterized by different thermonuclear reactions and processes, that, in turn, determine the physical conditions in their atmospheres. These have fundamental implications on the global parameters of the stars like luminosity and surface temperature.

GSs are old ($>$ 10 Gyr), hence they host stars with masses $\lesssim$ 1 $M_{\odot}$. The main stages of the stellar evolution which have been targeted by an invaluable number of studies in the last decades are Main Sequence, Sub Giant Branch, Red Giant Branch, Horizontal Branch and Asymptotic Giant Branch. In the following we will summarize the main properties of each evolutionary sequence as observed in the color magnitude diagram of GCs (see Figure 2.1).

- Main Sequence (MS) - The MS is the evolutionary stage where stars spend most of their lifetime (more than 90%). This stage is characterized by the thermonuclear burning of hydrogen in the core, through which hydrogen is converted in helium. This can happen with two different reactions: the "proton-proton chain", which mainly occurs in stars with a mass lower than 1.3 $M_{\odot}$ where a temperature larger than $\sim 10^7$ K is reached in

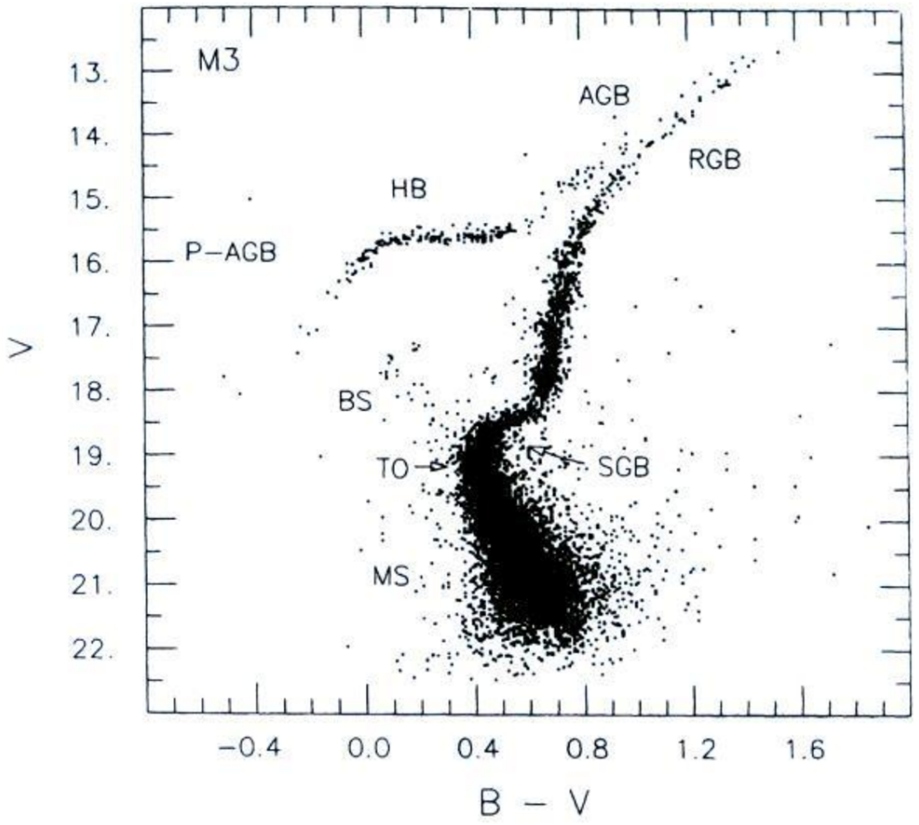

Figure 2.1 The CMD of the GC M3 from Buonanno et al. (1986). The main evolutive stages of the stars are also higlighted.

the core, and the so-called "CNO-cycle" which occurs in stars with a M $>$ 1.3 $M_{\odot}$ with a temperature greater than $\sim 15 \times 10^7$ K. For low mass stars this stage is very long (a few Gyr) since the time spent in MS is an inverse function of the stellar mass (this is because, in order to sustain the stellar structure, high-mass stars burn hydrogen at a very high rate, while low-mass stars can burn their fuel reservoir at much lower rates). In any case, each star, sooner or later, will finish its hydrogen reservoir in the core. When this happens the thermonuclear reactions in the core end.

- Sub Giant Branch (SGB) - At the end of the MS, when the core thermonuclear reactions are going to end, hydrogen is ignited in a thick shell surrounding the stellar nucleus, where the temperature are high enough for this burning to occur. As time goes on, the shell moves outwards, becoming progressively thinner. This phase lasts from a few tens to several hundreds Myr, depending on the mass and metallicity of the star, and it is characterized by an important variation in the surface temperature, while the luminosity

does not change appreciably.

- Red Giant Branch (RGB) - After the SGB phase, a phase begins in which the temperature does not change much, while the luminosity increases significantly. The RGB phase lasts only a small fraction ($\sim 10\%$) of the MS time. During this phase, the hydrogen burning shell ignited during the SGB phase reachs a stable rate and progressively determines an increase of the star luminosity. In this phase stars are partially convective. The progressive penetration of the convection produces the first dredge-up (FDU), in which the outer convection zone progressively engulfs deeper regions, dredging for the first time to the surface matter which has been partially processed through H-burning during the MS. The chemical elements affected by the FDU are essentially C, N, Li, and He. Both He and N abundances increase, whilst Li and C decreases. However, the FDU is not the only important event that occurs during the RGB, in fact, when the incoming H-burning shell crosses the chemical discontinuity left in the deep layers by the convective envelope after the FDU, the stellar luminosity temporarily decreases, and then stars to increase again. The macroscopic effect of these events produce the so-called RGB-Bump, which appears as a "local" (at a given magnitude) excess of stars in the RGB luminosity function of GCs (see e.g. Fusi Pecci et al., 1990; Ferraro et al., 2000; Valenti et al., 2004). It is important to recall also that, during the RGB, an important mass-loss phase occurs and can remove up to 15-20$\%$ (i.e. 0.1-0.2 $M_{\odot}$) of the mass held at the turn-off. The RGB phase ends when helium in the stellar core is ignited with a thermal runaway, the so-called "Helium-flash", which releases a huge quantity of energy. This energy, however, is not released as luminosity but it is used to remove the degeneracy of the helium core. From this moment the star is able to burn helium into carbon through the triple-α process and it moves toward the next evolutive stage, i.e. the HB phase.

- Horizontal Branch (HB) - The HB phase begins when the He burning process starts into the non-degenerate core. In this phase, which lasts roughly $\sim 1\%$ of the time spent in the MS, stars are powered by helium burning in the core and by hydrogen burning in a shell surrounding the core. Each star begins its He-burning phase starting from a "reference" sequence in the CMD: the so-called Zero Age Horizontal Branch (ZAHB). It potentially extends from $\sim$ 4000 up to 40000 K. The position occupied by the star on the ZAHB is determined by its surface temperature and it depends primarily on the star mass. Generally speaking, more massive stars tend to occupy the red part of the HB,

while less massive stars lie in the bluest part. The mass with which stars reach the HB is, of course, a function of the global parameters of the stellar population, like age and metallicity, but it also depends on the mass-loss occurred during the RGB phase. While the metallicity is identified as the dominant parameter determining the HB morphology, several studies in the GCs of our Galaxy suggest that additional parameters are required (see e.g. Ferraro et al., 1997b, 1998). This is the so called "second parameter problem" and several options have been proposed, e.g. Helium content, mass-loss, etc. The next evolutive stage of stars with masses larger than 0.55-0.60 $M_{\odot}$ is the AGB phase, this is due to the fact that these stars have at least 0.1 $M_{\odot}$ to ignite the hydrogen and helium burning in the layers surrounding the nucleus of carbon now off. On the contrary, the less massive HB stars, mostly located in the bluest part the HB, evolve directly through the White Dwarf (WD) cooling sequence.

- Asymptotic Giant Branch (AGB) - At the end of the HB phase, when thermonuclear reactions in the core stop, the He burning shifts in a shell surrounding the C-O core. This flags the beginning of the AGB phase, which is characterized by a slightly decrease of the surface temperature while the luminosity sensibly increases. The AGB phase is the last evolutive stage of intermediate and low-mass stars before they end their lives as WD and is a very rapid phase which typically lasts a few percent of the time spend in the HB, i.e. some Myr. The AGB phase is usually divided in two main stages: the "early" AGB (E-AGB) and the "thermal pulses" AGB (TP-AGB). The E-AGB begins when the He burning shell becomes active, the energy released pushes outwards the overlying H burning shell, which expands and became inactive due to the temperature drop. However, soon after its ignition the He burning shell loses efficiency and switch off. When this happen the contraction of the stellar atmosphere and the subsequent increase of temperature make the H burning shell active. The temporary stop of the He burning shell flags the beginning of AGB phase, in which the He and H shells become alternately active. Only in AGB stars with progenitor masses $>$ 1.2-1.3 $M_{\odot}$ (which are all evolved as WDs or died in Galactic GCs) the TP phase is accompanied by additional dredge-up processes.

2.2 Overall chemistry

GCs have been traditionally assumed to be SSPs, i.e. made of single, coeval and chemically homogeneous stars.

However, soon after the very first spectroscopic observations in the late seventies, it became clear that the chemistry of GCs is more complex. Thanks to the huge technological development of spectroscopic facilities with high spectral resolution and multi-object capabilities in the last two decades, large samples of giant stars in GCs have been observed and abundances of several chemical elements have been obtained. These measurements indicate that different chemical elements show different abundance spreads. In particular, these can exceed a few tenths of dex in the cases of C, N, O, Na, Mg and Al, suggesting that some self-enrichment process should have occurred during the first stages of the GC evolution, on typical timescales of a few hundreds Myrs. Such a behaviour is not peculiar to our Galactic environment but it has been also found in the GCs of M31, Large Magellanic Cloud (LMC) and Fornax dwarf galaxy (Colucci et al., 2009; Johnson et al., 2006; Mucciarelli et al., 2009; Letarte et al., 2006).

2.2.1 Metallicity distribution

At the very early stage of the study of GC systems one of the main issues was the derivation of a proper metallicity scale. The first attempt to derive homogeneous metallicities for GCs was performed by Zinn & West (1984) who observed 60 Galactic clusters obtaining values of [Fe/H] ranging from -2.58 to $+0.24$ dex. This scale was refined by Carretta & Gratton (1997) using for the first time medium-resolution spectra collected with the CASPEC spectrograph mounted at the 3.6m ESO telescope and based on 160 stars observed in 24 Galactic GCs (see also Origlia et al., 1997). They have found no hints of intrinsic iron dispersion in the studied sample. Kraft & Ivans (2003) derived a new metallicity scale by using FeII lines in a sample of 149 stars in 11 GCs. They argued that a reliable derivation of [Fe/H] should be based on FeII lines instead of FeI in order to avoid possible effects related to Local Thermodynamic Equilibrum (LTE) departures, which mainly affect the abundances derived from neutral lines. Also in this case, the authors found no metallicity spread in the analysed sample. The most recent attempt to refine the previous metallicity scale for GCs was performed by Carretta et al. (2009b), who have used medium- and high-resolution spectra collected with FLAMES@VLT to study a sample of $\sim$ 2000 stars in 19 Galactic

GCs. They have not found any noticeable iron spread in the studied sample, the intrinsic scatter being less than 0.05 dex for the majority of GCs. Only for some of the most massive GCs they found some evidence of iron spread and of a mild correlation with the cluster mass.

However, there are at least two major exceptions where a wide metallicity distribution has been found.

- ω Centauri $-$ This object is the most massive (M $> 10^6$ M$_\odot$) and most luminous (M$_V$ < -10 mag) stellar system of the Milky Way. It has a complex color-magnitude morphology, which has been interpreted as due to the presence of several stellar populations (Lee et al., 1999; Pancino et al., 2000; Ferraro et al., 2004a; Bedin et al., 2004; Sollima et al., 2005; Villanova et al., 2007; Pancino et al., 2011a,b). Nowadays, from the analysis of the SGB morphology, which can help in the identification of different components, at least 6 different stellar populations have been clearly detected (Villanova et al., 2014). The metallicity distribution of the system is very wide, ranging from a [Fe/H] ~ -2.0 to ~ -0.2 dex. Of course, such a wide mettalicity distribution coupled with the existence of several stellar populations with different properties makes ω Centauri an "anomalous GC". In fact, due to some similarities with the satellites of our Galaxy it was suggested that ω Centauri could be the remnant of a dwarf spheroidal accreted by the Milky Way in the past. However, this complex stellar system shows several peculiarities which may challenge also this conclusion. In fact, Origlia et al. (2003) and Gratton et al. (2011) have measured enhanced α-element abundances in the most metal-rich population of the cluser, which seems incompatible with the deficiency of α-elements usually observed in the metal-rich stars of dwarf spheroidals.

- Terzan 5 $-$ This system was originally catalogued as a GC and is located in the Galactic Bulge in a very extincted region where the $E(B-V)$ ranges from 2.15 to 2.82 mag (Massari et al., 2012). For this reason, accurate photometric measurements have been possible only by means of infrared observations in J, H and K bands. Ferraro et al. (2009a) by using the Multi-Conjugate Adaptive Optics Demonstrator (MAD) mounted at the VLT have detected the presence of two distinct Red Clumps (RC) belonging to two different populations. Subsequent spectroscopic observations have demonstrated that these two populations have very different metal content: an average [Fe/H] = -0.25 ± 0.07 dex for the metal-poor population and [Fe/H] = $+0.27 \pm 0.04$ dex for the metal-rich

one (Origlia et al., 2011). Moreover, Terzan 5 does not show the typical anticorrelations observed in the majority of GCs. Recently, also another very metal-poor component with an average [Fe/H] = -0.8 dex has been detected (Origlia et al., 2013; Massari et al., 2014a,b), thus leading to an iron distribution wider than 1 dex. The chemical patterns observed in Terzan 5, when interpreted in the context of a self-enrichment scenario, require that the proto-Terzan5 system was originally more massive in order to retain the high-velocity SN ejecta (Ferraro et al., 2009a; Lanzoni et al., 2010). For these reasons, Terzan 5 is no longer considered as a genuine GC but it was suggested to be the remnant of one of the pristine building-blocks from which the Galactic Bulge was born (Immeli et al., 2004).

In a few other GCs some iron spreads, at a level of a few tenths of a de, have been also claimed.

- M22 $-$ This is a metal-poor GC which is suspected to have an intrinsic iron spread. This suspect was originally based on the large colour spread of the RGB in the CMD (Monaco et al., 2004). However, M22 resides in a region deeply affected by differential reddening which makes difficult to properly assess whether the observed colour broadening is due or not to an intrinsic metal spread (Monaco et al., 2004). From a spectroscopic point of view, divergent results have been obtained, all being based, however, on small samples (Cohen, 1981; Pilachowski et al., 1982; Gratton, 1982). Recently, Marino et al. (2009, 2011) have analysed high-resolution spectra of 35 giant stars finding a $\sim$0.4 dex wide [Fe/H] distribution. Also, they highlighted that M22 is composed by two groups of stars, characterized by different metallicity, CNO and s-process element abundances: the first group with an average iron abundance of [Fe/H] = -1.82 dex, [(C+N+O)/Fe] = $+0.28$ dex and solar-scaled [s/Fe] abundance ratios, while the second group has [Fe/H] = -1.67 dex, [(C+N+O)/Fe] = $+0.41$ dex and an enhancement of $+0.3/+0.4$ dex for the [s/Fe] ratios. As a reasonable explanation the authors have suggested that in the past M22 was massive enough to retain the ejecta of SNe and AGB stars, being these stars the main site of s-process element production.

- M54 $-$ This GC is a peculiar system which is located in the center of the Sagittarius dwarf spheroidal, the remnant of a galaxy that is going to be disrupted by the interaction with the Milky Way (Ibata et al., 1994; Bellazzini et al., 1999). M54 has a complex CMD morphology, which is the result of the presence of two main components: the metal-poor

stars associated with the Sagittarius dwarf galaxy, and those belonging to the GC (Siegel et al., 2007). From the analysis of 76 RGB stars associated to the original population of the cluster, Carretta et al. (2010b) have detected a small iron spread of ~ 0.19 dex and the presence of the Na-O anticorrelation. A comparable, but slightly smaller, spread of ~ 0.15 dex was also found by Mucciarelli et al. (2014) from the anaysis of a sample of 51 stars belonging to the cluster. In any case, the presence of Na-O anticorrelation is thought to be a genuine characteristic of GCs, which tend to exclude the idea that M54 is the remnant of the nucleus of the Sagittarius dwarf galaxy. This idea was supported also by the results of Bellazzini et al. (2008), who suggested that the current position of M54 is due to the decay of the original orbit due to dynamical friction. A possible speculative explanation has been proposed by Carretta et al. (2010b) who suggested that M54 is an anomalous cluster who have experienced a prolonged period of star formation occurred at high rate if compared to normal GCs.

- NGC3201 − Among the anomalous GC candidates, NGC3201 is a controversial case because different analyses provide conflicting results about its level of iron homogeneity. Gonzalez & Wallerstein (1998) first analysed a sample of CTIO high-resolution spectra of 18 cluster stars, finding a large iron variations (Δ[Fe/H] ~ 0.4 dex). Further analyses by Carretta et al. (2009c) and Muñoz et al. (2013) based on high-resolution, high signal-to-noise ratio (S/N) spectra (FLAMES@VLT and MIKE@Magellan, respectively), do not highlight similar spreads, ruling out large star-to-star variations. However, both studies are based on small star samples (13 and 8 respectively), so they may suffer from low statistics. On the other hand, Simmerer et al. (2013) analyzed UVES@FLAMES and MIKE@Magellan high-resolution spectra of 24 giant stars, revealing a metallicity distribution as large as 0.4 dex (not explainable within the uncertainties) and with an evident metal-poor tail (5 out of 24 stars). This iron spread, qualitatively similar to that observed in M22 by Marino et al. (2009, 2011), would make NGC3201 the least massive GC ($\sim 1.1 \times 10^5\ M_\odot$; McLaughlin & van der Marel 2005) with evidence of SN ejecta retention.

- M2 − This massive system is characterized by a complex CMD morphology which flags the presence of multiple RGB and SGB components (Piotto et al., 2012; Milone et al., 2015). In particular, M2 is known to host a second, redder, RGB interpreted as due to the presence of a population with different C and N abundances (Lardo et al., 2012). Lardo et al. (2012) have also confirmed that two C-enhanced stars previously detected by

Smith & Mateo (1990) belong to this peculiar RGB. In a subsequent analysis, Lardo et al. (2013) have also detected a peculiar pattern for the s-process elements of the second RGB, in particular for what concerns Sr and Ba. Finally, Yong et al. (2014) have found that M2 hosts at least three populations with different average metallicities ([Fe/H] ~ -1.7, -1.5 and -1.0 dex) and the star-to-star variations are not limited to iron but are also detected for both s- and r-process elements. Hence, also for M2, a firm conclusion about its star formation history and evolution cannot be firmly drawn.

- NGC5286 − This cluster has been recently investigated by Marino et al. (2015) who have analysed a sample of 62 RGB stars by using FLAMES@VLT data. They highlighted that NGC5286 well resembles the case of M22, in which two populations with different [Fe/H] and s-process elements are present. The iron-poor component resulted to be also poor in s-process elements, while the iron-rich component is also s-process rich. Moreover, they concluded that both the components show important iron star-to-star variations, which globally tags NGC5286 as an anomalous GC with a non-negligible metallicity dispersion. Accordingly, Marino et al. (2015) have suggested that this object was probably more massive in the past, and thus able to retain SNe ejecta, or even that it could be the remnant of the nucleus of a dwarf galaxy tidally disrupted by the interactions with the Milky Way.

2.2.2 Pre-enrichment

Lithium, together with hydrogen and helium, is a product of the Big Bang nucleosynthesis. Hence, the first generation of stars in GCs are expected to have a Li abundance close to the cosmological value, while in the subsequent stellar generations we may expect to find only Li-poor or Li-free stars. This is due to the fact that Li burns at $\sim 2.5 \times 10^6$ K, a temperature that is roughly one order of magnitude lower than any other characteristic temperature ($> 10^7$ K) of thermonuclear reactions occurring in stars. However, observations have revealed a more complex scenario: three Na-rich stars with low Li abundance have been detected in NGC6397 (Lind et al., 2009a), while most of the observed stars display a uniform Li abundance (compatible with the cosmological value) but a large range of Na abundances. M4 displays a very small intrinsic Li dispersion, without correlation between O and Li abundances (Mucciarelli et al., 2011) and with a weak Li–Na anticorrelation (Monaco et al., 2012).

The study of the Helium content of stars in GCs is crucial for a number of fundamental

aspects. First of all, the He content in GC stars is thought to be a good tracer of the primordial He abundance because these are among the first stars formed in the Universe and the mixing episodes occurring during their evolution only marginally affect their surface He abundance (Sweigart, 1997).

However, there are a number of direct and indirect pieces of evidence that different subpopulations in GCs can have different He abundance. For example, a different He content has been invoked as one of the possible "second parameters" (together with age, CNO/Fe ratio, stellar density; see e.g., Dotter et al., 2010; Gratton & Carretta, 2010; Dalessandro et al., 2013), to explain the observed distribution of stars along the HB, with the overall metallicity being the first parameter. Stars on the bluest side of the HB may have a higher He content. Recently, a differential analysis performed by Pasquini et al. (2011) on two giants in NGC2808 with different Na content indicates that the Na-rich star is also He enriched at odds with the Na-poor one. Villanova et al. (2009, 2012) derived He, Na and O abundances for HB stars in NGC6752 and M4, respectively, finding that the stars along the reddest part of the HB of NGC6752 have a standard He content, as well as Na and O abundances compatible with the first generation, while the stars in the bluest part of the HB of M4 are slightly He-enhanced (by ~ 0.05), with Na and O abundance ratios compatible with the second stellar generation. In a similar way, Marino et al. (2014) found clear evidence of He enhancement (by ~ 0.09) among the bluest HB stars in NGC2808 that are also all Na-rich.

SNII are likely the first, main polluters of the Intra-Cluster Medium (ICM) after the Big Bang nucleosynthesis from which stars in GCs formed. These objects originate from the core collapse of massive stars, which have very short lifetimes. Hence, SNII can be responsible for a rapid pre-enrichment of gas with α-elements and some iron, thus explaining why to date no GCs with [Fe/H] ≤ -2.5 dex have been found and why the [α/Fe] abundance ratios are normally enhanced by a factor of 2-3.

The α-element tipically measured in GC giants are O, Mg, Si, Ca and Ti. While O and Mg can show significant star-to-star variations (see Section 2.2.3), Si, Ca and Ti do not. The average values of [Si/Fe] and [Ca/Fe] in GCs at different metallicities (see Figure 2.2) well match the typical values observed in the halo stars (Gratton et al., 2004). This suggests that the nucleosynthesis processes occurred in GCs were not able to alter the abundance of these elements, which probably reflects the original composition of the material from which they have formed.

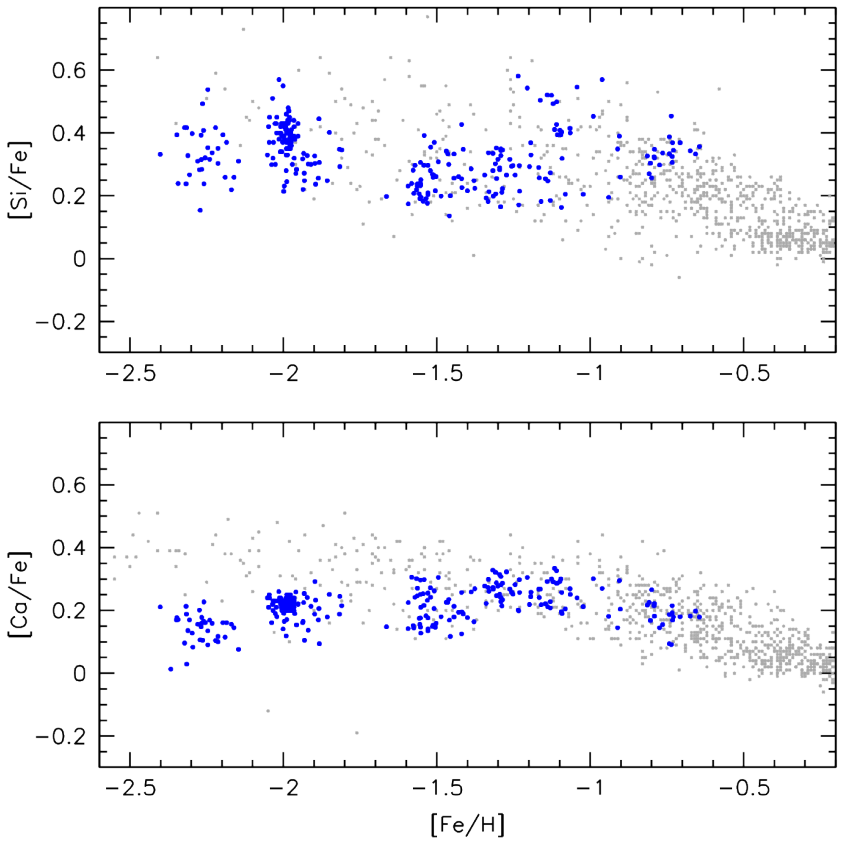

Figure 2.2 The behaviour of [Si/Fe] and [Ca/Fe] as a function of [Fe/H] (large blue dots) measured in several GCs by Carretta et al. (2009a). Values measured in field halo and disk stars (light gray, small dots) by Edvardsson et al. (1993); Fulbright (2000); Bensby et al. (2003); Gratton et al. (2003); Reddy et al. (2003, 2006) are also plotted for comparison.

2.2.3 Star-to-star variations and signatures of self-enrichment

Historically, the first example of chemical star-to-star variations within a GC has been observed in the strengths of molecular bands of CH, CN and NH (Kraft, 1979; Freeman & Norris, 1981; Smith & Norris, 1984; Smith, 1987) and in the depths of lines of OI, NaI, MgI and AlI (Pilachowski et al., 1983; Smith & Wirth, 1991; Gratton et al., 2001). One of the first hints of the presence of anticorrelated variations between CH and CN abundances have been detected in RGB star samples of several GCs (Norris, 1981; Norris et al., 1981b; Norris & Freeman, 1982; Smith & Norris, 1982). Recently, C and N abundance measurements have been also obtained from low resolution spectroscopy of blue-optical CN-CH molecular bands (see e.g. Alves-Brito et al., 2008; Martell et al., 2008; Pancino et al., 2010) providing evidence of CN bimodality and CN-CH anticorrelation. Such a behaviour can-

not be univocally explained by standard nucleosynthesis, which converts both carbon and oxygen into nitrogen through the CNO cycle and brings the processed material to the star surface by means of the first dredge-up mixing process (Iben, 1965), occurring soon after the star leaves the MS.

From the very first samples of RGB stars analysed by using high-resolution spectra it was also found that those depleted in carbon and enhanced in nitrogen are also depleted in oxygen and magnesium (Cottrell & Da Costa, 1981), while they are enhanced in sodium and aluminium (Sneden et al., 1992; Carretta et al., 2010a). The presence of Na-O and Mg-Al anticorrelations (see Figure 2.3) seems to suggest a common origin strictly linked to the formation channels of these elements in the stellar interiors, where a series of proton-captures happen thanks to the high-temperatures reached. In Figure 2.4 the main chains of the NeNa and MgAl cycles are shown.

In the NeNa cycle, ^{20}Ne is progressively converted in ^{23}Na by several proton captures while in the MgAl chains, ^{24}Mg is finally converted in ^{26}Al (Denisenkov & Denisenkova, 1989; Langer et al., 1993; Cavallo et al., 1996; Prantzos et al., 2007; Straniero et al., 2013). These two cycles, however, require temperatures of about 3×10^7 K and $\sim 7\times10^7$ K to take place, i.e. temperature much higher than that at which the CNO-cycle occurs in low mass stars (Langer et al., 1997). Interestingly, these anticorrelations have been detected in the majority of Galactic GCs (Carretta et al., 2009a), althought these systems host low mass stars only. It is thus impossible to justify the presence of chemical anomalies by assuming that they are the result of nuclear reactions occurred in these stars, and some sort of external pollution is unavoidably required.

Thus, the presence of anticorrelations, involving elements from carbon to aluminium, is likely the result of some pre-enrichment of the gas from which stars originated. This of course has raised new questions about the nature of the polluters.

One of the first attempt to explain the presence of anticorrelations claimed some enrichment from SNII. However, this scenario faces two main problems: (a) the total energy released in a SNII explosion is of the order of $\sim 10^{51}$ ergs (Salaris & Cassisi, 2006), which is comparable to the typical GC binding energy; hence, the materials ejected by the star can easily escape the GC potential well and (b) just before the explosion, a SNII has an onion-like structure with layers rich of C, O, Mg, Si, Ca but poor in Na and Al (Salaris & Cassisi, 2006), so the contribution of these stars does not favor the development of anticorrelations. In the latest years a number of different polluters of the ICM have been suggested: interme-

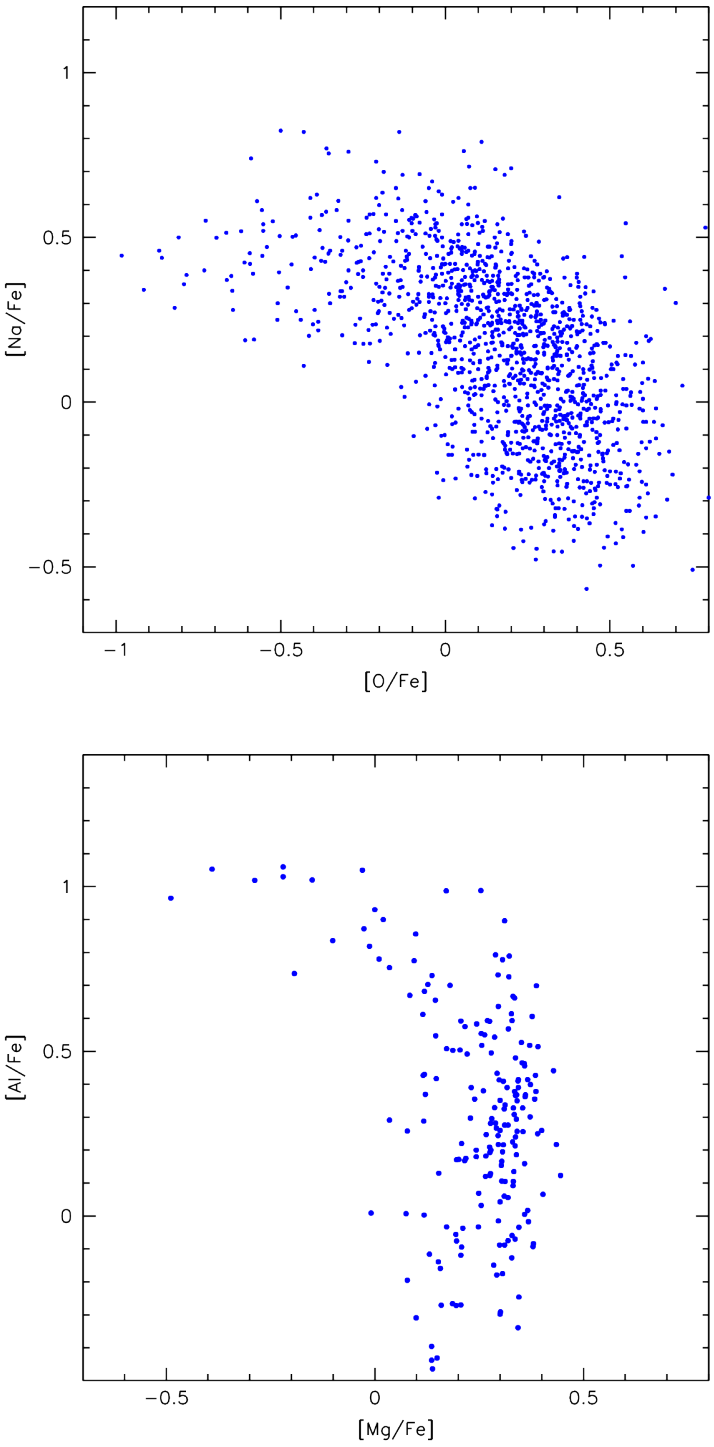

Figure 2.3 The Na-O and Mg-Al anticorrelations observed in GCs, from data collected with FLAMES and UVES spectrographs by Carretta et al. (2004a, 2006, 2009a,b, 2014).

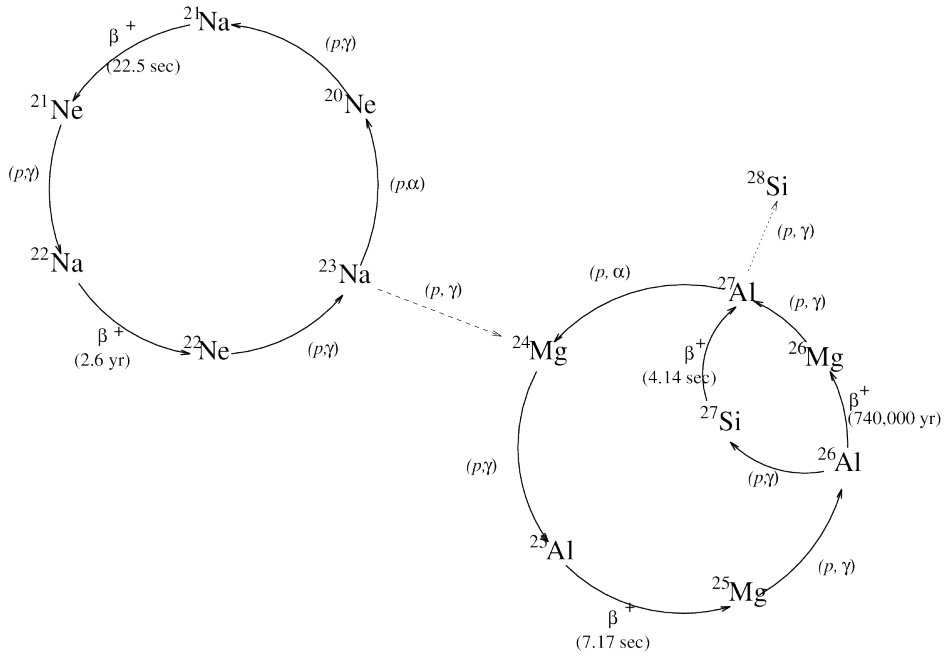

Figure 2.4 Schematic view of the NeNa and MgAl cycles (from Cavallo et al., 1996). The labels near the arrows show the reactions occurring in each step.

diate mass AGB stars (Ventura et al., 2001; Fenner et al., 2004; Ventura & D'Antona, 2005), fast rotating massive stars (FRMS) (Decressin et al., 2007), massive interacting binaries (de Mink et al., 2009) and novae (Smith & Kraft, 1996; Maccarone & Zurek, 2012). The ejecta of these stars have the main advantage that they are able to remain in the potential well of GCs and pollute the ICM with different chemical imprints on different timescales. However, the complex chemical patterns observed to date in GCs, which often also differ from cluster to cluster, are likely the result of the interplay between different polluters (Marcolini et al., 2009; Bastian et al., 2013).

Among the light element abundances measured in GC giants there are also those of fluorine and potassium, whose trends and overall nucleosynthesis are however still debated.

Fluorine is one of the most elusive species measurable in stars, but it has a particular importance since it is extremely sensitive to the physical conditions within the stellar atmospheres. Very few and sparse abundance estimates in GCs are available in literature: Cunha et al. (2003) measured F in red giants in the Large Magellanic Cloud and ω Centauri finding that the F/O ratio declines as the O abundance decreases and the two giants observed in ω Centauri have particularly low F/O values. They argue that these results are consistent with most F production coming from either neutrino nucleosynthesis or W-R stars rather than

from AGB stars in these systems. On the contrary, the abundance of fluorine is found to correlate with oxygen and anticorrelate with the sodium and aluminium abundances in 7 giants of M4 (Smith et al., 2005) and in 6 giants NGC6721 (Yong et al., 2008). The same correlations have been found from the analysis of six cool giant stars in M22 by D'Orazi et al. (2013), however they also found that the F content positively correlates with two different sub-groups of s-process rich and s-process poor. The comparison with theoretical models has suggested that AGB stars of intermediate mass may be responsible for this chemical pattern.

Very few abundance measurements of potassium are available in GCs. This element is thought to be formed during hydrostatic oxygen burning in massive stars, so a behaviour not so different from those of α-elements is expected. However, Mucciarelli et al. (2012), from the analysis of a sample of 49 giant stars belonging to the GC NGC2419, have detected a clear anticorrelation between K and Mg. The analysis of a sample of 119 stars in the GC NGC2808 by Mucciarelli et al. (2015c) highlighted the same trend. This is not expected since, in the framework of SNII yields, K abundances are expected to correlate with Mg ones. Mucciarelli et al. (2015c) have suggested that the behaviour of K could be the result of the self-enrichment processes occurred in GCs with the contribution of different polluters.

The abundances of neutron-capture elements measured so far in GCs also show some peculiarities that change from cluster to cluster. Regarding the s-process elements, the most deeply investigated element is Ba. This is due to the fact that some strong Ba transitions are available in the blue/optical spectrum and they can be observed and measured also in low-SNR spectra. In GCs, the largest survey of Ba abundances has been performed by D'Orazi et al. (2010), who have measured Ba abundances in more than 1200 individual stars in 15 Galactic GCs (see Figure 2.5). The studied GCs cover a range in metallicity of up to $\sim$ 1.6 dex, from [Fe/H] = -2.3 dex (NGC7099) up to [Fe/H] = -0.7 dex (47Tuc). They have found that in each GC the [Ba/Fe] ratios show a dispersion of the order of 0.15-0.3 dex, compatible with the measurement errors, so no clear hint of intrinsic star-to-star variations in the Ba content has been found. Slightly different is the comparison with the average [Ba/Fe] of clusters at similar metallicities. For the GCs with [Fe/H] < -2.0 dex D'Orazi et al. (2010) have found a solar [Ba/Fe] values, while for those with [Fe/H] > -1.7 dex they have found [Ba/Fe] values which increase from $\sim +0.2$ dex up to $+0.7$ dex (see their Figure 1). No clusters present a correlation between Na and Ba abundances, indicating that there is no significant contribution from low-mass AGB stars to the intracluster pollution.

The same behaviour has been observed also for other two s-process elements like Sr and Y, although not so striking. James et al. (2004), from the analysis of a sample of MS and SGB stars belonging to the GCs NGC6397, NGC6752 and 47Tuc have detected a mild increasing trend of [Sr/Fe] as [Fe/H] increase, while for [Y/Fe] they have found values roughly compatible with the solar value. The authors have concluded that the observed behaviour for light- and heavy-elements in GCs cannot be explained with a self-pollution scenario.

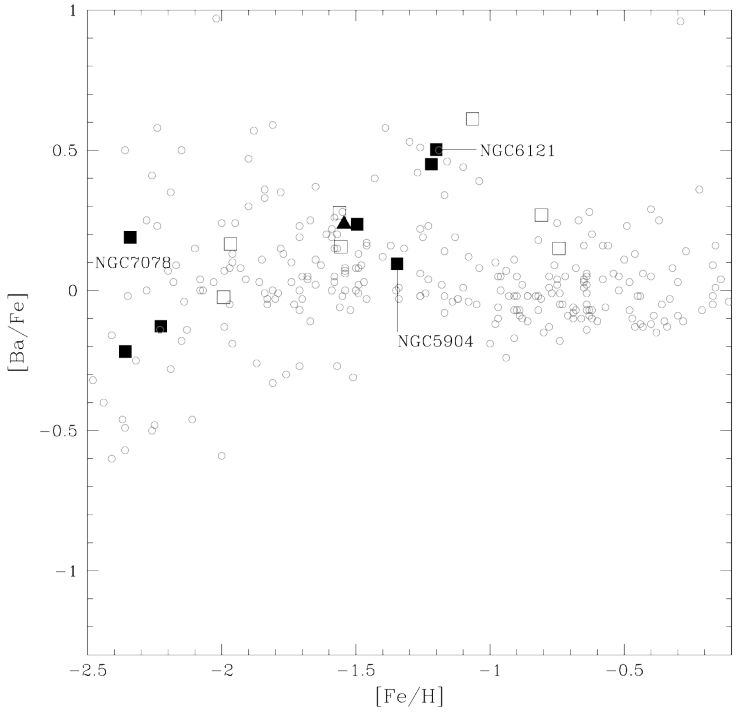

Figure 2.5 The behaviour of [Ba/Fe] as a function of [Fe/H] measured in several GCs (large symbols) by D'Orazi et al. (2010). Empty and filled squares are for disk/bulge and inner halo GCs, while the filled triangle is for the only outer halo cluster NGC1904. The small gray dots mark the values measured in field stars.

It is interesting to note that for the majority of the GCs in which an iron spread has been found also some peculiar behaviours of the s-process abundances have been observed. In ω Centauri there is a positive correlation between [Fe/H] and neutron-capture elements, suggesting that s-processes have been increasingly efficient during the evolution of the system (see Johnson & Pilachowski 2010; Marino et al. 2012). For M22, Marino et al. (2009, 2011, 2012) have highlighted the presence of two populations with a difference in [Fe/H] of $\sim$ 0.15 dex which show also a difference in s-process elements. Moreover, these two

population seems to follow their own Na-O anticorrelation. The same behaviour has been observed in the GC NGC1851 where the s-process elements appear to be correlated with Na and Al abundances (Yong & Grundahl, 2008). For these two clusters, there are also hints of an overabundance of CNO sum for the observed stars (Marino et al., 2012; Yong et al., 2009). This is a strong evidence pointing toward a chemical imprint left by AGB stars. These stars seems to be a natural explanation for these peculiar chemical patterns since they can account for the presence of the Na-O anticorrelation and they are the main source of s-process elements during thermal pulses. Furthermore, AGB stars are able to release CNO-processed materials, thus altering the CNO sum in subsequent stellar populations.

Among the r-process elements, Eu is the one mostly measured in GC giants, however, the widely used feature is the weak line at 6645 Å, which requires high-quality and high-SNR spectra. This makes the Eu measurements quite difficult and only sparse derivations are available. Shetrone (1996a) has derived Eu abundances in several Galactic GCs covering a metallicity range from roughly [Fe/H] ~ -2.2 up to -0.8 dex. The author found an average [Eu/Fe] which remains almost constant at about $+0.4$ dex. Moreover, within each cluster, a very small dispersion of [Eu/Fe] abundances has been measured. The lack of correlation with O abundances measured in the same stars suggests that, if SNII are the source of both elements, one of the two elements should be produced in a metallicity-independent way. The small dispersion of [Eu/Fe] detected in the majority of GCs, however, is not always observed. An important exception is the GC M15 in which [Eu/Fe] ranges over 0.5 dex at constant [Fe/H] (Sneden et al., 1997), which may challenge the idea that Eu is produced exclusively by r-processes.

2.2.4 Open questions

The observed light-element abundance anomalies in GCs are currently interpreted as signatures of the presence of at least two stellar generations.

The first generation (FG) stars formed in the very early epoch of the GC formation while the second generation (SG) stars formed after some hundreds Myr and the chemical imprint of each stellar generation takes a fundamental role in defining the chemical properties of the descendants.

However, there are still several open questions: **(1)** how many star formation episodes actually occurred in GCs? Which is the mechanism that triggered these events? **(2)** Which mechanism is responsible of the pollution of the gas from which the second stellar gen-

eration formed? How the gas polluted by the FG stars could remain bound in the system despite the shallow potential well? **(3)** Considering that, nowadays, GCs are almost devoid of gas, which mechanism has been able to remove the residual gas after the star formation episodes? **(4)** In several GCs the number of FG stars is roughly equal to the number of SG ones, while the FG component is expected to be numerically more consistent; thus which was the fate of the missing FG stars?

Several authors attempted to answer these questions by suggesting plausible scenarios based on both theoretical and observational arguments. In the following we will briefly summarize them:

- D'Ercole et al. scenario - By means of hydrodynamical and N-body simulations D'Ercole et al. (2008) have suggested that GCs were at least 10-20 times more massive in the past. The FG stars, which have formed from a pristine gas mainly enriched by SNII, release in the ICM yields with chemical patterns associated to super-AGB and massive AGB nucleosynthesis (Pumo et al., 2008; Ventura & D'Antona, 2009). In this way, the SG component mainly forms in the center of the cluster where these materials have been settled. D'Ercole et al. (2008) also suggested that, according to this, the stars that escape the cluster during its lifetime belong to the FG component. This idea can explain why the SG stars are more centrally concentrated and why nowadays the proportion between FG and SG is roughly the same. After the SG formation, the first stars which explode as SNIa are responsible of the quenching of the star formation (SF), removing most of the residual gas from the cluster. After some time, this gas may flow again in the central region driven by cooling mechanisms and mix with low-velocity AGB ejecta triggering a new SF episode, which should produce subsequent stellar generations. These new stellar generations may have a very peculiar chemical composition which should explain, at least in part, the presence "extreme" stars in the NaO and MgAl planes.

- Conroy & Spergel scenario - In this scenario the GCs are assumed to have a initial mass similar to the current one. The FG stars are assumed to form from material pre-enriched in metals (i.e. with the present-day metallicity) and the SF episode ends when the first SNII explode and sweep out the gas from the system. After this phase, the ICM of the cluster is polluted by the AGB ejecta which can mix with the materials accreted from the environment surrounding the GC. This freshly available gas can now take part in the SG star formation. Also this SF episode produces a number of SNII and subsequent

SNIa, which are able to remove the residual gas from the cluster, thus quenching any subsequent SF event. This scenario has the main advantage that it can naturally explain the presence of multiple stellar populations and the absence of residual gas in the clusters. However, D'Ercole et al. (2011) have highlighted that it does not account for the high helium content observed in some clusters (which it cannot be released by FG stars only).

- Carretta et al. scenario - According to this scenario, the GCs that we observe today are the remnants of more massive structures, which have been tidally disrupted by the interactions with the Galaxy. The FG stars formed from a gas pre-enriched by SNII and they can pollute the ICM with typical imprint of massive-AGB and FRMS. The ICM pre-enriched in this way is mainly located in the center of the systems, where the SG stars form. After some Myr also the more massive SG stars end their lives as core-collapse SNe and quench the SF processes by removing the residual gas from the cluster. During their evolution, GCs are expected to loose the majority of the original mass and all dark matter component, and also the primordial population of stars is almost completely lost. Indeed, the scenario suggested by Carretta et al. (2010c) seems to explain why metal-poor stars, with [Fe/H] < -2.5 dex, have not been found in GCs: they supposed to be lost and currently form the halo population.

- Valcarce & Catelan scenario - This scenario suggests that the main actor in defining the presence of star-to-star abundance scatter and the presence of multiple stellar populations is the mass of the *precursor*, i.e. the mass of the cloud that formed the system. The most massive precursors are able to retain the ejecta of massive stars and core-collapse SNe, thus they can explain both chemical anomalies and the presence of multiple stellar populations. The intermediate-mass precursors can only retain the gas ejected by massive stars through stellar winds, while they are unable to keep the ejecta of core-collapse SNe. The systems formed by small precursors are able to retain only the slow wind of massive stars and low-mass AGBs. In any case, an important mass-loss during the system lives needed to account for the lack of a fraction of FG stars. At the same time, after the formation of the FG component, the pristine gas located in the outskirts of the system begin to fall in the central region, thus triggering a new SF episode. This scenario is thus able to explain the presence of multiple stellar populations and the different behaviour of anticorrelations. In fact it is suggested that the extreme high-Na/low-O stars are formed with materials processed by high-mass stars while the normal high-Na/low-O stars have

been formed from massive- and intermediate-AGB ejecta.

- Decressin et al. scenario - This scenario is mainly based on the enrichment due to FRMS (Decressin et al., 2007). They postulated that the initial mass segregation determines the formation of massive stars in the very central part of the system, and since SF occurs locally around the massive stars, also the SG component is concentrated in the center of the system. So the mass-loss, which preferentially take place in the most external regions of the system, will reduce the number of FG stars. However, even this loss is not able to balance the ratio between FG and SG stars, which was observationally estimated in several GCs and resulted to be near 50:50. Hence, an additional mechanism is needed to efficiently expel a non negligible fraction of FG stars. Decressin et al. (2010) have suggested that the gas expelled by the very first SNe is able to lower the GC potential well and make easier the expulsion of the most external FG stars.

Chapter 3

Chemical abundances of AGB stars in globular clusters

In principle, MS stars would be the ideal tracers of the chemical enrichment history of GCs since they did not undergo mixing processes and hence all their surface abundances fully reflect the initial composition of the gas from which they formed. However, being much fainter than evolved stars, they can be observed mainly at low-medium resolution in the closest GCs.

Hence, up to now, most of the chemical abundance measures in GC stars have been obtained by observing RGB and Red Clump (RC) stars, which are luminous enough to be studied with the current generation of spectrographs with medium-high resolutions at 8-10mt class telescopes. The spectra of these stars have many metal lines sampling all the most important chemical species.

Among the bright evolved stars in GCs there are those evolving along the AGB, which can also provide crucial constraints on the surface abundance change of chemical species like CNO and s-process elements due to mixing processes in the stellar interiors during the post-MS evolutionary stages.

However, due to their short lifetimes, the number of AGB stars observable in an old GC is small, about a factor of 4-5 smaller than the number of RGB stars of comparable luminosity. Additionally, high-quality photometry and large color baselines are needed to properly separate genuine AGB from RGB stars. Hence, despite their luminosity, massive and systematic chemical studies of AGB stars in GCs are still lacking. Accurate determinations of their atmospheric parameters and abundances based on high-resolution spectroscopy are available for a few GCs only, namely M4 (Ivans et al., 1999), M5 (Ivans et al., 2001; Koch & McWilliam, 2010) and 47Tuc (hereafter 47Tuc, Wylie et al., 2006; Koch &

McWilliam, 2008; Worley et al., 2009), and they are all based on small samples (no more than 6 AGB stars in each of the quoted clusters). A few other studies have been focused on the determinations of C, N and Na abundances. Mallia (1978) and Norris (1981) have used medium- and high-resolution spectra to study RGB and AGB star samples in the GCs 47Tuc, NGC6397, NGC6656 and NGC6752 finding the presence of CN-strong and CN-weak stars. The same investigation has been performed by Briley et al. (1993) on a sample of 24 giant stars in M55, finding only one star compatible with CN enhancement. Finally, Campbell et al. (2013) and Johnson et al. (2015) have investigated the behaviour of Na abundances in NGC6752 and 47Tuc, by using medium-resolution FLAMES spectra.

However, three studies in particular have recently provided quite unexpected results, which opened new questions about the physics of AGB stellar atmospheres and their properties in GCs. In the following we will briefly examine them.

3.1 NLTE effects in AGB stars

Ivans et al. (2001) performed a detailed analysis of a sample of 36 AGB and RGB stars belonging to the GC M5 by using high-resolution spectra taken with HIRES@KECK spectrograph. In the analysis they adopted the full spectroscopic approach to compute the abundance of chemical species, implying that the surface gravity has been constrained by imposing ionization equilibrium of iron lines. They found that the average [Fe/H] of AGB stars is ~ 0.2 dex lower than that computed from RGB stars. After several checks on the adopted procedure they found that, if photometric gravities are assumed, the average [FeII/H] of AGB stars is in perfect agreement with that derived from RGB stars, while the average [FeI/H] of AGB stars remains lower than that derived for RGB stars. This discrepancy cannot be explained by measurement uncertainties or an incorrect derivation of the atmospheric parameters, and it was not observed in RGB stars belonging to the same cluster and analysed in a homogeneous way. The authors interpreted this evidence in terms of possible NLTE (Non Local Thermodynamic Equilibrium) effects in the atmospheres of the AGB stars, since these effects mainly affect the neutral lines while leaving unaltered the ionized ones.

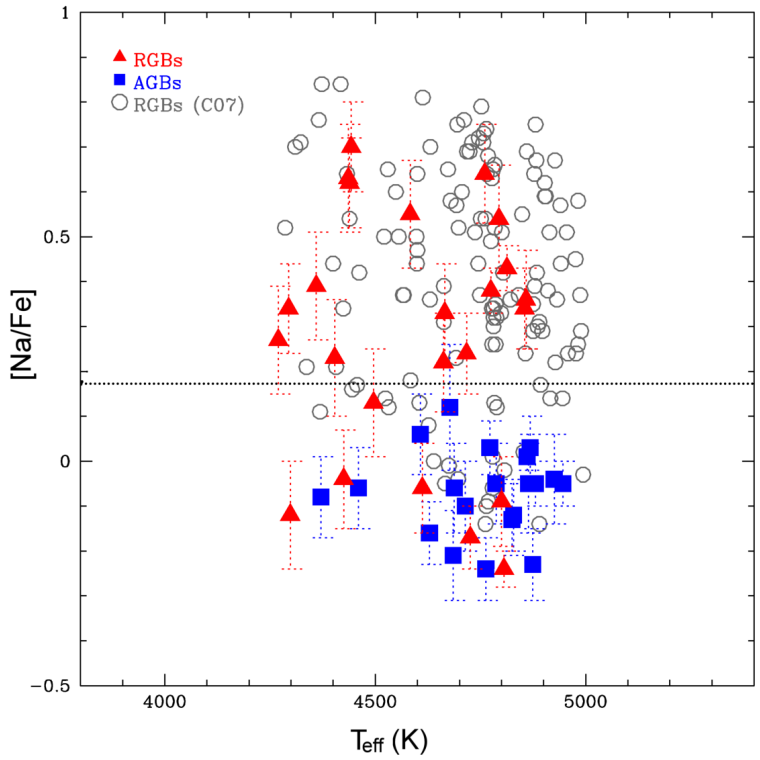

Figure 3.1 The behaviour of [Na/Fe] as a function of T_{eff} for RGB (red triangles, 24 stars) and AGB stars (blue squares, 20 stars) found by Campbell et al. (2013). For comparison, the RGB stars analysed by Carretta et al. (2007) are showed as large empty dots.

3.2 The lack of SG AGB stars in GCs

As discussed in Secion 2.2.3, the Na abundances of the stars in GCs is usually used as a proxy to distinguish the different stellar populations within the same cluster. Recently, Campbell et al. (2013) have analysed a sample of 20 AGB and 24 RGB stars belonging to the GC NGC6752 observed with the FLAMES@VLT spectrograph. They have found that the RGB stars show the presence of both Na-rich and Na-poor stars, spanning a range fully compatible with previous determinations available in literature (see Figure 3.1). However, all the AGB stars in their sample resulted to be Na-poor, with [Na/Fe] values compatible with those observed in FG stars. Campbell et al. (2013) have concluded that all SG stars fail to ascend the AGB. This result is even more challenging by considering that the second-generation population contains the majority (70%) of the stars in NGC6752, hence the presence of Na-rich SG AGB stars is expected. The authors have also critically discussed some possible explanations; however, up to now it is still unclear why and how the the SG stars of NGC6752 can skip the AGB phase.

3.3 AGB overconcentration in the core of 47Tuc

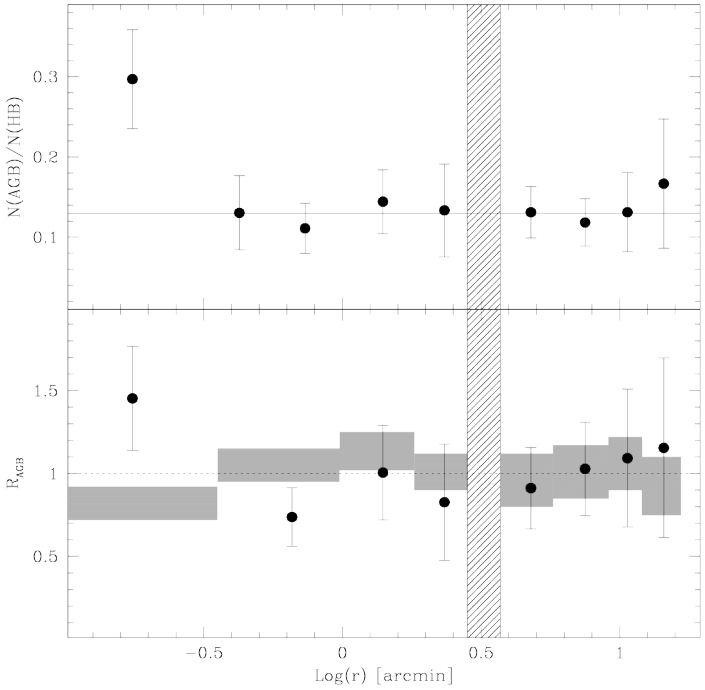

Figure 3.2 Relative frequency of AGB-to-HB stars (upper panel) and double-normalized specific frequency of AGB stars (lower panel) as a function of the projected distance from the center of the GC 47Tuc by Beccari et al. (2006). In the innermost radial bin the number of AGB stars is roughly twice the average value (black horizontal line).

Beccari et al. (2006) have computed the radial distribution of RGB, HB, bright-HB (hereafter bHB, defined as stars slightly brighter than in normal HB stars) and AGB stars in the GC 47Tuc by using several photometric images obtained with the ACS camera mounted on board the HST. They have detected an "overconcentration" of bHB and AGB stars toward the cluster central region, with respect to RGB and HB stars. In particular, for the AGB sample a number count excess of about 30% has been found within the innermost 21 arcsec (see the innermost point in Figure 3.2), while in the outer cluster regions, the AGB stars follow the same radial distribution of the other populations. This overconcentration cannot be justified by invoking the standard stellar evolution theory and cannot be explained by dynamical processes (as mass segregation) acting on genuine AGB stars. This evidence (overabundance and central segregation) suggests the presence among the AGB stars of an extrapopulation of massive objects, probably related to the evolution of binary systems (for

instance, like evolved Blue Straggler Stars: BSSs). Thus, AGB stars in the innermost region of 47Tuc promise to be an ideal sample where evolved BSS could be detected.

3.3.1 Blue straggler stars in GCs

BSSs are commonly defined as stars brighter and bluer than the MS turn-off point in the CMD of the host stellar cluster. Firstly identified by Allan Sandage in the GC M3 (see Figure 3.3), they are thought to be central hydrogen-burning stars, more massive than the MS stars (Shara et al., 1997; Gilliland et al., 1998; Fiorentino et al., 2014). In GCs, BSSs have typical masses in the range 1.2-1.6 $M_{\odot}$ (Ferraro et al., 2006a; Tian et al., 2006; Lanzoni et al., 2007; Sills et al., 2009). Two main formation channels have been proposed: mass-transfer in binary systems (McCrea, 1964) and direct stellar collisions (Hills & Day, 1976). Since BSSs are more massive than normal cluster stars, they suffer from the effect of dynamical friction, which makes them progressively sinking towards the cluster center (Mapelli et al., 2006; Lanzoni et al., 2007; Alessandrini et al., 2014), and for this reason they have been found to be powerful probes of the internal dynamical evolution of the host cluster (Ferraro et al., 2012, 2015; Miocchi et al., 2015).

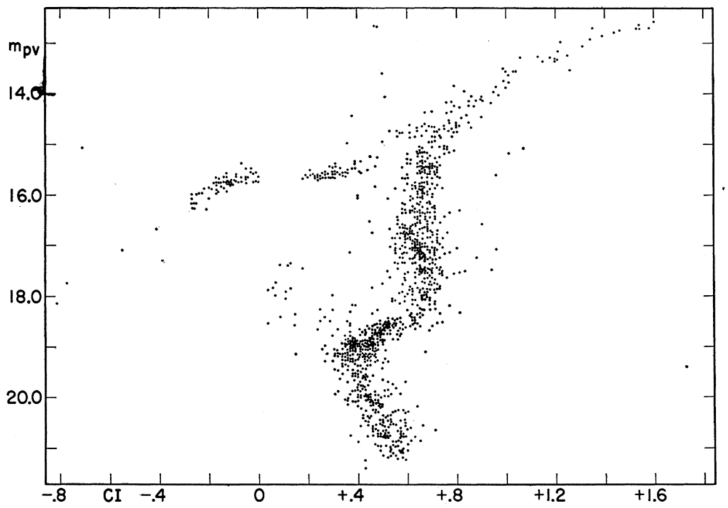

Figure 3.3 CMD of the GC M3 taken from Sandage (1953), where the BSS stars have been identified for the first time.

While BSSs can be easily identified during their core hydrogen-burning phase, they are photometrically indistinguishable from their low-mass sisters in advanced stages of the subsequent evolution. This is the reason why, although BSSs have been routinely observed for decades in GCs (Ferraro et al., 2003a; Piotto et al., 2004; Leigh et al., 2007), in several

open clusters (Geller & Mathieu, 2011; Gosnell et al., 2014) and also in dwarf galaxies (Mapelli et al., 2009; Monelli et al., 2012), only a few identifications of evolved BSSs have been obtained so far. Three candidates have been recently identified from asteroseismology studies in two open clusters (NGC6791 and NGC6819; Brogaard et al., 2012; Corsaro et al., 2012) and with an estimated mass in the range 1.2-1.5 $M_{\odot}$. Only a candidate evolved BSS is known in GCs: the anomalous cepheid V19 in NGC5466 (Zinn & King, 1982; McCarthy & Nemec, 1997) with an estimated mass of 1.6 $M_{\odot}$. Photometric criteria have been suggested to optimize the search for candidate evolved BSSs: for instance Renzini & Fusi Pecci (1988) and Fusi Pecci et al. (1992) suggested to look at a region of the CMD between the horizontal branch (HB) and the base of the asymptotic giant branch (AGB, the so-called AGB-clump; Ferraro et al., 1999a), where evolved BSSs experiencing the core helium burning phase (predicted to be brighter than that of *canonical*, lower mass, HB stars) are expected to lie. Following this prescription, evidence suggesting the presence of evolved BSSs "contaminating" the genuine HB-AGB cluster population has been found in M3 (Ferraro et al., 1997a), M80 (Ferraro et al., 1999b) and 47Tuc (Beccari et al., 2006).

3.4 A few words on the NLTE effect

The interpretation of observed spectra of stars in terms of fundamental stellar properties is a key problem in astrophysics. For FGK-type stars, the radiative transfer models are often computed using the assumption of Local Thermodynamic Equilibrium (LTE). As often happens in astrophysics research, the reason for adopting LTE is that it substantially simplifies the calculation of number densities of atoms and molecules. However, by definition, this is only an "assumption", since the atmospheres of the stars are better described as a series of different layers in which the temperature and gas density change continuously. Hence, in the following we consider a simple one-dimensional hydrostatic model of a stellar atmosphere, in which temperature and density are linked to the depth and the radiation is transported outward. At each depth point, we can assume that matter particles (ions, atoms, electrons, molecules) are in LTE with each other. This equilibrium is established by intra-particle collisions, i.e. the energy distribution of matter depends on the collisions between particles. The LTE condition is usually expressed as $J_{\nu} = B_{\nu}$, where J_{ν} is the radiation field component while B_{ν} is the Planck function. In the dense part of the stellar atmosphere the collision rate is very high and the photon mean free path l_{λ} is smaller than the scale over

which the physical variables (temperature, pressure) change. For this reason the radiation and the particles can be assumed to be in equilibrium (guaranteed by collisions). The departure from LTE condition (NLTE) happens when l_λ becomes larger than the scale height of the material. Thus, as photons diffuse outward, their decoupling from matter increases, and the radiation field becomes "non-local" (i.e. suddenly changes even between close points), anisotropic, and strongly non-Planckian, i.e. $J_\nu \neq B_\nu$.

The same occurs in the outermost layers where density decreases and collisions become progressively less frequent. Accordingly, the collisions are not able to thermalize the matter any more, while the radiative excitations/de-excitations become important. In giant stars it is usually possible to observe neutral and single ionized lines. By definition, the neutral lines are formed in the outer part of the stellar atmosphere, where the energetics is not high enough to ionize the atoms. On the contrary, the single ionized lines are formed much deeper inside, were the higher energetics is able to ionize the atoms. This is the reason why the NLTE phenomenon mainly affects the neutral lines, while it leaves quite unaltered the single ionized lines formed deep inside the atmosphere. However, also other mechanisms contribute to the departures from LTE conditions (see Bergemann & Nordlander, 2014, for an extended discussion).

In the last decades, the treatment of NLTE in stellar atmospheres has made huge progress, and several NLTE correction grids for the abundances of different elements are available (see e.g. the INSPECT project[1]). However, deriving proper NLTE corrections is a quite hard task, because of two main reasons: (1) the development of reliable atoms and molecules models, which should take into account all the possible transitions from all the energetic levels and (2) the treatment of the collision rate with neutral hydrogen atoms (the S_H parameter). In particular, the S_H coefficient is usually computed with the Drawin's formula (Drawin, 1969), which laboratory measurements and quantum mechanical calculations indicate that it overestimates the rate coefficient for optically allowed transitions by one to seven orders of magnitude. Therefore, various approaches have been adopted to empirically constrain the S_H parameter, however, up to now, a fully consistent treatment of the collision rates with hydrogen atoms is still lacking. In any case, big progresses have already been made for some species like Fe, Na and Li (see e.g. Thévenin & Idiart, 1999; Lind et al., 2009a, 2011).

[1] http://www.inspect-stars.com/

Chapter 4

Non Local Thermodynamic Equilibrium Effects on Asymptotic Giant Branch Stars in 47Tucanae

Published in Lapenna et al. 2014, ApJ, 797, 124L

We present the iron abundance of 24 asymptotic giant branch (AGB) stars members of the globular cluster 47 Tucanae, obtained with high-resolution spectra collected with the FEROS spectrograph at the MPG/ESO-2.2m Telescope. We find that the iron abundances derived from neutral lines (with mean value [FeI/H] = -0.94 ± 0.01*, $\sigma = 0.08$ dex) are systematically lower than those derived from single ionized lines ([FeII/H] =* -0.83 ± 0.01*, $\sigma = 0.05$ dex). Only the latter are in agreement with those obtained for a sample of red giant branch (RGB) cluster stars, for which FeI and FeII lines provide the same iron abundance. This finding suggests that Non Local Thermodynamical Equilibrium (NLTE) effects driven by overionization mechanisms are present in the atmosphere of AGB stars and significantly affect FeI lines, while leaving FeII features unaltered. On the other hand, the very good ionization equilibrium found for RGB stars indicates that these NLTE effects may depend on the evolutionary stage. We discuss the impact of this finding both on the chemical analysis of AGB stars, and on the search for evolved blue stragglers.*

4.1 Observations

We acquired high resolution spectra of 24 AGB stars in 47 Tuc (Program ID 090.D-0153, PI: Lanzoni) by using the Fibre-fed Extended Range Optical Spectrograph (FEROS; Kaufer et al., 1999) mounted at the MPG/ESO-2.2m telescope. The spectra cover a wavelength range between $\lambda \sim 3500$ Å and $\lambda \sim 9200$ Å, with a spectral resolution of ~ 48000. FEROS

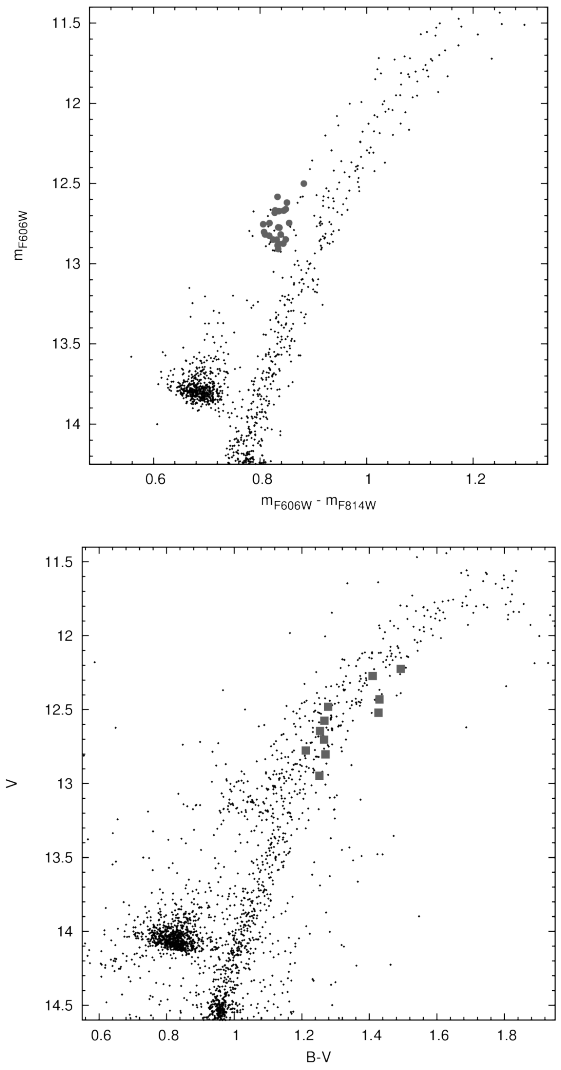

Figure 4.1 Top panel: $(m_{\rm F606W}, m_{\rm F606W} - m_{\rm F814W})$ color magnitude diagram of 47 Tuc from Beccari et al. (2006). The large solid circles mark the 24 targets studied in the present work. Bottom panel: $(V, V - I)$ color magnitude diagram of 47 Tuc obtained from WFI data by Ferraro et al. (2004b). The large solid squares mark the 11 RGB stars used for comparison.

allows to allocate simultaneously two fibers at a relative distance of $2.9'$, one on the source and the other on the sky. The targets have been selected from the photometric catalog of Beccari et al. (2006), within $\sim 100''$ from the cluster center. In the color-magnitude diagram (CMD) of 47 Tuc they are located in the AGB clump (corresponding to the beginning of this evolutionary phase; Ferraro et al., 1999a), at $m_{\rm F606W} \sim 12.8$ and $(m_{\rm F606W} - m_{\rm F814W}) \simeq 0.8$ (see top panel of Figure 4.1). Only isolated stars have been selected, in order to avoid contamination of the spectra from close objects of larger or comparable luminosity. The identification number, coordinates and magnitudes of each target are listed in Table 4.1.

For each target a single exposure of ∼30-40 min has been acquired, reaching signal-to-noise ratios S/N$\geq$ 70 per pixel. The data reduction was performed by using the ESO FEROS pipeline, including bias subtraction, flat fielding, wavelength calibration by using a Th-Ar-Ne reference lamp, spectrum extraction and final merging and rebinning of the orders. Since the background level of the sky is negligible ($< 1\%$) compared to the brightness of the observed targets, we did not perform the sky subtraction from the final spectra in order to preserve its maximum quality. We accurately checked that the lack of sky subtraction has no impact on the derived abundances, by comparing the equivalent widths (EWs) measured for some spectra with and without the sky subtraction.

4.2 Analysis

4.2.1 Radial velocities

The radial velocity of each target has been obtained by means of the code DAOSPEC (Stetson & Pancino, 2008), measuring the positions of more than 300 metallic lines. The accuracy of the wavelength calibration has been checked by measuring telluric absorptions and oxygen sky lines, finding no significant zero-point offsets. Uncertainties have been computed as the dispersion of the measured radial velocities divided by the square root of the number of used lines, and they turned out to be smaller than 0.04 km s^{-1}. Heliocentric corrections obtained with the IRAF task RVCORRECT have been adopted. The heliocentric radial velocities for all the targets are listed in Table 4.1. They range between ~ -41.5 and $\sim +9.5$ km s^{-1}, with mean value of -17.6 ± 2.3 km s^{-1} and dispersion $\sigma = 11.5$ km s^{-1}. These values are in good agreement with previous determinations of the systemic radial velocity of 47 Tuc (see e.g. Mayor et al., 1983; Meylan et al., 1991; Gebhardt et al., 1995; Carretta et al., 2004b; Alves-Brito et al., 2005; Koch & McWilliam, 2008; Lane et al., 2010a). All the targets have been considered as members of the cluster, according to their radial velocities and distance from the cluster center.

4.2.2 Chemical analysis

The chemical abundances have been derived by using the package GALA[1] (Mucciarelli et al., 2013a) which matches the measured and the theoretical equivalent widths (see Castelli, 2005, for a detailed description of this method). The model atmospheres have been com-

[1] http://www.cosmic-lab.eu/gala/gala.php

puted by using the ATLAS9 code, under the assumption of plane-parallel geometry, local thermodynamical equilibrium (LTE) and no overshooting in the computation of the convective flux. We adopted the last release of the opacity distribution functions from Castelli & Kurucz (2004), assuming a global metallicity of [M/H] = -1 dex with [α/Fe]= $+0.4$ dex for the model atmospheres.

The effective temperatures ($T_{\rm eff}$) and surface gravities (log g) of the targets have been derived photometrically, by projecting the position of each star in the CMD onto the isochrone best fitting the main evolutionary sequences of 47 Tuc. The isochrone has been extracted from the BaSTI database (Pietrinferni et al., 2006) assuming an age of 12 Gyr, metallicity Z $=$ 0.008 and α-enhanced chemical mixture. We adopted a distance modulus $(m - M)_V = 13.32$ mag and a color excess $E(B - V) = 0.04$ mag (Ferraro et al., 1999a). Microturbulent velocities ($v_{\rm turb}$) have been derived by requiring that no trends exist between FeI abundances and the reduced EWs, defined as $\log(EW/\lambda)$. The adopted atmospheric parameters are listed in Table 4.2.

Only absorption lines that are predicted to be unblended at the FEROS resolution have been included in our analysis. The line selection has been performed through a careful inspection of synthetic spectra calculated with the code SYNTHE (Sbordone et al., 2005) assuming the typical atmospheric parameters of our targets and the typical metallicity of 47 Tuc. We considered only transitions with accurate theoretical/laboratory atomic data taken from the last version of the Kurucz/Castelli compilation.[2] The EWs have been obtained with DAOSPEC (Stetson & Pancino, 2008), iteratively launched by means of the package 4DAO[3](Mucciarelli, 2013b) that allows an analysis cascade of a large sample of stellar spectra and a visual inspection of the Gaussian fit obtained for all the investigated lines. Due to the extreme crowding of spectral lines in the region between $\lambda \sim 3800$ Å and $\lambda \sim 4500$ Å, and to the presence of several absorption telluric line bands beyond ~ 6800 Å, we restricted the analysis to the spectral range between ~ 4500 Å and ~ 6800 Å. In order to avoid too weak or saturated features, we considered only lines with reduced EWs between -5.6 and -4.7 (these correspond to EW = 11 mÅ and 90 mÅ at $\lambda \sim 4500$ Å, and EW = 17 mÅ and 135 mÅ at $\lambda \sim 6800$ Å, respectively). Moreover, we discarded from the analysis also the lines with EW uncertainties larger than 20%, where the uncertainty of each individual line is provided by DAOSPEC on the basis of the fit residuals. With these

[2]http://wwwuser.oat.ts.astro.it/castelli/linelists.html
[3]http://www.cosmic-lab.eu/4dao/4dao.php

limitations, the iron abundance has been derived, on average, from $\sim$ 150 FeI lines and $\sim$ 13 FeII lines. In the computation of the final iron abundances we adopted as reference solar value A(Fe)$_{\odot}$ = 7.50 dex (Grevesse & Sauval, 1998).

Uncertainties on the derived abundances have been computed for each target by adding in quadrature the two main error sources: *(a)* those arising from the EW measurements, which have been estimated as the line-to-line abundance scatter divided by the square root of the number of lines used, and *(b)* the uncertainties arising from the atmospheric parameters, computed varying by the corresponding uncertainty only one parameter at a time, while keeping the others fixed. The abundance variations thus obtained have been added in quadrature. Term (a) is of the order of less than 0.01 dex for FeI and 0.03 dex for FeII. Since the atmospheric parameters have been estimated from photometry, by projecting the position of each target in the CMD onto the isochrone, we estimated term (b) from the photometric uncertainties. By assuming a conservative uncertainty of 0.1 mag for the magnitudes of our targets we obtained an uncertainty of about $\pm$50 K and $\pm$0.05 dex on the final T$_{eff}$ and log g, respectively. The total uncertainties in [FeI/H] are of the order of 0.04-0.05 dex, while in [FeII/H] are of about 0.08-0.10 dex (due to the higher sensitivity of FeII lines to $T_{\rm eff}$ and log g).

4.3 Iron abundance

The [FeI/H] and [FeII/H] abundance ratios measured for each target are listed in Table 4.2, together with the total uncertainties and the number of lines used. Their distributions are shown in Figure 4.2. A systematic difference between [FeI/H] and [FeII/H] is evident, with the abundances derived from FeI lines being, on average, 0.1 dex smaller than those obtained from FeII: the mean values of the distributions are [FeI/H] $= -0.94 \pm 0.01$ ($\sigma = 0.08$ dex) and [FeII/H] $= -0.83 \pm 0.01$ ($\sigma = 0.05$ dex). These values are clearly incompatible each other. Moreover, only [FeII/H] is in agreement with the metallicity quoted in the literature and based on sub-giant or RGB stars (Carretta et al., 2004a; Alves-Brito et al., 2005; Koch & McWilliam, 2008; Carretta et al., 2009b), while the iron abundance obtained from FeI lines is significantly smaller. The distribution of the difference [FeI/H]$-$[FeII/H] is shown as a function of [FeII/H] in Figure 4.3 (black circles). It is quite broad, ranging from -0.25 to $+0.01$ dex.

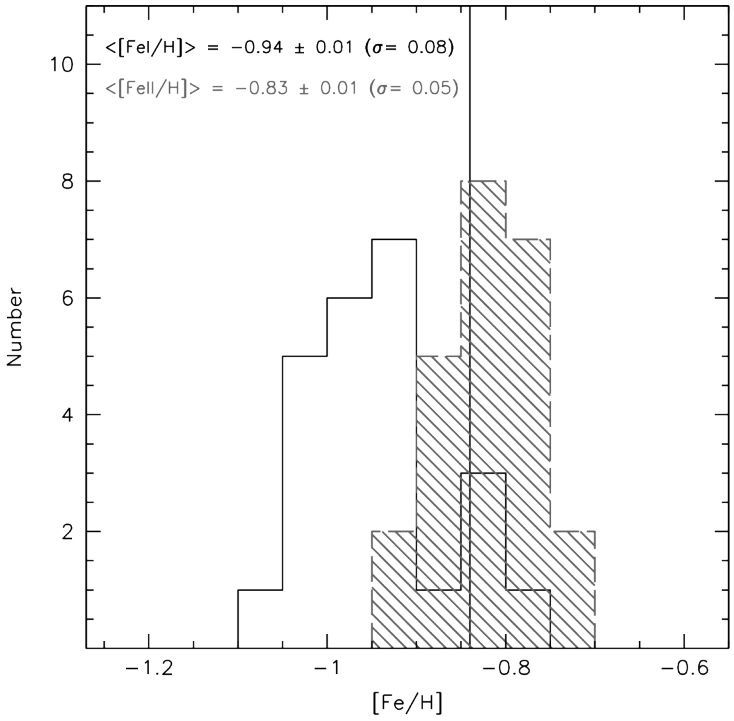

Figure 4.2 Distribution of the iron abundance ratios measured for the 24 AGB stars in our sample, from FeI lines (empty histogram) and from FeII lines (shaded histogram). The vertical line indicates the average iron abundance derived from 11 RGB stars.

4.3.1 Sanity checks

The difference in the derived [FeI/H] and [FeII/H] abundances cannot be easily explained (especially if considering the high quality of the acquired spectra and the very large number of used iron lines) and it clearly needs to be understood. In order to test the correctness of our analysis and to exclude possible bias or systematic effects, we therefore performed a number of sanity checks.

Checks on the chemical analysis procedure

To test the reliability of our chemical analysis, we studied a sample of RGB stars in 47 Tuc, the standard star 104 Tau, Arcturus and the Sun by following the same procedure adopted for the AGB targets discussed above (i.e., by using the same linelist, model atmospheres, and method to infer the atmospheric parameters).

RGB stars in 47 Tuc – We measured the iron abundance for a sample of 11 RGB stars in 47 Tuc, for which high-resolution (R$\sim$45000) FLAMES-UVES spectra are available in the

ESO Archive (Program ID: 073.D-0211). The location of these stars in the $(V, V-I)$ CMD from Ferraro et al. (2004b) is shown in Figure 4.1 (bottom panel). Their atmospheric parameters and [FeI/H] and [FeII/H] abundance ratios are listed in Table 4.3. The distribution of the [FeI/H]-[FeII/H] differences is shown in Figure 4.3 (large gray squares). We found an average $[\mathrm{FeI/H}]_{\mathrm{RGB}} = -0.83 \pm 0.01$ dex ($\sigma = 0.02$ dex) and $[\mathrm{FeII/H}]_{\mathrm{RGB}} = -0.84 \pm 0.01$ dex ($\sigma = 0.03$ dex). These values are fully consistent with previous determinations. In fact, the careful comparison with the results of Carretta et al. (2009b), who analyzed the same 11 RGB spectra, shows that the average differences in the adopted parameters are: Δ T_{eff} = 36 $\pm$ 8 K (σ = 26 K), Δlog g = 0.07 $\pm$ 0.01 (σ = 0.04), Δ v_{turb} = 0.01 $\pm$ 0.04 km s^{-1} (σ = 0.14 km s^{-1}). By taking into account also the differences among the adopted atomic data, model atmospheres and procedure to measure the EWs, the derived abundances turn out to be in very good agreement within the uncertainties, the mean difference between our values and those of Carretta et al. (2009b) being Δ[FeI/H] = –0.06 $\pm$ 0.03 dex and Δ[FeII/H] = –0.02 $\pm$ 0.03 dex.

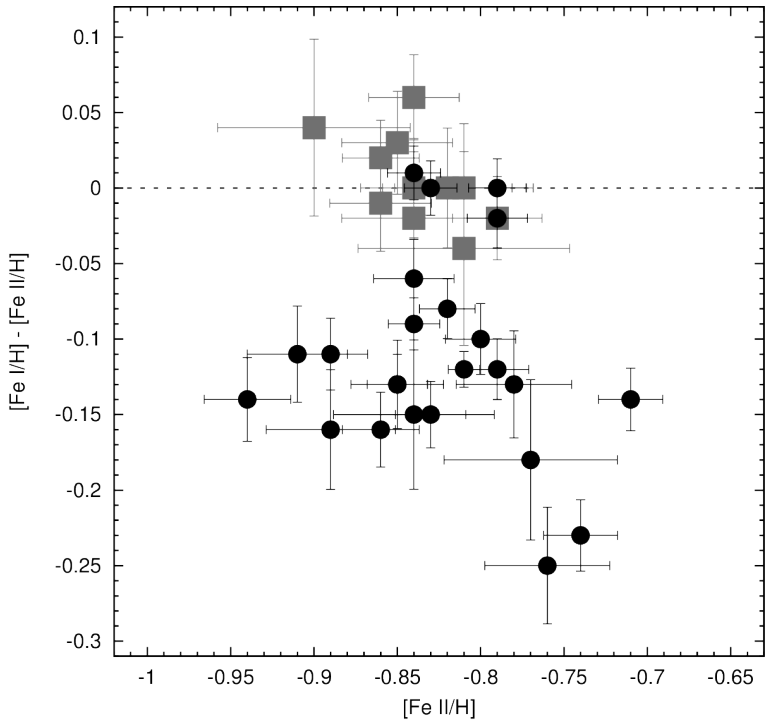

Figure 4.3 Difference between [FeI/H] and [FeII/H] as a function of [FeII/H] for the 24 AGB stars (black circles) and the 11 RGB stars (gray squares) in our 47 Tuc samples.

104 Tau – We applied the same procedure of data reduction and spectroscopic analysis to the star 104 Tau (HD 32923), which was observed during the first observing night as a radial

velocity standard star. The spectrum has been reduced with the same set of calibrations (i.e., bias, flat-fields, Th-Ar-Ne lamp) used for the main targets. We obtained a radial velocity of 20.96 ± 0.02 km s^{-1}, which is consistent with the value (20.62 ± 0.09 km s^{-1}) quoted by Nidever et al. (2002). We adopted the average values of $T_{\rm eff}$ and log g provided by Takeda et al. (2005) and Ramírez et al. (2009) in previous analyses of the star ($T_{\rm eff}$= 5695 K and log $g = 4.05$), while $v_{\rm turb}$ has been constrained spectroscopically. We derived [FeI/H] $= -0.17 \pm 0.01$ (σ = 0.09 dex) and [FeII/H] $= -0.20 \pm 0.02$ (σ = 0.07 dex), well matching, within a few hundredth of dex, the values quoted by Takeda et al. (2005) and Ramírez et al. (2009).

Arcturus and the Sun – In order to test the robustness of the used linelist (and in particular to check for possible systematic offsets due to the adopted oscillator strengths of FeI and FeII lines), we adopted the same procedure to measure the iron abundance of Arcturus (HD 124897) and the Sun, both having well established atmospheric parameters. In the case of Arcturus we retrieved a FEROS spectrum from the ESO archive (Program ID: 074.D-0016), adopting $T_{\rm eff}$ = 4300 K, log g = 1.5, $v_{\rm turb}$ = 1.5 km s^{-1} and [M/H]$= -0.5$ as derived by Lecureur et al. (2007). We obtained [FeI/H]$= -0.56 \pm 0.01$ dex and [FeII/H]$= -0.57 \pm 0.01$ dex, in very good agreement with previous determinations (Fulbright et al., 2006; Lecureur et al., 2007; Ramírez & Allende Prieto, 2011). We repeated the same test on a FLAMES-UVES ($R \sim 45000$) twilight spectrum of the Sun[4], adopting $T_{\rm eff}$ = 5777 K, log g = 4.44 and $v_{\rm turb}$ = 1.0 km s^{-1} and finding absolute Fe abundances of 7.49 $\pm$ 0.01 dex and 7.50 $\pm$ 0.02 dex from neutral and single ionized iron lines, respectively.

Checks on the atmospheric parameters

Effective temperature and gravity from spectroscopy – We checked whether atmospheric parameters derived spectroscopically could help to reconcile the [FeI/H] and [FeII/H] abundance ratios. The adopted photometric estimates of $T_{\rm eff}$ well satisfy the *excitation balance* (i.e. there is no slope between abundances and excitation potential). Hence very small (if any) adjustments, with a negligible impact on the derived abundances, can be admitted. Instead, the values adopted for the surface gravity can have a significant impact on the difference between [FeI/H] and [FeII/H]. In fact, the abundances derived from FeII lines are a factor of ~ 5 more sensitive to variations of log g with respect to those obtained from FeI lines: for instance, a variation of -0.1 dex in log g leads to negligible variation (~ -0.01

[4]http://www.eso.org/observing/dfo/quality/GIRAFFE/pipeline/solar.html

dex) in the FeI abundance, while [FeII/H] decreases by 0.05 dex. Hence, a lower value of the surface gravity could, in principle, erase the difference between [FeI/H] and [FeII/H].

We found that the derived spectroscopic gravities are on average lower than the photometric ones by 0.25 dex, with a maximum difference of $\sim$0.5 dex. As an example, the photometric analysis of star #100103 provides [FeI/H]$= -1.01 \pm 0.01$ (σ = 0.11 dex) and [FeII/H] $= -0.76 \pm 0.04$ (σ = 0.13 dex), with $T_{\rm eff}$ = 4450 K, log g = 1.60 and $v_{\rm turb}$ = 1.15 km s^{-1}. When a fully spectroscopic analysis is performed (thus optimizing all the atmospheric parameters simultaneously), we obtain $T_{\rm eff}$ = 4475 K, log g = 1.10 and $v_{\rm turb}$ = 1.25 km s^{-1}, and the derived abundances are [FeI/H] $= -1.09 \pm 0.01$ and [FeII/H] = -1.10 ± 0.02. As expected, the spectroscopic values of $T_{\rm eff}$ and $v_{\rm turb}$ are very similar to those adopted in the photometric analysis. A large difference is found for log g, but the final iron abundances are both too low with respect to the literature and the 11 RGB star values to be considered acceptable. Similar results are obtained for all the other AGB targets in our sample.

Small surface gravity values as those found from the fully spectroscopic analysis would require that stars reach the AGB phase with an average mass of 0.4 $M_{\odot}$ (keeping $T_{\rm eff}$ and luminosity fixed). This is lower than the value expected by considering a main sequence turnoff mass of 0.9 $M_{\odot}$ and a $\sim$ 0.25 $M_{\odot}$ mass loss during the RGB phase (Origlia et al., 2007, 2014). Note that for some stars where [FeI/H]$-$[FeII/H]≤ -0.20 dex, the derived spectroscopic gravity would require a stellar mass of $\sim$ 0.2 $M_{\odot}$, which is even more unlikely for GC stars in this evolutionary stage, also by taking into account the mass loss rate uncertainties (Origlia et al., 2014). Alternatively, these values of log g can be obtained by assuming a significantly larger (by about 0.5 mag) distance modulus. However, this would be incompatible with all the previous distance determinations for 47Tuc (see e.g. Ferraro et al., 1999a; McLaughlin et al., 2006; Bergbusch & Stetson, 2009).

Effective temperature and gravity from a different photometric approach – We repeated the analysis by adopting effective temperatures estimated from the de-reddened color of each target and the $(V-I)_0$-$T_{\rm eff}$ relation provided by Alonso et al. (1999), based on the Infrared Flux Method (see Blackwell et al., 1990, and references therein). Because this color-$T_{\rm eff}$ relation is defined in the Johnson photometric system, we converted the target magnitudes in that system, following the prescriptions of Sirianni et al. (2005). Moreover, gravities have been computed from the Stefan-Boltzmann relation, by using the derived values of $T_{\rm eff}$, the luminosities obtained from the observed V-band magnitudes, assuming

a mass of 0.8 $M_{\odot}$ for all the stars (according to the best-fit isochrone discussed above) and adopting the bolometric corrections computed according to Buzzoni et al. (2010). The average difference between the $T_{\rm eff}$ values obtained from the isochrone and those derived from the Alonso et al. (1999) relation is of 3 K (σ = 50 K). For gravities we obtained an average difference of 0.05 dex (σ = 0.03 dex) and for the microturbulent velocities we found 0.01 km s^{-1} (σ = 0.04 km s^{-1}). We repeated the chemical analysis with the new parameters, finding that they do not alleviate the difference between the average [FeI/H] and [FeII/H] abundance ratios: we obtained [FeI/H] $= -0.94 \pm 0.01$ dex (σ = 0.06 dex) and [FeI/H] $= -0.84 \pm 0.01$ dex (σ = 0.07 dex). Thus, the iron abundances estimated from FeI lines remain systematically lower than those obtained from FeII lines and those found in the RGB stars.

Microturbulent velocity – We note that the (spectroscopically) derived values of $v_{\rm turb}$ span a large range (between 1 and 2 km s^{-1} for most of the targets). Also, a small trend between the average abundances and $v_{\rm turb}$ is detected, [FeI/H] increasing by 0.15 dex/km s^{-1} and [FeII/H] varying by 0.08 dex/km s^{-1}. The very large number of lines ($\sim$150) used to constrain $v_{\rm turb}$, as well as the wide range of line strengths covered by the selected transitions, ensure that no bias due to small number statistics or small range of line strengths occurs in the determination of $v_{\rm turb}$ (note that no specific trend between [Fe/H] and $v_{\rm turb}$ is found among the RGB stars). Also, the values of $v_{\rm turb}$ do not change significantly changing the range of used reduced EWs (see Section 4.2.2).

We checked the impact of a different $v_{\rm turb}$ scale, adopting the $v_{\rm turb}$–log g relation provided by Kirby et al. (2009). Because our targets have very similar gravities, they have ultimately the same value of $v_{\rm turb}$ ($\sim$ 1.7 km s^{-1}), and the situation worsens: in several stars the dispersion around the mean abundance significantly increases (up to $\sim$0.3 dex, in comparison with σ = 0.15 dex found with the spectroscopic estimate of $v_{\rm turb}$). This is a consequence of the trends found between abundances and line strengths introduced by not optimized $v_{\rm turb}$. The new average abundances of the entire sample are [FeI/H] $= -1.03 \pm 0.04$ dex (σ = 0.18 dex) and [FeII/H] $= -0.89 \pm 0.02$ dex (σ = 0.12 dex). Hence, with a different assumption about $v_{\rm turb}$ not only the star-to-star dispersion increases by a factor of 2 for both the abundance ratios, but, also, the systematic difference between [FeI/H] and [FeII/H] remains in place.

Model atmospheres – The plane-parallel geometry is adopted both in the ATLAS9 model atmospheres and in the line-formation calculation performed by GALA. As pointed

out by Heiter & Eriksson (2006), that investigated the impact of the geometry on the abundance analysis of giant stars, the geometry has a small effect on line formation. In order to quantify these effects, we reanalyzed the target stars by using the last version of the MARCS model atmospheres (Gustafsson et al., 2008), which adopt spherical geometry. The average abundance differences between the analysis performed with MARCS and that performed with ATLAS9 are of –0.005 dex (σ = 0.01 dex) and +0.02 dex (σ = 0.04 dex) for FeI and FeII, respectively. Hence, the use of MARCS model atmospheres does not change our finding about FeI and FeII abundances (both in AGB and in RGB stars). Note that Heiter & Eriksson (2006) conclude that abundances derived with spherical models and plane-parallel transfer are in excellent agreement with those obtained with a fully spherical treatment.

4.4 Discussion

4.4.1 A possible signature of NLTE effects?

For the 24 AGB stars studied in 47 Tuc, the iron abundance obtained from single ionized lines well matches that measured in RGB stars (from both FeI and FeII lines). Instead, systematically lower iron abundances are found for the AGB sample from the analysis of FeI. All the checks discussed in Section 4.3.1 confirm that such a discrepancy is not due to some bias in the analysis or to the adopted atmospheric parameters, and there are no ways to reconcile the abundances from Fe lines with those observed in the RGB stars.

The only chemical analyses performed so far on AGB stars in 47 Tuc have been presented by Wylie et al. (2006) and Worley et al. (2009). In both cases all the parameters have been constrained spectroscopically (in particular, $\log g$ is obtained by forcing [FeI/H] and [FeII/H] to be equal within the uncertainties). Wylie et al. (2006) analysed 5 AGB stars (brighter than those discussed in this work), finding [FeI/H] $= -0.60 \pm 0.06$ dex and [FeII/H] $=-0.64 \pm 0.10$ dex. The same methodology to derive the parameters has been used by Worley et al. (2009) to analyse a bright AGB star, finding [FeI/H]$= -0.72 \pm 0.16$ dex and [FeII/H]$= -0.74 \pm 0.08$ dex. Unfortunately, the spectroscopic determination of the gravity does not allow to understand whether also for these AGB stars a real discrepancy of [FeI/H] and [FeII/H] does exist.

A natural explanation for the negative values of [FeI/H]$-$[FeII/H] measured for our AGB sample would be that these stars suffer for departures from the LTE condition, which mainly affects the less abundant species (in this case FeI), while leaving virtually unaltered

the dominant species (i.e. FeII; Mashonkina et al., 2011). In late-type stars, NLTE effects are mainly driven by overionization mechanisms, occurring when the intensity of the radiation field overcomes the Planck function (see Asplund, 2005, for a complete review of these effects). These effects are predicted to increase for decreasing metallicity and for decreasing atmospheric densities (i.e., lower surface gravities at a given $T_{\rm eff}$), as pointed out by a vast literature (see e.g. Thévenin & Idiart, 1999; Asplund, 2005; Mashonkina et al., 2011; Lind, Bergemann & Asplund, 2012; Bergemann & Nordlander, 2014). At the metallicity of 47 Tuc, significant deviations are expected only for stars approaching the RGB-Tip. Bergemann et al. (2012) and Lind, Bergemann & Asplund (2012) computed a grid of NLTE corrections for a sample of Fe I and FeII lines in late-type stars over a large range of metallicity. Assuming the atmospheric parameters of the 11 RGB stars in our sample and the measured EWs of the iron lines in common with their grid (25 FeI and 9 FeII lines), the predicted NLTE corrections are [Fe/H]$_{\rm NLTE}-$[Fe/H]$_{\rm LTE} \simeq +0.04$ dex. This is consistent with no significant differences between [FeI/H] and [FeII/H] found in our analysis (Section 4.3.1) and in previous studies (see e.g. Carretta et al., 2004b; Koch & McWilliam, 2008; Carretta et al., 2009b). Instead, a larger difference ([FeI/H]$-$[FeII/H]$= -0.08$ dex) has been found for the brightest RGB stars in 47 Tuc (Koch & McWilliam, 2008), as expected. [5]

However, if we use the same grid to estimate the NLTE corrections for our sample of AGB stars, we find [Fe/H]$_{\rm NLTE}-$[Fe/H]$_{\rm LTE} = +0.06$ dex. This value is consistent with the NLTE corrections predicted for RGB stars and smaller than the difference we observe between FeI and FeII in our sample of AGB stars. Interestingly, a situation similar to that encountered in the present work has been met by Ivans et al. (2001) in the spectroscopic analysis of giant stars in the GC M5. Their sample includes 6 AGB and 19 RGB stars, ranging from the luminosity level of the AGB clump, up to the RGB-Tip. Also in their analysis, [FeI/H] in AGB stars is systematically lower (by about 0.15 dex) than [FeII/H], while no differences are found for the RGB stars. The authors performed different kinds of analysis, finding that the only way to reconcile the iron abundance in AGB stars with the values obtained in RGB stars is to adopt the photometric gravities and rely on the FeII lines only, which are essentially insensitive to LTE departures. Our findings, coupled with the results of Ivans et al. (2001) in M5, suggest that the NLTE effects could depend on the evolutionary stage (being more evident in AGB stars with respect to RGB stars), also at

[5] For sake of comparison, Mucciarelli et al. (2013c) analysed RGB stars close to the RGB Tip in the metal-poor GC NGC 5694 ([Fe/H] ~ -2.0 dex), finding an average difference between [FeI/H] and [FeII/H] of -0.14 dex, consistent with the expected overionization effects.

metallicities where these effects should be negligible (like in the case of 47 Tuc that is more metal-rich than M5). This result is somewhat surprising, because a dependence of NLTE effects on the evolutionary stage is not expected by the theoretical models.

In our sample, we identify 4 AGB stars (namely #100169, #100171, #200021 and #200023) where the absolute difference between [FeI/H] and [FeII/H] is quite small (less than 0.05 dex; see Figure 4.3). According to the different behaviour observed between the AGB and the RGB samples, one could suspect that these objects are RGB stars. However, we checked their position on the CMD also by using an independent photometry (Sarajedini et al., 2007), confirming that these 4 targets are indeed genuine AGB stars. Figure 4.4 compares two iron lines of the spectra of targets #100171 and #100174, which are located in the same position of the CMD (thus being characterized by the same atmospheric parameters), but have [FeI/H]$-$[FeII/H]$= 0$ and -0.16 dex, respectively. Clearly, the Fe II lines of the two stars have very similar depths, suggesting the same iron abundance, while the FeI line of #100174 (black spectrum) is significantly shallower than that in the other star. This likely suggests that NLTE effects among the AGB stars have different magnitudes, the overionization being more or less pronounced depending on the star.

The origin of this behaviour, as well as the unexpected occurrence of NLTE effects in AGB stars of these metallicity and atmospheric parameters, are not easy to interpret and their detailed investigation is beyond the scope of this paper. Suitable theoretical models of the line formation under NLTE conditions in AGB stars should be computed in order to explain the observed difference in the FeI and FeII abundances. We cannot exclude that some inadequacies of the 1-dimensional model atmospheres can play a role in the derived results. Up to now, 3-dimensional hydrodynamics simulations of the convective effects in AGB stars have been performed only for a typical AGB star during the thermal pulses phase and with very low $T_{\rm eff}$, $\sim$2800 K (Freytag & Hofner, 2008). Similar sophisticated models for earlier and warmer phases of the AGB are urged.

4.4.2 Impact on traditional chemical analyses

This result has a significant impact on the approach traditionally used for the chemical analysis of AGB stars. In particular, two main aspects deserve specific care:

(1) the FeI lines should not be used to determine the iron abundance of AGB stars. In fact, when photometric parameters are adopted, the [FeI/H] abundance ratio can be systematically lower than that obtained from FeII lines. Indeed, the most reliable route to derive

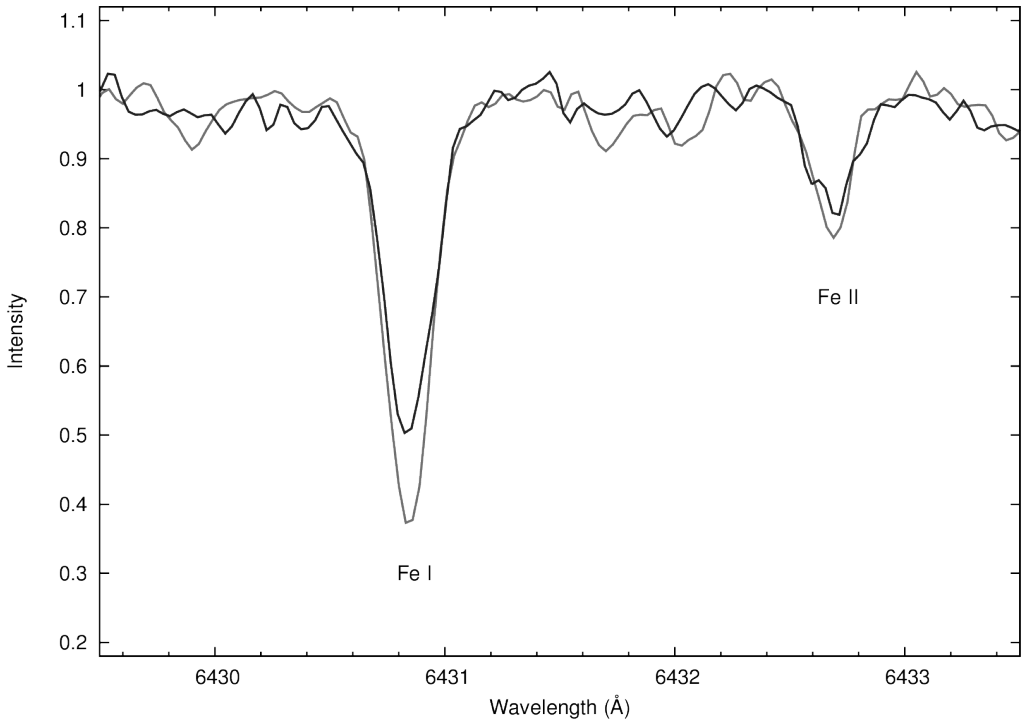

Figure 4.4 Comparison between the normalized spectra of target #100171 (grey line) and #100174 (black line). The position of a FeI line and a FeII line is marked.

the iron abundance in AGB stars is to use the FeII lines, that are essentially unaffected by NLTE effects and provide the same abundances for both RGB and AGB objects. This strategy requires high-resolution, high-quality spectra, because of the low number of FeII lines available in the optical range (smaller by a factor of ~ 10 with respect to the number of FeI lines). This is especially true at low metallicity since the lines are shallower and the NLTE effects are expected to be stronger;

(2) another point of caution is that AGB stars must be analysed by adopting the photometric gravities (derived from a theoretical isochrone or through the Stefan-Boltzmann equation) and not by using the spectroscopic method of the ionization balance (at variance with the case of RGB stars, where this approach is still valid). This method, which is widely adopted in the chemical analysis of optical stellar spectra, constrains $\log g$ by imposing the same abundance for given species as obtained from lines of two different ionization stages. Variations of $\log g$ lead to variations in the abundances measured from ionized lines (which are very sensitive to the electronic pressure), while the neutral lines are quite insensitive to these variations. Because of the systematically lower FeI abundance, this procedure leads to improbably low surface gravities in AGB stars (as demonstrated in Section 4.3.1).

If the FeI line are used as main diagnostic of the iron abundance, a *blind* analysis, where AGB and RGB stars are not analysed separately, can lead to a spurious detection of large iron spreads in GCs. In light of these considerations, the use of FeII lines is recommended to determine the metallicity of AGB objects, regardless of their metallicity and luminosity. On the other hand, the systematic difference between FeI abundances in AGB and RGB stars could, in principle, be used to recognize AGB stars when reliable photometric selections cannot be performed.

4.4.3 Searching for evolved BSSs among AGB stars: a new diagnostic?

The discovery of such an unexpected NLTE effect in AGB stars might help to identify possible e-BSSs among AGB stars. In fact, BSSs spend their RGB phase in a region of the CMD which is superimposed to that of the cluster AGB (e.g., Beccari et al., 2006; Dalessandro et al., 2009). Thus, e-BSSs are indistinguishable from genuine AGB stars in terms of colors and magnitudes, but they have larger masses at comparable radii. Hence, their surface gravity is also expected to be larger (by about 0.2-0.3 dex) than that of "canonical" AGB stars of similar temperature and luminosity. Unfortunately, the spectroscopic measurement of log g cannot be used to distinguish between genuine AGB stars and e-BSSs, since the ionization balance method cannot be applied in the presence of the NLTE effects affecting the AGB (see Sect. 4.4.2). However, because of the seemingly dependence of the NLTE effects on the evolutionary phase, the measurement of different values of [FeI/H] and [FeII/H] should allow to recognize genuine AGB stars from e-BSSs evolving along their RGB within a sample of objects observed in the AGB clump of a GC.

Of course, this expectation holds only if the lack of NLTE effects found for low-mass ($\sim$ 0.8 $M_{\odot}$) RGB stars also holds for larger masses ($\sim$ 1.2 $M_{\odot}$), typical of e-BSSs in GCs. In order to check this hypothesis, we retrieved from the ESO archive FLAMES-UVES spectra for 7 giant stars in the open cluster Berkeley 32 (ID Program: 074.D-0571). This cluster has an age of $\sim$6-7 Gyr (D'Orazi et al., 2006), corresponding to a turnoff mass of $\sim$ 1 $M_{\odot}$, comparable with the typical masses of the BSSs observed in Galactic GCs (e.g., Shara et al., 1997; De Marco et al., 2005; Ferraro et al., 2006a; Lanzoni et al., 2007; Fiorentino et al., 2014). We analyzed the spectra following the same procedure used for the AGB stars in 47 Tuc. The derived abundances are [FeI/H]= -0.34 ± 0.01 dex (σ = 0.04 dex) and [FeII/H]= -0.38 ± 0.02 dex (σ = 0.06 dex), in nice agreement with the results of Sestito et al. (2006) based on the same dataset. The small difference between the

abundances from FeI and FeII lines confirms the evidence arising from the RGB sample of 47 Tuc: in metal-rich RGB stars no sign of overionization is found, also for stellar masses larger than those typical of Galactic GC stars.

Within this framework, we checked whether some e-BSSs could be hidden in the analysed sample of putative AGB stars, especially among the four objects with negligible difference between FeI and FeII abundances. To this end we derived new atmospheric parameters for all targets projecting their position in the CMD on a grid of evolutionary BaSTI tracks crossing the mean locus of the studied stars: these are the RGB tracks for stellar masses of 1.2, 1.3 and 1.4 $M_{\odot}$ (see Beccari et al., 2006). On average, the new values of $T_{\rm eff}$ are slightly larger than those obtained in Section 4.2.2, while gravities are systematically larger, by up to $\sim$0.3 dex. For increasing mass of the adopted track, the general behaviour is that [FeI/H] slightly increases (mainly because of a small increase of $T_{\rm eff}$), while [FeII/H] decreases (because of the combined growth of both $T_{\rm eff}$ and log g). However, none of the measured AGB stars show [FeI/H]$\sim$[FeII/H]$\sim$[Fe/H]$_{\rm RGB}$ with the new sets of parameters. This suggests that no e-BSSs are hidden within our observed AGB sample. In particular, we found that for the four AGB stars with no evidence of overionization, the [FeII/H] abundance ratios derived with the new parameters are larger than those obtained from [FeI/H] (due to the increase in log g) and for RGB stars. This indicates that the atmospheric parameters estimated from the AGB portion of the isochrone are the most appropriate and these four objects are indeed genuine AGB stars. As an additional check, we measured the iron abundances assuming atmospheric parameters from theoretical tracks of massive (1-2 $M_{\odot}$) AGB stars. In this case, the situation improves. In particular, by using an AGB track of 1.2 $M_{\odot}$, because of the combined effect of larger $T_{\rm eff}$ ($\sim$+100 K) and log g ($\sim$+0.2), we find average values of [FeI/H]$= -0.85$ dex and [FeII/H]$= -0.81$ dex. However, this scenario is unlikely because the probability to detect an e-BSS during its AGB phase is a factor of ~ 10 lower than the probability to observe it during the RGB phase (consistently with the time duration of these evolutionary phases).

As a general rule, however, we stress that, the dependence of NLTE effects on the evolutionary stage (if confirmed) can be used as a diagnostic of the real nature of the observed AGB stars and to identify e-BSSs hidden in a putatively genuine AGB sample.

4.5 Summary

We have measured the iron abundance of 24 AGB stars members of the GC 47 Tuc, by using high-resolution FEROS spectra. By adopting photometric estimates of $T_{\rm eff}$ and log g, we derived average iron abundances [FeI/H]$= -0.94 \pm 0.01$ dex (σ = 0.08 dex) and [FeII/H]$= -0.83 \pm 0.01$ dex (σ = 0.05 dex). Thus, while the abundance estimated from ionized lines (-0.83 dex) well matches the one obtained for RGB stars, the values measured from neutral lines appear to be systematically lower. We carefully checked all the steps of our chemical analysis procedure and the adopted atmospheric parameters, finding no ways to alleviate this discrepancy.

Such a difference is compatible with the occurrence of NLTE effects driven by iron overionization, confirming the previous claim by Ivans et al. (2001) for a sample of AGB stars in M5. Our findings suggest that (i) the departures from the LTE approximation can be more significant than previously thought, even at relatively high metallicities ([Fe/H]~ -0.83) and for stars much fainter than the RGB-Tip, (ii) iron overionization can be more or less pronounced depending on the star (in fact, four stars in our sample turn out to be unaffected), and (iii) these effects depend on the evolutionary stage (they are not observed among RGB stars). We discussed the impacts of this effect on the traditional chemical analysis of AGB stars: if FeI lines are used and/or surface gravities are derived from the ionization balance, artificial under-estimates and/or spreads of the iron abundances can be obtained. If the dependence of these NLTE effects on the evolutionary stage is confirmed, the systematic difference between [FeI/H] and [FeII/H] abundance ratios can, in principle, be used to identify e-BSSs within a sample of genuine AGB stars (these two populations sharing the same locus in the CMD).

From the theoretical point of view, new and accurate models are needed to account for these findings, in particular to explain the dependence on the evolutionary stage. Observationally, further analyses of high-resolution spectra of AGB stars are crucial and urged to firmly establish the occurrence of these effects and to investigate their behaviour as a function of other parameters, like the cluster metallicity, the stellar mass and the stellar luminosity.

Table 4.1. Photometric properties and radial velocities of the AGB sample

ID	RA (J2000)	Dec (J2000)	$m_{\rm F606W}$	$m_{\rm F814W}$	RV (km s^{-1})
100094	6.1013041	–72.0745785	12.50	11.61	–28.20 ± 0.02
100103	6.0415972	–72.0787949	12.58	11.75	–19.03 ± 0.03
100110	6.0212020	–72.0791089	12.61	11.76	–24.71 ± 0.02
100115	6.0253911	–72.0763508	12.66	11.81	+9.42 ± 0.03
100118	6.0021239	–72.0797989	12.66	11.83	–22.55 ± 0.03
100119	5.9937010	–72.1048573	12.66	11.82	–0.83 ± 0.02
100120	6.0686535	–72.0977710	12.67	11.83	–36.76 ± 0.02
100125	6.0229324	–72.0843986	12.68	11.85	–28.72 ± 0.03
100133	6.0062382	–72.0914060	12.74	11.92	–12.33 ± 0.02
100136	6.0116940	–72.0848407	12.75	11.94	–13.21 ± 0.02
100141	6.0474465	–72.0917594	12.77	11.93	–13.46 ± 0.02
100142	6.0474090	–72.1034811	12.77	11.93	–20.41 ± 0.03
100148	6.0283392	–72.0802692	12.80	11.99	–26.31 ± 0.03
100151	5.9726093	–72.1059031	12.81	12.00	–8.50 ± 0.03
100152	6.0354605	–72.0975184	12.81	11.97	–2.45 ± 0.02
100154	6.0171898	–72.0853225	12.82	12.00	–4.70 ± 0.03
100161	6.0075116	–72.0971679	12.84	12.00	–22.37 ± 0.02
100162	6.0212298	–72.0768974	12.85	12.01	–41.45 ± 0.03
100167	6.0406724	–72.0919126	12.87	12.03	–13.98 ± 0.04
100169	6.0416117	–72.1082069	12.87	12.04	–21.38 ± 0.02
100171	6.0479798	–72.0906284	12.88	12.05	–12.69 ± 0.02
100174	6.0424039	–72.0857888	12.90	12.07	–13.81 ± 0.03
200021	6.1149444	–72.0892243	12.74	11.89	–21.07 ± 0.02
200023	6.1184182	–72.0838295	12.85	12.02	–22.19 ± 0.02

Note. — Identification number, coordinates, $m_{\rm F606W}$ and $m_{\rm F814W}$ magnitudes (Beccari et al., 2006), and radial velocities for the 24 AGB stars analyzed.

Table 4.2. Atmospheric parameters and iron abundances of the AGB sample

ID	$T_{\rm eff}^{\rm phot}$ (K)	log $g^{\rm phot}$ (dex)	$v_{\rm turb}$ (km s^{-1})	[FeI/H] (dex)	n(FeI)	[FeII/H] (dex)	n(FeII)
100094	4425	1.55	2.00	–0.91±0.04	134	–0.79±0.08	13
100103	4450	1.60	1.15	–1.01±0.05	170	–0.76±0.10	14
100110	4475	1.60	1.10	–0.98±0.04	165	–0.85±0.07	12
100115	4500	1.65	0.55	–0.99±0.05	171	–0.84±0.09	13
100118	4500	1.65	1.30	–0.98±0.05	161	–0.85±0.08	15
100119	4500	1.65	1.80	–0.85±0.04	138	–0.71±0.07	15
100120	4500	1.65	1.70	–0.97±0.05	138	–0.74±0.07	13
100125	4500	1.65	0.95	–1.08±0.04	171	–0.94±0.08	14
100133	4550	1.70	1.50	–0.98±0.04	147	–0.83±0.08	14
100136	4550	1.70	1.30	–0.93±0.04	166	–0.84±0.07	15
100141	4550	1.70	1.65	–0.93±0.04	155	–0.81±0.07	11
100142	4550	1.70	1.60	–0.90±0.05	140	–0.80±0.07	12
100148	4575	1.75	0.95	–1.05±0.04	173	–0.89±0.08	13
100151	4575	1.75	1.85	–0.90±0.05	141	–0.82±0.07	12
100152	4575	1.75	1.80	–0.91±0.04	156	–0.78±0.07	14
100154	4575	1.75	1.20	–1.00±0.04	159	–0.89±0.07	15
100161	4575	1.75	1.40	–0.90±0.05	158	–0.84±0.08	13
100162	4600	1.75	0.75	–1.02±0.05	174	–0.91±0.07	13
100167	4600	1.80	1.20	–0.95±0.05	158	–0.77±0.09	13
100169	4600	1.80	1.80	–0.79±0.04	154	–0.79±0.07	14
100171	4600	1.80	1.60	–0.83±0.04	155	–0.83±0.07	11
100174	4600	1.80	1.10	–1.02±0.06	144	–0.86±0.08	13
200021	4550	1.70	1.90	–0.83±0.04	145	–0.84±0.07	14
200023	4575	1.75	1.80	–0.81±0.04	147	–0.79±0.07	15
				$\langle$[FeI/H]$\rangle$		$\langle$[FeII/H]$\rangle$	
				–0.94±0.01		–0.83±0.01	

Note. — Identification number, photometric temperature and gravities, microturbulent velocities, [Fe/H] abundance ratios with total uncertainty and number of used lines, as measured from neutral and single ionized lines. For all the stars a global metallicity of [M/H]$= -1.0$ dex has been assumed for the model atmosphere. The adopted solar value is 7.50 (Grevesse & Sauval, 1998).

Table 4.3. Atmospheric parameters and iron abundances of the RGB sample

ID	$T_{\rm eff}^{\rm phot}$ (K)	log $g^{\rm phot}$ (dex)	$v_{\rm turb}$ (km s^{-1})	[FeI/H] (dex)	n(FeI)	[FeII/H] (dex)	n(FeII)
5270	4035	1.10	1.50	–0.85±0.05	140	–0.81±0.13	12
12272	4130	1.25	1.50	–0.87±0.05	147	–0.86±0.11	13
13795	4170	1.35	1.60	–0.81±0.05	141	–0.79±0.11	14
14583	4305	1.60	1.50	–0.81±0.05	150	–0.81±0.10	13
17657	4005	1.05	1.50	–0.86±0.04	133	–0.90±0.10	12
18623	4250	1.50	1.50	–0.84±0.05	144	–0.86±0.10	12
20002	4200	1.40	1.50	–0.86±0.05	147	–0.84±0.10	12
23821	4250	1.50	1.20	–0.84±0.04	147	–0.84±0.09	14
34847	4095	1.20	1.40	–0.82±0.05	141	–0.82±0.12	13
36828	4215	1.40	1.40	–0.78±0.05	142	–0.84±0.11	11
41654	4130	1.25	1.50	–0.82±0.05	142	–0.85±0.11	13
				$\langle$[FeI/H]$\rangle$		$\langle$[FeII/H]$\rangle$	
				–0.83±0.01		–0.84±0.01	

Note. — Columns are as in Table 2. For all the stars a global metallicity of [M/H]= -1.0 dex has been assumed for the model atmosphere. The adopted solar value is 7.50 (Grevesse & Sauval, 1998).

Chapter 5

The Origin of the Spurious Iron Spread in the Globular Cluster NGC3201

Published in Mucciarelli et al. 2015, ApJ, 801, 69M

NGC3201 is a globular cluster suspected to have an intrinsic spread in the iron content. We re-analysed a sample of 21 cluster stars observed with UVES-FLAMES at the Very Large Telescope and for which Simmerer et al. found a 0.4 dex wide [Fe/H] distribution with a metal-poor tail. We confirmed that when spectroscopic gravities are adopted, the derived [Fe/H] distribution spans ∼0.4 dex. On the other hand, when photometric gravities are used, the metallicity distribution from FeI lines remains large, while that derived from FeII lines is narrow and compatible with no iron spread. We demonstrate that the metal-poor component claimed by Simmerer et al. is composed by asymptotic giant branch stars that could be affected by non local thermodynamical equilibrium effects driven by iron overionization. This leads to a decrease of the FeI abundance, while leaving the FeII abundance unaltered. A similar finding has been already found in asymptotic giant branch stars of the globular clusters M5 and 47Tucanae. We conclude that NGC3201 is a normal cluster, with no evidence of intrinsic iron spread.

5.1 Observations

High-resolution spectra taken with UVES-FLAMES@VLT (Pasquini et al., 2000) for 21 giant stars members of NGC3201 have been retrieved from the ESO archive. The spectra have been acquired with the UVES grating 580 Red Arm CD#3, that provides a high spectral resolution (R∼45000) and a large spectral coverage (∼4800-6800 Å). The spectra have

been reduced using the dedicated ESO pipeline[1], performing bias subtraction, flat-fielding, wavelength calibration, spectral extraction and order merging. In each exposure one fiber is dedicated to sample the sky background and used to subtract this contribution from each individual spectrum.

Spectroscopic targets have been identified in our photometric catalog, obtained by combining high resolution images acquired with the HST-ACS camera and wide-field images acquired with the ESO-WFI imager. Both the photometric datasets have been obtained through the V and I filters. A total of 13 targets lie in the innermost cluster region, covered by ACS, while 8 stars are in the external region, covered by WFI. The membership of all the targets is confirmed by their very high radial velocity ($< RV_{helio} >= +494.6 \pm 0.8$ km s^{-1}, $\sigma = 3.6$ km s^{-1}) that allows to easily distinguish the cluster members from the surrounding field stars.

The position of the targets in the color-magnitude diagrams (CMDs) is shown in Figure A.3. These CMDs have been corrected for differential reddening using the method described in Massari et al. (2012) and adopting the extinction law by Cardelli, Clayton & Mathis (1989). In order to calculate guess values for the atmospheric parameters of the target stars, we fitted the CMDs with an appropriate theoretical isochrone from the BaSTI dataset (Pietrinferni et al., 2006), computed with an age of 11 Gyr (Marin-Franch et al., 2009), Z = 0.001 and α-enhanced chemical mixture, finding a color excess $E(B-V)$ = 0.31 mag and a true distance modulus $(m-M)_0$ = 13.35 mag.

Table 5.1 lists the main information about the targets, by adopting the same identification numbers used by Simmerer et al. (2013) who adopted the original names by Cote et al. (1994).

5.2 Analysis

Iron abundances have been derived with the package GALA[2](Mucciarelli et al., 2013a) by matching the measured and theoretical equivalent widths (EWs). Model atmospheres have been calculated with the code ATLAS9[3]. We selected FeI and FeII lines predicted to be unblended at the UVES resolution and at the typical atmospheric parameters and metallicity of the observed stars, through the careful inspection of synthetic spectra calculated with the

[1]http://www.eso.org/sci/software/pipelines/
[2]http://www.cosmic-lab.eu/gala/gala.php
[3]http://wwwuser.oats.inaf.it/castelli/sources/atlas9codes.html

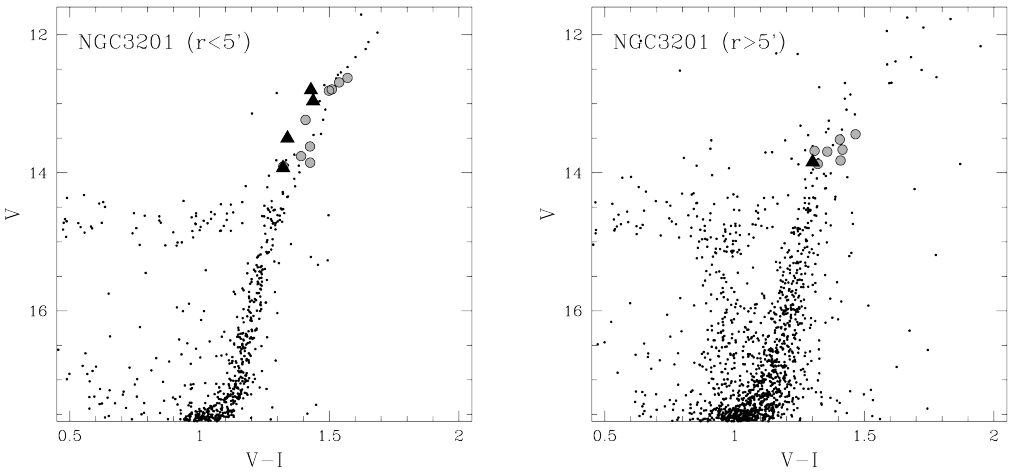

Figure 5.1 CMDs for central and external regions of NGC3201 (left and right panels, respectively), corrected for differential reddening. Large circles are the spectroscopic targets flagged as *metal-rich* ([Fe/H]>−1.58 dex) in Simmerer et al. (2013), while large triangles those identified as *metal-poor* ([Fe/H]≤−1.58 dex).

SYNTHE package (Sbordone et al., 2005). Atomic data of the transitions of interest are from the last release of the Kurucz/Castelli linelist [4]. The final iron abundances are based on ∼130-150 FeI and ∼15-20 FeII lines. EWs have been measured with DAOSPEC (Stetson & Pancino, 2008), run iteratively by means of the package 4DAO[5](Mucciarelli, 2013b). EW, oscillator strength and excitation potential for all the measured transitions are listed in Table 5.2 (available in its entirety in the online version).

5.2.1 Analysis with spectroscopic gravities

First, we performed a fully spectroscopic analysis, as done by Simmerer et al. (2013), in order to verify whether we obtain the same evidence of a metallicity dispersion. In this analysis the atmospheric parameters have been constrained as follows: *(a)* for the effective temperatures ($T_{\rm eff}$) we requested that no trend exists between abundances and excitation potential, *(b)* for the surface gravities (*log g*) we imposed that the same abundance is obtained (within the uncertainties) from FeI and FeII lines, *(c)* for the microturbulent velocity ($v_{\rm turb}$) we requested that no trend exists between abundances from FeI lines and the reduced line strength. The derived values of $v_{\rm turb}$ are based on ∼130-150 FeI lines distributed over a large interval of reduced EWs, with log(EW/λ) ranging between –5.6 and –4.7.

[4]http://wwwuser.oats.inaf.it/castelli/linelists.html
[5]http://www.cosmic-lab.eu/4dao/4dao.php

We derived an average [FeI/H]=–1.46±0.02 dex (σ= 0.10 dex), with a distribution ranging from –1.62 dex to –1.27 dex. The [FeI/H] and [FeII/H] abundance distributions are shown in Figure 5.2 as generalized histograms. This result well matches that obtained by Simmerer et al. (2013) that find an average abundance [Fe/H]=–1.48±0.02 dex (σ= 0.11 dex)[6] with a comparable iron range ($\Delta[Fe/H]$ ∼0.4 dex). This spectroscopic analysis fully confirms the claim by Simmerer et al. (2013): when analysed with atmospheric parameters derived following the constraints listed above, the stars of NGC3201 reveal a clear star-to-star scatter in the iron content. The 5 stars labelled as *metal-poor* by Simmerer et al. (2013), with [Fe/H]<–1.58 dex, are the most metal-poor also in our metallicity distribution.

5.2.2 Analysis with photometric gravities

As pointed out by Lapenna et al. (2014), possible NLTE effects in AGB stars can be easily detected by assuming photometric values for *log g* and measuring FeI and FeII independently[7]. In order to see whether this effect is present in the NGC3201 data, we adopted the following procedure. $T_{\rm eff}$ has been derived spectroscopically, by imposing the excitation equilibrium as described above. Thanks to the high quality of the spectra (with S/N ratio per pixel higher than 100) and the large number of FeI lines distributed over a large range of excitation potentials, very accurate spectroscopic $T_{\rm eff}$ can be estimated, with internal uncertainties of about 20-30 K. As a guess value we adopted $T_{\rm eff}$ calculated from the $(V-I)_0 - T_{\rm eff}$ calibration by Alonso et al. (1999) and assuming a color excess $E(B-V)$=0.31 mag. Gravities have been derived from the Stefan-Boltzmann equation, assuming $E(B-V)$=0.31 mag, $(m-M)_0$=13.35 mag, bolometric corrections from Alonso et al. (1999) and a mass of 0.82 $M_{\odot}$ (according to the best-fit isochrone, the latter is a suitable value for RGB stars brighter than the RGB Bump magnitude level). Because $T_{\rm eff}$ is derived spectroscopically, the gravity is recomputed through the Stefan-Boltzmann equation in each iteration according to the new value of $T_{\rm eff}$. The mass value of 0.82 $M_{\odot}$ is appropriate for RGB stars but probably too high for AGB stars, because of mass loss phenomena during the

[6]Note that Simmerer et al. (2013) adopted as solar reference value 7.56 obtained from their own solar analysis, while we used 7.50 by Grevesse & Sauval (1998). Througout the paper we refer to the abundances by Simmerer et al. (2013) corrected for the different solar zero-point.

[7]Recently, Johnson et al. (2015) analysed a sample of 35 AGB stars in 47 Tucanae, finding no clear evidence of NLTE effects. Even if a detailed comparison between the two analyses is not the scope of this paper, we highlight some main differences between the two works: the spectral resolution (48000 in Lapenna et al. (2014) and 22000 in Johnson et al., 2015), the number of FeII lines (13 in Lapenna et al. (2014) and 4 in Johnson et al., 2015, , on average) and the adopted linelists for AGB and RGB stars (Lapenna et al. (2014) adopted the same linelist for both the groups of stars, at variance with Johnson et al. (2015) that used a linelist consistent, but not exactly the same, with that adopted by Cordero et al. (2014) where the reference RGB stars are discussed).

RGB phase (Rood, 1973; Origlia et al., 2002, 2007, 2014). In fact, Gratton et al. (2010b) provide the masses for a sample of HB stars in NGC3201, finding values between 0.62 and 0.71 $M_{\odot}$. We initially analysed all the targets assuming the mass of a RGB star. Then, the AGB candidates, selected according to their position in $T_{\rm eff}$–log g plane (as discussed in Section 5.3) have been re-analysed by assuming the median value (0.68 $M_{\odot}$) of the HB stars estimated by Gratton et al. (2010b).

This method allows us to take advantage of the high-quality of the spectra, deriving accurate $T_{\rm eff}$ thanks to the large number of transitions spanning a large range of excitation potentials. On the other hand, this approach does not require a fully spectroscopic determination of *log g* that is instead calculated using both photometric information and spectroscopic $T_{\rm eff}$, avoiding any possible bias related to NLTE effects.

The [FeI/H] and [FeII/H] abundances obtained with this method are listed in Table 5.1. The right panel of Figure 5.2 shows the [FeI/H] and [FeII/H] distributions represented as generalized histograms obtained from this analysis. The two distributions turn out to be quite different. The iron distribution obtained from FeI lines resembles that obtained with the spectroscopic parameters (left panel of Figure 5.2), with an average value of [FeI/H]=–1.46±0.02 dex (σ= 0.10 dex), while the distribution obtained from FeII lines has a narrow gaussian-shape ([FeII/H]>=–1.40±0.01 dex, σ= 0.05 dex) pointing to a quite homogeneous iron content.

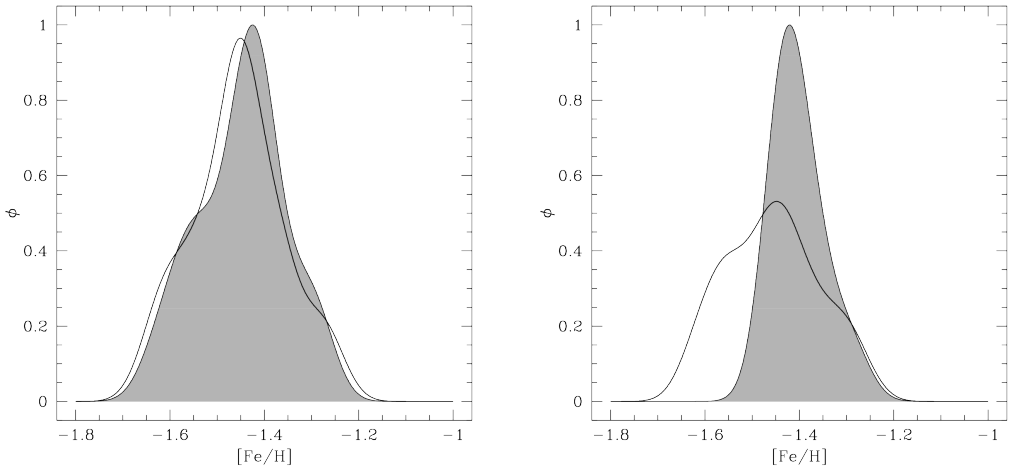

Figure 5.2 Generalized histograms for [FeI/H] (empty histogram) and [FeII/H] (grey histogram) obtained from the analysis performed with spectroscopic gravities (left panel) and with photometric gravities (right panel).

5.2.3 Uncertanties

Internal uncertainties in the derived Fe abundances have been calculated by adding in quadrature two sources of uncertainties:
(1) those arising from the EW measurement. For each target, we estimated this term as the line-to-line dispersion normalized to the root mean square of the number of lines. Because of the high quality of the used spectra, the line-to-line scatters are smaller than 0.1 dex, leading to internal uncertainties of about 0.005-0.008 dex for [FeI/H] and of about 0.010-0.025 dex for [FeII/H].
(2) those arising from the atmospheric parameters. To estimate this term, we follow the approach described by Cayrel et al. (2004) to take into account the covariance terms due to the correlations among the atmospheric parameters. For each target, the temperature has been varied by $\pm 1\sigma_{T_{\rm eff}}$, the gravity has been re-calculated through the Stefan-Boltzmann equation adopting the new values of $T_{\rm eff}$ and the microturbulent velocity re-optmized spectroscopically.

Table 5.1 lists the total uncertainty including both the terms (1) and (2). Also, Table 5.3 shows for two representative targets (one RGB and one AGB star) the abundance uncertainty obtained following the prescriptions by Cayrel et al. (2004) (second column) and those obtained with the usual method of independently varying each parameter (an approach that obviously does not take into account the correlation among the parameters and can overestimate the total uncertainty).

5.3 Discussion

In this paper we present a new analysis of the UVES-FLAMES spectra of 21 member stars of NGC3201 already discussed in Simmerer et al. (2013). The Fe abundances have been calculated both using spectroscopic gravities (obtained by imposing the ionization balance between FeI and FeII abundances) and photometric ones (obtained through the Stefan-Boltzmann equation). The two methods provide different results concerning [FeI/H] and [FeII/H]. In particular, the use of spectroscopic *log g* provides a wide [Fe/H] distribution (al large as $\sim$0.4 dex), in agreement with the finding of Simmerer et al. (2013) who adopted the same method. On the other hand, when photometric gravities are used, the [FeI/H] distribution remains quite large, while that of [FeII/H] is narrow. We compute the intrinsic spread of the two Fe distributions adopting the Maximum Likelihood algorithm described

in Mucciarelli et al. (2012). Concerning [FeI/H] we derive $\sigma_{int} = 0.09 \pm 0.01$ dex, while for [FeII/H] $\sigma_{int} = 0.00 \pm 0.02$ dex. Hence, the [FeII/H] distribution is compatible with no iron spread.

Simmerer et al. (2013) highlight that the 5 most metal-poor stars of their sample are bluer than the other stars, as expected in cases of a lower metallicity. The left panel of Figure 5.3 shows the position of the targets in the $T_{\rm eff}$–*log g* plane, with superimposed, as reference, two isochrones with the same age but different metallicity: Z= 0.001 (solid line) and Z= 0.0006 (dashed line). The RGB of the isochrone with Z= 0.0006 overlaps the position of the AGB of the Z= 0.001 isochrone. Seven targets (including the 5 candidate metal-poor stars) are located in a position compatible with both the scenarios: metal-poorer RGB or AGB at the cluster metallicity. These seven targets have average abundances of [FeI/H]=–1.57±0.01 dex and [FeII/H]=–1.41±0.01 dex, while the RGB stars have [FeI/H]=–1.42±0.02 dex and [FeII/H]=–1.40±0.01 dex.

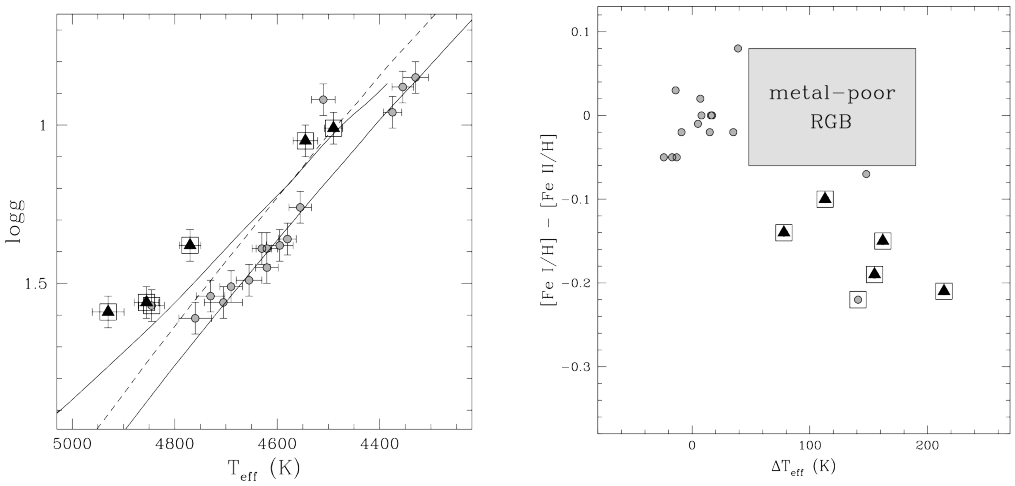

Figure 5.3 *Left panel*: position of the targets in the $T_{\rm eff}$–*log g* plane. A BaSTI isochrone with age of 11 Gyr, Z=0.001 and α-enhancement chemical mixture (solid line) is superimposed for sake of comparison. The dashed line indicates the position of the RGB for a BaSTI isochrone with age of 11 Gyr and Z=0.0006. Grey triangles are the metal-poor stars of Simmerer et al. (2013). Empty grey squares are the stars in our analysis with [FeI/H] - [FeII/H]<–0.1 dex. *Right panel*: Behaviour of [FeI/H] - [FeII/H] as a function of the difference between the spectroscopic temperature of each target and the photometric value estimate from the isochrone with Z=0.001 shown in the left panel. Same symbols as in the left panel. The grey light area indicates the expected mean locus for metal-poor ([Fe/H]∼–1.6 dex) RGB stars.

However, if these stars were metal-poor RGB stars, the iron abundance derived from FeI lines should be in agreement with that obtained from FeII, since NLTE effects are not

observed in RGB stars of comparable luminosity and metallicity. The right panel of Figure 5.3 shows the behaviour of ([FeI/H] - [FeII/H]) as a function of the difference between the spectroscopic values of $T_{\rm eff}$ and those obtained from the projection along the RGB of the best-fit isochrone. The stars located along the RGB ($\Delta T_{\rm eff}$ $\sim$0) have similar [FeI/H] and [FeII/H] abundances, compatible with no NLTE effects. The stars hotter than the reference RGB have differences between [FeI/H] and [FeII/H] ranging from –0.07 to –0.22 dex, with a mean value of –0.15 dex. The grey region marks the expected position for metal-poorer RGB stars: they should be hotter than the reference RGB, but with [FeI/H] - [FeII/H]$\sim$0, as commonly measured in the RGB stars. This reveals the true nature of these stars: they are genuine AGB stars, with the same metallicity of the cluster (as measured from their FeII lines) but affected by NLTE effects leading to a systematic decrease of [FeI/H]. This is the same effect observed by Ivans et al. (2001) and Lapenna et al. (2014) in the AGB stars of M5 and 47 Tucanae, respectively.

A direct inspection of the spectra reveals the different behaviour of FeI and FeII lines in AGB and RGB stars. Figure A.1 shows three FeI lines (chosen with different excitation potential) and one FeII line in the spectra of the AGB star #89 (upper panels) and of the RGB star #303 (lower panels). Synthetic spectra calculated with the appropriate atmospheric parameters and the metallicity derived from FeII lines (red lines). In the upper panels we also show the synthetic spectrum computed with the average [FeI/H] (blue dashed line). Clearly, the synthetic spectrum assuming the [FeII/H] abundance well reproduces all the observed lines in the case of the RGB star, while it fails to fit the FeI lines observed in the AGB star, regardless of the excitation potential (pointing out that this effect cannot be attributed to inadequacies in the adopted $T_{\rm eff}$). On the other hand, the abundance derived from FeI lines is too low to well reproduce the depth of the AGB FeII line plotted in Figure A.1. This clearly demonstrates a different behaviour of iron lines in AGB and RGB stars.

It is worth noting that this behaviour is somewhat puzzling, because theoretical models do not predict significant differences in the NLTE corrections for stars in the parameter space covered by our targets. For instance, the grid of NLTE corrections computed by Bergemann et al. (2012) and Lind, Bergemann & Asplund (2012) predicts that the FeI lines in AGB and RGB stars should be affected in a very similar way at the metallicity of NGC3201. However, some additional effects/mechanisms could play a role in the AGB photospheres, leading to the departure from the LTE condition, which are not yet accounted for in the available theoretical calculations.

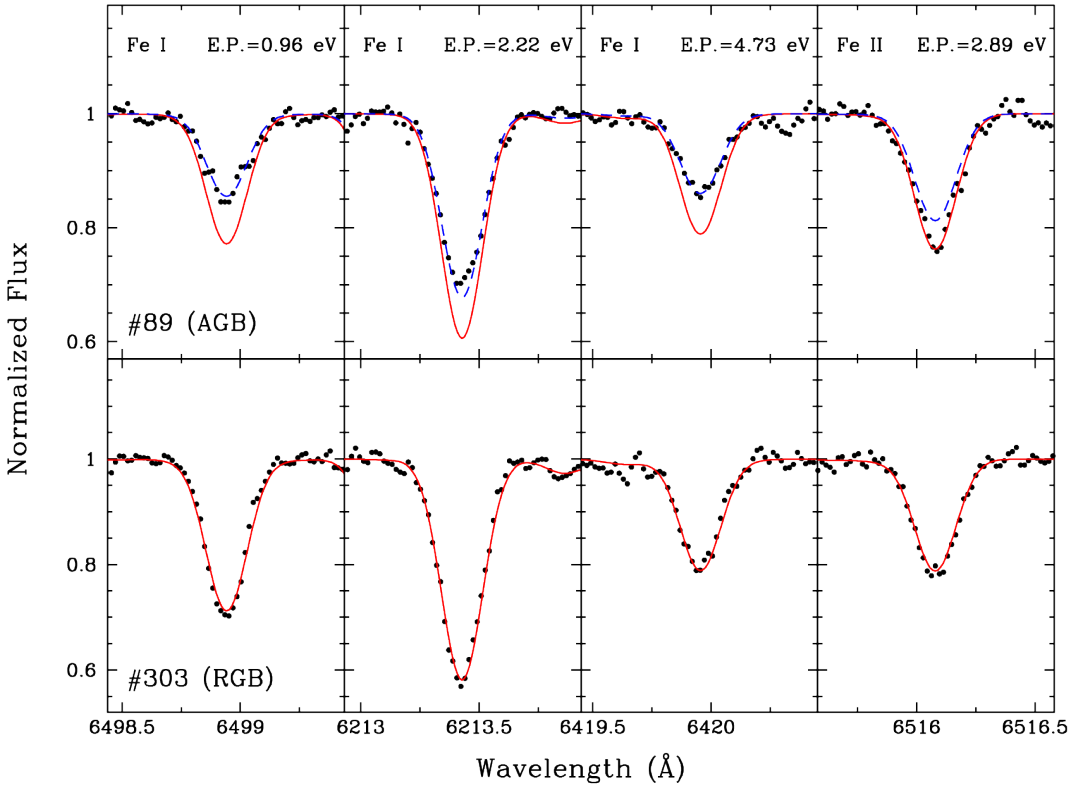

Figure 5.4 Spectral regions around three FeI lines with different excitation potential and one FeII line, for the AGB star #89 (upper panels) and the RGB star #303 (lower panels). Synthetic spectra calculated with the corresponding atmospheric parameters (see Table 5.1) and adopting the average iron abundance derived from FeII lines are superimposed as red curves. The blue dashed curve shown in the upper panels is the synthetic spectrum calculated with the iron abundance derived from FeI lines.

We checked whether the mass assumed for AGB stars could change our conclusions. The mass distribution of HB stars in NGC3201 provided by Gratton et al. (2010b) ranges from 0.62 to 0.71 $M_{\odot}$, with a median value of 0.68 $M_{\odot}$. The minimum and maximum mass values correspond to a difference in log g of 0.06, leading to a variation in [FeII/H] of only 0.02-0.025 dex (and a variation in [FeI/H] of 0.002-0.005 dex). On the other hand, if we adopt the RGB mass (0.82 $M_{\odot}$) for all targets, as it is often done because of the difficulty to observationally distinguish between RGB and AGB stars, the values of [FeII/H] increase by only 0.03 dex with respect to estimate obtained assuming 0.68 $M_{\odot}$. Hence, the precise value of the adopted mass (within a reasonable mass range) cannot reconcile the difference between [FeI/H] and [FeII/H].

As additional check, for each AGB stars, the stellar mass has been varied until the

ionization equilibrium was satisfied. The derived values range from $\sim$0.2 and $\sim$0.5 $M_{\odot}$: such masses are too low with respect to the mass distribution of the HB stars derived by Gratton et al. (2010b). In particular, for the stars #89, #181 and #240, that exhibit the largest difference between [FeI/H] and [FeII/H] ($\sim$–0.2 dex), a satisfying ionization equilibrium can be reached only with masses smaller than 0.2-0.25 $M_{\odot}$, which are very unlikely values for globular cluster AGB stars.

5.4 Conclusions

We demonstrated that the observed intrinsic star-to-star Fe scatter in the GC NGC3201 is due to unaccounted NLTE effects in the spectroscopic analysis of some AGB stars included in the sample. These stars suffer from NLTE effects driven by the iron overionization, a mechanism that affects mainly the less abundant species like FeI, but has no a significant effect on the dominant species (e.g. FeII). When the gravity of these stars is obtained spectroscopically, forcing to have the same abundance from FeI and FeII lines, the derived [Fe/H] abundance turns out to be under-estimated.

Our findings confirm the conclusion by Lapenna et al. (2014) that the chemical analysis of samples of stars including both AGB and RGB stars, and based on spectroscopic gravities, can lead to spurious broadening of the iron distribution.

We conclude that NGC3201 is a normal GC, without evidence of intrinsic iron scatter. In light of this result, it is not necessary to suppose that NGC3201 was more massive in the past to retain the SN ejecta, as invoked by Simmerer et al. (2013).

Table 5.1.

Star	RA (J2000)	Dec (J2000)	V	I	RV_{helio} (km/s)	$T_{\rm eff}$ (K)	*log g*	$v_{\rm turb}$ (km/s)	[FeI/H] (dex)	[FeII/H] (dex)
63	154.3084680	-46.4125790	13.76	12.42	495.9±0.6	4730	1.54	1.45	-1.27±0.03	-1.35±0.05
89	154.3346190	-46.3860090	13.87	12.56	498.8±0.5	4855	1.63	1.60	-1.57±0.02	-1.35±0.03
91	154.3359600	-46.3355290	13.81	12.41	490.4±0.6	4705	1.56	1.50	-1.36±0.05	-1.35±0.05
105	154.3439854	-46.4201000	13.94	12.59	493.9±0.9	4760	1.61	1.45	-1.31±0.03	-1.29±0.05
124	154.3601786	-46.4140432	12.85	11.32	498.5±0.2	4375	0.96	1.55	-1.37±0.02	-1.40±0.05
129	154.3623900	-46.4312480	13.54	12.13	491.8±0.4	4580	1.36	1.50	-1.48±0.02	-1.43±0.04
181	154.3876490	-46.4126379	13.89	12.58	497.5±0.4	4920	1.65	1.65	-1.62±0.03	-1.37±0.04
200	154.3949420	-46.3972062	12.79	11.30	495.1±0.4	4515	0.99	1.85	-1.50±0.02	-1.40±0.04
222	154.4031199	-46.4257714	12.69	11.15	491.0±0.5	4355	0.88	1.65	-1.47±0.02	-1.45±0.05
231	154.4067690	-46.4012923	13.52	12.18	491.2±0.5	4785	1.45	1.60	-1.54±0.02	-1.39±0.03
240	154.4091582	-46.4277707	13.91	12.59	495.2±0.6	4855	1.64	1.55	-1.61±0.03	-1.38±0.04
244	154.4097946	-46.4024205	13.77	12.38	492.2±0.3	4690	1.51	1.50	-1.44±0.02	-1.44±0.05
249	154.4104867	-46.4270988	12.99	11.54	498.1±0.3	4545	1.11	1.60	-1.56±0.02	-1.42±0.04
277	154.4198397	-46.4124756	13.60	12.18	497.6±0.3	4620	1.39	1.50	-1.40±0.02	-1.42±0.05
279	154.4208433	-46.3954964	13.34	11.89	499.0±0.3	4555	1.26	1.50	-1.43±0.03	-1.43±0.04
303	154.4288640	-46.3800960	13.58	12.20	491.7±0.4	4630	1.39	1.50	-1.45±0.02	-1.45±0.04
308	154.4304349	-46.4108231	13.76	12.37	487.2±0.4	4620	1.45	1.45	-1.50±0.02	-1.45±0.04
312	154.4342122	-46.4240651	12.71	11.10	494.9±0.3	4330	0.85	1.65	-1.44±0.03	-1.44±0.06
332	154.4478331	-46.3982898	12.96	11.47	499.7±0.5	4500	1.08	1.65	-1.54±0.02	-1.38±0.04
344	154.4544130	-46.4162830	13.82	12.41	490.7±0.7	4655	1.49	1.40	-1.31±0.03	-1.29±0.05
374	154.5004800	-46.5194470	13.64	12.09	498.7±0.6	4595	1.38	1.50	-1.41±0.03	-1.36±0.05
									<[FeI/H]>	<[FeII/H]>
									–1.46±0.02	–1.40±0.01

Note. — Main information of the target stars. Identification numbers are the same adopted by Simmerer et al. (2013). [FeI/H] and [FeII/H] have been obtained adopting photometric gravities.

Table 5.2. Star identification number, wavelength, oscillator strength, excitation potential and measured EWs for all the used transitions.

Star	λ (Å)	Ion	log(gf)	E.P. (eV)	EW (mÅ)
63	4791.246	FeI	-2.435	3.270	26.40
63	4834.507	FeI	-3.330	2.420	27.90
63	4842.788	FeI	-1.530	4.100	16.30
63	4892.859	FeI	-1.290	4.220	29.50
63	4911.779	FeI	-1.760	3.930	19.50
63	4917.230	FeI	-1.160	4.190	35.90
63	4918.013	FeI	-1.340	4.230	28.30
63	4950.106	FeI	-1.670	3.420	54.10
63	4962.572	FeI	-1.182	4.180	32.30
63	4969.917	FeI	-0.710	4.220	46.00
63	4985.253	FeI	-0.560	3.930	75.30
63	5002.793	FeI	-1.530	3.400	67.20
63	5014.942	FeI	-0.303	3.940	86.70
63	5022.236	FeI	-0.560	3.980	76.40
63	5028.126	FeI	-1.123	3.570	68.30

Note. — This table is available in its entirety in a machine-readable form in the online journal. A portion is shown here for guidance regarding its form and content.

Table 5.3. Abundance uncertanties due to the atmospheric parameters for the stars #63 and #89.

Ion	Parameters Uncertainty (dex)	$\delta T_{\rm eff}$ $\pm$50 K (dex)	δlog g $\pm$0.1 (dex)	$\delta v_{\rm turb}$ $\pm$0.1 km/s (dex)
		#63 (RGB)		
F I	$\pm$0.03	$\pm$0.05	$\pm$0.00	$\mp$0.03
FeII	$\pm$0.04	$\mp$0.02	$\pm$0.04	$\pm$0.03
		#89 (AGB)		
FeI	$\pm$0.02	$\pm$0.04	$\pm$0.00	$\mp$0.03
FeII	$\pm$0.03	$\mp$0.02	$\pm$0.04	$\pm$0.02

Note. — The second column is the total uncertainty calculated according to Cayrel et al. (2004). The other columns list the abundance variations related to the variation of only one parameter.

Chapter 6

A Chemical *Trompe-l'œil*: No Iron Spread in the Globular Cluster M22

Published in Mucciarelli et al. 2015, ApJ, 809, 128M

We present the analysis of high-resolution spectra obtained with UVES and UVES-FLAMES at the Very Large Telescope of 17 giants in the globular cluster M22, a stellar system suspected to have an intrinsic spread in the iron abundance. We find that when surface gravities are derived spectroscopically (by imposing to obtain the same iron abundance from FeI and FeII lines) the [Fe/H] distribution spans ∼0.5 dex, according to previous analyses. However, the gravities obtained in this way correspond to unrealistic low stellar masses (0.1-0.5 $M_{\odot}$) for most of the surveyed giants. Instead, when photometric gravities are adopted, the [FeII/H] distribution shows no evidence of spread at variance with the [FeI/H] distribution. This difference has been recently observed in other clusters and could be due to non-local thermodynamical equilibrium effects driven by over-ionization mechanisms, that mainly affect the neutral species (thus providing lower [FeI/H]) but leave [FeII/H] unaltered. We confirm that the s-process elements show significant star-to-star variations and their abundances appear to be correlated with the difference between [FeI/H] and [FeII/H]. This puzzling finding suggests that the peculiar chemical composition of some cluster stars may be related to effects able to spuriously decrease [FeI/H]. We conclude that M22 is a globular cluster with no evidence of intrinsic iron spread, ruling out that it has retained the supernovae ejecta in its gravitational potential well.

6.1 Observations

The spectroscopic dataset analysed here is the same used by (Marino et al., 2009, , hereafter M09) and includes six giant stars observed with UVES@VLT (Dekker et al., 2000) on

18-21 March 2002, and 11 giant stars observed with UVES-FLAMES@VLT (Pasquini et al., 2000) on 24-26 May 2003, adopting the Red Arm 580 grating that ranges from ∼4800 to ∼6800 Å with a typical spectral resolution R= 47000. All the spectra have been reduced with the dedicated ESO pipelines, including bias subtraction, flat-fielding, wavelength calibration, spectral extraction and order merging. The typical signal-to-noise ratio per pixel of the acquired spectra is ∼150 at ∼6000 Å.

The target stars, originally selected from the photometric catalog by Monaco et al. (2004), have been cross-identified in the UBVI ground-based catalog described in Kunder et al. (2013) and in the JHK_s 2MASS catalog (Skrutskie et al., 2006). Their position in the (V,B-V) CMD is shown in Figure A.3. Main information about the targets is available in M09.

For each target the correction for differential reddening has been derived as in Milone et al. (2012), adopting the extinction law by Cardelli, Clayton & Mathis (1989). We found that the maximum variation of E(B-V) across the area covered by the observed targets is of ∼0.07 mag, in nice agreement with Monaco et al. (2004) who quoted a maximum variation of ∼0.06 mag. The true distance modulus, $(m - M)_0$= 12.65 mag, and the color excess, E(B-V)= 0.34 mag, of the cluster have been estimated by fitting the CMD with an isochrone from the BaSTI dataset (Pietrinferni et al., 2006), computed with an age of 12 Gyr, a metallicity Z= 0.0006 and α-enhanced chemical mixture (corresponding to an iron content of [Fe/H]=–1.84 dex, in agreement with M09). The color excess is the same quoted by Harris 1996 (2010 edition), based on the photometry by Cudworth (1986), while we derived a slightly fainter (∼0.11 mag) distance modulus.

6.2 Iron abundance

The iron abundances have been derived by comparing observed and theoretical equivalent widths (EWs) by means of the code GALA (Mucciarelli et al., 2013a). EWs have been measured with the code DAOSPEC (Stetson & Pancino, 2008) run through the wrapper 4DAO (Mucciarelli, 2013b) that allows a visual inspection of the best-fit Gaussian profile for each individual line. Model atmospheres have been computed with the code ATLAS9[1] assuming 1-dimensional, plane-parallel geometry, no overshooting in the computation of the convective flux and adopting the new opacity distribution functions by Castelli & Kurucz

[1] http://wwwuser.oats.inaf.it/castelli/sources/atlas9codes.html

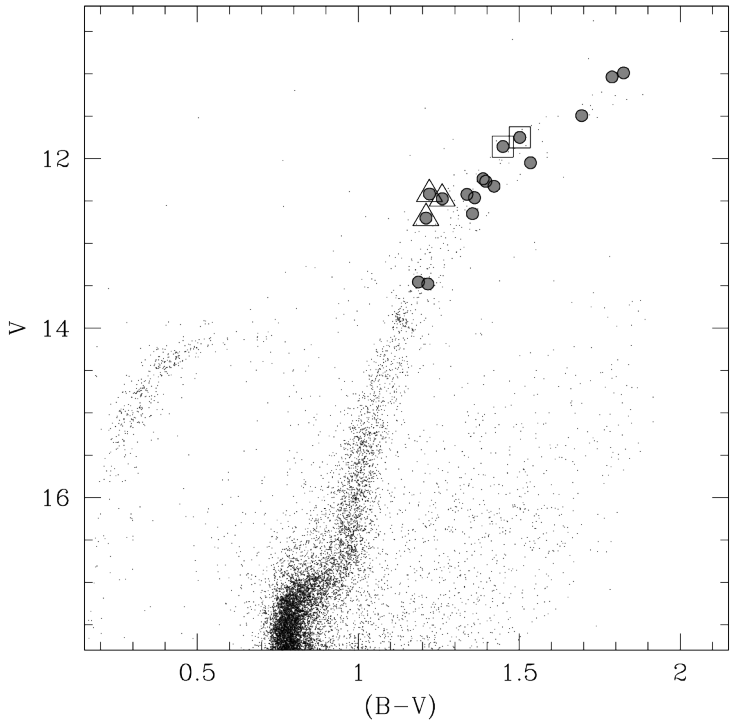

Figure 6.1 (B-V,V) color-magnitude diagram of M22 (Kunder et al., 2013) with marked as grey circles the spectroscopic targets. Empty triangles are the likely candidate AGB stars, while empty squares are possible (but not sure) AGB stars.

(2004) computed with an enhanced chemical composition for the α-elements (while for all the other elements a solar [X/Fe] abundance ratio is assumed). The metallicity [M/H] of the model atmosphere for each star has been chosen according to the average [Fe/H] derived from FeII lines, being most of the iron in the ionized stage in the atmosphere of late-type stars.

First guess parameters for effective temperature (T_{eff}) and surface gravities (log g) have been calculated from the photometry. T_{eff} has been derived from the color-T_{eff} transformations by Alonso et al. (1999), by averaging the values obtained from different de-reddened broad-band colors, namely $(U - B)_0$, $(B - V)_0$, $(V - I)_0$, $(V - K_s)_0$ and $(J - K_s)_0$. Surface gravities have been derived through the Stefan-Boltzmann relation, assuming the average T_{eff} , the bolometric corrections by Alonso et al. (1999) computed with the average T_{eff} and the stellar masses obtained from the best-fit isochrone. For most of the stars we adopted a mass of 0.78 $M_\odot$ (appropriate for RGB stars, according to the best-fit theoretical isochrone). Three targets are identified as likely AGB stars, according

to their positions in the optical CMDs (they are marked as empty triangles in Figure A.3). We assumed for these stars a mass of 0.65 $M_{\odot}$, corresponding to the median value of the mass distribution of the horizontal branch stars of M22 (obtained by using the zero age horizontal branch models of the BaSTI database). The position of two other stars (marked as empty squares in Figure A.3) could also be compatible with the AGB but the small color separation from the RGB makes it difficult to unambiguously assign these targets to a given evolutionary sequence. For these two stars we assume conservatively a mass of 0.78 $M_{\odot}$ and checking that the impact of a different mass on the iron abundances is very small: assuming the AGB mass, [FeII/H] changes by $\sim$0.03 dex, while [FeI/H] does not change.

Because the targets span relatively large ranges in the parameter space (δT$_{eff}\sim$700 K and δlog $g\sim$1.5 dex, according to the photometric estimates), the use of an unique linelist is inadvisable, because the line blending conditions vary with the evolutionary stage of the stars. Hence, a suitable linelist has been defined for each individual target, by using a specific synthetic spectrum calculated with the code SYNTHE (see Sbordone et al., 2005, for details), adopting the photometric parameters and including only transitions predicted to be unblended and detectable in the observed spectrum. Each linelist has been refined iteratively: after a first analysis, the selected transitions have been checked with synthetic spectra calculated with the new parameters and including the precise chemical composition obtained from the analysis. The oscillator strengths for FeI lines are from the compilation by Fuhr, Martin & Wiese (1988) and Fuhr & Wiese (2006), while for FeII lines we adopted the recent atomic data by Melendez & Barbuy (2009). Concerning the van der Waals damping constants, the values calculated by Barklem, Piskunov & O'Mara (2000) are adopted whenever possible, while for other transitions they were computed according to the prescriptions of Castelli (2005). The reference solar value is 7.50 (Grevesse & Sauval, 1998). EW, excitation potential and oscillator strength are listed in Table 6.1.

The iron abundances have been derived from 130-200 FeI lines and 15-20 FeII lines, leading to internal uncertainties arising from the EW measurements (estimated as the line-to-line scatter divided to the square root of the number of used lines) of the order of 0.01 dex (or less) for FeI and 0.01-0.02 dex for FeII. The chemical analysis has been performed with three different approaches to constrain T$_{eff}$ and log g, while the microturbulent velocities (v$_{turb}$) have been constrained by imposing no trend between the iron abundance and the line strength, expressed as $\log(EW/\lambda)$. The total uncertainty in the chemical abundance has been computed by summing in quadrature the internal uncertainty and that arising from

the atmospheric parameters, the latter being estimated according to the different method adopted (as discussed below). Table 6.2 summarises the average [FeI/H] and [FeII/H] abundances obtained with the different methods.

6.2.1 Method (1): spectroscopic T_{eff} and log g

The values of T_{eff} have been derived by erasing any trend between the iron abundance obtained from FeI lines and the excitation potential (χ), while log g have been derived by requiring the same abundance from FeI and FeII lines. Because of the large number of FeI lines, well distributed over a wide range of χ values, the spectroscopic T_{eff} are constrained with internal uncertainties of about 30-50 K, while the internal uncertainties on log g are $\sim$0.03-0.05. Uncertainties in v_{turb} are of about 0.1 km/s (this value is valid also for the other methods where the same approach is used to derive v_{turb}). We assumed a typical uncertainty of $\pm$0.05 dex in the metallicity [M/H] of the model atmosphere; this has a negligible impact on [FeI/H] but leads to variations of $\pm$0.02-0.04 dex in [FeII/H].

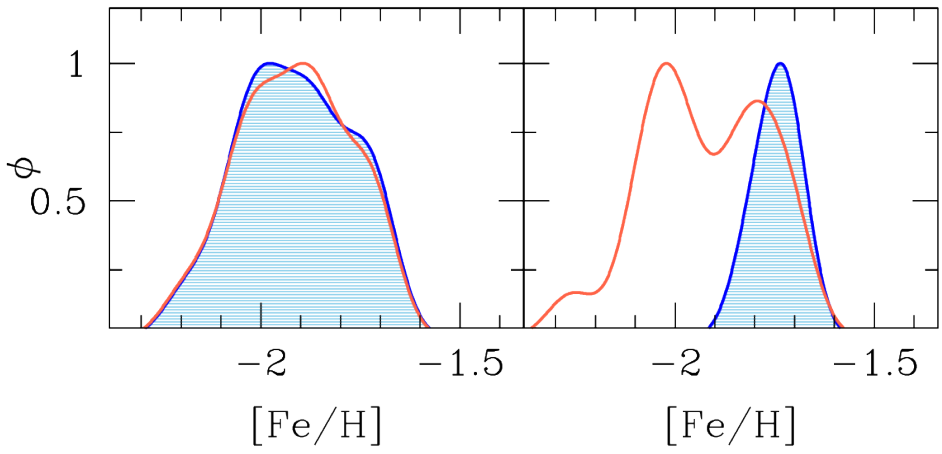

Figure 6.2 Generalized histograms for [FeI/H] (empty red histogram) and [FeII/H] (blue histogram) obtained from the analysis performed with spectroscopic gravities (method (1), left panel) and with photometric gravities (method (2), right panel).

The [Fe/H] distributions thus derived from neutral and single ionized lines are shown in the left panel of Figure 6.2, as generalized histograms. The two distributions are, by construction, very similar to each other (because of the adopted constraint to derive log g) and $\sim$0.5 dex wide, with an average value of [Fe/H]=–1.92$\pm$0.03 (σ=0.13 dex) for both [FeI/H] and [FeII/H]. In order to evaluate whether the observed scatter is compatible with an intrin-

sic spread, we adopted the maximum likelihood (ML) algorithm described in Mucciarelli et al. (2012), which provides the intrinsic scatter (σ_{int}) of the metallicity distributions by taking into account the uncertainties of each individual star. Both the iron distributions have a non-zero scatter, with σ_{int}=0.13$\pm$0.02 dex. This result is qualitatively similar to that of M09, who obtained a broad Fe distribution adopting the same approach to derive the atmospheric parameters.

6.2.2 Method (2): spectroscopic T_{eff} and photometric log g

The values of T_{eff} have been constrained spectroscopically, as done in the method (1), while those of log g have been derived through the Stefan-Boltzmann relation. In the computation of log g, we adopted the distance modulus, stellar masses, color excess and bolometric corrections used for the guess parameters, together with the spectroscopic T_{eff}. The internal uncertainty of the photometric log g has been computed including the uncertainties in the adopted T_{eff}, stellar mass, magnitudes and differential reddening corrections, leading to a total uncertainty of about 0.05 dex. Errors in distance modulus and color excess have been neglected because they impact systematically all the stars, while we are interested in the star-to-star uncertainties only. This approach allows to benefit at best from all the spectroscopic and photometric pieces of information in hand, minimizing the impact (mainly on T_{eff}) of the uncertainties in the differential and absolute reddening. The atmospheric parameters and the [FeI/H] and [FeII/H] abundance ratios derived with this method are listed in Table 6.3.

By adopting this method, which (at odds with the previous one) does not impose ionization balance, we find that, for most of the targets, a large difference between [FeI/H] and [FeII/H]. The [FeI/H] and [FeII/H] distributions are shown in the right panel of Figure 6.2. At variance with the previous case, the two distributions look very different: the distribution of [FeI/H] spans a range of $\sim$0.5 dex, with an average value of –1.92$\pm$0.04 (σ=0.16 dex), while the [FeII/H] distribution is narrow and symmetric, with an average value of –1.75$\pm$0.01 dex (σ= 0.04 dex). The ML algorithm provides an intrinsic spread σ_{int}=0.15$\pm$0.02 dex for the [FeI/H] distribution, while the [FeII/H] distribution is compatible with a negligible intrinsic scatter (σ_{int}= 0.00$\pm$0.02 dex).

To illustrate this difference between [FeI/H] and [FeII/H], Figure 6.3 shows some FeI and FeII lines in the spectra of stars #200080 (where [FeI/H] is 0.29 dex lower than [FeII/H]) and #88 (where [FeI/H] and [FeII/H] differ by 0.05 dex only). In the first case, the synthetic

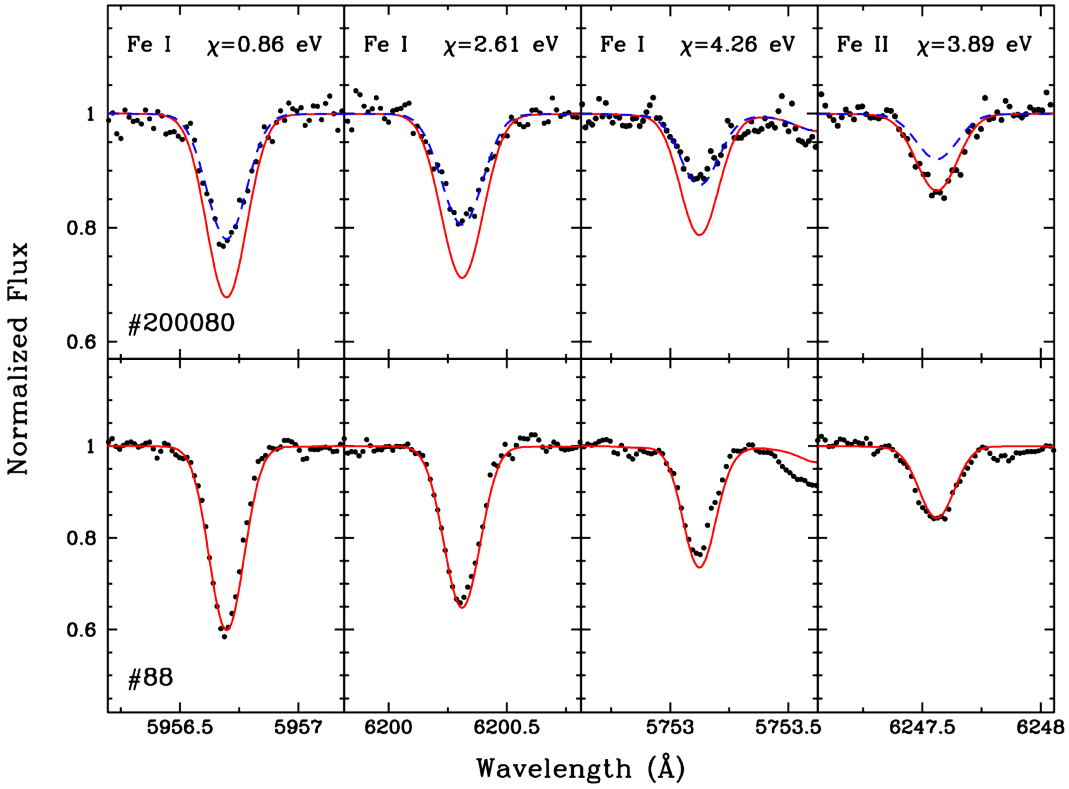

Figure 6.3 Spectral regions around three FeI lines with different excitation potential and one FeII line, for the target stars #200080 (upper panels) and #88 (lower panels). Synthetic spectra calculated with the corresponding atmospheric parameters (see Table 6.4) and adopting the average iron abundance derived from FeII lines are superimposed as red curves. The blue dashed curve shown in the upper panels is the synthetic spectrum calculated with the iron abundance derived from FeI lines.

spectrum calculated with the average abundance derived from FeII lines (red solid line) is not able to reproduce the FeI lines. The latter are always weaker than those of the synthetic spectrum, regardless of their χ and line strength, thus suggesting that the discrepancy is not due to inaccuracies in T_{eff} and/or v_{turb} (otherwise a better agreement would have been found for high-χ lines, less sensitive to T_{eff}, and/or for weak lines, less sensitive to v_{turb}). On the other hand, the synthetic spectrum computed with the [FeI/H] abundance (blue dashed line) does not fit the FeII line, that is stronger than that predicted by the synthetic spectrum. In the case of star #88 the situation is different and an unique Fe abundance is able to well reproduce both FeI and FeII lines.

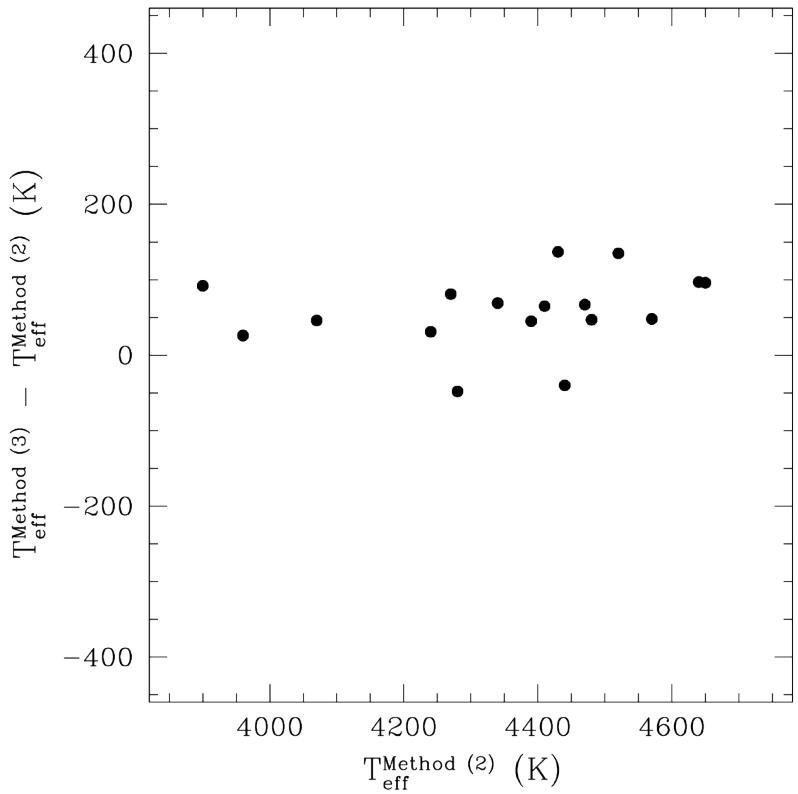

Figure 6.4 Behaviour of the difference between T_{eff} as derived with method (3) and (2) as a function of those derived with method (2).

6.2.3 Method (3): photometric T_{eff} and log g

As an additional check, the analysis has been performed keeping T_{eff} and log g fixed at the guess values derived from the photometry (see Section 8.2), and optimizing spectroscopically only v_{turb}. This set of parameters is very similar to that obtained with method (2), with the average differences, in the sense of method (3) - method (2), of +58$\pm$12 K (σ= 50 K) in T_{eff}, +0.02$\pm$0.005 (σ=0.02) in log g and +0.04$\pm$0.02 kms^{-1} (σ= 0.08 kms^{-1}) in v_{turb} . In particular, we note that spectroscopic and photometric T_{eff} agree very well, and their differences do not show trends with the photometric T_{eff}, as visible in Figure 6.4 where the difference between T_{eff} from method (3) and (2) are shown as a function of the spectroscopic T_{eff}.

Figure 6.5 shows the Fe abundance distributions obtained with the average photometric parameters (upper-left panel) and using the individual broad-band colors $(U-B)_0$, $(B-V)_0$, $(V-I)_0$, $(V-K_s)_0$, $(J-K_s)_0$. In all cases, the [FeII/H] distribution is single-peaked and

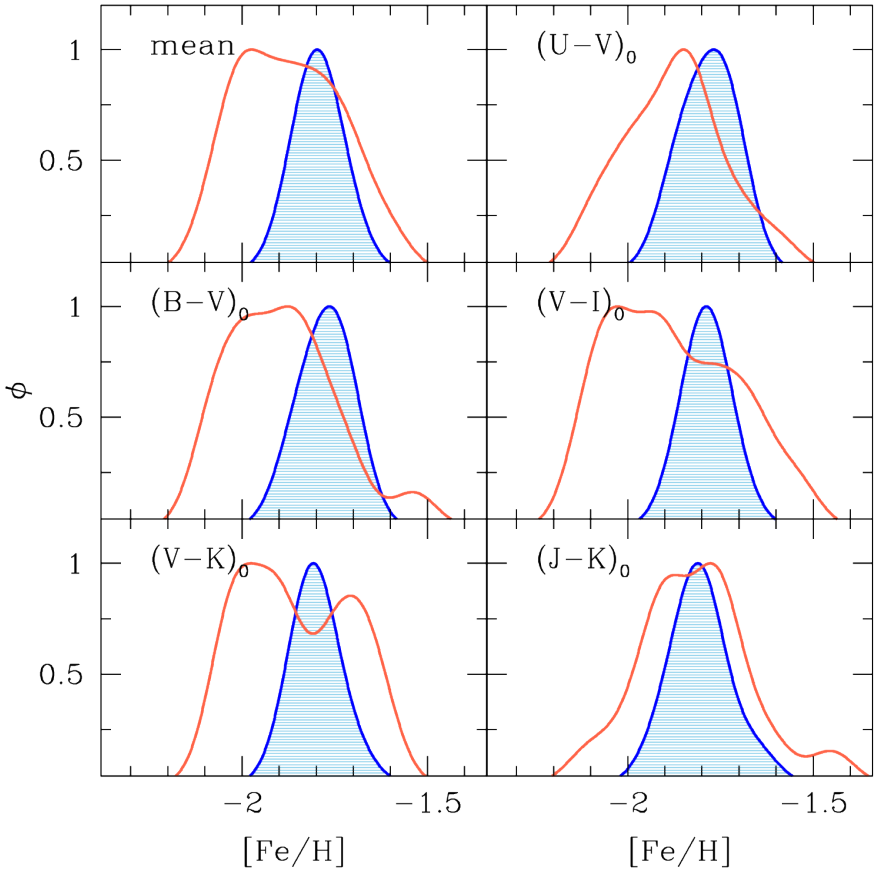

Figure 6.5 Generalized histograms for [FeI/H] and [FeII/H] (same colors of Figure 6.2) obtained with the method (3) (photometric T_{eff} and log g), adopting the mean parameters (left-upper panel) and those derived from individual broad-band colors.

narrow, well consistent with that obtained from method (2). Instead, whatever color is adopted, the [FeI/H] distribution always has a much larger (by a factor of 2-3) dispersion than that obtained for [FeII/H], similar to the finding of method (2). In particular, when we consider the average photometric parameters, the ML algorithm provides intrinsic scatter of 0.12±0.02 for [FeI/H] and 0.00±0.02 for [FeII/H]. Because the results obtained with this method agree with those obtained with method (2), and the star-to-star uncertainties in spectroscopic T_{eff} are smaller than the photometric ones (which are also affected by the uncertainties on the differential reddening corrections), in the following we refer only to method (2) as alternative approach to method (1).

6.3 A sanity check: NGC6752

As a sanity check, UVES-FLAMES archival spectra of 14 RGB stars in the GC NGC6752 observed with the Red Arm 580 grating have been analysed following the same procedure used for M22. NGC6752 is a well-studied GC that can be considered as a standard example of *genuine* GC, with no intrinsic iron spread (see e.g. Yong et al., 2005; Carretta et al., 2009b)[2] and with a metallicity comparable with that of M22. This approach allows to remove any systematics due to the adopted atomic data, solar reference values, model atmospheres, method to measure EWs and to derive the atmospheric parameters. When the parameters are derived following method (2), we derive average abundances [FeI/H]=–1.62±0.01 dex (σ= 0.04 dex) and [FeII/H]=–1.58±0.01 dex (σ= 0.04 dex), in good agreement with the previous estimates available in the literature. In this case, the two iron distributions (shown in Figure 6.6) have small observed dispersions, both compatible with a negligible scatter within the uncertainties, as demonstrated by the ML algorithm. The two distributions are compatible with each other also in terms of their shape, at variance with those of M22. The same results are obtained when the parameters are all derived spectroscopically. This test demonstrates that: (i) the different [FeI/H] and [FeII/H] distributions obtained for M22 with methods (2) and (3) are not due to the adopted procedure; (ii) in a normal GC the shape of [FeI/H] and [FeII/H] distributions are not significantly different.

6.4 No iron spread in M22

The new analysis of the sample of giant stars already discussed in M09 leads to an unexpected result: an iron abundance spread in M22 is found when FeI lines are used, independently of the adopted spectroscopic or photometric gravities. *This scatter totally vanishes when the iron abundance is derived from FeII lines and photometric gravities are used.* In the case of spectroscopic gravities, the abundances from FeII lines are forced to match those from FeI lines, thus producing a broad [FeII/H] distribution. Given that the adoption of photometric gravities leads to a broad [FeI/H] distribution and a narrow, mono-metallic [FeII/H] distribution, which one should we trust? In principle, FeII lines are most trustworthy than FeI lines to determine the iron abundance, because FeII is a dominant species in

[2] Yong et al. (2013) performed a strictly differential line-by-line analysis on 37 RGB stars of NGC6752 by using high-quality UVES spectra, finding an observed spread in [Fe/H], 0.02 dex, larger of a factor of 2 than the internal uncertainties. This small intrinsic spread could reflect He variations and/or real inhomogeneities in the cluster iron content. Because such chemical inhomogeneities can be revealed only when the internal uncertainties are smaller than ∼0.02 dex, for our purposes we can consider NGC6752 as a *genuine* GC.

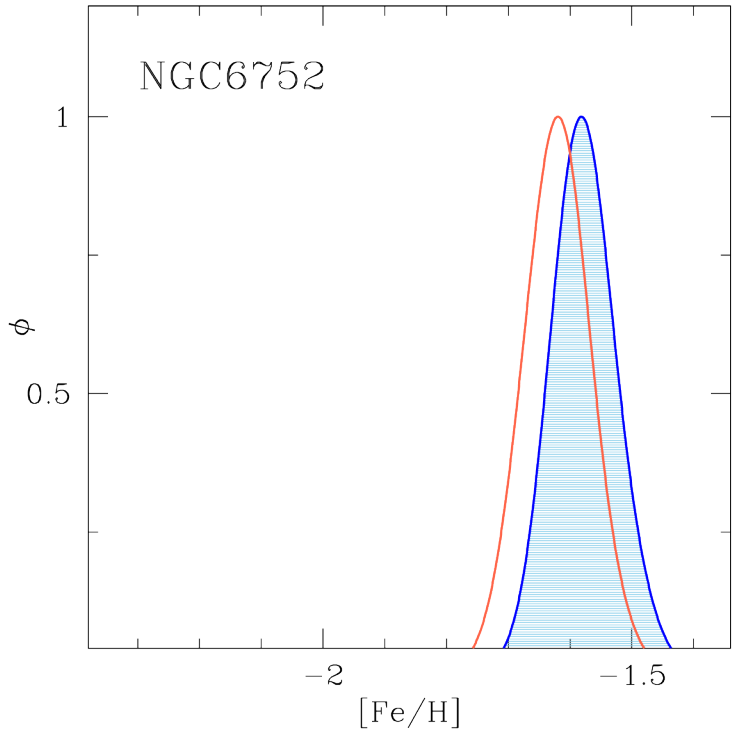

Figure 6.6 Generalized histograms for [FeI/H] and [FeII/H] (same colors of Figure 6.2) for a sample of 14 RGB stars in the GC NGC6752. The analysis has been performed adopting spectroscopic T_{eff} and photometric log g, the same method used for the right panel of Figure 6.2.

the atmospheres of late-type stars (where iron is almost completely ionized) and its lines are unaffected by NLTE effects, at variance with the FeI lines (see e.g. Kraft & Ivans, 2003; Mashonkina et al., 2011).

The analysis of the results shown in Figure 6.2 and 6.5 suggests that the adoption of method (1) tends to produce an artificial spread of [FeII/H] toward low metallicities. Since [FeII/H] strongly depends on the adopted values of logg, this implies that gravities are severly underestimated in method (1). This bias is clearly revealed when the stellar masses corresponding to the spectroscopic values of log g values are computed. We estimated the stellar masses by inverting the Stefan-Boltzmann equation and assuming the spectroscopic log g derived with method (1). The derived masses range from 0.12 to 0.79 $M_{\odot}$, with a mean value of 0.46 $M_{\odot}$ and a dispersion of 0.2 $M_{\odot}$. Note that $\sim$70% of the stars have masses below 0.6 $M_{\odot}$. Such low values, as well as the large dispersion of the mass distribution, are unlikely for a sample dominated by RGB stars, with expected masses close to 0.75-0.80 $M_{\odot}$. In particular, 10 target stars have log g that would require masses below 0.5 $M_{\odot}$,

thus smaller than the typical mass of the He-core of GC giant stars at the luminosity level of our targets. Such very low masses cannot be justified even in light of the uncertainties in the mass loss rate (Origlia et al., 2014). A similarly wide mass distribution is obtained by adopting the spectroscopic parameters by M09, leading to a mass range between 0.34 and 1.19 $M_{\odot}$. In that case, three stars have masses larger than 0.8 $M_{\odot}$, corresponding to the typical mass of a turnoff star of M22. For comparison, the masses derived from the spectroscopic log g of the spectral sample of NGC6752 (see Section 6.3) cover a small and well reasonable range, from 0.65 to 0.85 $M_{\odot}$, with an average value of 0.75 $M_{\odot}$ (σ=0.06 $M_{\odot}$).

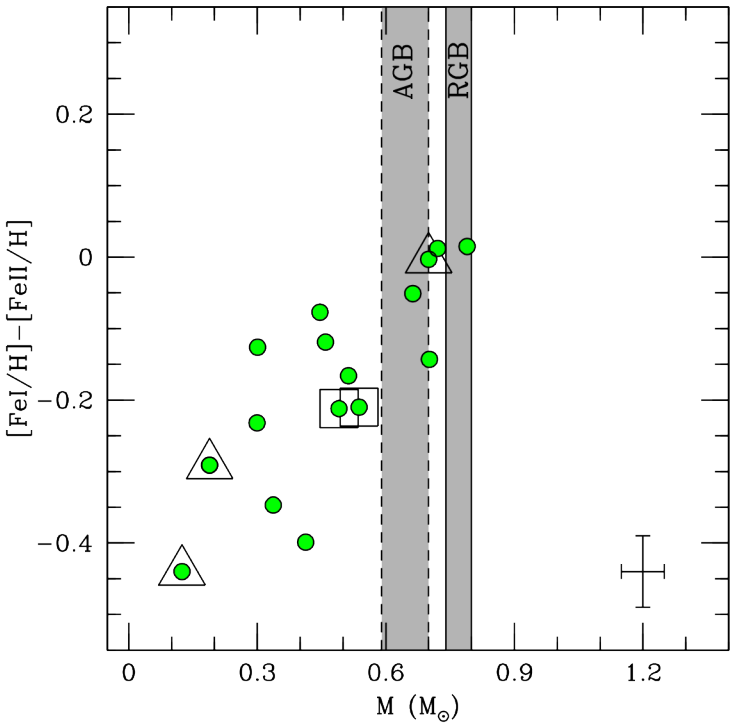

Figure 6.7 Behavior of the difference [FeI/H]-[FeII/H], as derived with method (2), of the spectroscopic targets as a function of the stellar masses inferred from the spectroscopic log g in method (1). The two shaded grey regions mark the mass range expected for AGB and RGB stars. Same symbols of Figure A.3.

Figure 6.7 shows the behavior of the difference [FeI/H]-[FeII/H], as derived with method (2), as a function of the stellar masses, as derived from the spectroscopic gravities in method (1). The mass intervals expected for RGB and AGB stars in the luminosity range of our spectroscopic targets are shown as grey shaded regions. A clear trend between the [FeI/H]-[FeII/H] difference and the stellar mass is found. The stars with the largest difference be-

tween FeI and FeII abundances are also those where the spectroscopic log g requires an unrealistically low mass, while for the stars where [FeI/H] is consistent with [FeII/H] the spectroscopic log g provide masses in reasonable agreement with the theoretical expectations. This demonstrates that the spectroscopic gravities needed to force [FeII/H] matching the low-abundance tail of the [FeI/H] distribution lead to unreliable stellar masses. Since this is the only case in which [Fe II/H] shows significant spread, we have to conclude that the observed large iron distribution is not real. The correct diagnostic of iron content therefore are the Fe II lines analyzed under the assumption of photometric gravities. These always lead to a narrow iron distribution (see Figures 6.2 and 6.5), thus implying that no iron spread is observed in M22.

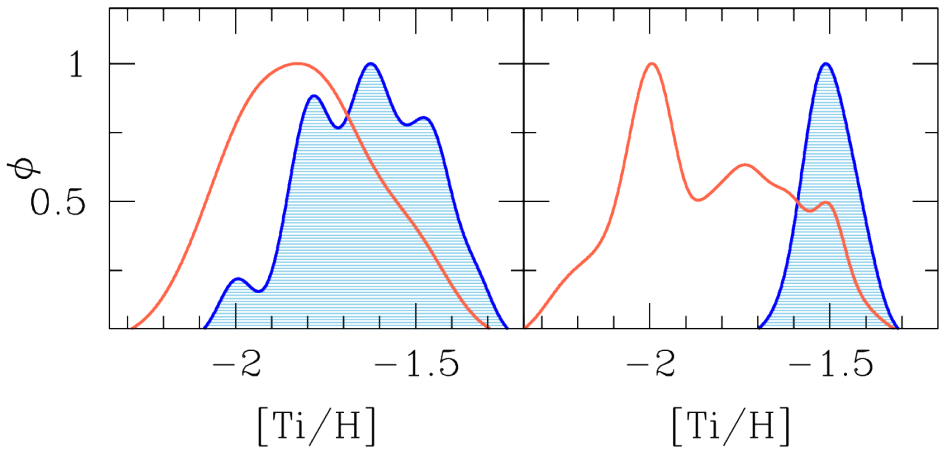

Figure 6.8 Generalized histograms for [TiI/H] (empty red histogram) and [TiII/H] (blue histogram) obtained adopting the spectroscopic (left panel) and photometric log g (right panel).

An additional confirmation of the different behavior of neutral and ionized lines in our sample is provided by the analysis of the titanium transitions, because this element is one of the few species that provides a large number of both neutral and single ionized lines. The oscillator strengths are from Martin, Fuhr & Wiese (1988) and Lawler et al. (2013) for TiI lines and from Wood et al. (2013) for TiII lines. The [TiI/H] and [TiII/H] abundances exhibit the same behavior discussed above for the Fe abundances. When the spectroscopic gravities are used, both the distributions are broad, with an observed scatter of $\sim$0.2 dex (see left panel of Figure 6.8). On the other hand, when the photometric gravities are adopted (see Table 6.3), the [TiII/H] distribution is consistent with null intrinsic scatters, while that of [TiI/H] remains broad and skewed toward low abundances (right panel of Figure 6.8). We note that

the difference [TiI/H]-[TiII/H] strongly correlates with the difference [FeI/H]-[FeII/H], with a Spearman rank correlation coefficient C_S=+0.956 that provides a probability of $\sim 10^{-8}$ that the two quantities are not correlated. Hence, the analysis of [TiI/H] and [TiII/H] reinforces the scenario where the abundances from neutral lines in most of the M22 stars are biased, providing distributions (artificially) larger than those from single ionized lines.

6.5 The s-process elements abundance

M09 and Marino et al. (2011) found that M22 has, together with a dispersion in the iron content, an intrinsic spread in the abundances of s-process elements. In light of the results described above, we derived abundances also for these elements, by adopting the parameters obtained with method (2) and measuring YII, BaII, LaII and NdII lines. For Y and Nd the abundances have been obtained with GALA from the EW measurement, as done for the Fe and Ti lines, and adopting the oscillator strengths available in the Kurucz/Castelli linelist. BaII and LaII lines are affected by hyperfine and isotopic splittings. The linelists for the LaII lines are from Lawler et al. (2001), while those for the BaII lines from the NIST database [3]. Only for these two elements, the abundances have been derived with our own code SALVADOR (A. Mucciarelli et al. in preparation) that performs a χ^2-minimization between observed and synthetic spectra calculated with the code SYNTHE.

For all these elements, we found that the absolute abundances show large star-to-star variations, with observed scatters between $\sim$0.2 and $\sim$0.3 dex, depending on the element. These spreads are not compatible within the uncertainties. Because of the possible occurrence of the NLTE effects, the abundance ratios [X/Fe] (see Table 6.4) have been estimated by using the FeII abundances as reference; in fact, for these elements the chemical abundances have been derived only from single ionized transitions, which are less sensitive to the overionization (or sensitive to it in a comparable way to the FeII lines; see e.g. the discussion in Ivans et al., 2001). The [X/FeII] abundance ratios show significant intrinsic spreads, as confirmed by the ML algorithm. Note that, if we adopt FeI abundances as reference, the [X/FeI] abundance ratios still display an intrinsic scatter, because the observed spread in the absolute abundances for these s-process elements is larger than that measured from the FeI lines.

Figure 6.9 shows the behavior of each s-process element abundance ratio as a function of

[3] http://physics.nist.gov/PhysRefData/ASD/lines_form.html

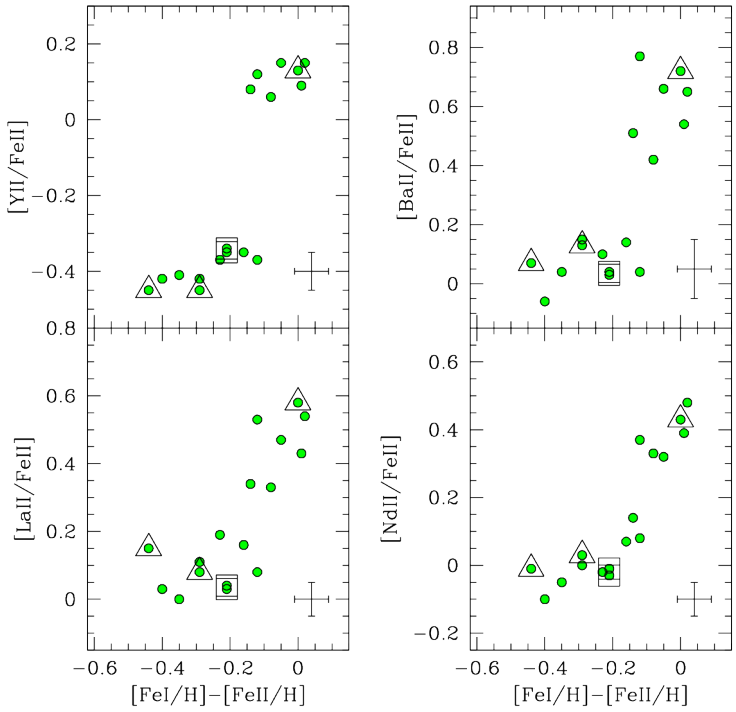

Figure 6.9 Behavior of the abundance of the s-process elements Y, La, Ba and Nd as a function of the difference between [FeI/H] and [FeII/H]. Same symbols of Figure A.3.

the difference between [FeI/H] and [FeII/H]. In all the cases, a clear trend between [X/FeII] and [FeI/H]-[FeII/H] is detected, in the sense that the stars characterized by higher s-process abundances display a better agreement between FeI and FeII. In the case of Y, Ba and Nd, we find two distinct and well separated groups of stars, while for La the behavior is continuous, with no clear gap. Finally, Figure 6.10 plots the behavior of <[s/FeII]>, obtained by averaging together the four abundance ratios, as a function of [FeI/H]-[FeII/H], confirming the existence of two groups of stars, with different [s/Fe] and [FeI/H] (but the same [FeII/H]). This finding resembles the results by M09 who identify two groups of stars, named *s-poor* and *s-rich*.

6.6 Discussion: re-thinking M22

The main results and conclusions of this work are summarized as follows:

- The new analysis of M22 presented here demonstrates that this GC is mono-metallic and that the previous claim of a metallicity scatter was due to a systematic under-estimate of the FeI abundance combined with the use of spectroscopic gravities. When photometric

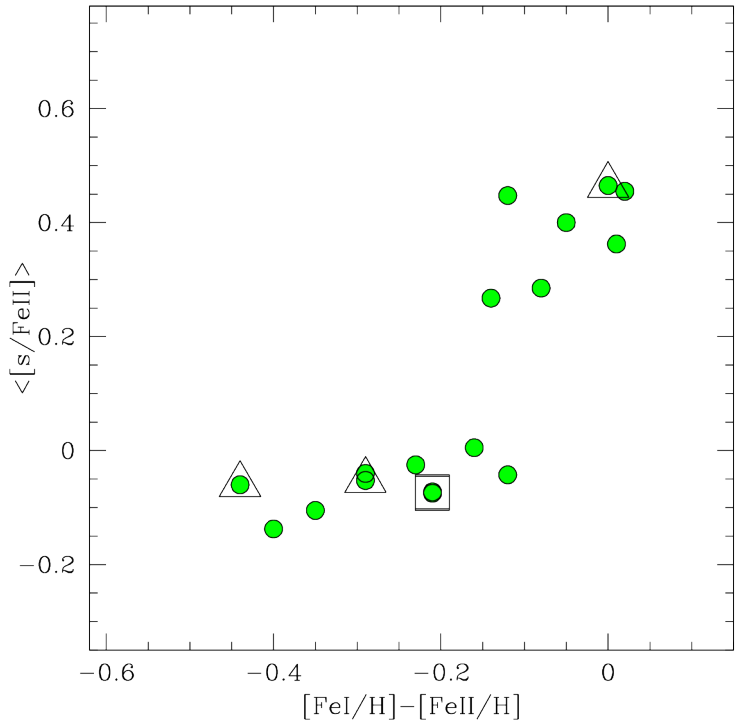

Figure 6.10 Behavior of the average abundance of s-process elements (derived by averaging together the abundances of Y, La, Ba and Nd) as a function of the difference between [FeI/H] and [FeII/H]. Same symbols of Figure A.3.

log g are adopted, the FeII lines provide the same abundance for all the stars, regardless of the adopted method to estimate T_{eff}.

- In light of this result, the formation/evolution scenario for M22 must be deeply re-thought. The homogeneity in its iron content suggests that M22 was not able to retain the SN ejecta in its gravitational well. Hence, it is not necessary to invoke that the cluster was significantly more massive at its birth and that it subsequently lost a large amount of its mass. The observed unimodal [FeII/H] distribution rules out the possibility that M22 is the remnant of a now disrupted dwarf galaxy, because these systems are characterized by a wide range of metallicity, due to the prolonged star-formation activity (see Tolstoy, Hill & Tosi, 2009, and references therein). Also, comparisons between M22 and ω Centauri (Da Costa & Marino, 2011) are undermined by the homogeneity in the [FeII/H] abundance of M22. On the other hand, M22 cannot be considered as a *genuine* GC, because of the intrinsic spread in heavy s-process elements abundances, pointing out the occurence of a peculiar chemical enrichment (probably from AGB stars) in this

cluster, at variance with most of the GCs where s-process elements do not show intrinsic scatters (D'Orazi et al., 2010).

- M09 and Marino et al. (2011) discussed the possibility that M22 is the product of a merging between two GCs with different chemical composition. In light of our new analysis, this scenario appears unlikely, even if it cannot be totally ruled out. In this framework, M22 should form from the merging between two clusters with the same Fe content, but characterized by different s-process element abundances. While clusters with comparable metallicity and different s-process abundance are indeed observed (for instance M4 and M5; Ivans et al., 1999, 2001), in this scenario the cluster with normal s-process abundances should be composed mainly by stars with a large difference between [FeI/H] and [FeII/H], while the second cluster should have stars with enhanced s-process abundances and similar [FeI/H] and [FeII/H] (see Figure 6.10).

- As a possible working hypothesis to explain the observed behavior of [FeI/H] and [FeII/H], we note that the difference between [FeI/H] and [FeII/H] is qualitatively compatible with the occurrence of NLTE effects driven by overionization. These effects are known to affect mainly the less abundant species, like FeI, and to have a negligible/null impact on the dominant species, like FeII (see e.g. Thévenin & Idiart, 1999; Mashonkina et al., 2011; Fabrizio et al., 2012). Under NLTE conditions, the spectral lines of neutral ions are weaker than in LTE. Hence, when the line formation is calculated in LTE conditions (as done in standard analyses), the resulting abundance of neutral lines will be correspondingly lower.

  The same interpretative scheme can be applied to M22. A large and intrinsically broad Fe distribution is obtained only from FeI lines, according to the systematic underestimate of the Fe abundance obtained when lines affected by overionization are analysed in LTE. On the other hand, FeII lines are not affected by NLTE and they provide (when photometric log g are used) the correct abundance, leading to a narrow abundance distribution.

- The mismatch between [FeI/H] and [FeII/H] observed in M22 resembles those found in the GCs M5 (Ivans et al., 2001), 47Tucanae (Lapenna et al., 2014) and NGC3201 (Mucciarelli et al., 2015a). In these cases, the different behavior observed for FeI and FeII lines is restricted to AGB stars only, where FeI lines provide abundances systematically lower than those from FeII lines, while RGB stars have similar [FeI/H] and [FeII/H]. However, the situation is more complex in M22, because a large difference between

[FeI/H] and [FeII/H] is observed in most of the stars and not only in AGB stars. Among the target stars of M22, three are identified as AGB stars, according to their positions in the CMDs. Two of them have a large Fe difference, [FeI/H]-[FeII/H]=–0.29 and –0.44 dex, while for the third star FeI and FeII lines provide almost the same abundance. The other two possible AGB stars (empty squares in Figure A.3) have Fe differences of –0.21 dex. On the other hand, comparable differences are observed among some RGB stars. For instance, the two faintest stars of the sample (#221 and #224) are clearly RGB stars (see Figure A.3 and 6.7), because they are located at the luminosity level where the color separation between RGB and AGB is the largest. On the other hand, these two stars (with very similar atmospheric parameters and [FeII/H]) have different [FeI/H] abundances: star #224 has a difference of [FeI/H]-[FeII/H]=–0.14 dex, while star #221 has [FeI/H]-[FeII/H]=–0.29 dex. If departures from LTE are the reasons for the observed discrepancy between [FeI/H] and [FeII/H] (and between [TiI/H] and [TiII/H]), this finding challenges the available NLTE calculations (see e.g. Lind, Bergemann & Asplund, 2012; Bergemann et al., 2012), in which stars with very similar parameters are expected to have the same NLTE corrections. New NLTE calculations should be performed to investigate this hypothesis, with the constraint to reproduce simultaneously the discrepancies in Fe and Ti.

- We found that the difference between [FeI/H] and [FeII/H] is correlated with the s-process element abundances. The behavior is quite puzzling, because the stars with an anomalous difference between [FeI/H] and [FeII/H] are those with *normal* s-process abundances, compatible with the abundances observed in most of the GCs and in the Galactic field stars of similar metallicity (see e.g. Figure 3 in Venn et al., 2004). On the other hand, the stars enriched in s-process elements show a good agreement between [FeI/H] and [FeII/H]. *Whatever the mechanism responsible to spread [FeI/H] is, it must be also responsible for the peculiar behavior of the s-process element abundances.*

- We confirm the claim already suggested by Lapenna et al. (2014) and Mucciarelli et al. (2015a): chemical analyses based on FeI lines and spectroscopic gravities can lead to spurious abundance spreads. In light of these results, any claim of intrinsic iron spread in GCs should be always confirmed with an analysis based on FeII lines and photometric gravities. If the abundance spread is real, it should be detected also when FeII lines and photometric log g are adopted, since FeII lines are the most reliable indicators of the iron

Table 6.1. Star identification number, wavelength, ion, excitation potential, oscillator strength and measured EWs for all the used transitions.

Star	λ (Å)	Ion	χ (eV)	log gf	EW (mÅ)
51	4805.415	TiI	2.340	0.070	30.4
51	4870.126	TiI	2.250	0.440	46.7
51	4885.079	TiI	1.890	0.410	76.1
51	4909.098	TiI	0.830	-2.370	15.8
51	4913.614	TiI	1.870	0.220	64.0
51	4915.229	TiI	1.890	-0.910	11.8
51	4919.860	TiI	2.160	-0.120	30.1
51	4926.148	TiI	0.820	-2.090	20.9
51	4937.726	TiI	0.810	-2.080	27.2
51	4997.096	TiI	0.000	-2.070	90.7
51	5009.645	TiI	0.020	-2.200	83.1
51	5016.161	TiI	0.850	-0.480	107.5
51	5020.026	TiI	0.840	-0.330	117.0
51	5036.464	TiI	1.440	0.140	98.9
51	5038.397	TiI	1.430	0.020	95.9
51	5043.584	TiI	0.840	-1.590	46.6
51	5045.415	TiI	0.850	-1.840	29.7
51	5052.870	TiI	2.170	-0.270	23.0
51	5062.103	TiI	2.160	-0.390	15.6
51	5065.985	TiI	1.440	-0.970	38.1

Note. — This table is available in its entirety in machine-readable form.

abundance. All the GCs with anomalous intrinsic Fe spreads observed so far (see Marino et al., 2015, for an updated list) deserve new analyses in light of this effect, in order to firmly establish whether these spreads are real or spurious.

Table 6.2. Observed and intrinsic scatters for [FeI/H] and [FeII/H] as derived from the ML algorithm and from the three methods described in the paper.

	[FeI/H]	σ_{obs}	σ_{int}	[FeII/H]	σ_{obs}	σ_{int}
Method 1	–1.92±0.03	0.14	0.13±0.02	–1.90±0.03	0.14	0.13±0.02
Method 2	–1.92±0.04	0.16	0.15±0.02	–1.75±0.01	0.04	0.00±0.02
Method 3	–1.86±0.03	0.13	0.12±0.02	–1.81±0.01	0.05	0.00±0.02

Table 6.3. Atmospheric parameters, [FeI/H], [FeII/H], [TiI/H] and [TiII/H] abundances for the spectroscopic targets of M22, as derived with method (1). The last line lists the average abundances with the statistical error.

Star	T_{eff} (K)	log g	v_{turb} (km/s)	[FeI/H]	[FeII/H]	[TiI/H]	[TiII/H]	Notes
51	4280	1.00	1.70	–1.70±0.02	–1.71±0.04	–1.50±0.04	–1.34±0.04	
61	4430	0.95	1.70	–1.85±0.05	–1.84±0.04	–1.74±0.06	–1.61±0.04	
71	4405	0.97	1.50	–1.90±0.04	–1.89±0.04	–1.77±0.04	–1.59±0.04	
88	4450	1.20	1.50	–1.78±0.05	–1.74±0.05	–1.67±0.08	–1.46±0.04	
221	4570	1.13	1.40	–2.04±0.04	–2.04±0.04	–2.00±0.04	–1.86±0.04	
224	4670	1.75	1.40	–1.87±0.04	–1.78±0.04	–1.76±0.05	–1.47±0.04	
200005	3920	0.00	2.20	–2.10±0.02	–1.92±0.06	–1.97±0.05	–1.74±0.05	
200006	3910	0.04	2.10	–1.84±0.03	–1.78±0.05	–1.69±0.05	–1.55±0.04	
200025	4060	0.57	1.90	–1.72±0.02	–1.75±0.05	–1.48±0.05	–1.45±0.04	
200031	4290	0.72	1.80	–1.96±0.03	–1.97±0.04	–1.85±0.05	–1.64±0.04	AGB?
200043	4300	0.73	1.70	–1.94±0.04	–1.95±0.04	–1.86±0.04	–1.69±0.05	AGB?
200068	4400	0.82	1.60	–2.00±0.04	–2.00±0.04	–1.93±0.05	–1.74±0.04	
200076	4390	0.80	1.60	–2.05±0.04	–2.06±0.04	–2.01±0.05	–1.82±0.04	
200080	4520	0.70	1.70	–2.01±0.04	–2.00±0.03	–1.96±0.05	–1.78±0.04	AGB
200083	4440	1.20	1.50	–1.73±0.04	–1.75±0.04	–1.60±0.05	–1.46±0.05	AGB
200101	4400	0.90	1.50	–1.89±0.05	–1.91±0.05	–1.77±0.05	–1.64±0.05	
200104	4490	0.59	1.70	–2.19±0.06	–2.19±0.03	–2.15±0.08	–2.00±0.03	AGB
				–1.92±0.03	–1.91±0.03	–1.81±0.04	–1.64±0.04	

Table 6.4. Atmospheric parameters, [FeI/H], [FeII/H], [TiI/H] and [TiII/H] abundances for the spectroscopic targets of M22, as derived with method (2). The last line lists the average abundances with the statistical error.

Star	T_{eff} (K)	log g	v_{turb} (km/s)	[FeI/H]	[FeII/H]	[TiI/H]	[TiII/H]	Notes
51	4280	0.99	1.70	–1.70±0.02	–1.72±0.04	–1.50±0.04	–1.41±0.05	
61	4440	1.17	1.60	–1.84±0.05	–1.72±0.04	–1.76±0.06	–1.49±0.05	
71	4390	1.15	1.60	–1.94±0.03	–1.78±0.04	–1.85±0.05	–1.51±0.05	
88	4470	1.30	1.50	–1.77±0.05	–1.72±0.05	–1.66±0.08	–1.44±0.06	
221	4640	1.81	1.30	–2.00±0.05	–1.71±0.04	–1.98±0.06	–1.53±0.05	
224	4650	1.80	1.30	–1.88±0.05	–1.74±0.04	–1.79±0.07	–1.42±0.05	
200005	3900	0.30	2.20	–2.07±0.03	–1.67±0.09	–2.07±0.10	–1.62±0.06	
200006	3960	0.34	2.10	–1.80±0.04	–1.72±0.09	–1.63±0.10	–1.48±0.06	
200025	4070	0.63	1.80	–1.70±0.04	–1.71±0.07	–1.45±0.08	–1.46±0.06	
200031	4240	0.86	1.80	–2.02±0.04	–1.81±0.05	–1.98±0.07	–1.53±0.05	AGB?
200043	4270	0.93	1.70	–1.98±0.04	–1.77±0.05	–1.96±0.05	–1.56±0.06	AGB?
200068	4340	1.16	1.60	–2.10±0.05	–1.75±0.05	–2.11±0.07	–1.54±0.05	
200076	4410	1.24	1.60	–2.05±0.04	–1.82±0.04	–2.03±0.05	–1.54±0.05	
200080	4570	1.28	1.70	–2.03±0.05	–1.74±0.04	–1.99±0.06	–1.52±0.05	AGB
200083	4430	1.18	1.60	–1.76±0.04	–1.76±0.05	–1.60±0.05	–1.48±0.05	AGB
200101	4480	1.37	1.50	–1.83±0.05	–1.71±0.05	–1.71±0.06	–1.44±0.06	
200104	4520	1.36	1.70	–2.26±0.05	–1.82±0.04	–2.23±0.07	–1.55±0.05	AGB
				–1.92±0.04	–1.75±0.01	–1.84±0.05	–1.50±0.01	

Table 6.5. Atmospheric parameters, [FeI/H], [FeII/H], [TiI/H] and [TiII/H] abundances for the spectroscopic targets of M22, as derived with method (3). The last line lists the average abundances with the statistical error.

Star	T_{eff} (K)	log g	v_{turb} (km/s)	[FeI/H]	[FeII/H]	[TiI/H]	[TiII/H]	Notes
51	4232	0.96	1.70	–1.76±0.05	–1.72±0.06	–1.57±0.06	–1.37±0.06	
61	4400	1.16	1.60	–1.87±0.05	–1.73±0.05	–1.81±0.06	–1.50±0.07	
71	4435	1.17	1.50	–1.88±0.05	–1.82±0.05	–1.76±0.08	–1.50±0.08	
88	4537	1.32	1.60	–1.71±0.06	–1.80±0.06	–1.53±0.06	–1.49±0.07	
221	4737	1.84	1.50	–1.90±0.05	–1.81±0.05	–1.84±0.07	–1.57±0.07	
224	4746	1.84	1.50	–1.80±0.04	–1.82±0.04	–1.65±0.07	–1.48±0.06	
200005	3992	0.34	2.20	–2.08±0.04	–1.78±0.04	–1.88±0.06	–1.62±0.07	
200006	3986	0.36	2.10	–1.80±0.05	–1.77±0.05	–1.56±0.06	–1.47±0.07	
200025	4116	0.65	1.90	–1.68±0.05	–1.81±0.05	–1.36±0.08	–1.45±0.09	
200031	4271	0.87	1.80	–1.97±0.05	–1.88±0.05	–1.93±0.06	–1.54±0.07	AGB?
200043	4351	0.97	1.70	–1.89±0.04	–1.84±0.05	–1.81±0.08	–1.58±0.08	AGB?
200068	4409	1.19	1.60	–2.00±0.05	–1.85±0.07	–1.98±0.06	–1.56±0.07	
200076	4475	1.27	1.60	–1.98±0.05	–1.87±0.05	–1.92±0.06	–1.60±0.06	
200080	4618	1.30	1.80	–1.95±0.05	–1.80±0.07	–1.90±0.06	–1.55±0.07	AGB
200083	4567	1.24	1.60	–1.61±0.05	–1.84±0.05	–1.36±0.08	–1.49±0.06	AGB
200101	4527	1.39	1.60	–1.79±0.06	–1.80±0.04	–1.62±0.06	–1.52±0.07	
200104	4655	1.41	1.70	–2.04±0.07	–1.89±0.07	–1.99±0.07	–1.63±0.09	AGB
				–1.86±0.03	–1.81±0.01	–1.73±0.05	–1.52±0.02	

Table 6.6. Abundance ratios for the s-process elements Y, Ba, La and Nd.

Star	[YII/FeII]	[BaII/FeII]	[LaII/FeII]	[NdII/FeII]
51	+0.15±0.04	+0.65±0.07	+0.54±0.04	+0.48±0.04
61	–0.37±0.05	+0.04±0.08	+0.08±0.04	+0.08±0.04
71	–0.35±0.05	+0.14±0.08	+0.16±0.06	+0.07±0.04
88	+0.15±0.05	+0.66±0.08	+0.47±0.04	+0.32±0.05
221	–0.42±0.04	+0.15±0.10	+0.11±0.04	+0.00±0.05
224	+0.08±0.05	+0.51±0.07	+0.34±0.06	+0.14±0.04
200005	–0.42±0.06	+0.06±0.12	+0.03±0.05	–0.10±0.05
200006	+0.06±0.08	+0.42±0.11	+0.33±0.05	+0.33±0.05
200025	+0.09±0.05	+0.54±0.06	+0.43±0.06	+0.39±0.05
200031	–0.35±0.04	+0.03±0.08	+0.03±0.06	–0.01±0.04
200043	–0.34±0.05	+0.04±0.07	+0.04±0.04	–0.03±0.04
200068	–0.41±0.04	+0.04±0.08	+0.00±0.05	–0.05±0.04
200076	–0.37±0.04	+0.10±0.08	+0.19±0.05	–0.02±0.04
200080	–0.45±0.04	+0.13±0.09	+0.08±0.05	+0.03±0.05
200083	+0.13±0.06	+0.72±0.08	+0.58±0.04	+0.43±0.04
200101	+0.12±0.06	+0.77±0.09	+0.53±0.04	+0.37±0.05
200104	–0.45±0.04	+0.07±0.09	+0.15±0.06	–0.01±0.05

Chapter 7

Chemical Analysis of Asymptotic Giant Branch Stars in M62

Published in Lapenna et al. 2015, ApJ, 813, 97L

We have collected UVES-FLAMES high-resolution spectra for a sample of 6 asymptotic giant branch (AGB) and 13 red giant branch (RGB) stars in the Galactic globular cluster M62 (NGC6266). Here we present the detailed abundance analysis of iron, titanium, and light-elements (O, Na, Al and Mg). For the majority (5 out 6) of the AGB targets we find that the abundances, of both iron and titanium, determined from neutral lines are significantly underestimated with respect to those obtained from ionized features, the latter being, instead, in agreement with those measured for the RGB targets. This is similar to recent findings in other clusters and may suggest the presence of Non-Local Thermodynamical Equilibrium (NLTE) effects. In the O-Na, Al-Mg and Na-Al planes, the RGB stars show the typical correlations observed for globular cluster stars. Instead, all the AGB targets are clumped in the regions where first generation stars are expected to lie, similarly to what recently found for the AGB population of NGC6752. While the sodium and aluminum abundance could be underestimated as a consequence of the NLTE bias affecting iron and titanium, the used oxygen line does not suffer from the same effects and the lack of O-poor AGB stars therefore is solid. We can thus conclude that none of the investigated AGB stars belong to the second stellar generation of M62. We also find a RGB star with extremely high sodium abundance ([Na/Fe]$= +1.08$ *dex).*

7.1 Observations and spectral analysis

We have observed a sample of 19 giant stars in the GC M62 by using the UVES-FLAMES@VLT spectrograph (Pasquini et al., 2000) within the Large Program 193.D-0232 (PI: Ferraro).

The spectra have been acquired by using the grating 580 Red Arm CD#3, which provides a high spectral resolution (R$\sim$40000) and a spectral coverage between 4800 and 6800Å. The 19 targets have been sampled by means of four different fiber configurations, in five pointings of 30 min each (one configuration has been repeated twice), during the nights of 2014, April 16 and June 2, 3 and 19. In each configuration, one or two fibers have been used to sample the sky for background subtraction purposes. After careful visual inspection, only the (19) spectra with a signal-to-noise larger than 50 have been kept in the analysis. The spectra have been reduced by using the dedicated ESO pipeline[1] performing bias subtraction, flat-fielding, wavelength calibration, spectral extraction and order merging. The sky background has been subtracted from each individual spectrum.

The target stars have been selected from the photometric catalog of Beccari et al. (2006), obtained from HST-WFPC2 observations. Only stars brighter than $V = 15$ and sufficiently isolated (i.e., with no stellar sources of comparable or larger luminosity within a distance of $2''$, and with no fainter stars within $1''$) have been selected. Figure A.3 shows the $(V, U-V)$ color-magnitude diagram (CMD) corrected for differential reddening following the procedure described in Massari et al. (2012) and adopting the extinction law by McCall (2004). The final sample includes 6 AGB and 13 RGB stars. All the target stars are located within $\sim 85''$ from the cluster center. Their identification number, coordinates, and magnitudes are listed in Table 7.1.

7.1.1 Radial velocities

The radial velocities of our targets have been obtained by using the code DAOSPEC (Stetson & Pancino, 2008) and by measuring the position of over 300 metallic lines distributed along the whole spectral range covered by the 580 Red Arm of UVES-FLAMES. The uncertainties have been computed as the dispersion of the velocities measured from each line divided by the square root of the number of lines used, and they turned out to be smaller than 0.05 km s^{-1}. Finally, we applied the heliocentric corrections computed with the IRAF task RVCORRECT. For each spectrum, the zero-point of the wavelength calibration has been accurately checked by means of a few emission lines of the sky. The final velocities are listed in Table 7.1. They range from -109.8 km s^{-1} to -53.4 km s^{-1}, with a mean value of -76.7 ± 3.6 km s^{-1} and a dispersion $\sigma = 15.6$ km s^{-1}. These values are in good agreement with the derivations of Dubath et al. (1997, $v_r = -71.8 \pm 1.6$ km s^{-1}, $\sigma = 16.0$

[1] http://www.eso.org/sci/software/pipelines/

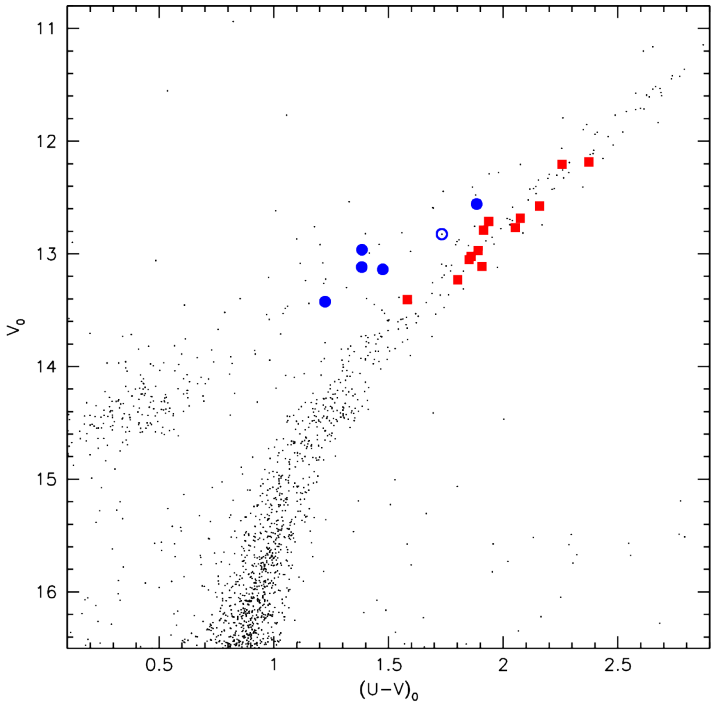

Figure 7.1 Reddening-corrected color-magnitude diagram of M62, with the targets of the present study highlighted: 13 RGB stars (red squares) and 6 AGB objects (blue circles). The empty circle marks AGB star 96.

km s^{-1}) and Yong et al. (2014, $v_r = -70.1 \pm 1.4$ km s^{-1}, $\sigma = 14.3$ km s^{-1}), the small differences being likely due to the small statistics.

The most discrepant target (id=79), with a radial velocity of -109.85 km s^{-1}, is still within 2σ from the systemic velocity of the cluster. By using the Besançon Galactic model (Robin et al., 2003), we extracted a sample of about 5300 field stars in the direction of M62, finding a quite broad and asymmetric radial velocity distribution, with mean $v_r \simeq -60$ km s^{-1} and dispersion $\sigma = 80$ km s^{-1}, which partially overlaps with that of the cluster. On the other hand, only a few percent of the stars studied in that region close to the Galactic bulge have a [Fe/H] < -1.0 dex (see e.g. Zoccali et al., 2008; Hill et al., 2011; Johnson et al., 2013; Ness et al., 2013). Thus, taking into account the metallicity of star 79 (see below), its position in the CMD, and its distance from the cluster center ($d \sim 38.5''$), we conclude that it is likely a genuine cluster member and we therefore keep it in the following analysis.

7.1.2 Atmospheric parameters and stellar masses

First guess effective temperature ($T_{\rm eff}$) and surface gravity ($\log g$) values for each target have been derived by using the photometric information. Temperatures have been estimated by using the $(U-V)_0 - T_{\rm eff}$ calibration of Alonso et al. (1999). Gravities have been computed with the Stefan-Boltzmann equation by adopting the color excess quoted above, a distance modulus $(m-M)_0 = 14.16$ mag (Harris 1996, 2010 edition) and the bolometric correction from Alonso et al. (1999). For the RGB stars we adopted a mass of 0.82 $M_{\odot}$, according to the best fit isochrone retrieved from the PARSEC dataset (Bressan et al., 2012), and computed for an age of 12 Gyr and a metallicity Z=0.0013. For the AGB stars we adopted a mass of 0.61 $M_{\odot}$, according to the median value of the HB mass range estimated by Gratton et al. (2010b).

Then we have performed a spectroscopic analysis as done in Lapenna et al. (2014) and Mucciarelli et al. (2015a), constraining the atmospheric parameters as follows: (1) spectroscopic temperatures have been obtained by requiring that no trend exists between iron abundance and excitation potential, (2) the gravity was derived by using the Stefan-Boltzmann equation with the value of $T_{\rm eff}$ thus obtained and (3) the microturbulent velocity was determined by requiring that no trend exists between iron abundance and line strength. In order to evaluate the effects of a different procedure in the derivation of the atmospheric parameters and abundances, we have also performed a spectroscopic determination of the surface gravities by modifying condition (2) and imposing that the same abundance is obtained from neutral and single-ionized iron lines (ionization balance).

7.1.3 Chemical abundances

The chemical abundances of Fe, Ti, Na, Al and Mg have been derived with the package GALA[2] (Mucciarelli et al., 2013a), which adopts the classical method to derive the abundances from the measured EWs of metallic unblended lines. The EW and the error of each line were obtained using DAOSPEC, iteratively launched by means of the 4DAO[3] code (Mucciarelli, 2013b). The lines considered in the analysis have been selected from suitable synthetic spectra at the UVES-FLAMES resolution and computed with the SYNTHE package (Sbordone et al., 2005) by using the guess atmospheric parameters and the metallicity derived by Yong et al. (2014). The model atmospheres have been computed with the

[2] http://www.cosmic-lab.eu/gala/gala.php
[3] http://www.cosmic-lab.eu/4dao/4dao.php

ATLAS9[4] code. We adopted the atomic and molecular data from the last release of the Kurucz/Castelli compilation[5] and selected only the lines predicted to be unblended. The selected lines and the atomic data adopted in the analysis are listed in Table 7.2.

As detailed in Table 7.3, we used 100-150 FeI lines and 7-12 FeII lines to derive the iron abundances, 25-60 lines of TiI and 6-15 lines of TiII to derive the abundances of titanium. For NaI, MgI and AlI only few lines are available, namely those at 5682-5688Å and 6154-6160Å for NaI, the line at 5711Å and the doublet at 6318-6319Å for MgI, and the doublet at 6696-6698Å for AlI. The O abundances have been derived from spectral synthesis in order to take into account the blending between the forbidden [OI] line at 6300.3Å and a Ni transition. For the Ni we adopted the average abundance obtained by Yong et al. (2014), while for stars located in the upper-RGB we assumed average C and N abundances according to Gratton et al. (2000), all rescaled to the assumed solar reference values (Grevesse & Sauval, 1998). Because in some spectra the [OI] line was partially blended also with a telluric line, the spectra have been cleaned by using suitable synthetic spectra obtained with the TAPAS tool (Bertaux et al., 2014). For some stars, the [OI] line is not detectable, thus only upper limits are obtained. As solar reference abundances we adopted the Caffau et al. (2011) value for O, and those of Grevesse & Sauval (1998) for all the other elements.

For the computation of the global uncertainties on the final abundances we took into account two main sources of errors, which have been added in quadrature:

1) the error arising from the EW measurements. For each star we computed this term by dividing the line-to-line dispersion by the square root of the number of lines used. Thanks to the high-quality of the spectra and to the number of lines that can be exploited, this term turned out to be very small, especially for FeI and TiI (providing up to 150 lines). For these species the line-to-line scatter is smaller than 0.1 dex, leading to internal uncertainties lower than 0.01-0.02 dex. For FeII and TiII the number of lines ranges from 7 up to 15, leading to an uncertainty of about 0.02-0.03 dex. For the other chemical species the number of measured lines is much smaller (1-4). Hence, the average uncertainties are of the order of 0.06-0.08 dex for OI, NaI, MgI and AlI.

2) the error arising from atmospheric parameters. For the computation of this term we varied each parameter by the 1σ error obtained from the previous analysis. We have found that representative errors for $T_{\rm eff}$, $\log g$ and v_{turb} are ~ 50 K, 0.1 dex and 0.1 km

[4]http://wwwuser.oats.inaf.it/castelli/sources/atlas9codes.html
[5]http://wwwuser.oats.inaf.it/castelli/linelists.html

s^{-1}, respectively, for both the RGB and the AGB samples. Thus we decided to adopt these values as 1σ error for all stars. We also checked the effect of a ± 0.1 dex change in the metallicity of the model atmosphere, finding variations smaller than ± 0.01 dex on the final abundances.

7.2 Results

The determination of abundances and abundance ratios of the various chemical elements is described below. The adopted atmospheric parameters and the measured iron and titanium abundances for the observed RGB and AGB stars are listed in Table 7.3, while the abundances of the light-elements are listed in Table 7.4. In Table 7.5 we present the global abundance uncertainty of one RGB and one AGB star, as well as the uncertainties obtained by varying each atmospheric parameter independently. Since this approach does not take into account the correlations among different parameters, the global error can be slightly overestimated.

Since star 96 presents an anomalous behavior with respect to the other AGB targets, in the following analysis it is not included in the AGB sample (thus counting five stars), and it is discussed separately at the end of Section 7.2.1.

7.2.1 Iron and titanium

By using spectroscopic gravities (thus imposing that the same iron abundance is obtained from neutral and from single-ionized lines), the average values measured for the RGB and the AGB sub-samples are $[\mathrm{Fe/H}]_{\mathrm{RGB}} = -1.10 \pm 0.01$ ($\sigma = 0.04$ dex) and $[\mathrm{Fe/H}]_{\mathrm{AGB}} = -1.18 \pm 0.01$ ($\sigma = 0.03$ dex). These values are consistent (within 1-2 σ) with previous abundance determinations of M62 giants, regardless they are on the RGB or on the AGB: [Fe/H]$= -1.12$ dex (Kraft & Ivans, 2003)[6], [Fe/H] = -1.18 ± 0.07 dex (Carretta et al., 2009b), and [Fe/H] = -1.15 ± 0.02 dex ($\sigma = 0.05$ dex, Yong et al., 2014).

By using photometric gravities (and not imposing ionization balance), we determined the iron abundances separately from neutral and from single-ionized lines. For the 13 RGB stars we obtained $[\mathrm{FeI/H}]_{\mathrm{RGB}} = -1.07 \pm 0.01$ dex ($\sigma = 0.04$ dex) and $[\mathrm{FeII/H}]_{\mathrm{RGB}} = -1.04 \pm 0.02$ dex ($\sigma = 0.06$ dex). For the 5 AGB stars we measured $[\mathrm{FeI/H}]_{\mathrm{AGB}} = -1.19 \pm 0.01$ dex ($\sigma = 0.04$ dex) and $[\mathrm{FeII/H}]_{\mathrm{AGB}} = -1.06 \pm 0.02$ dex ($\sigma = 0.06$ dex). The

[6]We refer to the average value computed with Kurucz models without overshooting; see Kraft & Ivans (2003) for details.

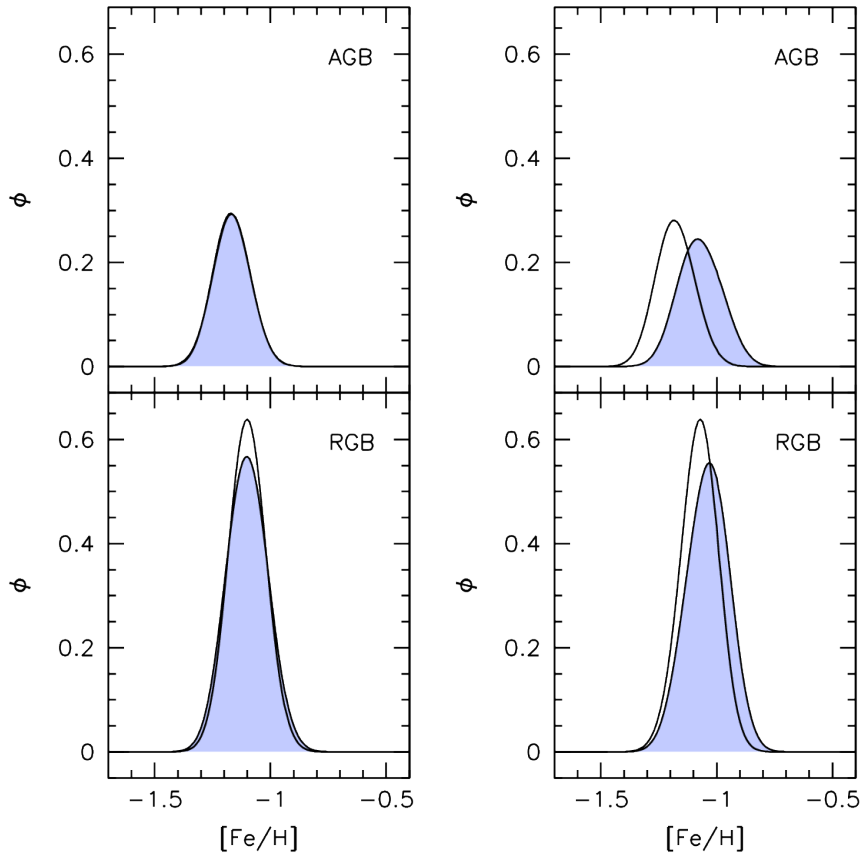

Figure 7.2 *Left panels:* generalized histograms for [FeI/H] (empty histograms) and [FeII/H] (blue shaded histograms) obtained by adopting spectroscopic gravities, for AGB stars (top panel) and the RGB sample (bottom panel). *Right panels:* as in the left panels, but for the iron abundances obtained by adopting photometric gravities.

average difference between the values of $\log g$ derived spectroscopically and those derived photometrically are 0.09 dex ($\sigma = 0.10$ dex) and 0.30 dex ($\sigma = 0.20$ dex) for the RGB and the AGB samples, respectively. Figure 7.2 shows the generalized histograms of the iron abundances for the RGB and the AGB samples separately, obtained by using spectroscopic (left panels) and photometric gravities (right panels). By construction, the distributions of [FeI/H] and [FeII/H] essentially coincide if spectroscopic gravities are assumed. Instead, the two distributions significantly differ in the case of AGB stars if photometric gravities are adopted. In particular, the average iron abundances of RGB stars measured from neutral and single-ionized lines are consistent within the uncertainties, while a difference of -0.13 dex, exceeding 5σ, is found for the AGB sample. Moreover, RGB and AGB stars show very similar (well within 1σ) average values of [FeII/H], while the neutral abundances of AGB

stars are significantly lower (by 0.12 dex) than those of the RGB targets.

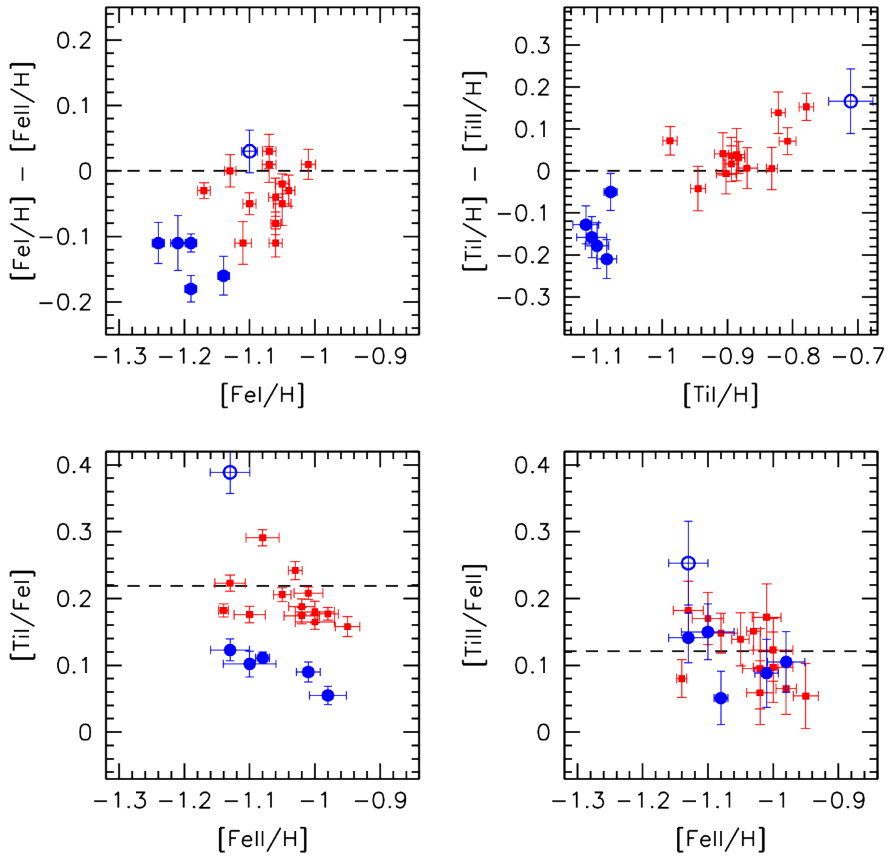

Figure 7.3 *Top panels:* difference between the chemical abundances derived from neutral and single ionized lines, as a function of that obtained from neutral lines, for iron (left panel) and titanium (right panel). Symbols are as in Figure A.3. *Bottom panels:* [TiI/FeI] and [TiII/FeII] abundance ratios as a function of [FeII/H] for the studied samples.

When using photometric gravities similar results are obtained for titanium, the only other chemical species presenting a large number of neutral and single-ionized lines. For the RGB sample we find $[\mathrm{TiI/H}]_{\mathrm{RGB}} = -0.88 \pm 0.01$ dex ($\sigma = 0.06$ dex) and $[\mathrm{TiII/H}]_{\mathrm{RGB}} = -0.92 \pm 0.01$ dex ($\sigma = 0.05$ dex). For the AGB stars we measure $[\mathrm{TiI/H}]_{\mathrm{AGB}} = -1.10 \pm 0.01$ dex ($\sigma = 0.02$ dex) and $[\mathrm{TiII/H}]_{\mathrm{AGB}} = -0.95 \pm 0.02$ dex ($\sigma = 0.06$ dex). In this case, the average abundance of AGB stars from neutral lines is lower than that of the RGB sample by 0.21 dex (while such a difference amounts to only 0.04 dex for the RGB sample). In Figure 7.3 we report the differences between the iron (top left panel) and the titanium (top right panel) abundances derived from neutral and from single-ionized lines, as a function of the abundances from the neutral species, obtained for each observed star

assuming photometric gravities. Clearly, with the only exception of star 96 (plotted as an empty circle in the figure), the AGB and the RGB samples occupy distinct regions in these planes, because of systematically lower values of the AGB abundances derived from the neutral species.

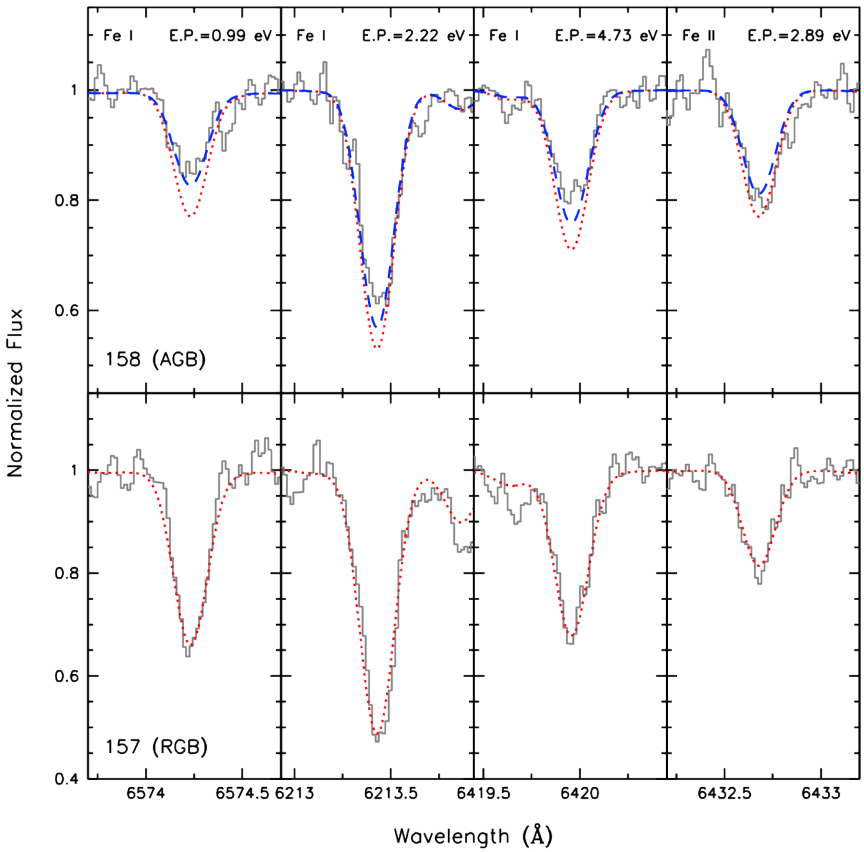

Figure 7.4 Comparison between observed and synthetic spectra for AGB star 158 (upper panels) and RGB star 15 (lower panels), around three FeI lines with different excitation potentials and one FeII line (see labels). The observed spectra are marked with gray lines. The synthetic spectra have been computed by using the measured [FeI/H] (blue dashed line) and [FeII/H] (red dotted lines) abundances. Since the two abundances are practically identical for the RGB star, only one synthetic spectrum is shown in the lower panels.

Such a difference can be also directly appreciated by visually inspecting the line strengths in the observed spectra and their synthetic best-fits. As an example, in Figure A.1 we show the observed spectra of an RGB and an AGB star around some FeI and FeII lines, together with synthetic spectra calculated with the appropriate atmospheric parameters and the metallicity derived from FeII and from FeI lines. As apparent, the synthetic spectrum

computed adopting the FeII abundance well reproduces all the observed lines in the case of the RGB star, while it fails to fit the neutral features observed in the AGB target, independently of the excitation potential (thus guaranteeing that the effect cannot be due to inadequacies in the adopted temperature). On the other hand, the abundance measured from FeI lines is too low to properly reproduce the depth of the ionized features of the AGB star. This clearly demonstrates a different behaviour of iron lines in AGB and RGB stars.

To investigate the origin of the discrepancy between FeI and FeII abundances obtained for the AGB sample, we checked the impact of the adopted stellar mass on the estimate of the photometric gravity. As described in Section 7.1.2, for the AGB stars we assumed a mass of 0.61 $M_{\odot}$, corresponding to the median value of the distribution obtained for HB stars by Gratton et al. (2010b), ranging from 0.51 to 0.67 $M_{\odot}$. By adopting the lowest mass (0.51 $M_{\odot}$), the average value of $\log g$ decreases by ~ 0.08 dex, while assuming the largest value, $\log g$ increases by 0.04 dex. Such small gravity variations[7] have a negligible impact on the abundances derived from the neutral iron lines, and the impact is still modest (at a level of a few hundredths of a dex) on the abundances derived from single-ionized lines. The only way to obtain (by construction) the same abundance from FeI and FeII lines is to use the spectroscopic values of $\log g$ derived from the ionization balance (Section 7.1.2). However, these gravities correspond to stellar masses in the range 0.25-0.3 $M_{\odot}$, which are totally unphysical for evolved stars in GCs.

A possible explanation of the observed discrepancy could be a departure from LTE condition in the atmosphere of AGB stars. In fact, lines originated by atoms in the minority ionization state usually suffer from NLTE effects, while those originated by atoms in the dominant ionization state are unaffected (see, e.g., Mashonkina et al. 2011). Thus, if this is the case, the most reliable determination of the iron abundance is that provided by [FeII/H], since the majority of iron atoms is in the first ionized state in giant stars. Moreover, following Ivans et al. (2001), the degree of overionization of the neutral species should be (at least at a first order) the same as the one affecting FeI lines. Hence, the correct way to obtain a [X/Fe] abundance ratio is to compute it with respect to the FeI abundance if [X/H] is derived from minority species, and with respect to FeII if [X/H] is obtained from majority species. In the lower panels of Figure 7.3 we present the [TiII/FeII] and the [TiI/FeI] abundance ratios as a function of the iron abundance derived from single-ionized lines.

[7]Note that the increase of $\log g$ is essentially the same (0.05 dex) even if the mass provided by the best-fit isochrone (0.72 $M_{\odot}$) is adopted.

As expected, the abundances of AGB stars agree with those of the RGB sample when single ionized (dominant state) titanium lines are used. For [TiI/FeI] a systematic offset of the AGB sample toward lower values is still observable (although reduced), thus indicating the possible presence of residual NLTE effects. We also note a systematic offset of +0.08 dex between [TiI/FeI] and [TiII/FeII], especially for RGB stars. However, taking into account that the oscillator strength values of the TiII lines are highly uncertain and that the offset is still reasonably small, we can conclude that the [X/Fe] abundance ratio can be safely constrained either by neutral or by single-ionized lines. It is also interesting to note that the average [TiI/Fe] and [TiII/Fe] abundance ratios (+0.16 dex and +0.25 dex, respectively) of Yong et al. (2014) show a relative offset of -0.09 dex, which is similar to ours but in the opposite direction. This suggests that there is an intrinsic (although small) uncertainty in the zero point scale of the titanium abundance.

AGB star 96 – As apparent from Figure 7.3, AGB star 96 shows a difference between neutral and ionized abundances, both for iron and titanium, which is incompatible with those found for the other AGB targets, and which is much more similar to the values measured for RGB stars. Interestingly, star 96 presents atmospheric parameters compatible with those spanned by the RGB targets (but with a surface gravity which is 0.15-0.2 lower than that of RGB stars at the same temperature). This case is similar to that encountered in 47Tuc, where the FeI abundance of a small sub-sample of AGB stars (4 out of 24) has been found to agree with the value obtained from ionized lines, thus suggesting that one of the possible explanations could be the lack of LTE departures for these objects (Lapenna et al., 2014). Also in M22, one (out of five) AGB star shows a perfect agreement between [FeI/H] and [FeII/H], while the other AGB stars show systematically low [FeI/H] values (Mucciarelli et al., 2015b).

7.2.2 Oxygen, sodium, magnesium and aluminum

In most Galactic GCs, the abundances of oxygen, sodium, magnesium and aluminium are known to show large star-to-star variations, organized in clear correlations (see Gratton et al. 2012 for a review). These are usually interpreted as the signature of self-enrichment processes occurring in the early stages of GC evolution and giving rise to at least two stellar generations with a very small (if any) age difference, commonly labelled as first and second generations (FG and SG, respectively). In particular, the variations observed in O, Na, Mg and Al are thought to be due to the ejecta from still unclear polluters, like massive AGB

stars, fast-rotating massive stars and/or massive binaries (Fenner et al., 2004; Ventura & D'Antona, 2005; Decressin et al., 2007; de Mink et al., 2009; Marcolini et al., 2009; Bastian et al., 2013, 2015).

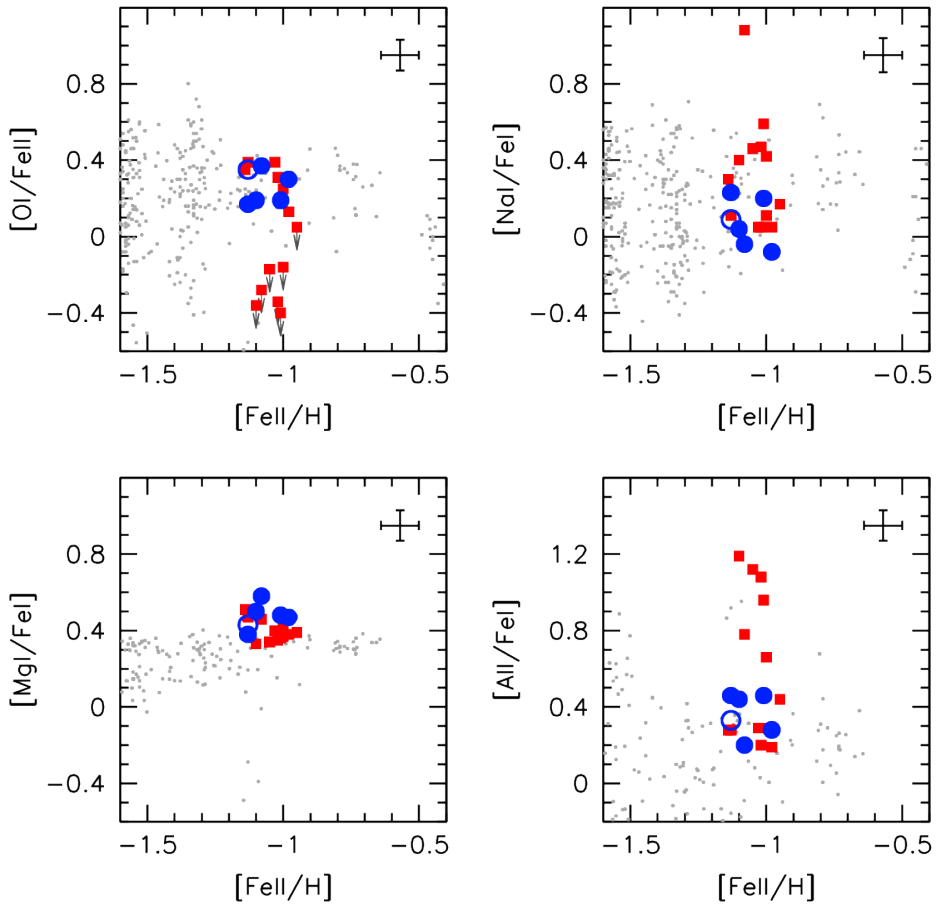

Figure 7.5 From top-left to bottom-right, oxygen, sodium, magnesium and aluminum abundance ratios as a function of [FeII/H] for the studied sample of stars (same symbols as in Figure A.3). For a sub-sample of (O-poor) RGB stars, only upper limits to the oxygen abundance could be measured from the acquired spectra (see arrows). Representative error bars are marked in the top-right corner of each panel. The values measured in large samples of giant stars in 20 Galactic GCs (from GIRAFFE and UVES spectra by Carretta et al., 2009a,c, 2014), rescaled to the solar values adopted in this work, are shown for reference as grey dots.

To verify the presence of these key features also in our sample of giants, we derived the abundances of O, Na, Al, and Mg from the observed spectra. The results are shown in Figure 7.5, where all abundance ratios are plotted as a function of the iron content as measured from the ionized lines. Since the oxygen abundance derived from the forbidden

[OI] line at 6300.3 Å is not affected by NLTE, its abundance ratio is expressed with respect to the "true" iron content (measured from FeII lines). Instead, the other species are known to suffer from NLTE effects and their abundances are therefore plotted with respect to FeI (see Section 7.2.1). This is true also for sodium, although we have applied the NLTE corrections of Gratton et al. (1999), which take into account departures from LTE conditions driven by over-recombination (Bergemann & Nordlander, 2014)[8]. In any case, we have verified that the same results are obtained if the Na, Al and Mg abundances are computed with respect to FeII or H. In agreement with what commonly observed in Galactic GCs, we find that the Mg abundance is constant within the uncertainties, while O, Na, and Al show significant (several tenths of a dex) star-to-star variations in the RGB sample (see also Yong et al., 2014). As shown in Figures 7.6 and 7.7, the observed star-to-star variations are organized in the same correlations observed for GCs. In particular, oxygen and sodium are anti-correlated, independently of using FeI or FeII for the computation of the sodium abundance ratio (Figure 7.6), while aluminum and sodium are positively correlated and [AlI/FeI] shows a $\sim$ 1 dex spread for fixed magnesium (Figure 7.7). Very interestingly, instead, all abundance ratios are constant for the AGB sample, with values mainly consistent with those commonly associated to the FG.

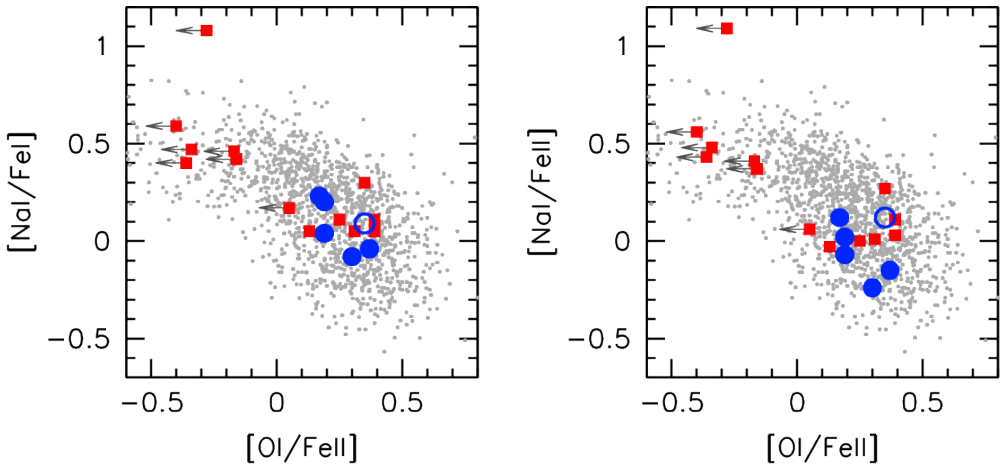

Figure 7.6 Oxygen-sodium anti-correlation measured for the observed stars (same symbols as in Figure 7.5). The corrections for NLTE effects provided by Gratton et al. (1999) have been applied to the Na abundances. This is then expressed with respect to FeI and to FeII in the left and right panels, respectively. Grey dots are as in Figure 7.5.

[8]By adopting the NLTE corrections of Lind et al. (2011), the differential behaviour between AGB and RGB stars remains the same.

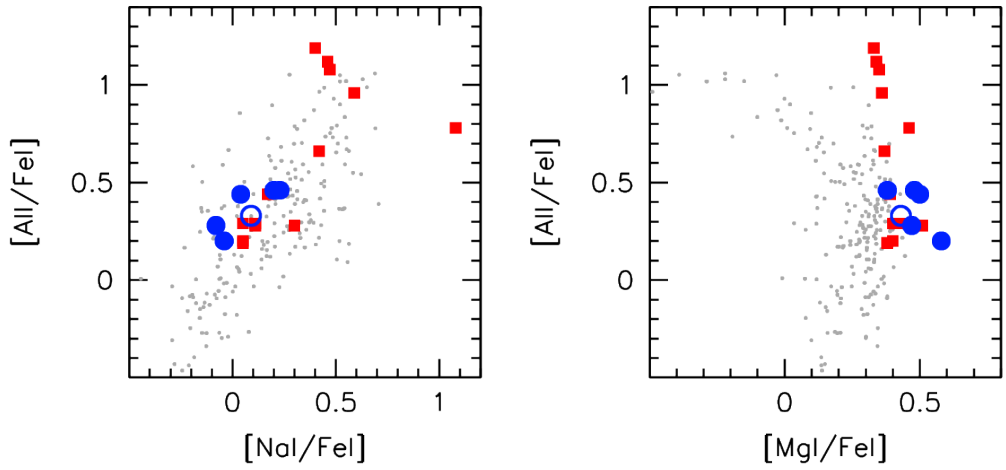

Figure 7.7 Aluminum-sodium correlation (left panel) and aluminum-magnesium anti-correlations (right panel) for the observed stars (same symbols as in Figure 7.5). Grey dots as in Figure 7.5.

The Na-O anti-correlation derived from our RGB sample is qualitatively compatible with that measured by Yong et al. (2014), who found two groups of stars well-separated both in [Na/Fe] and [O/Fe]. We note that the oxygen abundances quoted by Yong et al. (2014) are larger than ours, with an average offset of +0.5 dex for the O-rich stars. The origin of this discrepancy can be ascribable to different factors (like atomic data, telluric correction, etc.), but it is beyond the aims of this paper. A good agreement with the results of Yong et al. (2014) is found also for the [Al/Fe] and [Mg/Fe] distributions.

The derived Na-O anti-correlation of M62 is more extended than those observed in most Galactic GCs. Two discrete groups of stars can be recognized, a first one with [O/Fe]$\sim$+0.2/+0.3 dex and [Na/Fe]$\sim$+0.1 dex, and a second group with [O/Fe]$<$0.0 dex (only upper limits) and [Na/Fe] at $\sim$+0.5 dex. In particular, the sub-solar O-poor component (the so-called "extreme population"; see Carretta et al., 2010c) is quite prominent in M62, while these stars are usually rare, observed only in some massive systems, as NGC2808 (Carretta et al., 2009c), M54 (Carretta et al., 2010b), and ω Centauri (Johnson & Pilachowski, 2010). We also find a significant lack of "intermediate population" stars (with enhanced Na abundances and mild oxygen depletion Carretta et al., 2010c), which are instead the dominant component in most GCs.

We finally note that the RGB star 89 exhibits a Na abundance [Na/Fe]=+1.08 dex, which is $\sim$0.5 dex larger than that measured for all the other O-poor stars. In Figure 7.8 we

compare the spectrum of star 89 with that of another RGB target (id=95) having very similar atmospheric parameters and iron abundances (see Table 7.3). As apparent, all lines have the same strengths, with the notable exception of the two Na doublets, which are significantly stronger in star 89.

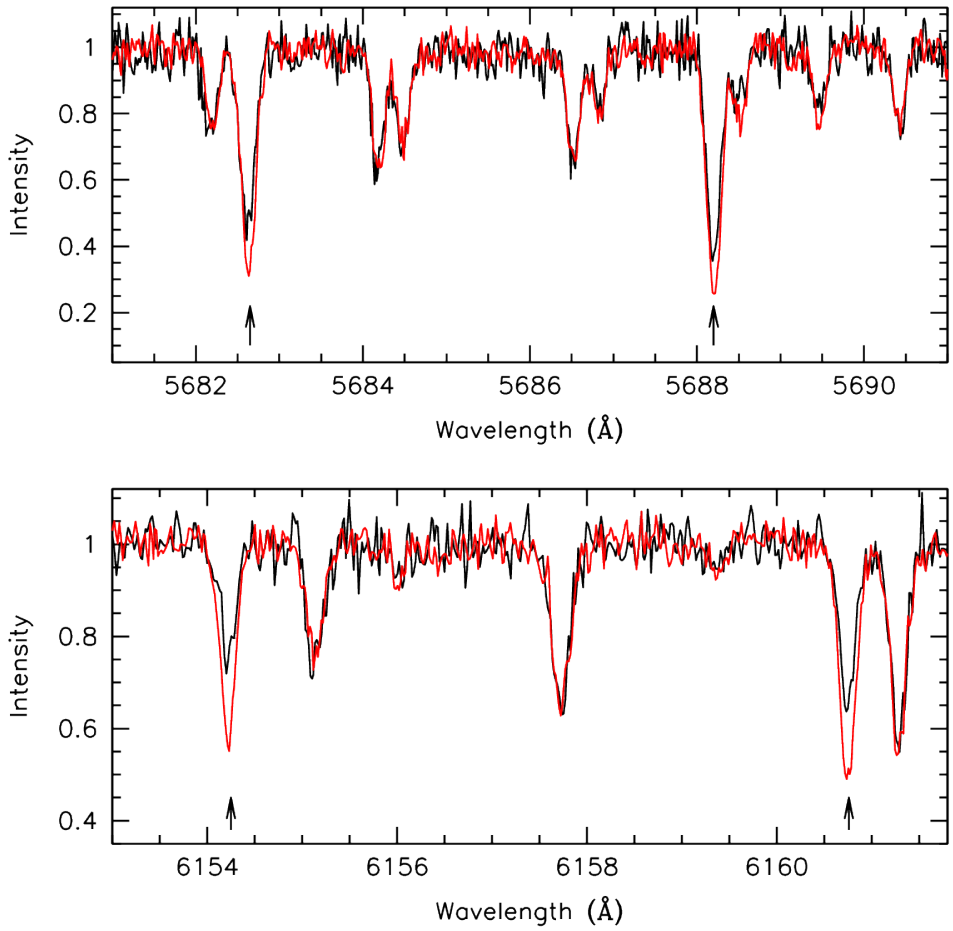

Figure 7.8 Comparison between the spectra of the RGB stars 89 (red line) and 95 (black line) for the NaI lines at 5682-5688 Å (top-panel) and 6154-6160 Å (bottom-panel). The black arrows mark the position of the Na lines.

To our knowledge, this is one of the most Na-rich giant ever detected in a genuine GC (see also the comparison with literature data in Figure 7.6), with a [Na/Fe] abundance even higher than the most Na-rich stars observed in NGC2808 (Carretta et al., 2006) and NGC4833 (Carretta et al., 2014), and comparable to a few extremely Na-rich objects observed in the multi-iron system ω Centauri (Marino et al., 2011a).

7.3 Discussion and conclusions

The differences in the iron and titanium abundances measured from neutral and from single-ionized lines in five AGB stars of M62 closely resemble those found in M5 (Ivans et al., 2001), 47Tuc (Lapenna et al., 2014) and NGC 3201 (Mucciarelli et al., 2015a). These results might be explained as the consequences of departures from LTE conditions, affecting the neutral species, while leaving unaltered the ionized lines. The final effect is a systematic underestimate of the chemical abundances if measured from neutral features. Interestingly, the findings in M5, 47Tuc and NGC 3201 seem to suggest that this effect concerns most, but not all, AGB stars, while it is essentially negligible for RGB targets. This is inconsistent with the available NLTE calculations (e.g. Lind, Bergemann & Asplund, 2012; Bergemann et al., 2012), which predict the same corrections for stars with similar parameters. Moreover, the results recently obtained in M22 show that the situation is even more complex. In M22, in fact, neutral iron abundances systematically lower than [FeII/H] have been measured also for RGB stars (Mucciarelli et al., 2015b). However, the [FeI/H]-[FeII/H] difference in M22 clearly correlates with the abundance of s-process elements (that show intrinsic star-to-star variations unusual for GCs), suggesting that this could be a distinct, peculiar case. All these results seem to suggest that we are still missing some crucial detail about the behaviour of chemical abundances in the case of departures from LTE conditions, and/or that other ingredients (as full 3D, spherical hydro calculations, and the inclusion of chromospheric components) should be properly taken into account in modeling the atmospheres of these stars.

For all the studied stars we have also determined the abundances of O, Na, Al and Mg from the neutral lines available. As shown in Figures 7.6 and 7.7, our sample of RGB stars shows the typical behaviors observed in all massive GCs, with large and mutually correlated dispersions of O, Na and Al (and with one of the most Na-rich giant ever observed in a GC: RGB star 89, with [Na/Fe]=$+1.08$ dex). Instead, the light-element abundances of AGB stars are essentially constant and clumped at the low-end of the Na and Al values of the RGB sample.

If the (still unclear) NLTE effects impacting the FeI and TiI abundances of the AGB targets significantly weaken the minority species lines (as it seems reasonable to assume), also the measured abundances of sodium, aluminum and magnesium could be underestimated for these objects (even when referred to the neutral iron abundance, FeI). Thus, although

the observed star-to-star variation of Na in most GCs is often a factor of 5-10 larger than the suspected NLTE effects on Fe and Ti, we caution that it could be risky to derive firm conclusions about a lack of Na-rich AGB stars on the basis of the sodium abundance alone until these effects are properly understood and quantified (of course, the same holds for any other light-element potentially affected by NLTE effects, especially if the star-to-star variations of this element are intrinsically small). In fact, a lack of Na-rich AGB stars could be either real, or just due to a bias induced by NLTE effects. A solid evidence, instead, is obtained if the result is based on elemental species (like the oxygen abundance derived from the forbidden line considered here) that are virtually unaffected by NLTE effects. Hence, Figure 7.6, showing that the oxygen abundances of all AGB stars are larger than those expected for the SG population and measured, in fact, for a sub-sample of RGB giants, convincingly indicates that none of the AGB targets studied in M62 is compatible with the SG of the cluster.

Does this mean that the SG stars in M62 did not experience the AGB phase (as it has been suggested for NGC6752 by Campbell et al., 2013)? To answer this question we note that, although variable from cluster to cluster, the typical percentages of FG and SG stars in Galactic GCs are 30% and 70%, respectively (e.g. Carretta, 2013b; Bastian & Lardo, 2015). On this basis, we should have observed 4 second generation AGB stars in our sample. In alternative, from Figures 7.6 and 7.7 we see that 6 out of 13 (46%) RGB stars likely belong to the SG and, we could have therefore expected 2-3 AGB stars in the same group, at odds with what observed. On the other hand, a deficiency of CN-strong (second generation) AGB stars in several GCs is known since the pioneering work of Norris (1981) and it has been recently found to be most severe in GCs with the bluest HB morphology (see, e.g., Gratton et al., 2010b, and references therein). While M62 has indeed a very extended HB, it shows no deficiency of AGB stars. In fact, by using ACS and WFC3 HST archive data acquired in the $m_{\rm F390W}$ and $m_{\rm F658N}$ filters, we counted the number of AGB and HB stars (86 and 640, respectively) in M62, finding that their ratio (the so-called R_2 parameter; Caputo et al., 1989) is $R_2 \simeq 0.13$. This value is in very good agreement with the theoretical predictions based on the ratio between the AGB and the HB evolutionary timescales (e.g. Cassisi et al., 2001). Hence, our observations show that all the sampled AGB stars belong to the FG, but we cannot exclude that some SG object is present along the AGB of M62.

Clearly, if a complete lack of SG AGB stars is confirmed by future studies in M62, NGC 6752, M13 (see e.g. Sneden et al., 2000b; Johnson & Pilachowski, 2012) or any other GC,

this will represent a new challenge for the formation and evolution models of these stellar systems (as already discussed, e.g., by Charbonnel et al., 2013 and Cassisi et al., 2014).

Table 7.1. Photometric properties and radial velocities of the RGB and AGB sample

ID	R.A. (J2000)	Decl. (J2000)	U (mag)	V (mag)	U_0 (mag)	V_0 (mag)	RV (km s^{-1})	Type
50	255.2961736	–30.1122536	17.458	14.061	14.558	12.184	–95.41 ± 0.06	R
54	255.2968276	–30.1110148	17.465	14.149	14.462	12.206	–68.41 ± 0.04	R
76	255.3016326	–30.0879873	17.578	14.416	14.734	12.576	–69.34 ± 0.06	R
82	255.2908040	–30.1230200	17.378	14.478	14.649	12.712	–56.67 ± 0.04	R
89	255.3053120	–30.1235390	17.694	14.584	14.759	12.685	–68.78 ± 0.04	R
95	255.2683150	–30.1061800	17.689	14.624	14.821	12.768	–85.92 ± 0.06	R
97	255.2746210	–30.1078150	17.551	14.632	14.703	12.789	–92.22 ± 0.06	R
104	255.2990264	–30.1195799	17.502	14.680	14.861	12.971	–81.19 ± 0.04	R
118	255.2953240	–30.1054710	17.584	14.771	14.883	13.023	–90.41 ± 0.06	R
127	255.3064600	–30.0967810	17.775	14.895	15.020	13.112	–55.24 ± 0.06	R
133	255.3025803	–30.1265560	17.819	14.939	14.903	13.052	–90.70 ± 0.05	R
145	255.2959190	–30.1263240	17.831	15.041	15.031	13.229	–63.56 ± 0.05	R
157	255.2998135	–30.0934941	17.720	15.174	14.988	13.406	–74.04 ± 0.05	R
79	255.3060883	–30.1031433	17.335	14.430	14.443	12.558	–109.85 ± 0.06	A
96	255.2885360	–30.1173880	17.345	14.629	14.558	12.826	–81.49 ± 0.07	A
116	255.2778880	–30.1205350	17.130	14.764	14.348	12.963	–87.57 ± 0.09	A
128	255.2980470	–30.1078870	17.248	14.895	14.501	13.117	–72.72 ± 0.08	A
135	255.2914560	–30.1287900	17.416	14.952	14.613	13.138	–60.08 ± 0.07	A
158	255.3017290	–30.1013070	17.361	15.180	14.647	13.424	–53.49 ± 0.07	A

Note. — Identification number, coordinates, U, V, U_0 and V_0 magnitudes, heliocentric radial velocity, and type of star (R=RGB, A=AGB).

Table 7.2. Wavelength, element, oscillator strength, excitation potential, and reference source of adopted lines.

Wavelength (Å)	El.	log gf	E.P. (eV)	Ref.
4962.572	FeI	–1.182	4.178	Fuhr & Wiese (2006)
4967.897	FeI	–0.534	4.191	K
4969.917	FeI	–0.710	4.217	Fuhr, Martin & Wiese (1988)
4982.499	FeI	0.164	4.103	K
4983.250	FeI	–0.111	4.154	K
4985.547	FeI	–1.331	2.865	Fuhr & Wiese (2006)
4950.106	FeI	–1.670	3.417	Fuhr, Martin & Wiese (1988)
4962.572	FeI	–1.182	4.178	Fuhr & Wiese (2006)
4967.897	FeI	–0.534	4.191	K
4969.917	FeI	–0.710	4.217	Fuhr, Martin & Wiese (1988)

Note. — K = Oscillator strengths (OS) from the R.L.Kurucz on-line database of observed and predicted atomic transitions (see http://kurucz.harvard.edu), NIST = OS from NIST database (see http://www.nist.gov/pml/data/asd.cfm) S = OS from solar analysis by F. Castelli (see http://wwwuser.oats.inaf.it/castelli/linelists.html). For AlI lines we derived astrophysical oscillator strengths (labeled as S*) by using the solar flux spectra of Neckel & Labs (1984) and the model atmosphere for the Sun computed by F. Castelli[9] adopting the solar abundances of Grevesse & Sauval (1998). The entire Table is available in the on-line version, a portion is shown here for guidance about its form and content.

Table 7.3. Atmospheric parameters, iron and titanium abundances of the measured RGB and AGB stars.

ID	$T_{\rm eff}$ (K)	log g (dex)	$v_{\rm turb}$ (km s^{-1})	[FeI/H] (dex)	$n_{\rm FeI}$	[FeII/H] (dex)	$n_{\rm FeII}$	[TiI/H] (dex)	$n_{\rm TiI}$	[TiII/H] (dex)	$n_{\rm TiII}$
50	4225	0.85	1.30	–1.13 ± 0.01	128	–1.13 ± 0.02	12	–0.91 ± 0.01	58	–0.95 ± 0.05	12
54	4215	0.85	1.40	–1.17 ± 0.01	130	–1.14 ± 0.01	7	–0.99 ± 0.01	63	–1.06 ± 0.03	14
76	4375	1.15	1.35	–1.05 ± 0.01	106	–1.00 ± 0.03	7	–0.87 ± 0.02	37	–0.88 ± 0.05	6
82	4295	1.15	1.30	–1.06 ± 0.01	104	–1.02 ± 0.03	11	–0.89 ± 0.01	45	–0.92 ± 0.06	7
89	4355	1.15	1.50	–1.07 ± 0.01	127	–1.08 ± 0.03	10	–0.78 ± 0.01	62	–0.93 ± 0.03	14
95	4365	1.20	1.45	–1.07 ± 0.01	134	–1.10 ± 0.02	11	–0.89 ± 0.01	58	–0.93 ± 0.04	15
97	4425	1.25	1.40	–1.01 ± 0.01	142	–1.02 ± 0.02	12	–0.82 ± 0.01	50	–0.96 ± 0.05	14
104	4325	1.20	1.30	–1.11 ± 0.01	108	–1.00 ± 0.03	7	–0.94 ± 0.01	40	–0.90 ± 0.05	7
118	4450	1.35	1.40	–1.05 ± 0.01	140	–1.03 ± 0.01	8	–0.81 ± 0.01	56	–0.88 ± 0.03	13
127	4425	1.35	1.35	–1.06 ± 0.01	102	–0.95 ± 0.02	10	–0.90 ± 0.02	57	–0.90 ± 0.05	15
133	4450	1.35	1.40	–1.10 ± 0.01	142	–1.05 ± 0.01	9	–0.89 ± 0.01	57	–0.91 ± 0.04	15
145	4475	1.45	1.30	–1.06 ± 0.01	146	–0.98 ± 0.02	10	–0.88 ± 0.01	47	–0.92 ± 0.04	13
157	4545	1.55	1.45	–1.04 ± 0.01	136	–1.01 ± 0.02	10	–0.83 ± 0.01	52	–0.84 ± 0.05	13
79	4415	1.00	1.55	–1.19 ± 0.01	131	–1.08 ± 0.01	8	–1.08 ± 0.01	48	–1.03 ± 0.04	15
96	4450	1.15	1.50	–1.10 ± 0.01	130	–1.13 ± 0.03	11	–0.71 ± 0.03	33	–0.88 ± 0.07	9
116	4760	1.35	1.80	–1.24 ± 0.01	134	–1.13 ± 0.03	9	–1.12 ± 0.02	27	–0.99 ± 0.04	13
128	4760	1.45	1.60	–1.21 ± 0.01	138	–1.10 ± 0.04	12	–1.11 ± 0.02	33	–0.95 ± 0.04	14
135	4635	1.40	1.55	–1.14 ± 0.01	128	–0.98 ± 0.03	10	–1.08 ± 0.02	33	–0.88 ± 0.04	13
158	4840	1.60	1.65	–1.19 ± 0.01	142	–1.01 ± 0.02	11	–1.10 ± 0.02	27	–0.92 ± 0.05	14

Note. — Identification number, spectroscopic temperature and photometric gravities, microturbulent velocities, iron and titanium abundances with internal uncertainty and number of used lines, as measured from neutral and single-ionized lines. For all the stars a global metallicity of [M/H]= -1.0 dex has been assumed for the model atmosphere. The adopted solar values are from Grevesse & Sauval (1998).

Table 7.4. OI, NaI, MgI, AlI, TiI and TiII abundances of the RGB and AGB sample

ID	[OI/FeII] (dex)	$[NaI/FeI]_{LTE}$ (dex)	$[NaI/FeI]_{NLTE}$ (dex)	n_{Na}	[MgI/FeI] (dex)	n_{Mg}	[AlI/FeI] (dex)	n_{Al}	[TiI/FeI] (dex)	n_{TiI}	[TiII/FeII] (dex)	n_{TiII}
50	0.39 ± 0.05	-0.01 ± 0.12	0.11 ± 0.09	4	0.47 ± 0.03	3	0.28 ± 0.01	2	0.22 ± 0.02	58	0.18 ± 0.05	12
54	0.35 ± 0.04	0.17 ± 0.10	0.30 ± 0.06	4	0.51 ± 0.02	3	0.28 ± 0.00	2	0.18 ± 0.01	63	0.08 ± 0.03	14
76	< -0.16	0.34 ± 0.11	0.42 ± 0.07	4	0.37 ± 0.02	3	0.66 ± 0.02	2	0.18 ± 0.02	37	0.12 ± 0.05	6
82	0.31 ± 0.07	-0.05 ± 0.08	0.05 ± 0.04	4	0.40 ± 0.03	3	0.20 ± 0.02	2	0.17 ± 0.02	45	0.09 ± 0.07	7
89	< -0.28	1.04 ± 0.06	1.08 ± 0.02	4	0.46 ± 0.02	3	0.78 ± 0.04	2	0.29 ± 0.02	62	0.15 ± 0.04	14
95	< -0.36	0.31 ± 0.17	0.40 ± 0.16	4	0.33 ± 0.05	3	1.19 ± 0.06	2	0.18 ± 0.02	58	0.17 ± 0.05	15
97	< -0.34	0.41 ± 0.14	0.47 ± 0.09	4	0.35 ± 0.06	2	1.08 ± 0.04	2	0.19 ± 0.02	50	0.06 ± 0.05	14
104	0.25 ± 0.08	0.01 ± 0.11	0.11 ± 0.07	4	0.43 ± 0.06	3	0.29 ± 0.05	1	0.17 ± 0.02	40	0.10 ± 0.06	7
118	0.39 ± 0.05	-0.03 ± 0.10	0.05 ± 0.07	4	0.40 ± 0.06	2	0.29 ± 0.03	2	0.24 ± 0.02	56	0.15 ± 0.03	13
127	0.05 ± 0.09	0.08 ± 0.11	0.17 ± 0.07	4	0.39 ± 0.02	3	0.44 ± 0.04	1	0.16 ± 0.02	57	0.05 ± 0.05	15
133	< -0.17	0.40 ± 0.10	0.46 ± 0.06	4	0.34 ± 0.05	2	1.12 ± 0.06	2	0.21 ± 0.01	57	0.14 ± 0.04	15
145	0.13 ± 0.07	-0.03 ± 0.08	0.05 ± 0.06	4	0.38 ± 0.01	3	0.19 ± 0.04	2	0.18 ± 0.01	47	0.07 ± 0.04	13
157	< -0.40	0.55 ± 0.10	0.59 ± 0.06	4	0.36 ± 0.02	3	0.96 ± 0.03	2	0.21 ± 0.01	52	0.17 ± 0.05	13
79	0.37 ± 0.05	-0.20 ± 0.06	-0.04 ± 0.04	4	0.58 ± 0.08	2	0.20 ± 0.07	1	0.11 ± 0.01	48	0.05 ± 0.04	15
96	0.35 ± 0.06	-0.03 ± 0.08	0.09 ± 0.04	4	0.43 ± 0.05	3	0.33 ± 0.06	1	0.39 ± 0.04	33	0.25 ± 0.08	9
116	0.17 ± 0.07	0.13 ± 0.06	0.23 ± 0.03	4	0.38 ± 0.04	2	0.46 ± 0.05	1	0.12 ± 0.02	27	0.14 ± 0.05	13
128	0.19 ± 0.06	-0.06 ± 0.10	0.04 ± 0.09	4	0.50 ± 0.09	3	0.44 ± 0.07	1	0.10 ± 0.03	33	0.15 ± 0.06	14
135	0.30 ± 0.07	-0.20 ± 0.04	-0.08 ± 0.03	4	0.47 ± 0.03	3	0.28 ± 0.07	1	0.06 ± 0.02	33	0.11 ± 0.05	13
158	0.19 ± 0.05	0.13 ± 0.06	0.20 ± 0.03	3	0.48 ± 0.08	3	0.46 ± 0.05	1	0.09 ± 0.02	27	0.09 ± 0.05	14

Note. — The oxygen abundance has been derived from the 6300.3Å [OI] line, the abundances of sodium have been reported without and with NLTE corrections computed following Gratton et al. (1999). The reference solar values are taken from Caffau et al. (2011) for the oxygen, from Grevesse & Sauval (1998) for the other species.

Table 7.5. Abundance uncertainties due to the atmospheric parameters for the stars 157 and 158.

Species	Global Uncertainty (dex)	$\delta T_{\rm eff}$ $\pm 50K$ (dex)	$\delta \log g$ ± 0.1 (dex)	$\delta v_{\rm turb}$ $\pm 0.1 kms^{-1}$ (dex)
		157 (RGB)		
FeI	$\pm$0.07	$\pm$0.04	$\pm$0.00	$\mp$0.06
FeII	$\pm$0.08	$\mp$0.05	$\pm$0.05	$\mp$0.04
OI	$\pm$0.04	$\pm$0.01	$\pm$0.03	$\mp$0.02
NaI	$\pm$0.05	$\pm$0.04	$\mp$0.01	$\mp$0.02
MgI	$\pm$0.04	$\pm$0.03	$\pm$0.00	$\mp$0.03
AlI	$\pm$0.04	$\pm$0.04	$\pm$0.00	$\mp$0.02
TiI	$\pm$0.09	$\pm$0.08	$\pm$0.00	$\mp$0.03
TiII	$\pm$0.05	$\mp$0.02	$\pm$0.04	$\mp$0.03
		158 (AGB)		
FeI	$\pm$0.07	$\pm$0.06	$\pm$0.00	$\mp$0.04
FeII	$\pm$0.07	$\mp$0.03	$\pm$0.05	$\mp$0.03
OI	$\pm$0.05	$\pm$0.02	$\pm$0.04	$\mp$0.02
NaI	$\pm$0.04	$\pm$0.04	$\pm$0.00	$\mp$0.01
MgI	$\pm$0.03	$\pm$0.03	$\pm$0.00	$\mp$0.01
AlI	$\pm$0.03	$\pm$0.03	$\pm$0.00	$\mp$0.00
TiI	$\pm$0.08	$\pm$0.08	$\pm$0.00	$\mp$0.01
TiII	$\pm$0.06	$\mp$0.01	$\pm$0.05	$\mp$0.03

Note. — The second column shows the global uncertainty calculated by adding in quadrature the single uncertainties. The other columns list the uncertainties obtained by varying only one parameter at a time, while keeping the others fixed.

Chapter 8

Weighing Stars: the Identification of an Evolved Blue Straggler Star in the Globular Cluster 47Tucanae

Ferraro et al. 2015, accepted by ApJ

Globular clusters are known to host peculiar objects, named Blue Straggler Stars (BSSs), significantly heavier than the normal stellar population. While these stars can be easily identified during their core hydrogen-burning phase, they are photometrically indistinguishable from their low-mass sisters in advanced stages of the subsequent evolution. A clear-cut identification of these objects would require the direct measurement of the stellar mass, which is a very difficult task in Astrophysics. We used the detailed comparison between chemical abundances derived from neutral and from ionized spectral lines as a powerful stellar "weighing device" to measure stellar mass and to identify an evolved BSS in the globular cluster 47 Tucanae. In particular, high-resolution spectra of three bright stars located slightly above the level of the "canonical" horizontal branch sequence in the color-magnitude diagram of 47 Tucanae, in a region where evolved BSSs are expected to lie, have been obtained with UVES-FLAMES at the ESO Very Large Telescope. The measurements of iron and titanium abundances performed separately from neutral and ionized lines reveal that two targets have stellar parameters fully consistent with those expected for low-mass post-horizontal branch objects, while for the other target the elemental ionization balance is obtained only by assuming a mass of $\sim$ 1.4 $M_{\odot}$, which is significantly larger than the main sequence turn-off mass of the cluster ($\sim$ 0.85 $M_{\odot}$). The comparison with theoretical stellar tracks suggests that this blue straggler descendant is possibly experiencing its core helium-burning phase. The large applicability of the proposed method to most of

the globular clusters in our Galaxy opens the possibility to initiate systematic searches for evolved BSSs, thus giving access to still unexplored phases of their evolution and providing deep insights even into their (still unclear) formation scenarios.

8.1 Observations and membership

In the context of the ESO Large Programme 193.D-0232 (PI: Ferraro) aimed at studying the internal kinematics of Galactic globular clusters, we have secured UVES-FLAMES (Pasquini et al., 2000) high-resolution spectra of three stars in 47 Tuc. The targets (hereafter named bHB1, bHB2 and E-BSS1). have been selected in a regionof the CMD slightly brighter than the red clump (see Figure A.3), where evolved BSSs experiencing the core helium burning process are expected to lie (see also Beccari et al., 2006). All the targets lie within a distance of $\sim 132''$ from the cluster center, corresponding to 4.5 r_c or 0.6 $r_{\rm hm}$ ($r_c = 29''$ and $r_{\rm hm} = 213''$ being, respectively, the core and half-mass radii of 47 Tuc; Miocchi et al., 2013). Figure A.3 shows the $(V, V-I)$ CMD obtained from the HST-ACS photometric catalog of Sarajedini et al. (2007), with the target selection box marked. The color and magnitude of bHB2 (which is located beyond the ACS field of view) are from ground-based wide field data (Ferraro et al., 2004b) homogenized to the Johnson-Cousin photometric system. The coordinates, V band magnitude, $V-I$ color, and distance from the center of each target are listed in Table 8.1.

The target spectra have been acquired with the grating 580 Red Arm CD#3, which provides a spectral resolution $R \sim 40000$ between 4800Å and 6800Å. All the spectra have been reduced by using the dedicated ESO pipeline, performing bias subtraction, flat-fielding, wavelength calibration and order merging. During the observations, a number of fibers were allocated on empty regions to sample the sky background, which has then been subtracted from the target spectra. The total exposure time is $\sim$ 30 min for each star, providing a signal-to-noise ratio (S/N) $\geq$ 50 per pixel.

The three stars are all cluster members, as assessed by their radial velocity (see Table 8.1) and the systemic velocity and velocity dispersion of 47 Tuc ($V_r = -17.6$ km s^{-1} and σ = 11.5 km s^{-1}, respectively, from Lapenna et al., 2014; see also Carretta et al., 2004a; Alves-Brito et al., 2005; Ferraro et al., 2006a; Koch & McWilliam, 2008; Lane et al., 2010a; Gratton et al., 2013; Cordero et al., 2014; Thygesen et al., 2014; Johnson et al., 2015). The radial velocities have been determined with the code DAOSPEC (Stetson & Pancino, 2008),

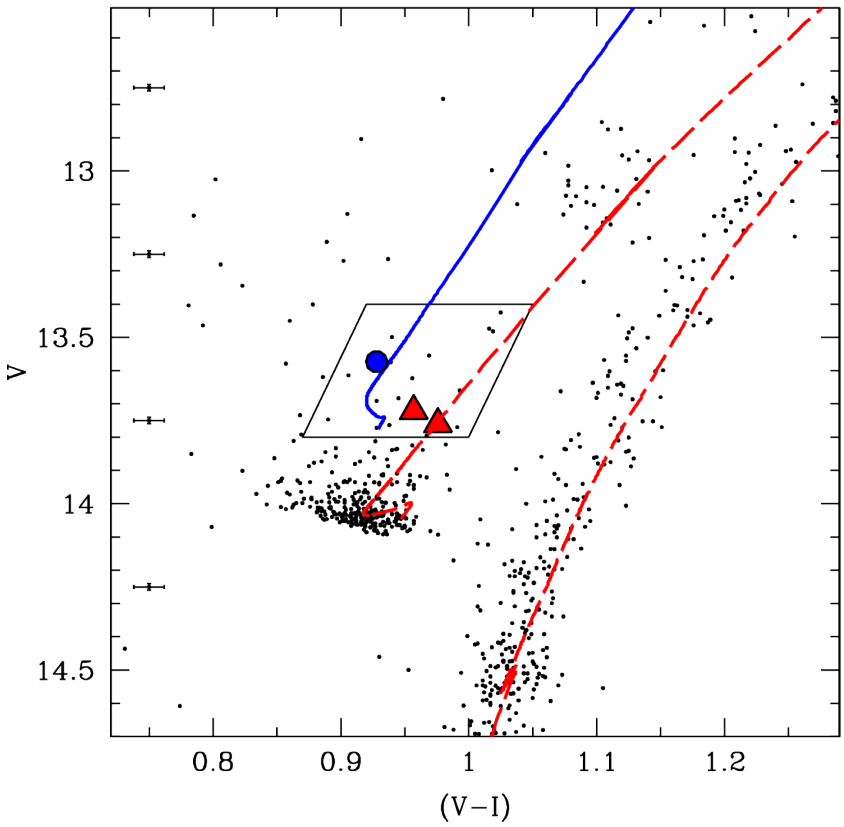

Figure 8.1 Magnified portion of the $(V, V-I)$ CMD of 47 Tuc around the horizontal branch. The large blue circle marks the position of E-BSS1. The position of the two reference targets (bHB1 and bHB2) are marked with red triangles. For reference, only stars within $50''$ from the center are plotted (small black dots). Error bars are marked at different magnitude levels. The red dashed line corresponds to the evolutionary track (Pietrinferni et al., 2006) of a single star of 0.9 $M_{\odot}$ well reproducing the cluster main evolutionary sequences. The evolutionary track, from the HB to the AGB, for a star with a MS mass of 1.5 $M_{\odot}$ is also shown (blue solid line). Because of mass loss during the RGB, the stellar mass at the HB level for this evolutionary track is $\sim$ 1.4 $M_{\odot}$, well in agreement with the spectroscopic estimate for E-BSS1. The marked box delimitates the region where evolved BSSs experiencing the HB stage are expected to lie: the blue and red boundaries of the box are approximately set by the tracks corresponding to MS turn-off masses of 1.8 $M_{\odot}$ and 0.9 $M_{\odot}$, respectively.

by measuring the position of up to 300 metallic lines. The final uncertainty was obtained by dividing the dispersion of the velocities by the square root of the number of lines used.

To further check the possible contamination by field stars, we extracted the distribution of radial velocities and metallicities of a sample of about 1700 field objects from the the Besançon Galactic model (Robin et al., 2003). We found that no field stars are present in the CMD region corresponding to the position of the targets and with radial velocities and metallicities similar to those of 47 Tuc. We can also safely exclude a contamination from

stars belonging to the Small Magellanic Cloud (SMC), since the brightest SMC objects (at the RGB tip) are located at much fainter magnitudes ($V \sim 16.5$ mag) and have quite different radial velocities (between $+50$ e $+250$ km s^{-1}; Harris 1996, 2010 edition).

8.2 Chemical analysis

The chemical analysis has been performed following the same approach already used in Lapenna et al. (2014). The equivalent width (EW) and the relative uncertainty have been measured with DAOSPEC, iteratively launched by the 4DAO[1] code (Mucciarelli, 2013b). Abundances were obtained with the code GALA[2] (Mucciarelli et al., 2013a), by matching the measured and theoretical EWs, and adopting the ATLAS9 model atmospheres and the solar values of Grevesse & Sauval (1998). We have used only the lines with reduced EWs, defined as $\log(EW/\lambda$ (with λ being the wavelength), ranging between -5.6 and -4.5 to avoid saturated or too weak lines, and we discarded those with EW uncertainties larger than 20%. The computation of the final iron abundances has been performed by using up to 127 FeI lines and 9 FeII lines. To derive the abundances of titanium we exploited 20 TiI lines and 11 TiII lines.

The microturbulence velocity (see Table 8.2) has been optimized spectroscopically by requiring that no trends exist between the abundance derived from FeI lines and the reduced EWs. To determine the stellar surface gravity ($\log g$) an estimate of the stellar mass and radius is needed. The latter is obtained from the Stefan-Boltzmann equation once the surface temperature (see Table 8.1) has been determined from the $(V-I)_0$ color-temperature relation of Alonso et al. (1999), after transforming the Johnson-Cousin $(V-I)_0$ color into the Johnson system following appropriate transformations (Bessell, 1979). *As for the stellar mass, which value is expected for the three targets?* Due to the mass-loss occurring along the RGB, stars evolving on the HB are expected to be less massive than MS turn-off stars by $\sim$ 0.1-0.15 $M_{\odot}$ (Renzini & Fusi Pecci, 1988; Origlia et al., 2007, 2010, 2014). Recently, Gratton et al. (2010b) derived the mass distribution of HB stars in several globular clusters, obtaining values between $\sim$ 0.6 and 0.7 $M_{\odot}$ in the case of 47 Tuc. These values are 0.1-0.2 $M_{\odot}$ lower than the turn-off mass of the best-fit isochrone (0.85 $M_{\odot}$), in full agreement with the expected amount of mass-loss during the RGB. Adopting a mass of 0.6 $M_{\odot}$ and the photometric measure of the effective temperature, we obtained surface gravities of ~ 2.0

[1] http://www.cosmic-lab.eu/4dao/4dao.php
[2] http://www.cosmic-lab.eu/gala/gala.php

and we derived the FeI and FeII abundances of the three targets (see Table 8.2).

For all the targets we found values of [FeI/H[in agreement with the mean metallicity of 47 Tuc ([Fe/H]$= -0.83, \sigma = 0.03$ dex; Lapenna et al., 2014). This suggests that the target stars are not affected by departures from local thermal equilibrium (LTE)[3] and the abundance derived from FeI lines is a reliable measure of the iron content of the stars. However, only for two objects (namely bHB1 and bHB2) the value of the iron abundance obtained from the ionized lines (FeII) agrees, within 0.01 dex, with that derived from FeI, while it is sensibly (~ 0.2 dex) lower for E-BSS1. This is the opposite of what is predicted and observed in the case of departures from LTE conditions, while it could be explained as an effect of surface gravity and, hence, of stellar mass. In fact the absorption lines of ionized elements are sensitive to changes in surface gravity, while neutral lines are not. Taking this into account, we evaluated the effect of increasing the stellar mass by re-performing the spectral analysis for different values of the surface gravity.

In Table 8.2 we list the values of [FeI/H] and [FeII/H] obtained by varying the star mass in steps of 0.1 $M_{\odot}$ while keeping the effective temperature fixed. The upper panel of Figure 8.2 shows the resulting behavior. As expected, in all cases the FeI abundance remains essentially unaltered (and consistent with the cluster metallicity), while [FeII/H] systematically increases for increasing mass (gravity). The behavior of the difference between FeII and FeI abundances as a function of the adopted stellar mass is plotted in the left panels of Figure 8.3 for the three targets. Clearly, while for two stars (bHB1 and bHB2) a good agreement between the FeI and FeII abundances is reached at 0.6 $M_{\odot}$, for E-BSS1 a significantly larger stellar mass (1.3-1.4 $M_{\odot}$, corresponding to a gravity log g = 2.4 dex) is needed. Thus, a mass larger than twice the mass expected for a canonical post-HB cluster star is needed in order to reconcile the FeI and FeII abundances of E-BSS1. Conversely, the difference [FeII/H]-[FeI/H] for the other two targets tends to diverge for increasing stellar mass (see Figure 8.3), indicating that the adopted values of the surface gravity become progressively unreasonable.

As a double check, the same procedure has been performed on the titanium lines, since this is one of the few other elements providing large numbers of both neutral and single ionized lines. Also in this case, the same abundance of TiI and TiII is reached, within the errors, only if a mass of 1.4 $M_{\odot}$ is adopted for E-BSS1, while the best agreement is reached

[3] In fact, departures from LTE conditions affect the minority species, leading to an under-estimate of [FeI/H], while they have no impact on the abundances obtained from the dominant species, as single ionized iron lines (see also Ivans et al., 2001; Mashonkina et al., 2011; Mucciarelli et al., 2015a)

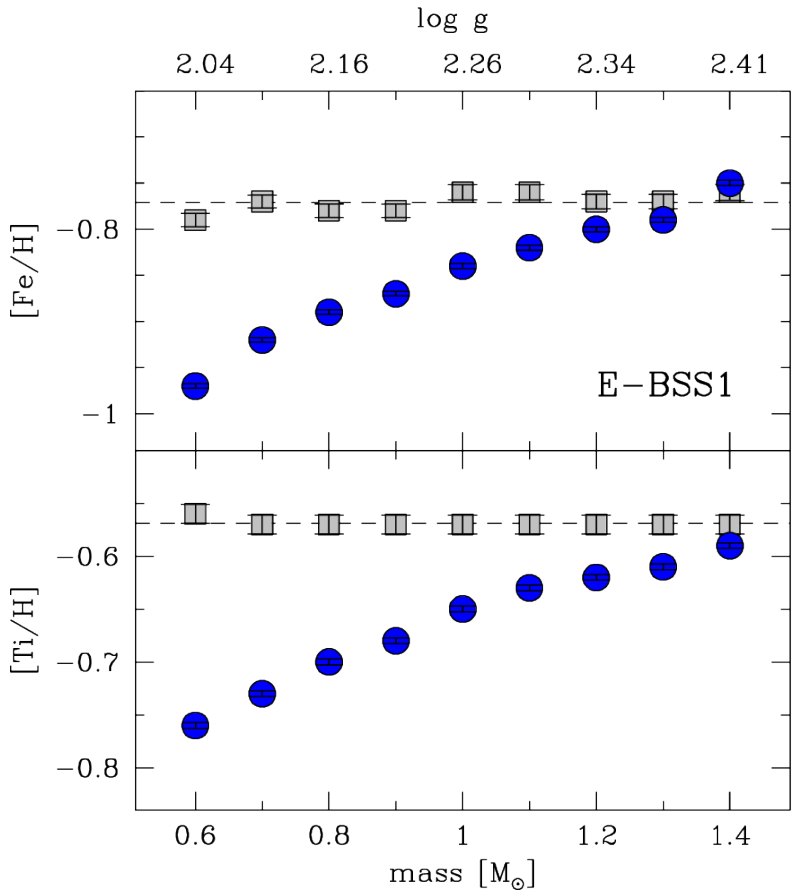

Figure 8.2 *Top panel:* Iron abundance of E-BSS1 derived from FeI lines (grey squares) and FeII lines (blue circles), as a function of the assumed stellar mass. Errors in the derived abundances are smaller than the symbol sizes. The dashed line marks the average FeI abundance (well corresponding to the metallicity of 47 Tuc: [Fe/H]$= -0.83$ dex; e.g., Lapenna et al., 2014). In the top axis of the panel, the logarithmic values of the stellar surface gravity corresponding to the various adopted masses are labeled. *Bottom panel:* Same as the top panel, but for the Ti abundance, as derived from TiI lines (grey squares) and TiII lines (blue circles).

at 0.6-0.7 $M_{\odot}$ for bHB1 and bHB2 (see the right panels of Figure 8.3). This fully confirms the results obtained from the iron abundance analysis, pointing out that EBSS-1 is an object significantly more massive than the others.

Additional support comes from the inspection of another feature that is known to be sensitive to the stellar surface gravity: the wings of the MgI b triplet at 5167.3, 5172.6 and 5183.6Å. In Figure 8.4 we show a comparison between the observed spectrum of EBSS-1 and two synthetic spectra computed by assuming the atmospheric parameters listed in Table 8.1 and the measured Mg abundance; only the surface gravity has been varied: we adopted log g = 2.03 and log g = 2.40 dex (corresponding to 0.6 and 1.4 $M_{\odot}$ respectively).

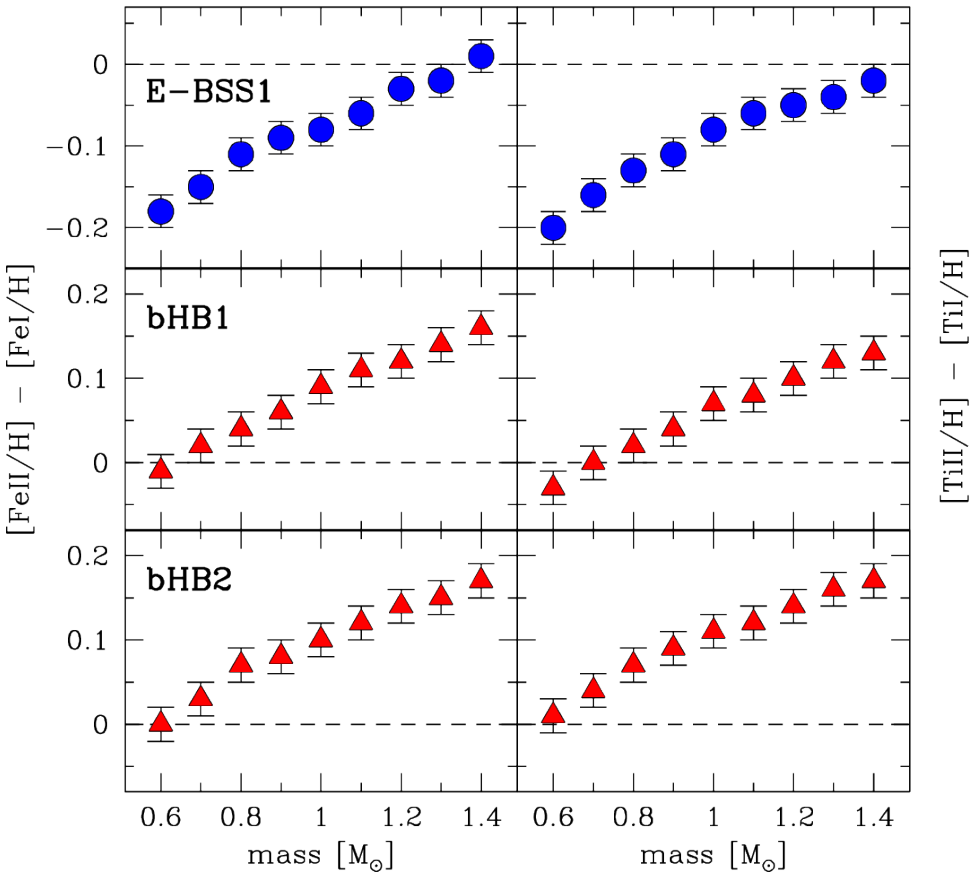

Figure 8.3 *Top panel:* Difference between the iron abundances derived from ionized lines and that obtained from neutral lines, as a function of the assumed stellar mass (left-hand panel) for E-BSS1. The same, but for the titanium abundances is shown in the right-hand panels. *Mid panel:* As in the top panel, but for target bHB1. *Bottom panel:* As in the top panel, but for target bHB2.

Clearly, the synthetic spectrum computed for log g = 2.03 dex fails to fit the wings of the MgI b triplet, while that computed assuming a 1.4 $M_{\odot}$ stellar mass closely reproduces the observed spectrum. All these findings point out that E-BSS1 is an object significantly more massive than the other targets and canonical cluster stars.

8.2.1 Uncertanties

It is worth noticing that, in doing the comparison between the abundances derived from the ionized and the neutral species, we performed a differential analysis, with the most critical parameters (as temperature, microturbulence and gravity) set to the same value. Hence only internal errors, due to the quality of the spectra and the number of the absorption lines used, need to be considered, while potential external sources of errors can be neglected.

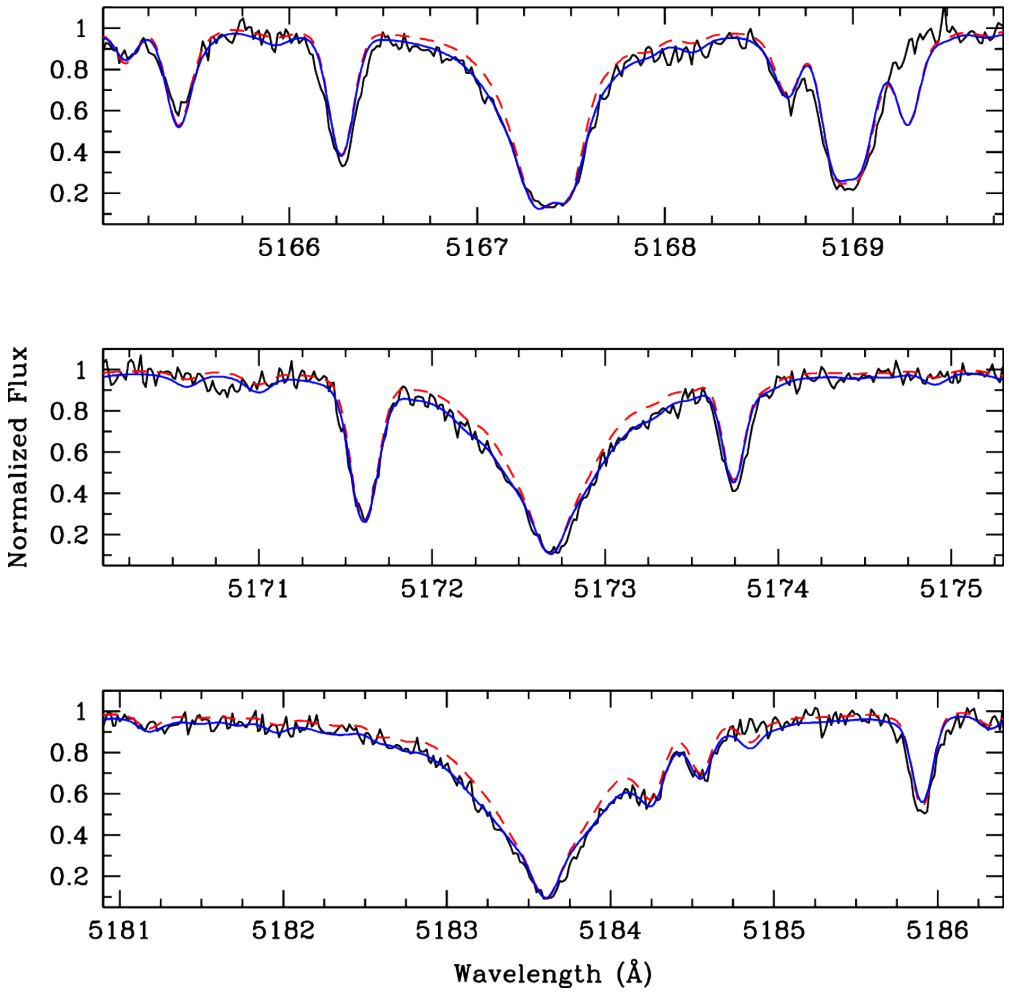

Figure 8.4 Comparison between the observed spectrum (solid black line) and two synthetic spectra for the MgI lines at 5167.3, 5172.6 and 5183.6Å. The synthetic spectra have been computed by adopting $T_{\rm eff} = 5013$ K and $v_{\rm turb} = 1.20$ km s^{-1} and by adopting two different values of the surface gravity: log $g = 2.03$ corresponding to a stellar mass of 0.6 $M_{\odot}$ (dashed red line) and log $g = 2.40$ corresponding to 1.4 $M_{\odot}$ (solid blue line). Clearly, the spectrum obtained for a 0.6 $M_{\odot}$ star is unable to reproduce the observations, while the observed wings of the MgI b triplet are very well matched under the assumption of a 1.4 $M_{\odot}$ stellar mass.

The global uncertainty on the difference between ionized and neutral chemical abundances has been determined by taking into account the effect of atmospheric parameter variations and the covariance terms due to their correlations (Cayrel et al., 2004). We estimate that the global effect of varying the temperature by 40 K (corresponding to an error in color of the order of 0.015 mag) produces a variation of 0.01 dex on the abundance difference. By adding in quadrature this term with the uncertainties due to the EW measurements (which are of the order of 0.01 dex for both the abundance ratios), we estimate a total error

of about 0.02 dex on the derived abundance differences.

We emphasize that the only way to make the FeII abundance in agreement with that of FeI, while simultaneously complying with the other constraints, is to assume a large mass (gravity) for E-BSS1. In fact, departures from LTE conditions would affect the neutral species (yielding to an under-estimate of [FeI/H]), leaving unaltered the abundances obtained from single ionized lines (Ivans et al., 2001; Mashonkina et al., 2011; Mucciarelli et al., 2015a). The micro-turbulence velocity has a negligible impact on the derived abundances, and its effect is the same (both in terms of absolute value and direction) on the abundances derived from neutral and from ionized lines: hence, it cannot help reconciling the value of [FeII/H] with that of [FeI/H]. Finally, if for E-BSS1 we assume a mass sensibly lower than 1.4 $M_{\odot}$ (for instance 0.6-0.8 $M_{\odot}$, as appropriate for HB and giant stars in 47 Tuc), FeII would agree with FeI only if the effective temperature is lowered by $\sim$ 130 K. However, this solution is not acceptable, because it implies a non-zero slope between the iron abundance and the excitation potential. Moreover, such a low value of $T_{\rm eff}$ corresponds to a photometric color that is completely inconsistent with the observed one (note the internal accuracy of the HST photometry for such a bright object is less than 0.01 mag). Thus, the spectra inevitably lead to the conclusion that E-BSS1 is significantly more massive than the other stars.

8.3 Discussion

Indeed the mass derived for E-BSS1 (1.4 $M_{\odot}$) is by far too large for a genuine HB cluster star evolving toward the AGB (the MS turn-off mass in 47 Tuc is 0.85 $M_{\odot}$; see Section 8.2). Moreover, the mass values that we obtained for targets bHB1 and bHB2 from our analysis turn out to be fully in agreement with the values (0.6-0.7 $M_{\odot}$) recently estimated for typical HB stars in 47 Tuc (Gratton et al., 2010b). Notably, these are also the values that we obtained for targets bHB1 and bHB2 from our analysis. These results clearly demonstrate that the detailed comparison between neutral and ionized chemical abundances is a powerful *weighing device* able to reliably determine stellar masses in a self-consistent and differential way (this is quite relevant since it gets rid of any possible zero-point offset among different methods).

If E-BSS1 were coeval to the other low-mass stars populating the cluster, such a massive object would have already evolved into a white dwarf several Gyr ago. The only possibility

is that it formed more recently, through a mass-enhancement process: it could therefore be the descendant of a BSS. As any other star, BSSs are then expected to evolve along the various post-MS phases. Indeed, E-BSS1 is located in the region of the CMD where evolved BSSs experiencing the core helium burning process are expected to lie. In fact, the collisional models of Sills et al. (2009) show that, during the core helium burning stage, the progeny of collisional BSSs should populate the CMD slightly blueward of the RGB, between 0.2 and 1 mag brighter than the "canonical" HB level of the host cluster[4]. Overall, the post-MS evolution of a collisional product in the CMD is very similar to that of a normal star of the same mass, the former being just a few tens of degree hotter (see Figure 6 of Sills et al., 2009 for the model of a $\sim$ 1.4 $M_{\odot}$ star). In the following analysis, we therefore adopted "normal" evolutionary tracks. In Figure A.3 we have superimposed[5] to the CMD of 47 Tuc the evolutionary track (from Pietrinferni et al., 2006) of a 1.5 $M_{\odot}$ star. We note that EBSS-1 lies in the a region very close to the red clump level of this track, corresponding to an effective temperature $T_{\rm eff} \simeq 5011$ K and a surface gravity log $g \sim 2.47$ dex. These values are in very good agreement with those derived from the chemical analysis of this object. It seems therefore perfectly reasonable to identify our star with an evolved BSS that is currently experiencing its red clump (core helium burning) phase before ascending the AGB.

How rare evolved BSSs are? The number of evolved BSSs observable along the HB stage is predicted to be small even in a massive cluster like 47 Tuc. An estimate can be derived by combining the theoretical ratio between the characteristic MS and HB lifetimes, with the observed number of BSSs. The total BSS population of 47 Tuc likely counts ~ 200 objects. In fact, observational surveys (Ferraro et al., 2004b) sampling only on the brightest portion of the population counted 110 BSSs over the entire cluster extension, with approximately 40% of the population being segregated within 2 core radii ($r < 50''$) from the center, which is the distance where E-BSS1 is located. However deep UV observations of the very central region of the cluster, sampling the entire BSS sequence (Ferraro et al., 2001), demonstrated that the total population could be 1.7 times larger. Based on these numbers, it is reasonable to expect ~ 80 BSSs within $r < 50''$.

[4]Unfortunately no specific tracks for the post-MS evolution of mass-transfer BSSs in globular clusters are available at the moment. However the models specifically built for the open cluster M67 (Tian et al., 2006) and the globular cluster M30 (Xin et al., 2015) suggest that, after mass-transfer, BSSs behave largely as normal single stars of comparable mass. Hence they are also expected to populate the same region of the CMD.

[5]We assumed a distance of 4.45 kpc and a color excess $E(B-V) = 0.04$ (see Harris 1996, 2010 edition).

On the other hand, evolutionary tracks of collisional BSSs (Sills et al., 2009) show that the HB lifetime is approximately constant ($\sim 10^8$ years, similar to the HB duration for low-mass single stars), regardless of the original stellar masses at the time of the collision. Instead the MS lifetime of collisional BSSs can change by 3 orders of magnitude, being $40 - 70\%$ smaller than that of a normal single star with similar mass. Thus the predicted number of BSSs in the HB evolutionary stage sensibly depends on the mass of the BSS progenitor. For instance, the average value of the ratio between the MS and the HB lifetimes is $t_{\rm MS}/t_{\rm HB} = 17.7$, while for a 1.4 $M_{\odot}$ BSS originated from the collision of a 0.8+0.6 $M_{\odot}$ pair, we expect $t_{\rm MS} = 0.82$ Gyr and $t_{\rm HB} = 0.096$ Gyr, thus yielding $t_{\rm MS}/t_{\rm HB} = 8.5$. This value is more than two times smaller than that predicted for a 1.4 $M_{\odot}$ single star ($t_{\rm MS}/t_{\rm HB} = 19.3$; Sills et al., 2009). By considering these two values as reasonable extremes for the ratio $t_{\rm MS}/t_{\rm HB}$, we expect to observe 4-8 evolved BSSs experiencing the helium burning phase out of a total population of 80 BSSs (in the MS stage).

Note that in the same region of the cluster ($r < 50''$), several hundreds genuine low-mass stars, with quite similar photometric properties and experiencing the same evolutionary phase, are observed. However, because of their larger mass, evolved BSSs in the HB stage are expected to appear brighter than "normal" low-mass HB stars and to lie along the path of low-mass stars evolving toward the AGB. For genuine low-mass stars the transition from the HB to the AGB phase (see the box in Figure A.3) is quite rapid: ~ 3.5 million years, corresponding to approximately 4% of the time they spent in the HB phase. Based on these considerations and the fact that within $50''$ from the cluster center we count 270 objects in the HB clump, we would have expected to observe ~ 11 stars within the box drawn in Figure A.3. Instead 20 stars are counted. According to these estimates, roughly half of the stars within $50''$ from the cluster center and lying in the selection box could be evolved BSSs. Hence beside E-BSS1, 8 additional stars in the box could be evolved BSSs. This is in very good agreement with the prediction above, based on the number of BSSs observed on the MS. It is also consistent with previous evidence (Beccari et al., 2006) showing that the radial distribution of supra-HB stars in 47 Tuc is anomalously segregated in the center, as expected if a significant fraction of them is made of objects heavier than the average, sunk to the bottom of the potential well because of the cluster dynamical evolution (Ferraro et al., 2012).

8.4 Summary and conclusions

In this work we have performed the chemical analysis of three stars observed between the HB and the AGB regions in the CMD of the Galactic globular cluster 47 Tuc. By using high-resolution spectra acquired at the Very Large Telescope, we have used the difference between iron and titanium abundances derived from neutral and ionized lines as a *weighing machine* to derive the stellar mass. This provided convincing evidence that one target (E-BSS1) is significantly more massive ($\sim$ 1.4 $M_{\odot}$) than normal cluster stars, while the other two targets (bHB1 and bHB2) have masses of 0.6-0.7 $M_{\odot}$, perfectly consistent with the theoretical expectations. These results clearly demonstrate that the detailed comparison between neutral and ionized chemical abundances is a powerful *weighing device* able to reliably determine stellar masses in a self-consistent and differential way. The presence of such a high-mass star in that region of the CMD strongly suggests that it is an evolved descendants of a BSS, caught during its core He-burning phase. Interestingly, the ratio between the characteristic MS and HB evolutionary times and the number of BSSs observed in 47 Tuc suggest that a few other evolved BSSs should populate the same region of the CMD.

The identification of evolved BSSs is crucial in the context of BSS formation and evolution models, and the proposed *weighing device* can provide a major advance in this field by efficiently pinpointing (heavy) evolved BSSs into the dominant and photometrically indistinguishable population of genuine (low-mass) stars. The collection of complete samples of these objects in globular clusters (where BSSs and their descendants are expected to be numerous enough) allows the determination of meaningful population ratios from which the characteristic evolutionary time-scales can be empirically constrained. Moreover, since evolved BSSs are 20 times more luminous than their progenitors, detailed spectroscopic follow-up studies are largely facilitated and open the possibility to even go back to the formation channel. In fact, a few characterizing features impressed by the formation process could be still observable in such advanced stages of the evolution. One of the most solid predictions of the mass-transfer scenario is that mass-transfer BSSs should be bound in a binary system with a compact (degenerate) companion star (the peeled core of the donor, probably a helium white dwarf). This was recently confirmed in an open cluster (Gosnell et al., 2014). Thanks to the high luminosity of evolved BSSs, spectroscopic follow-up observations would make such a prediction easily testable through the measurement of periodic

radial velocity variations. Since no companion is expected in the collisional scenario (which ends up with the merger of the two progenitors), this kind of studies is particularly important in globular clusters, where both formation channels are expected to be active but their relative efficiency is still unknown. Moreover, detailed spectroscopic follow-ups providing the entire chemical pattern of evolved BSSs represent an additional and highly fruitful route toward the full characterization of their evolution. In fact, significant depletion of chemical species like carbon and oxygen has been observed in a sub-sample of BSSs in 47 Tuc and it has been interpreted as the chemical signature of the mass-transfer origin of these objects (Ferraro et al., 2006a). However it is still unknown whether this signature is transient and on which time-scales. Hence, any additional information obtained from more advanced stages of the evolution can provide new clues about the degree of mixing experienced by these stars. Indeed, after the detection of E-BSS1, the proposed *weighing device* promises to boost the identifications of evolved BSSs, thus providing unprecedented constraints to the theoretical modeling of these exotica and opening a new perspective on the comprehension of their evolutionary paths and formation processes.

Table 8.1. Observational parameters of the three targets

Name	ID	R.A. (J2000)	Dec (J2000)	V	$(V-I)$	r (arcsec)	$T_{\rm eff}$ (K)	V_r (km s^{-1})
EBSS-1	1090214	6.0601164	-72.0726528	13.573	0.928	50.6	5013	-24.3 ± 0.05
bHB1	1109049	6.0001040	-72.0720222	13.761	0.976	42.1	4896	-7.8 ± 0.06
bHB2	2625792	5.9343037	-72.1054776	13.722	0.957	132.2	4940	-11.7 ± 0.06

Note. — Coordinates, V band magnitude, $(V-I)$ color, distance from the center, effective temperature and radial velocity of the three target stars. The cluster center used to compute the distance from the center is from Miocchi et al. (2013).

Table 8.2. Abundance ratios of Fe and Ti obtained by adopting different stellar mass (gravity) values

Mass ($M_\odot$)	log g^{phot} (dex)	v_{turb}^{spec} (km s^{-1})	[FeI/H] (dex)	n(FeI)	[FeII/H] (dex)	n(FeII)	[TiI/H] (dex)	n(TiI)	[TiII/H] (dex)	n(TiII)
					E-BSS1					
0.60	2.03	1.30	–0.79 ± 0.01	122	–0.97 ± 0.01	9	–0.56 ± 0.01	21	–0.76 ± 0.05	11
0.70	2.10	1.25	–0.77 ± 0.01	122	–0.92 ± 0.01	9	–0.57 ± 0.01	20	–0.73 ± 0.05	11
0.80	2.15	1.25	–0.78 ± 0.01	121	–0.90 ± 0.01	9	–0.57 ± 0.01	20	–0.71 ± 0.05	11
0.90	2.21	1.25	–0.78 ± 0.01	121	–0.87 ± 0.01	9	–0.57 ± 0.01	20	–0.68 ± 0.05	11
1.00	2.25	1.20	–0.76 ± 0.01	123	–0.84 ± 0.01	9	–0.57 ± 0.01	20	–0.66 ± 0.05	11
1.10	2.30	1.20	–0.76 ± 0.01	123	–0.82 ± 0.01	9	–0.57 ± 0.01	21	–0.63 ± 0.05	11
1.20	2.33	1.20	–0.77 ± 0.01	122	–0.80 ± 0.01	9	–0.57 ± 0.01	21	–0.62 ± 0.05	11
1.30	2.37	1.20	–0.77 ± 0.01	125	–0.79 ± 0.01	9	–0.57 ± 0.01	21	–0.61 ± 0.05	11
1.40	2.40	1.15	–0.76 ± 0.01	127	–0.76 ± 0.01	9	–0.57 ± 0.01	20	–0.59 ± 0.05	11
					bHB1					
0.60	2.06	1.35	–0.84 ± 0.01	129	–0.85 ± 0.01	12	–0.66 ± 0.01	26	–0.69 ± 0.05	14
0.70	2.13	1.35	–0.84 ± 0.01	128	–0.82 ± 0.01	12	–0.66 ± 0.01	26	–0.66 ± 0.05	14
0.80	2.18	1.35	–0.84 ± 0.01	128	–0.80 ± 0.01	12	–0.66 ± 0.01	26	–0.64 ± 0.05	14
0.90	2.23	1.35	–0.84 ± 0.01	127	–0.78 ± 0.01	12	–0.66 ± 0.01	26	–0.62 ± 0.05	14
1.00	2.28	1.35	–0.84 ± 0.01	126	–0.75 ± 0.01	12	–0.66 ± 0.01	26	–0.59 ± 0.05	14
1.10	2.32	1.35	–0.84 ± 0.01	126	–0.73 ± 0.01	12	–0.66 ± 0.01	26	–0.58 ± 0.05	14
1.20	2.36	1.35	–0.84 ± 0.01	126	–0.72 ± 0.01	12	–0.67 ± 0.01	26	–0.57 ± 0.05	14
1.30	2.39	1.30	–0.83 ± 0.01	126	–0.69 ± 0.01	12	–0.67 ± 0.01	26	–0.55 ± 0.05	14
1.40	2.43	1.30	–0.83 ± 0.01	127	–0.67 ± 0.01	12	–0.67 ± 0.01	26	–0.54 ± 0.05	14

Table 8.2 (cont'd)

Mass ($M_\odot$)	log g^{phot} (dex)	v_{turb}^{spec} (km s^{-1})	[FeI/H] (dex)	n(FeI)	[FeII/H] (dex)	n(FeII)	[TiI/H] (dex)	n(TiI)	[TiII/H] (dex)	n(TiII)
					bHB2					
0.60	2.06	1.20	–0.81 ± 0.01	124	–0.81 ± 0.02	10	–0.68 ± 0.01	22	–0.67 ± 0.05	13
0.70	2.13	1.20	–0.81 ± 0.01	128	–0.78 ± 0.02	10	–0.68 ± 0.01	22	–0.64 ± 0.05	13
0.80	2.19	1.20	–0.82 ± 0.01	129	–0.75 ± 0.02	10	–0.68 ± 0.01	22	–0.61 ± 0.05	13
0.90	2.24	1.15	–0.80 ± 0.01	128	–0.72 ± 0.02	11	–0.68 ± 0.01	22	–0.59 ± 0.05	13
1.00	2.29	1.15	–0.78 ± 0.01	127	–0.68 ± 0.02	11	–0.68 ± 0.01	22	–0.57 ± 0.05	13
1.10	2.33	1.15	–0.80 ± 0.01	125	–0.68 ± 0.02	11	–0.68 ± 0.01	22	–0.56 ± 0.05	13
1.20	2.37	1.10	–0.79 ± 0.01	125	–0.65 ± 0.02	11	–0.68 ± 0.01	22	–0.54 ± 0.05	13
1.30	2.40	1.10	–0.78 ± 0.01	124	–0.63 ± 0.02	11	–0.69 ± 0.01	22	–0.53 ± 0.05	13
1.40	2.43	1.10	–0.79 ± 0.01	124	–0.62 ± 0.02	11	–0.69 ± 0.01	22	–0.52 ± 0.05	13

Note. — Iron and titanium abundance ratios obtained for the program stars by adopting the mass values listed in the first column. During the analysis the effective temperature (listed in Table 8.1) and surface gravity (column 2) have been kept fixed, while the microturbulent velocity (column 3) has been spectroscopically optimized. The abundances obtained from neutral and ionized lines, and the number of lines used are listed in columns 4–11 (see labels). We adopted the solar reference values of Grevesse & Sauval (1998).

Conclusions

The PhD work presented in this manuscript is aimed at clarifying one of the least studied (yet highly significant) phases of stellar evolution: the asymptotic giant branch (AGB). As discussed in the previous chapters, the AGB evolutionary stage is poorly studied in the literature, especially from the point of view of high-resolution spectroscopy. However, it may provide important information about exotic stellar species (like Blue Straggler Stars; see Beccari et al., 2006) and the evolutionary history of multiple-populations (Campbell et al., 2013) in the parent cluster. The thesis work is based on the analysis of a high-quality, high-resolution spectra acquired at the Very Large Telescope (ESO) and at the MPG/ESO-2.2m telescope. New unexpected results about the chemical composition of AGB stars have been found, with important consequences for our understanding of this evolutionary phase and recent claims of significant iron spread in a few GCs. The main result is the discovery of a previously unknown mechanism affecting the neutral species of some chemical elements in the atmosphere of most AGB stars: because of it, the abundances derived from neutral lines are systematically underestimated, while those measured from ionized lines remain unaffected. Such a behaviour exactly corresponds to what expected in the case of non-local thermodynamic equilibrium (NLTE) in the star atmosphere. However, the observed effect is larger than predicted by the current NLTE models, thus demonstrating either that these models are not adequate enough, or that some more complex mechanism is occurring in AGB star atmospheres. With this caveat in mind, we refer to this effect as "NLTE effect". It affects most (but not all) AGB stars in all the investigated GCs and it is particularly evident for iron and titanium elements, which provide the largest number of both neutral and ionized lines. In the case of M22, also some red giant branch (RGB) stars turn out to suffer from the same "problem". A deep understanding of the detected phenomenon is crucial for a proper determination of the chemical abundance patterns and enrichment history of GCs. In detail, the main results of the thesis can be summarized as follows.

- (1) *The discovery of NLTE effects in an unsuspected metallicity regime* - The first evidence of the "NLTE effect" has been obtained from the proper spectroscopic analysis of a sample of 24 AGB stars in 47Tucanae, observed with FEROS at the MPG/ESO-2.2m telescope. We analyzed neutral and ionized iron lines separately, finding that, for most of the targets (20 out of 24), the former provide iron abundances systematically lower (by -0.1 dex on average) that those obtained from ionized species and from a sample of RGB stars. The importance of this result is that, at odds with previous findings (Ivans et al., 2001), NLTE effects have been observed for the first time in metal-rich ([Fe/H] = -0.8 dex) stars, a metallicity regime where models predict that NLTE should be negligible.

- (2) *The intrinsic iron spread claimed in a few GCs seems to be spurious* - The case of NGC3201: The high-resolution spectroscopic analysis of 21 giant stars in NGC3201 presented in this work, demonstrated that, contrary to RGB stars of similar luminosity, AGB stars show a clear discrepancy between the abundances derived from neutral and from single-ionized iron lines, confirming the behaviour observed in 47Tucanae. Hence, the iron spread claimed by Simmerer et al. (2013) turned out to be spurious, and due to (neglected) NLTE effects. In fact, no iron spread is obtained by considering the iron abundance only from (the unaffected) ionized lines. The case of M22: M22 is another GC for which a significant iron spread (Δ[Fe/H] = 0.2 dex) has been claimed (Marino et al., 2009, 2011). Our analysis of a sample of 17 giant stars used by Marino et al. demonstrates that important NLTE effects are present in the majority of AGB stars. However, in the case of M22, we have observed marginal NLTE effects also among RGB stars, suggesting that the situation is even more complex. In any case, the iron abundances derived from ionized lines, both for RGB and for AGB stars, show no intrinsic spread.

  Note that the presence of any intrinsic iron spread necessarily implies that the high-velocity supernova ejecta were retained within the system potential well, thus requiring a much larger mass than currently observed. Hence, our findings show that, in the cases of both NGC3201 and M22, no exotic scenario requiring that the clusters were significantly more massive at their birth is needed. The observed unimodal [FeII/H] distribution rules out the possibility that these systems are the remnants of now disrupted dwarf galaxies, with a crucial impact on the current interpretation of GC formation and evolutionary history. In a more general context, our findings indicate that any claim of intrinsic iron

spread in GCs should be always confirmed with an analysis based on FeII lines and photometric gravities. If the abundance spread is real, it should be detected also when FeII lines and photometric log g are adopted, since FeII lines are the most reliable indicators of the iron abundance.

- (3) *Additional clues from the AGB population of M62* - The high-resolution spectroscopic analysis of a sample of 19 giant stars in M62 has revealed, for the first time, that the same NLTE mechanism affects also the titanium lines. Moreover, the abundances derived for light elements, like oxygen, sodium and aluminum, have shown that all the studied AGB stars are compatible with the first stellar generation (made of O-rich, Na-poor, and Al-poor stars), while the RGB component includes both first and second generation stars. This result is quite puzzling and closely resembles the case of NGC6752 in which (Campbell et al., 2013) recently claimed the lack of second generation component in the AGB phase.

- (4) *Ionization balance as a powerful weighing machine for stars* - We used the ionization balance between chemical abundances derived from neutral and from ionized elements to define a powerful weighing device. In fact, the abundance of a given chemical element obtained from ionized atoms is sensitively dependent on the stellar gravity, while such a dependence is negligible for neutral spectral lines of the same element. Hence, by forcing the former to match the latter, the surface gravity of the star can be estimated. We used this approach to identify an anomalously heavy (1.4 $M_{\odot}$) star in 47Tucanae. Because of its position in the Colour-Magnitude Diagram, this star is probably a Blue Straggler caught during its helium burning phase.

  These results clearly demonstrate that the proposed weighting device is able to reliably determine stellar masses in a self-consistent and differential way: this is crucial, since it gets rid of any possible zero-point offset among different methods. The large applicability of the proposed method to most of the GCs in our Galaxy opens the possibility to initiate systematic searches for evolved BSSs, thus giving access to still unexplored phases of their evolution by efficiently pinpointing (heavy) evolved-BSSs into the dominant and photometrically indistinguishable population of genuine (low-mass) stars. The collection of complete samples of these objects in globular clusters (where BSSs and their descendants are expected to be numerous enough) finally opens the possibility to determine the characteristic BSS evolutionary time-scales, thus providing crucial con-

straints to the formation and evolution models of these exotica.

- (5) *"Side-products"* - A side product of this thesis work is the characterization of the performances of new-generation spectrographs, as GIANO at TNG and KMOS at VLT. In particular, in the case of KMOS the work was aimed at the validation of the quality of the radial velocities obtainable with this instrument, in the context of a Large Program designed to determine the next generation of velocity dispersion and rotation profiles for a representative sample of Galactic GCs. In the case of GIANO, the work purpose was twofold: (1) to determine position and intensity of OH sky lines for wavelength calibration and rest-frame reference; (2) to determine the overall continuum airglow emission in the H-band, which is important for the design of faint-object infrared spectrographs.

Appendix A

Radial Velocities from VLT-KMOS Spectra of Giant Stars in the Globular Cluster NGC6388

Published in Lapenna et al. 2015, ApJ, 798, 23

We present new radial velocity measurements for 82 stars, members of the Galactic globular cluster NGC6388, obtained from ESO-VLT KMOS spectra acquired during the instrument Science Verification. The accuracy of the wavelength calibration is discussed and a number of tests of the KMOS response are presented. The cluster systemic velocity obtained (81.3 ± 1.5 *km* s^{-1}*) is in very good agreement with previous determinations. While a hint of ordered rotation is found between* $9''$ *and* $20''$ *from the cluster centre, where the distribution of radial velocities is clearly bimodal, more data are needed before drawing any firm conclusions. The acquired sample of radial velocities has been also used to determine the cluster velocity dispersion profile between* $\sim 9''$ *and* $70''$*, supplementing previous measurements at* $r < 2''$ *and* $r > 60''$ *obtained with ESO-SINFONI and ESO-FLAMES spectroscopy, respectively. The new portion of the velocity dispersion profile nicely matches the previous ones, better defining the knee of the distribution. The present work clearly shows the effectiveness of a deployable Integral Field Unit in measuring the radial velocities of individual stars for determining the velocity dispersion profile of Galactic globular clusters. It represents the pilot project for an ongoing large program with KMOS and FLAMES at the ESO-VLT, aimed at determining the next generation of velocity dispersion and rotation profiles for a representative sample of globular clusters.*

A.1 Introduction

Galactic globular clusters (GCs) are massive ($10^4 - 10^6\ M_\odot$) stellar aggregates, where the two-body relaxation time-scale is shorter than the age (e.g., Binney & Tremaine, 1987). For this reason, they have been traditionally assumed to be quasi-relaxed, non rotating systems, characterized by spherical symmetry and orbital isotropy. Hence spherical, isotropic and non-rotating models, with a truncated distribution function close to a Maxwellian (King, 1966; Wilson, 1975) are commonly used to fit the observed surface brightness or density profiles, and to estimate the main GC structural parameters, like the core and half-mass radii, the concentration parameter and even the total mass (e.g. Harris 1996, 2010 edition; McLaughlin & van der Marel, 2005).

However, recent theoretical results indicate that these systems may have not attained complete energy equipartition (Trenti & van der Marel, 2013) and, depending on the degree of dynamical evolution suffered and the effect of an external tidal field, they may still preserve some characteristic kinematical feature (Vesperini et al., 2014). In particular, non zero angular momentum has been recognized to affect the entire dynamical evolution of star clusters (Einsel & Spurzem, 1999), and central rotation might still be present in GCs hosting an intermediate mass ($10^2 - 10^4\ M_\odot$) black hole (IMBH; Fiestas & Spurzem, 2010). Moreover, it is well known that the density profile alone is not sufficient to fully characterize a gravitational system, and the information about internal dynamics is also necessary (e.g. Binney & Tremaine, 1987; Meylan & Heggie, 1997, and references therein).

For instance, a star density profile with a shallow cusp deviating from a King (1966) model and a velocity dispersion (VD) profile with a keplerian central behavior are predicted in the presence of an IMBH (e.g. Baumgardt, Makino, & Hut, 2005; Miocchi, 2007). Despite its importance, the kinematical properties of Galactic GCs are still poorly explored from the observational point of view, although the number of dedicated studies aimed at building their VD and rotation profiles has significantly increased in the last years (see, e.g., Anderson & van der Marel, 2010; Noyola et al., 2010; Lane et al., 2010b; Bellazzini et al., 2012; McNamara et al., 2012; Lützgendorf et al., 2013; Fabricius et al., 2014; Kacharov et al., 2014, and references therein). In this context, interesting insights on specific dynamical processes occurring in the central regions of some clusters have been obtained by using "exotic" stellar populations, like millisecond pulsars and blue straggler stars (see Ferraro et al., 2003b, 2009b, 2012). However proper VD and rotation profiles, especially in their

innermost regions where the presence of the long-searched IMBHs is expected to leave characteristic signatures (as a VD cusp and systemic rotation; Baumgardt, Makino, & Hut, 2005; Miocchi, 2007; Einsel & Spurzem, 1999), are still badly constrained. This is due to the observationally difficulties, affecting both proper motion studies and the investigations of the velocity line-of-sight component.

As for the latter, while determining the line-of-sight rotation curve and VD profile in external galaxies is relatively simple (requiring the measurement, respectively, of the Doppler shift and the broadening of spectral lines in integrated-light spectra), it is much less straightforward in resolved stellar populations as Galactic GCs. In these systems, in fact, the dominant contribution of a few bright stars may artificially broaden the spectral lines, making the resulting value a non-representative measure of the true VD of the underlying stellar population (this is commonly refereed as "shot noise bias"; e.g. Dubath et al., 1997; Noyola et al., 2010; Lützgendorf et al., 2011). The alternative approach is to measure the dispersion about the mean of the radial velocities of statistically significant samples of individual stars. Clearly, this methodology is not prone to the shot-noise bias, provided that the individual stars are well resolved, sufficiently isolated and bright enough to be negligibly contaminated by the unresolved stellar background.

The latter approach is becoming increasingly feasible thanks to the current generation of adaptive-optics (AO) assisted spectrograph with an integral field unit (IFU), and the improved data analysis techniques (e.g. Lanzoni et al., 2013, hereafter L13; Kamann et al., 2013), as clearly demonstrated by the case of NGC 6388. The VD profile of this cluster derived from the line broadening of integrated-light spectra shows a steep cusp with a central value of 23-25 km s^{-1}, which is best-fitted by assuming that an IMBH of $2 \times 10^4\ M_\odot$ is hidden in the system (Lützgendorf et al., 2011). Instead, if the radial velocities of individual stars are used, a completely different result is found. By using SINFONI, an AO-assisted IFU spectrograph at the ESO-VLT, L13 measured the radial velocity of 52 individual stars in the innermost $2''$ of the cluster, finding a flat VD profile with a central value of only 13-14 km s^{-1}, which is well reproduced by no IMBH or, at most, a BH of $\sim 2000\ M_\odot$ (L13; see also Lanzoni et al., 2007). As discussed in detail in L13 (see their Sect. 4.1 and their Fig. 12), the integrated light spectra measured in the innermost part of the cluster are dominated by the contribution of two bright stars having opposite radial velocities with respect to the systemic one, despite the explicit effort by Lützgendorf et al. (2011) to correct for this. This produces a spuriously large line broadening and a consequent overestimate of the central

VD value.

The results obtained in NGC 6388 clearly demonstrate the feasibility of the individual radial velocity diagnostics and show that this is indeed the safest way to measure the stellar VD in Galactic GCs. To identify other multi-object facilities suitable for this kind of approach, we took advantage of the new K-band Multi Object Spectrograph (KMOS; Sharples et al., 2010), recently commissioned at the ESO-VLT. During the instrument Science Verification (SV) run, under proposal 60.A-9448(A) (PI: Lanzoni), we used KMOS multiple pointings to investigate the region within $\sim 9''$ and $70''$ from the center of NGC 6388. The results obtained from these observations are the subject of the present paper, and they prompted us to successfully apply for an ESO Large Program (193.D-0232, PI: Ferraro) aimed at constructing a new generation of VD profiles for a representative sample of Galactic GCs.

In Section A.2 we describe the observations and data reduction procedures. Section A.3 is devoted to the description of the kinematic analysis, including a number of tests about the performances of KMOS (Sect. A.3.1), the discussion of the determination of the radial velocities of individual stars (Sect. A.3.2), and the presentation of the derived VD profile (Sect. A.3.3). Discussion and conclusions are presented in Section A.4.

A.2 Observations and data reduction

KMOS is a second generation spectrograph equipped with 24 IFUs that can be allocated within a $7.2'$ diameter field of view. Each IFU covers a projected area on the sky of about $2.8'' \times 2.8''$, and it is sampled by an array of 14×14 spatial pixels (hereafter spaxels) with an angular size of $0.2''$ each. The 24 IFUs are managed by three identical spectrographs, each one handling 8 IFUs (1-8, 9-16 and 17-24, respectively). At the time of the observations discussed here, IFUs #13 and #16 were not usable. KMOS is equipped with four gratings providing a maximum spectral resolution R between $\sim$ 3200 and 4200 over the 0.8-2.5 μm wavelength range. We have used the YJ grating and observed in the 1.00-1.35 μm spectral range at a resolution R$\approx$3400, corresponding to a sampling of about 1.75 Å pixel^{-1}, i.e. $\sim$ 46 km s^{-1} pixel^{-1} at 1.15 μm. This instrumental setup is especially effective in simultaneously measuring a number of reference telluric lines in the spectra of giant stars, for an accurate calibration of the radial velocity, despite the relatively low spectral resolution. An example of the observed spectra is shown in Figure A.1, with a zoom around 1.15 μm

to show some isolated telluric lines, and around 1.06 and 1.20 μm to show some stellar features of interest.

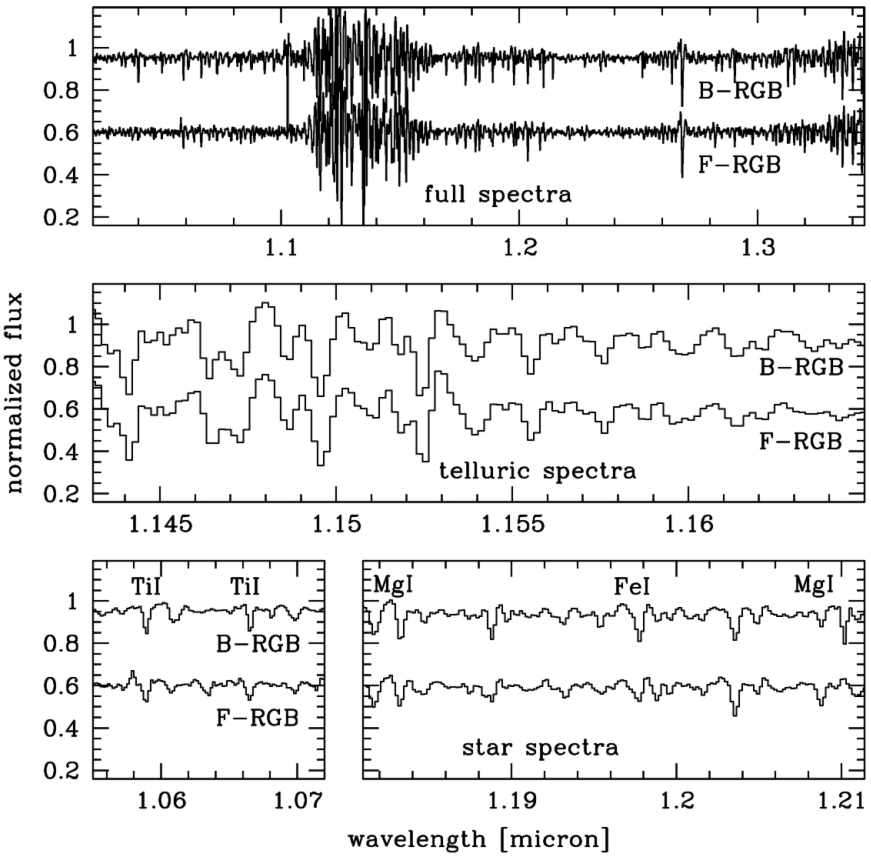

Figure A.1 An example of the observed KMOS YJ spectra of two giant stars: a bright B-RGB (star #245899, J = 10.24 mag, top spectra) and a faint F-RGB (star #43138, J = 12.90 mag, bottom spectra). Top panel: observed spectra. Middle panel: zoomed spectra around 1.15 μm, including a few isolated telluric lines. Bottom panel: zoomed spectra around 1.05 and 1.2 μm, including a few isolated stellar features of interest.

The data presented here have been acquired during the KMOS SV, with four different pointings on NGC6388. The total on-source integration time for each pointing was 3-5min and it has been obtained with three sub-exposures of 60-100s each, dithered by $0.2''$ for optimal flat-field correction. The typical signal-to-noise ratio (SNR) of the observed spectra is $\gtrsim 50$. We used the "nod to sky" KMOS observing mode and nodded the telescope to an off-set sky field at $\approx 6'$ North of the cluster center, for a proper background subtraction.

The spectroscopic targets have been selected from near-IR data acquired with SOFI at the ESO-NTT (Valenti et al., 2007), based on the star position in the color-magnitude

diagrams (CMD) and the radial distribution within the cluster.

We selected targets with $J < 14$ mag (in order to always have SNR > 50) and sufficiently isolated, without stars brighter than 15 mag within $1''$ from their center. We then used ACS-HST data in the V and I bands, from Lanzoni et al. (2007b), Sarajedini et al. (2007) and Dalessandro et al. (2008), to identify additional stars not present in the SOFI catalog.

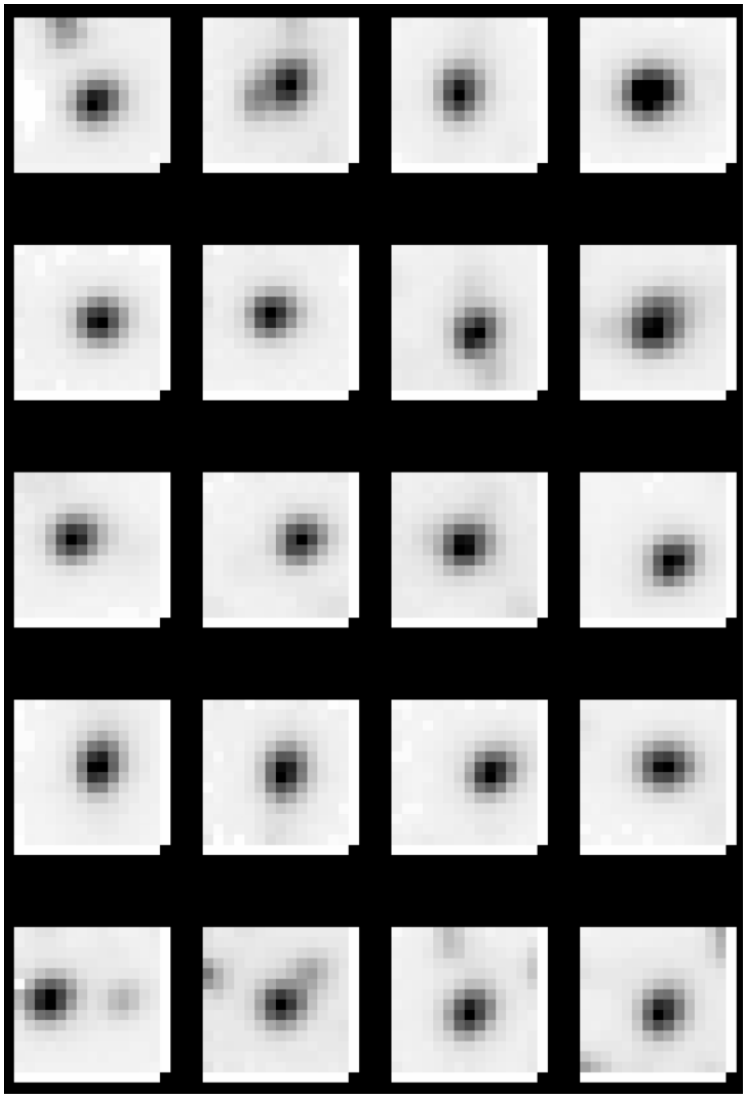

Figure A.2 Reconstructed images of 20 IFUs obtained during the first pointing. In some cases, other stars with a sufficient spectral SNR and not contaminated by the main target can be recovered from the same IFU.

The raw data have been reduced using the KMOS pipeline version 1.2.6, which performs background subtraction, flat field correction and wavelength calibration of the 2D spectra. The 1D spectra have been extracted manually by visually inspecting each IFU and

selecting the spectrum from to the brightest spaxel in correspondence of each target star centroid, in order to minimize the effects of possible residual contamination by nearby stars and/or by the unresolved stellar background. An example of the reconstructed images of the stars observed during the first pointing is shown in Figure A.2.

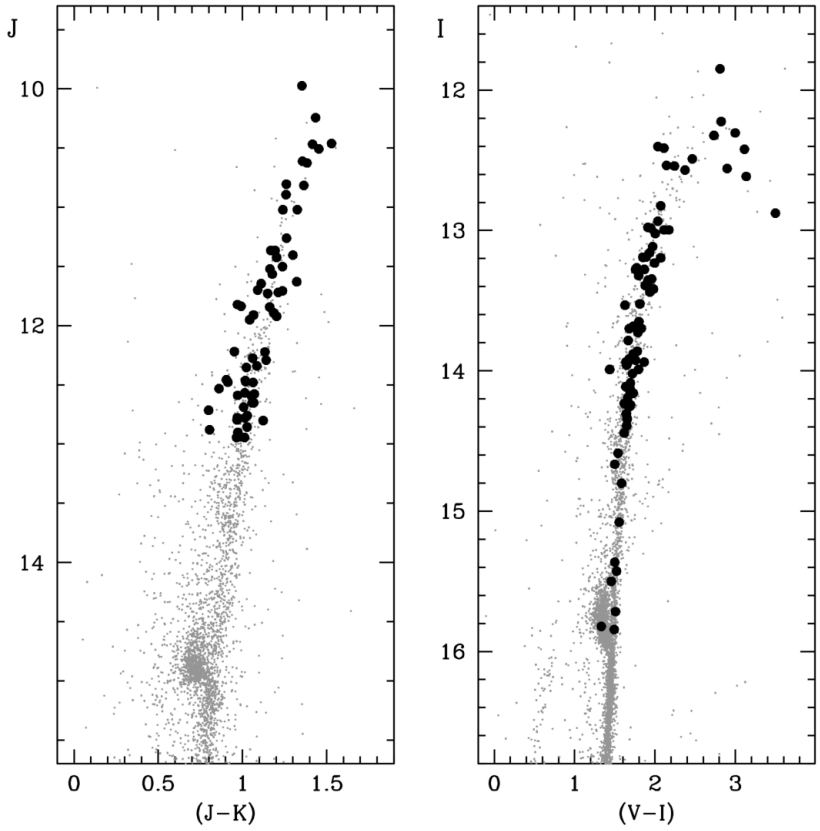

Figure A.3 The $(J, J-K)$ and $(I, V-I)$ color-magnitude diagrams (left and right panels, respectively) of NGC6388, with highlighted the KMOS targets.

We measured a total of 82 giant stars located within $\sim 70''$ from the center of NGC6388. Figure A.3 shows the position of the targets in the the $(I, V-I)$ and $(J, J-K)$ CMDs, while Figure A.4 displays their location in the RA and Dec plane. Identification number, coordinates and magnitudes of each target are listed in Table A.1 (the complete version of the table is available in electronic form). Twelve stars have been observed twice for cross-checking measurements from different pointings/exposures. Seven stars are in common with the FLAMES-VLT radial velocity sample of Lützgendorf et al. (2013, hereafter L13). In a few cases, within a single KMOS IFU we could extract the spectra of more than one

star and measure their radial velocity (see Figure A.2).

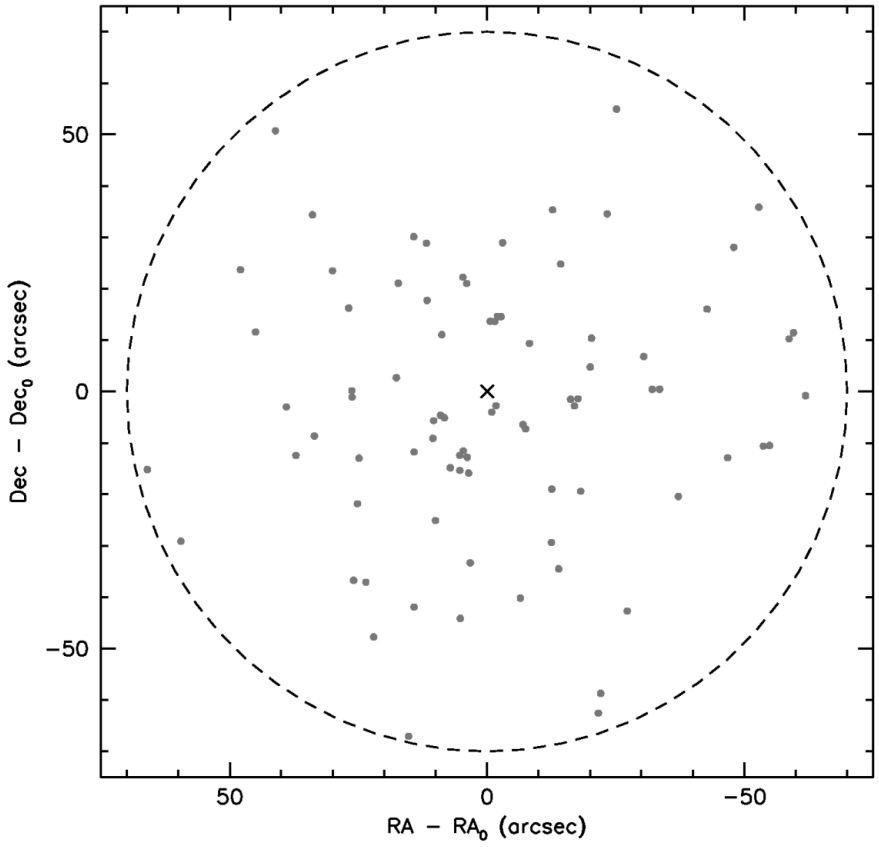

Figure A.4 The position of the observed target (gray circles) in the central region of NGC6388. The black cross marks the center of the cluster as derived in Lanzoni et al. (2007b) while the black annulus marks a region of $70''$ of radius.

A.3 Kinematic analysis

To accurately measure the radial velocities of the observed targets we made use of cross-correlation techniques with template spectra (in particular we used the IRAF task FXCOR). As telluric template we used a high resolution spectrum of the Earth's telluric feature [1], convolved at the KMOS YJ grating resolution. As stellar templates we used synthetic spectra computed with the TURBOSPECTRUM code (Alvarez & Plez, 1998; Plez, 2012), optimized for cool giants. We used a set of average templates with photospheric parameters representative of those of the observed stars and [Fe/H] = –0.5 dex, the metallicity of

[1] Retrieved from `http://www.eso.org/sci/facilities/paranal/decommissioned/isaac/tools/spectroscopic$_$standards.html`.

NGC6388 (see Harris 1996 2010 edition, 2010 edition). For a given star, we also checked the impact of using a different template with varying the temperature by $\Delta T_{eff} \pm 500$ K and the gravity by $\Delta log\ g \pm 0.5$ dex and we verified that it has a negligible effect on the final radial velocity measurements (< 1 km s^{-1}).

A.3.1 Accuracy of the wavelength calibration

With the purpose of quantifying the ultimate accuracy of the radial velocity measurements of individual giant stars in crowded fields, we performed a number of tests aimed at checking the reliability and repeatability of the wavelength calibration of each KMOS IFU. Since KMOS is mounted at a Nasmyth focus and rotates, some flexures are expected, with impact on the overall spatial and especially spectral accuracy of the reconstructed 2D spectra.

The KMOS Data Reduction Software (DRS) pipeline allows to take calibration exposures at several rotator angles and to choose the frames with the rotator angle closest to the one of the input science frame and eventually interpolate. The KMOS DRS pipeline has also the option of refining the wavelength solution by means of the observed OH lines. We reduced the spectra by selecting all these options to obtain the best possible accuracy in the spectral calibration.

However, residual velocity shifts in different spaxels of a given IFU, as well as in different IFUs, are still possible. In order to measure these residual shifts, we selected the spectral region between 1.14 and 1.16 μm (see Figure A.1) containing telluric lines only, and we cross-correlated the observed spectra from five different spaxels in a given IFU with the telluric template. The five spaxels are the ones where the star centroid is located (having the highest signal) and the four surrounding (cross-shape) spaxels. We then computed the residual wavelength/velocity shifts of the four surrounding spaxels with respect to the central one used as reference. As an example, Figure A.5 shows the results for IFU #15: four different stars (#245899, #250977, #198027 and #132259) have been observed in four pointings. The measured zero point shifts are normally well within $\pm$10 km s^{-1}, corresponding to 1/4 of a pixel at the spectral resolution of the KMOS YJ band[2], with average values of a few km s^{-1} and corresponding dispersions within 10 km s^{-1} (see Table A.2). For each IFU, we finally combined the spectra from the five spaxels, by using the IRAF task SCOMBINE, and we measured the radial velocity in the resulting combined one. The obtained values (see Figure A.5) are fully consistent with the average values from individual

[2]At this resolution, one pixel corresponds to ~ 46 km s^{-1}.

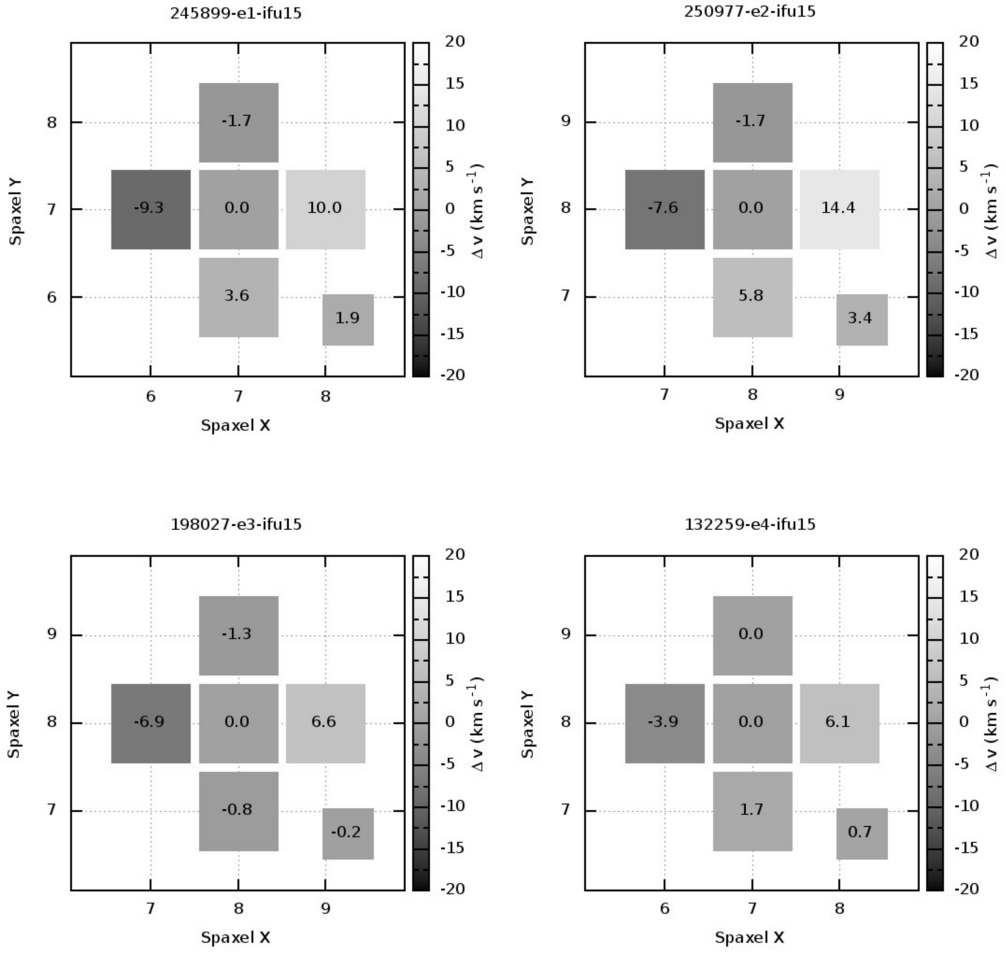

Figure A.5 The spaxel cross-shaped matrixes used in the wavelength calibration test. The matrixes are centered on the brightest spaxel of stars #245899, #198027, #250977 and #132259 observed with the IFU #15 during pointings 1, 2, 3, and 4, respectively. The number marked in each spaxel refers to the velocity shift (in km s^{-1}) with respect to the central spaxel, as measured by cross-correlating telluric lines. The small square in the bottom-right corner of each matrix marks the velocity shift with respect to the central spaxel, as obtained directly from cross-correlating the combined (from the five spaxels in the cross) spectrum.

spaxels (see Table A.2).

For the same four stars observed with IFU # 15, we also used five, isolated stellar lines in two spectral regions centered at 1.06 and 1.20 μm (see Figure A.1) to compute the velocity shifts. Also in this case, for each star we extracted the spectrum of the spaxel with the highest signal and the spectra of the surrounding (cross-shape) spaxels. We cross correlated them with suitable synthetic spectra having photospheric parameters as those of the target stars. The resulting velocity shifts with respect to the central reference spaxel have

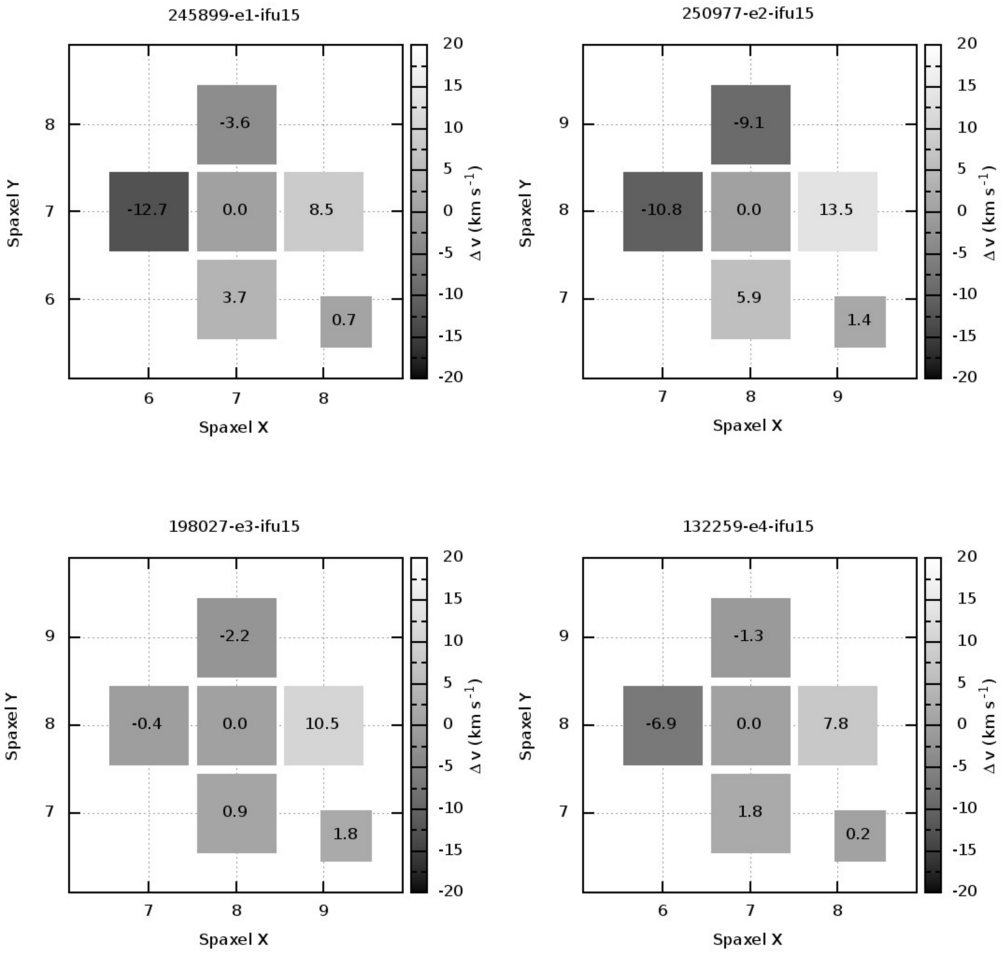

Figure A.6 As in Figure A.5, but for the velocity shifts measured by cross-correlating stellar lines.

been plotted in Figure A.6, while the average values are listed in Table A.2. The inferred average values and dispersions are fully consistent (at better than 1/10 of a pixel) with those obtained measuring the telluric lines. For each star, we finally combined the spectra from the five spaxels as done in the first test and we measured the radial velocity in the resulting spectra. The obtained values (see Figure A.5) are fully consistent with the average values from individual spaxels (see Table A.2), as well as with the shifts measured with the telluric lines.

We repeated the same tests by using other stars observed by different IFUs in different pointings. As an example, Table A.2 also reports the average shifts for other three stars, namely #124271, #325164 and #216954 observed by the IFUs #20, #11 and #2 and

collected during the pointings #1, #2 and #4, respectively. We found values very similar to those derived for the IFU #15, thus ensuring that the overall wavelength calibration provided by the KMOS DRS pipeline is normally accurate and stable in time at a level of a fraction (on average, within 1/10) of a pixel, both within each IFU and among different IFUs.

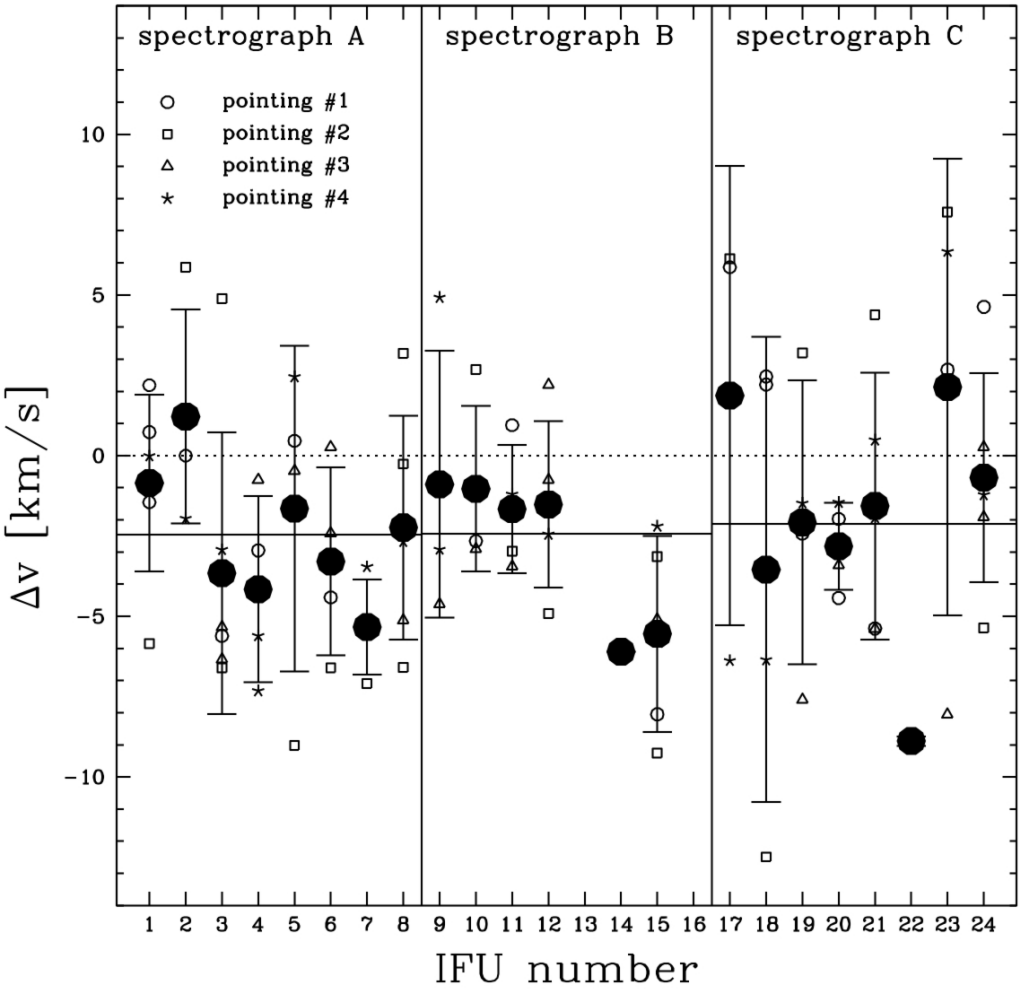

Figure A.7 The telluric velocity shifts (in units of km s^{-1}) of the spectra extracted from the spaxel with highest signal for all the target stars observed with the KMOS IFUs (small symbols). The shifts have been computed by using the telluric template as reference. The large dots mark the average values and the 1σ dispersion as measured for each IFU, while the horizontal, continuum lines mark the average values for each of the three spectrographs. IFUs #13 and #16 were not usable during those observations.

The tests performed so far, by using both telluric and stellar lines, have demonstrated

that the velocity shifts between the spectra extracted from the spaxel with the highest signal and those obtained by combining the spectra from the cross-shape spaxels are fully consistent one to each other, thus we decided to use the spectra of the brightest spaxel only, which is definitely dominated by the target light. Hence, as a final wavelength calibration check, we selected the spectrum corresponding to the spaxel with the highest signal in each observed star. We then cross-correlated this spectrum with the telluric template as reference, and computed the residual velocity shift. Figure A.7 shows the results for the active KMOS IFUs. We find that for a given IFU, the residual velocity shifts as measured in different stars observed during different pointings/exposures are normally consistent to each other with an average dispersion of 3.4 km s^{-1}. Such a dispersion is relatively small, taking into account that the four exposures on NGC6388 were obtained with KMOS at very different rotation angles with respect to the Nasmyth axis (261^{o}, 188^{o}, 326^{o}, and 97^{o} in pointing #1, #2, #3, and #4, respectively), indicating that the KMOS optimized calibration procedure is effective in correcting the effects of spectral flexures.

Since the 24 IFUs of KMOS are managed by three separate spectrographs, one can also compute the mean shift of each spectrograph, by averaging the mean shifts from IFUs #1 to #8, #9 to #16, and #17 to #24, respectively. We find very similar residual velocity shifts, of $\approx$-2 km s^{-1} and dispersion of 3-5 km s^{-1}.

A.3.2 Radial velocity measurements

The tests described in Section A.3.1 indicate that the wavelength calibration provided by the KMOS pipeline is well suited for kinematic studies of extragalactic sources. However, for precise radial velocity measurements of individual stars, it is necessary to refine the calibration, by correcting each spectrum for the corresponding residual velocity shift, as inferred from the telluric lines.

Once corrected for such a residual shift, the radial velocity of each star was computed by cross-correlating the observed spectra with suitable synthetic ones. We finally applied the heliocentric correction by using the IRAF task RVCORRECT. The final radial velocity errors have been computed from the dispersion of the velocities derived from each line divided by the number of lines used (that is $eV_r = \sigma/\sqrt{N_{lines}}$). The average uncertainty in the velocity estimates is 2.9 km s^{-1}.

Figure A.8 shows the inferred radial velocities as a function of the radial distance from the cluster center and the histogram of their distribution. Table A.1 lists the radial velocity

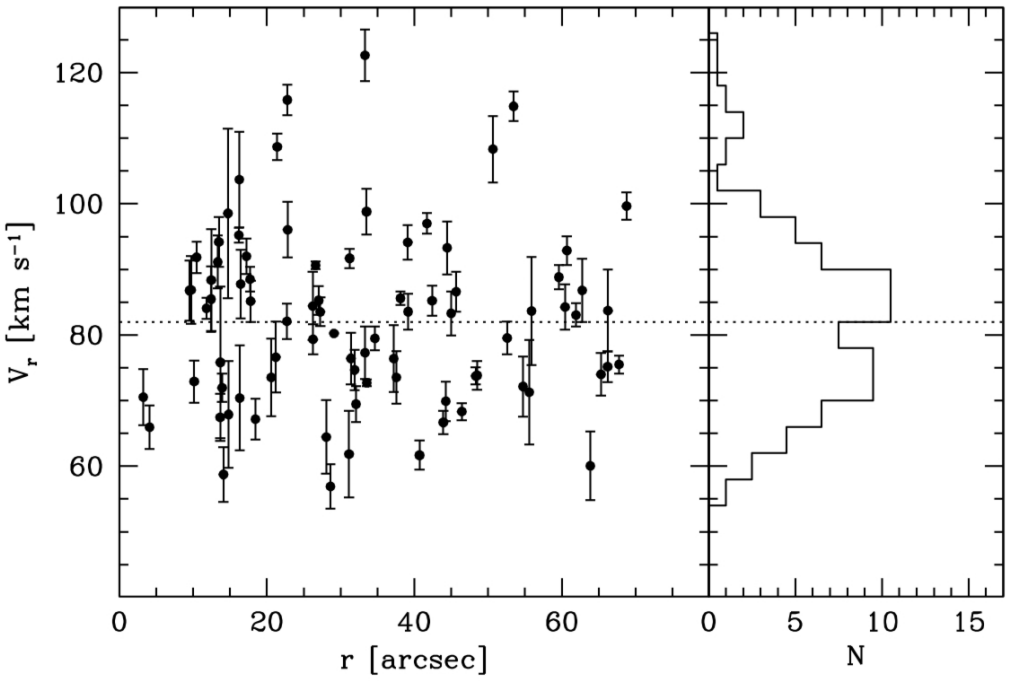

Figure A.8 Radial velocities as a function of the distance from the cluster center (left panel) and histogram of their distribution (right panel), for the 82 stars of NGC6388 observed with KMOS. The dotted line marks the systemic velocity of the cluster (82 km s^{-1}, from L13).

values and corresponding errors, as well as the KMOS IFU and pointing reference numbers. For the twelve stars observed twice, the average value of the measured radial velocities has been adopted. For these stars the measured radial velocities are in excellent agreement, with an average difference of $\sim$ 1 km s^{-1} between two different exposures and a dispersion of 3.6 km s^{-1}.

Only seven stars have been found in common with the FLAMES sample of L13, and the inferred radial velocities from the KMOS spectra turn out to be in good agreement with the FLAMES ones. In fact by applying a $2-\sigma$ rejection criterion, an average difference of $\langle \Delta V_{\rm KMOS-FLAMES} \rangle$ = –0.2 km s^{-1} (σ = 2.2 km s^{-1}) is found.

We computed the systemic velocity of the KMOS sample by conservatively using all stars with radial velocities between 60 and 105 km s^{-1}, as done in L13 for the SINFONI and FLAMES samples. In this velocity range, 75 stars are counted, representing 91% of the entire KMOS sample. We found 81.3 ± 1.5 km s^{-1}, in very good agreement with the value of 82.0 ± 0.5 km s^{-1} found by L13 and indicating that all samples are properly aligned on the same radial velocity scale.

A.3.3 Line-of-sight rotation and velocity dispersion profiles

To compute the projected rotation and VD profiles from the measured radial velocities of individual stars we adopted the same approach described in L13. All the 82 KMOS targets have been considered as cluster members, since they all have radial velocities between 50 and 130 km s^{-1}, which has been adopted as cluster membership criterion in L13.

To study the possible presence of a rotation signal, we restricted the analysis to the sample of targets providing a symmetric coverage of the surveyed area, namely 52 stars located between $9''$ and $40''$ from the centre. For further increasing the sample size, we took into account 6 additional stars in the same radial range from the L13 data-set. We then used the method described in Bellazzini et al. (2012, and references therein; see also L13). No significant rotation signal has been found from this sample. Interestingly, however, the distribution of radial velocities for stars within $20''$ from the cluster centre is clearly bimodal (see Figure A.8), thus suggesting the possible presence of ordered rotation. Unfortunately only 23 stars have been measured within this radial range and more data are needed before drawing any firm conclusion about ordered rotation in the central regions of NGC6388 (see also L13).

To compute the VD profile we used the entire KMOS sample (but the two innermost targets at $r < 5''$ have been conservatively excluded) and divided the surveyed area in three radial bins, each containing approximately the same number of stars: namely $9'' \leq r \leq 23''$ (29 stars), $23'' \leq r \leq 43''$ (26 stars), and $43'' \leq r \leq 70''$ (25 stars). The values obtained are 12.9 ± 2.0 km s^{-1}, at an average distance of $16''$, 12.8 ± 1.9 km s^{-1} at $r = 33''$, and 12.2 ± 1.9 km s^{-1} at $r = 56''$. The errors have been estimated by following Pryor & Meylan 1993. The corresponding profile is plotted in Figure A.9.

A.4 Discussion and conclusions

The velocity dispersion values obtained with KMOS are presented in Figure A.9. We have included for comparison the measurements obtained with SINFONI and FLAMES from L13 and those derived from integrated-light spectra by Lützgendorf et al. (2011). We note that the outermost point of the KMOS VD profile well matches the innermost FLAMES measure of L13. At the same time, the innermost point of the KMOS profile is also consistent with the most external value of Lützgendorf et al. (2011). Overall, the three new KMOS measurements allow us to sample the velocity dispersion profile in the spatial re-

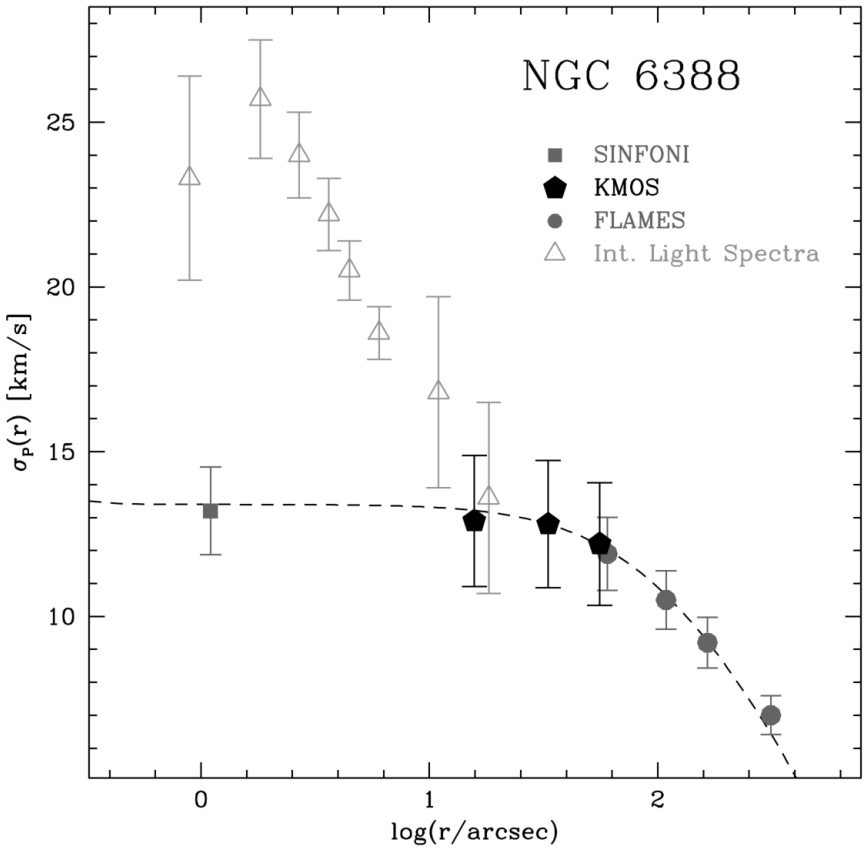

Figure A.9 Line-of-sight velocity dispersion profile of NGC6388 computed from the radial velocities of individual stars, as measured with KMOS (black pentagons, this paper), SINFONI and FLAMES (dark grey squares and circles, respectively; from L13). The dashed line correspond to the self-consistent King model plotted in Figure 13 of L13. The velocity dispersion profile obtained from integrated-light spectra (Lützgendorf et al., 2011) is also shown for comparison (light grey empty triangles).

gion between $9''$ and $70''$, and better define the knee of the distribution around $40''$ from the cluster center.

Unfortunately, both crowding and mechanical constraints did not allow us to allocate more than 1-2 KMOS IFUs per pointing in the very central region, i.e. at $r \leq 9''$. Hence, given the limited amount of observing time during the SV run, only a few stars have been measured in the innermost region, preventing us to compute a precise VD value closer to the center.

The final velocity dispersion profile of NGC6388, obtained from the combination of the entire sample (namely, SINFONI, KMOS and FLAMES spectra) is presented in Table A.3

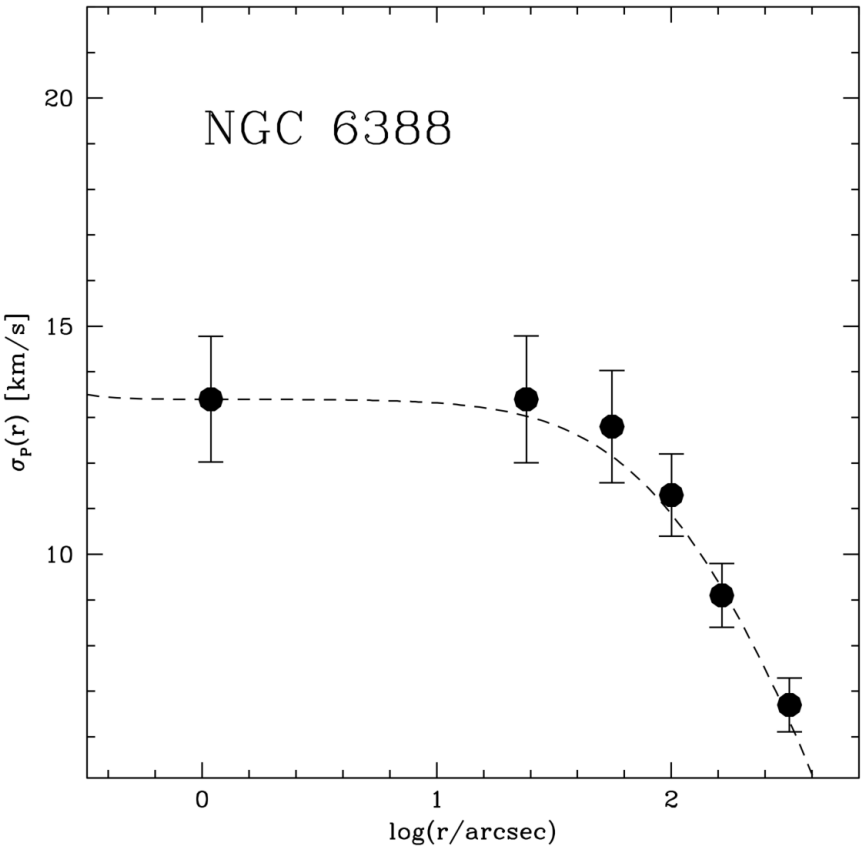

Figure A.10 Final velocity dispersion profile of NGC6388, obtained from the combined sample of individual radial velocities, as measured from SINFONI, KMOS and FLAMES spectra. The dashed line is as in Figure A.9.

and shown in Figure A.10.

The results presented here demonstrate the effectiveness of an IFU facility to perform multi-object spectroscopy of individual stars even in dense stellar systems and at a modest spectral resolution. The KMOS deployable IFU is especially useful in studying the internal kinematics of GCs for a number of reasons: 1) it allows to sample stars over a rather large and tunable field of view, according to the cluster central density and extension; 2) it allows to measure individual stars and their surroundings, avoiding slit losses and best-accounting for possible blending effects due to crowding and unresolved stellar background; 3) it covers a rather wide spectral range in a single exposure, to simultaneously record stellar features and telluric lines, and measure accurate radial velocities even at a spectral resolution R $\approx$3000.

Table A.1. Individual giant stars in NGC6388 observed with KMOS.

star #	RA (2000)	Dec (2000)	V	I	J	K	V_r	eV_r	IFU #	pointing
28786	264.0777424	-44.7539232	15.12	13.32	11.91	10.84	99.7	2.1	18	4
43138	264.0633117	-44.7526742	15.85	14.19	12.90	11.93	75.2	2.4	23	1
43163	264.0631292	-44.7516067	15.64	13.86	12.48	11.42	86.8	4.8	4,19	2,3
78741	264.0976030	-44.7395056	14.94	12.57	10.81	9.54	75.5	1.4	1,11	2,3
81865	264.0950571	-44.7433792	15.94	14.25	12.78	11.81	83.7	6.2	10	3
93646	264.0870297	-44.7361283	15.40	13.42	11.92	10.72	94.1	2.6	6	1
94946	264.0863051	-44.7387495	15.09	13.12	11.57	10.39	83.5	2.8	5	1
96560	264.0849040	-44.7377027	14.52	12.41	10.89	9.63	79.5	1.8	2	2
100296	264.0711060	-44.7360611	15.80	13.94	11.63	10.31	70.5	4.3	3	3
101667	264.0820265	-44.7355902	16.16	14.67	0.00	0.00	84.4	5.2	3	2

Note. — Identification number, coordinates, optical and NIR magnitudes, radial velocities (V_r) and errors (eV_r) in km s^{-1}, KMOS IFU and pointing numbers (two values are marked for the twelve targets observed twice). The full table is available in the online version of the paper.

Table A.2. Results of the wavelength calibration tests.

star #	$\langle \Delta v_{cross}^{telluric} \rangle$	$\langle \Delta v_{cross}^{stellar} \rangle$	IFU #	pointing
245899	$+0.7(8.2)$	$-1.0(9.2)$	15	1
250977	$-0.6(5.5)$	$+2.2(5.7)$	15	2
198027	$+2.7(9.5)$	$-0.1(11.8)$	15	3
132259	$+1.0(4.1)$	$+0.3(7.1)$	15	4
124271	$+0.3(8.2)$	$+0.7(9.7)$	20	1
325164	$+0.4(8.2)$	$+1.3(11.5)$	11	2
216954	$-0.1(5.7)$	$-0.5(7.8)$	2	4

Note. — Average velocity shifts and dispersion (in bracket) among different spaxels distributed in cross-shaped matrixes, with respect to the reference central spaxel. Velocity in km s^{-1}.

Table A.3. Velocity dispersion profile of NGC6388

r_i	r_e	r_m	$N_\star$	σ_P	e_{σ_P}
0.2	1.9	1.1	51	13.40	1.38
9.0	40.0	24.1	58	13.40	1.39
40.0	75.0	55.9	57	12.80	1.23
75.0	130.0	100.2	81	11.30	0.90
130.0	210.0	164.2	84	9.10	0.70
210.0	609.0	318.8	67	6.70	0.59

Note. — The final profile has been obtained from the combined sample of SINFONI, KMOS and FLAMES spectra. The three first columns give the internal, external and mean radii (in arcseconds) of each considered radial bin (r_m is computed as the average distance from the centre of all the stars belonging to the bin), $N_\star$ is the number of star in the bin, σ_P and e_{σ_P} are the velocity dispersion and its rms error (in km s^{-1}), respectively.

Appendix B

Lines and Continuum Sky Emission in the Near Infrared: Observational Constraints from Deep High Spectral Resolution Spectra with GIANO-TNG

Published in Oliva et al. 2015, A&A, 581, A47

Aim - Determining the intensity of lines and continuum airglow emission in the H-band is important for the design of faint-object infrared spectrographs. Existing spectra at low/medium resolution cannot disentangle the true sky-continuum from instrumental effects (e.g. diffuse light in the wings of strong lines). We aim to obtain, for the first time, a high resolution infrared spectrum deep enough to set significant constraints on the continuum emission between the lines in the H-band.

Methods - During the second commissioning run of the GIANO high-resolution infrared spectrograph at the La Palma Observatory, we pointed the instrument directly to the sky and obtained a deep spectrum that extends from 0.97 to 2.4 μm.

Results - The spectrum shows about 1500 emission lines, a factor of two more than in previous works. Of these, 80% are identified as OH transitions; half of these are from highly excited molecules (hot-OH component) that are not included in the OH airglow emission models normally used for astronomical applications. The other lines are attributable to O_2 or unidentified. Several of the faint lines are in spectral regions that were previously believed to be free of line emission. The continuum in the H-band is marginally detected

at a level of about 300 photons/m^2/s/arcsec^2/μm, equivalent to 20.1 AB-mag/arcsec^2. The observed spectrum and the list of observed sky-lines are published in electronic format.

Conclusions - Our measurements indicate that the sky continuum in the H-band could be even darker than previously believed. However, the myriad of airglow emission lines severely limits the spectral ranges where very low background can be effectively achieved with low/medium resolution spectrographs. We identify a few spectral bands that could still remain quite dark at the resolving power foreseen for VLT-MOONS (R$\simeq$6,600).

B.1 Introduction

The sky emission spectrum at infrared wavelengths and up to 1.8 μm (Y, J, H bands) is dominated by lines (airglow) emitted by OH and O_2 molecules; see e.g. Sharma (1985). These lines are intrinsically very narrow and, when observed at a high enough spectral resolution, they occupy only a small fraction of the spectrum. Therefore, by filtering the lines out, one could in principle decrease the sky background by orders of magnitudes, down to the level set by the sky continuum emission in between the lines. This apparently simple idea, often reported as "OH sky-suppression", has fostered a long and active field of research; see e.g. Oliva & Origlia (1992), Maihara et al. (1993), Herbst et al. (1994), Content et al. (1996), Ennico et al. (1998), Cuby et al. (2000), Rousselot et al. (2000), Iwamuro et al. (2001), Bland-Hawthorn et al. (2004), Iwamuro et al. (2006), Ellis et al. (2012), Trinh et al. (2013). However, in spite of the intense work devoted to measuring and modelling the properties of the sky spectrum, it is still not clear what is the real level of the sky continuum in between the airglow lines in the H-band (1.5-1.8 μm).

A detailed study of the infrared sky continuum emission was recently reported by Sullivan & Simcoe (2012). Using spectra at a resolving power R=6,000 they were able to correct the spectra for all instrumental effects and derive accurate measurements of the sky continuum at wavelengths shorter than 1.3 μm (Y, J bands). However, they could not obtain precise results in the H-band (1.5-1.8 μm) because the sky continuum is well below the light diffused in the instrumental wings of the airglow lines. This problem was already noted in earlier works. In particular, Bland-Hawthorn et al. (2004) claimed that the continuum level between the OH lines could be as low as the zodiacal light level and much lower than that measurable with classical (i.e. not properly OH suppressed) spectrographs. This claim was later retracted by Ellis et al. (2012) after measuring the interline contin-

uum with an optimised OH-suppression device based on a Bragg fibre grating. Trinh et al. (2013) subsequently attempted to model the interline continuum based on spectral models and measurements that did not reach the depth and completeness of the data presented in this paper.

The net - and somewhat surprising - result is that so far nobody has been able to improve the earliest measurements of Maihara et al. (1993) who reported a continuum emission of 590 photons/m^2/s/arcsec^2/μm measured at 1.665 μm (equivalent to 19.4 AB-mag/arcsec^2) using a spectrometer with resolving power R=17,000, equipped with one of the first-generation 256^2 HgCdTe infrared detectors

A proper understanding of the line and continuum emission from the sky is of fundamental importance when designing new infrared spectrographs optimised for observations of very faint targets. A representative case is that of MOONS, the multi-objects optical and near infrared spectrometer for the VLT, see Cirasuolo et al. (2011, 2014). This instrument includes an arm covering the H-band at a resolving power R$\simeq$6,600. The requirements on instrumental background and stray light strongly depend on the sky continuum one assumes, see Li Causi et al. (2014) for details.

In a previous work (Oliva et al., 2013) we presented, for the first time, observations of the infrared sky spectrum at high spectral resolution and covering a very wide spectral range. The spectrum revealed 750 emission lines, many of these never reported before. However, the data were not deep enough to provide significant constraints on the continuum emission in between the lines.

Here we present and discuss new measurements taken with GIANO during the second commissioning run at Telescopio Nazionale Galileo (TNG). In Section B.2 we briefly describe the instrument, the measurements, and the data reduction. In Sections B.3 and B.4 we present and discuss the results.

B.2 Observations and spectral analysis

GIANO is a cross-dispersed cryogenic spectrometer that simultaneously covers the spectral range from 0.97 μm to 2.4 μm with a maximum resolving power of R$\simeq$50,000 for a 2-pixels slit. The main disperser is a commercial R2 echelle grating with 23.2 lines/mm that works on a $\oslash$100 mm collimated beam. Cross dispersion is performed by prisms (one made of fused silica and two made of ZnSe) that work in double pass. The prisms cross-disperse

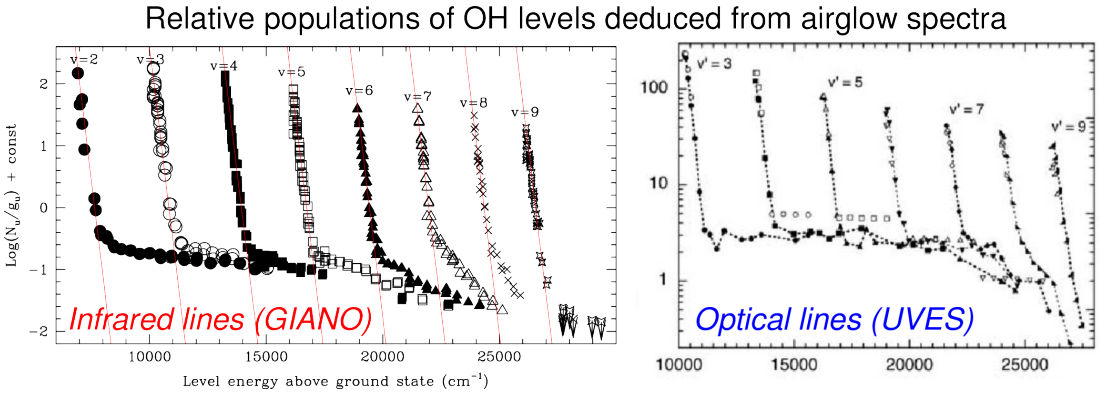

Figure B.1 Derived column densities of the OH levels plotted against the energy of the levels above the ground-state of the molecule. The left panel shows the values derived from the infrared lines discussed here while the right hand panel – reproduced under permission from Figure 16 of Cosby et al. (2007); © Canadian Science Publishing or its licensors – summarizes the results based on optical (UVES) spectra. The steep straight lines in the left panel show the distribution predicted by standard models with rotational levels thermalised at 200 K. The quasi-flat tails reveal the hot-OH component, see Section B.3.1 for details.

the light both before and after it is dispersed by the echelle gratings; this setup produces a curvature of the images of the spectral orders. The detector is a HgCdTe Hawaii-II-PACE with 2048^2 pixels. Its control system is extremely stable with a remarkably low read-out noise (see Oliva et al., 2012b). More technical details on the instrument can be found in Oliva et al. (2012a) and references therein.

GIANO was designed and built for direct light feeding from the TNG 3.5 m telescope. Unfortunately, the focal station originally reserved was not available when GIANO was commissioned. Therefore we were forced to position the spectrograph on the rotating building and develop a complex light-feed system using a pair of IR-transmitting ZBLAN fibres with two separate opto-mechanical interfaces. The first interface is used to feed the telescope light into the fibres; it also includes the guiding camera and the calibration unit. The second interface re-images the light from the fibres onto the cryogenic slit; see Tozzi et al. (2014) for more details.

The overall performances of GIANO are negatively affected by the complexity of the interfaces and by problems intrinsic to the fibres: the efficiency has been lowered by almost a factor of 3 and the spectra are affected by modal-noise, especially at longer wavelengths. Consequently, the observations of the sky taken during normal operations are not appropriate to reveal the faintest airglow lines and the continuum emission in between. To overcome this problem we took advantage of the early part of a test night (September 3, 2014) to

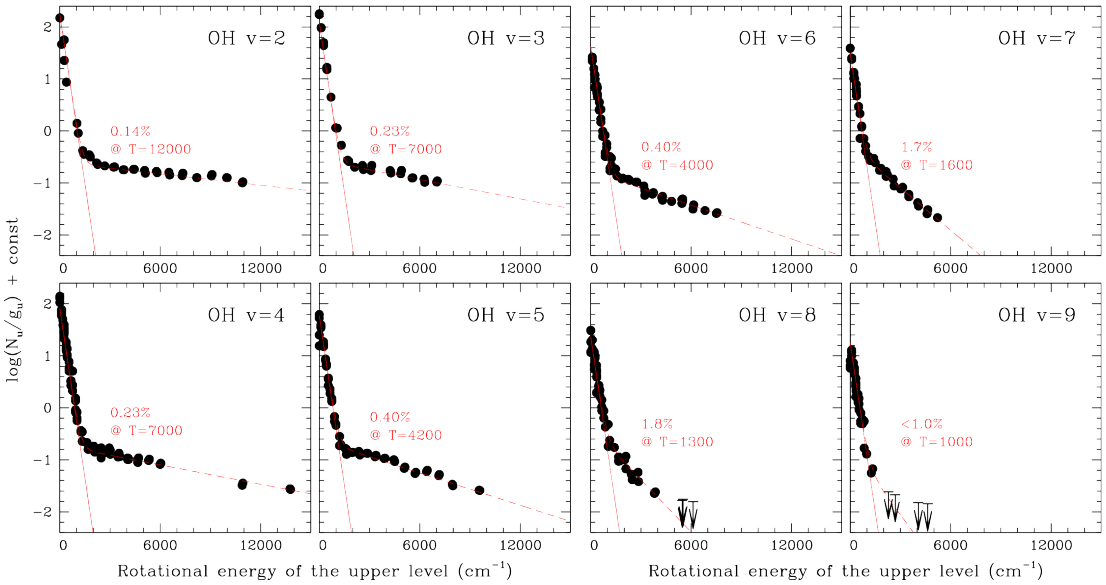

Figure B.2 Same as Figure B.1 but with separate panels for each vibrational level. The straight solid lines represent the cold-OH component while the dashed curves show the distribution obtained adding a fraction of hot-OH molecules. The numerical fraction and rotational temperature of the hot-OH molecules is reported within each panel. See text, Section B.3.1 for details.

secure a direct spectrum of the sky with GIANO. We moved the spectrograph to the main entrance of the TNG and arranged a simple pre-slit system (a lens doublet and two flat mirrors) to feed the cryogenic slit with the light from a sky-area in the ESE quadrant at a zenith distance of about 25 degrees. The half moon was in the SSW quadrant at a zenith distance of 50 degrees.

We integrated the sky for two hours using the 3-pixels slit that is normally used in combination with the fibre interface. This yields a resolving power R$\simeq$32,000. For calibration we took several long series of darks interspaced with flat frames. This strategy was chosen because the sky spectra showed some residuals (persistency) of a flat frame taken many hours before. We therefore re-created different pseudo-darks with different levels of persistency and, during the reduction, we selected the combination of pseudo-darks that best reproduced the persistency pattern. The criterion for selection relied on the assumption that the sky continuum emission is zero in the spectral regions were the atmosphere is opaque, i.e. in the 1.37-1.40 μm range (orders 54-56 of the GIANO echellogram). In other words, we took advantage of the fact that the flat and its residual persistency have similar intensities over the full spectral range, while the spectrum of any light source above the troposphere (i.e. astronomical targets and the sky airglow emission) is absorbed by the water bands.

The acquisitions were performed using the standard setup of the controller, i.e. on chip integrations of 5 minutes with multiple non-destructive read-outs every 10 seconds. All the read-outs were separately stored. The "ramped-frames" were constructed later-on using the algorithm described in Oliva et al. (2012b) that, besides applying the standard Fowler sampling, it also minimises the effects of reset-anomaly and cosmic rays.

The 1D spectra were extracted by summing 20 pixels along the slit. Wavelength calibration was performed using U-Ne lamp frames taken after the series of darks. The spectrometer is stable to <0.1 pixels (i.e. $\Delta\lambda/\lambda < 10^{-6}$ r.m.s.). The wavelengths of the uranium lines were taken from Redman et al. (2011), while for neon we used the table available on the NIST website[1]. The resulting wavelength accuracy was about 0.07 Å r.m.s. for lines in the H-band.

The flat exposures were used to determine and correct the variation of instrumental efficiency within each order. An approximate flux calibration was performed by assuming that the relative efficiencies of the orders are the same as when observing standard stars through the fibre-interface and the TNG telescope. This is a very reasonable assumption within the relatively narrow wavelength range covered by the H-band. However, it may cause systematic errors (up to 0.3 dex) in the relative fluxes of lines with very different wavelengths. Absolute flux calibration was roughly estimated by imposing that the flux of the OH [4-0]Q1(1.5) line at 1.5833 μm is 270 photons/m^2/s/arcsec^2; i.e. the typical value measured during normal observing nights.

B.3 The sky lines and continuum emission

A total of about 1500 airglow lines were detected in the spectrum. Compared to Paper 1, we have doubled the number of emission features measured. In the following we separately discuss the OH lines, the other emission features and the continuum emission in the Y, J, and H bands.

B.3.1 OH lines and the hot-OH component

Table 1 (available only in electronic format) lists the lines identified as OH transitions. For each Λ-doublet we give the wavelengths (in vacuum) and the total observed flux of the doublet, normalised to the brightest transition. For the fluxes we assumed that the two components of each doublet have equal intensities, i.e. that the 'e' and 'f' sub-levels are in

[1] physics.nist.gov/PhysRefData/ASD/lines_form.html

thermal equilibrium; this is appropriate for the density and temperature of the mesosphere. The listed wavelengths are derived from the newest OH molecular constants by Bernath et al. (2009). These include highly excited rotational states and allowed us to identify OH lines from rotational levels as high as J=22.5, thus adding important constraints on the hot component of OH emission. This component was already reported by Cosby et al. (2007) and in Paper 1. It is not included in any of the models of OH airglow emission normally used for astronomical applications. These assume that the OH molecules have a very high vibrational temperature ($T_{vib} \simeq 9000$ K) and a much lower rotational temperature ($T_{rot} \simeq 200$ K). In other words they assume that the gas density is high enough to make collisional transitions between rotational states much faster than radiative de-excitations. This brings the rotational temperature to values similar to the kinetic temperature of the gas. The net result is that all the lines from levels with rotational quantum number J>8.5 are normally predicted to be extremely faint and totally negligible. The number of lines that are missed by standard models can be directly visualised in Figure B.1 that plots the column densities of the upper levels of the measured lines as a function of the excitation energy of the levels. The steep lines show the distribution expected for a single gas component with rotational levels thermalised at T=200 K. The points in the quasi-flat tails represent emission lines from hot molecules that are not thermalised. According to Cosby et al. (2007), this hot component is related to low density clouds at higher altitudes. Here the gas density is lower than the critical density of the rotational levels and, therefore, the population of the levels remain similar to that set at the moment the OH molecule is formed.

In order to provide a practical tool to predict the intensities of all OH lines we have fitted the observed level distribution with a mixture of two components. The first is the standard model (cold-OH), while the second (hot-OH) has a rotational temperature that is empirically determined from the observed values. Each vibrational state must be separately fit to obtain a good matching.

This simple model works as follows: let N_u (cm^{-2}) be the column density of a given state (v, J, F) of the OH molecule. This quantity is related to the excitation temperatures by the standard Boltzmann equations, i.e.

$$\frac{N_u}{g_u N_{OH}} = e^{-E_v/kT_v} \quad \left[\eta_{rc} \frac{e^{-E_{J,F}/kT_{rc}}}{U(T_v, T_{rc})} + \eta_{rh} \frac{e^{-E_{J,F}/kT_{rh}}}{U(T_v, T_{rh})} \right] \tag{1}$$

where g_u is statistical weight of the level, N_{OH} is the total column density of OH molecules, E_v is the vibrational energy of the level, T_v is the vibrational temperature, $E_{J,F}$ is the

rotational energy of the level, T_{rc} is the rotational temperature of the cold component, η_{rc} is the fraction of cold molecules, T_{rh} is the rotational temperature of the hot component, η_{rh} is the fraction of hot molecules and $U(T_v, T_r)$ is the partition function. The photon-flux of a given transition arising from the same level is given by

$$I_{ul} = N_u \cdot A_{ul} \tag{2}$$

where A_{ul} (s^{-1}) is the transition probability. The points in Figures B.1, B.2 are computed from Eq. (2) using the observed line intensities together with the molecular parameters of Bernath et al. (2009) and the transition probabilities of van der Loo et al. (2007). The steep straight lines in the left panel of Figure B.1 plot the function defined in Eq. (1) for T_v=9000 K, T_{rc}=200 K and η_{rc}=1 (i.e. only cold-OH). The same function is displayed in Figure B.2 where the dashed curves show the results obtained adding a hot-OH component with parameters (η_{rh},T_{rh}) adjusted for each vibrational level; the values of the parameters are indicated in each panel.

The hot-OH component is most prominent in the lowest vibrational state (v=2) and becomes progressively weaker and cooler going to higher vibrational states; it virtually disappears at v=9.

B.3.2 O_2 and unidentified lines

The lines that cannot be associated with OH transitions are listed in Table 2 (this table is available only in electronic format). For the identification of the O_2 lines we used the HITRAN database (Rothman et al., 2009). Most of the identified transitions were already reported in Paper 1. A comparison between the two spectra shows that the intensity ratio between O_2 and OH lines has varied by almost a factor of 2 between the two epochs. This is not surprising: the Oxygen lines are known to vary by large factors even on timescales of hours. In our case the variation can be used to select those features that follow the time-behaviour of the O_2 lines. These lines are identified as "O2?" (i.e. probably O_2) in Table 2.

The remaining features are not identified. Of these 34 lines are closely spaced doublets with equal intensities. A representative example are the lines at $\lambda\lambda$17164.5, 17165.5 Å visible in the lower-right panel of Figure B.3. Several of these features were already detected in Paper 1.

They are very similar to other Λ-split OH doublets detected in our spectra. However, their wavelengths do not correspond to any OH transition with $J_u \leq 40.5$ and $v_u \leq 10$.

The possibility that these doublets are produced by OH isotopologues (e.g. ^{18}OH) should be investigated, but is beyond the aims of this paper.

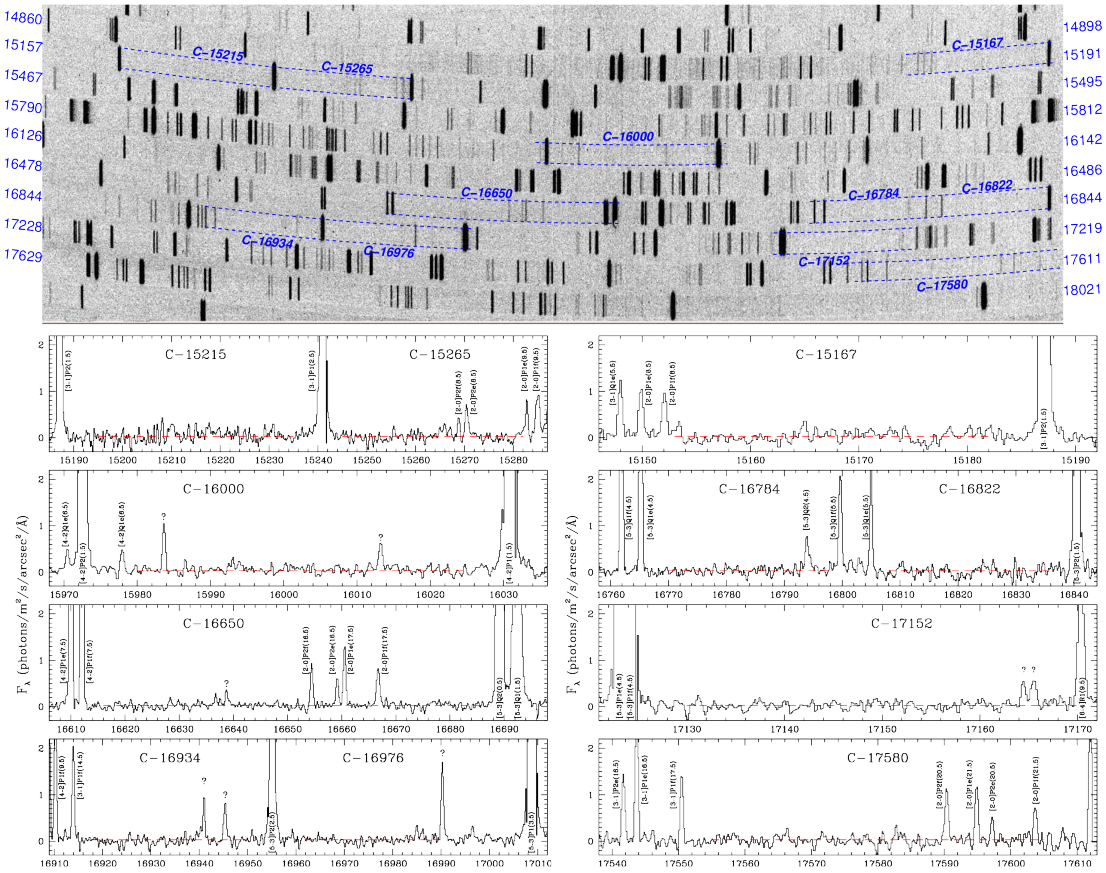

Figure B.3 Upper panel: GIANO echelle spectrum of the H atmospheric band. Lower panels: extracted spectra in regions relatively free of line emission. The horizontal dashed lines show the level of 300 photons/m^2/s/arcsec^2/μm (equivalent to 20.1 AB-mag/arcsec^2).

B.3.3 The sky continuum emission

Within the H-band (1.5–1.8 μm) we detected:

- 514 lines of OH, half of which are produced by the hot-OH component described in Section B.3.1;
- 41 lines of O_2, including two broad and prominent band-heads;
- 79 unidentified features.

Finding spectral regions free of emission features and far from bright airglow lines is already difficult in our spectra. It becomes virtually impossible at the lower resolving powers

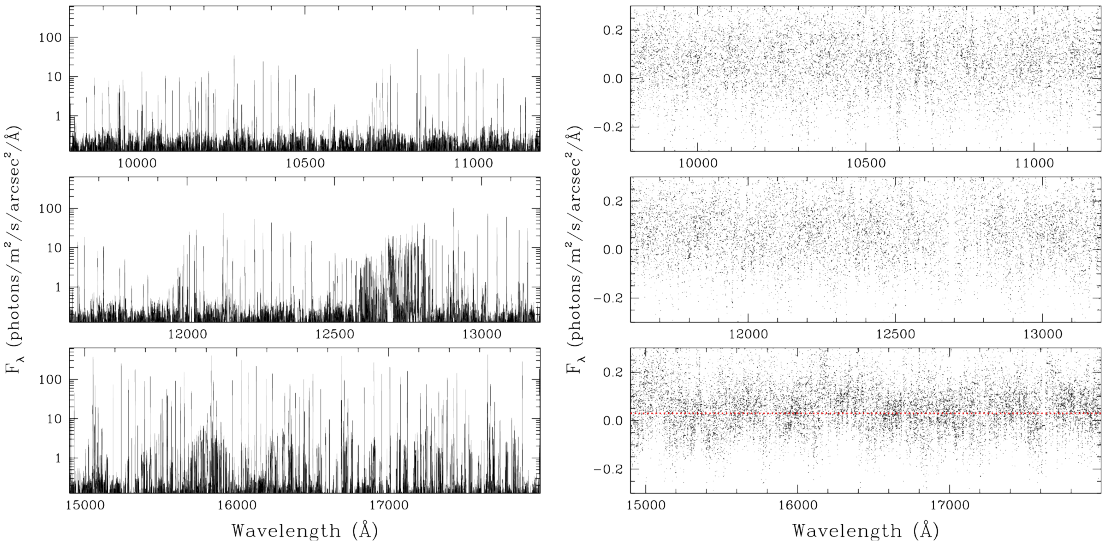

Figure B.4 Left-hand panel: overview of the GIANO spectrum of the airglow. Right-hand panel: downscale to low flux levels. The spectral measurements are shown as separate dots to avoid confusion. The horizontal dashed line in the lowest panel shows the level of 300 photons/m^2/s/arcsec^2/μm (equivalent to 20.1 AB-mag/arcsec^2).

foreseen for MOONS (R$\simeq$6,600) and other faint-object IR spectrometers. In Figure B.3 we show the observed 2D echellogram of GIANO and the extracted 1D spectra of selected regions with relatively low contamination from lines. Their main parameters are listed in Table B.3. They were selected with the following criteria:

- The width of the band must correspond to at least 10 resolution elements of MOONS (i.e. $\Delta\lambda/\lambda > 1/660$)
- The band must include only faint lines whose total flux, averaged over the band-width, is less than 500 photons/m^2/s/arcsec^2/μm (equivalent to 19.6 AB-mag/arcsec^2).

The broadest band is C-16650. It coincides with the region used by Maihara et al. (1993) to measure an average sky-continuum of 590 photons/m^2/s/arcsec^2/μm (equivalent to 19.4 AB-mag/arcsec^2). We find that about 65% of this flux can be ascribed to five emission features (4 lines from hot-OH and one unidentified, see Figure B.3) that lie close to the centre of this band. Taken at face value, this would imply that the true continuum is $\simeq$200 photons/m^2/s/arcsec^2/μm (equivalent to 20.6 AB-mag/arcsec^2). However, this number is affected by large uncertainties intrinsic to the procedure used to extract/average the continuum level from the spectrum and to variations of the sky lines between different epochs. Indeed, to reach a more reliable conclusion one would should re-analyse the raw data of

Table B.3 Spectral bands with low contamination from lines.

Band	λ-range (Å)	$\Delta\lambda/\lambda$	Lines Flux(1)
C-15167	15153 – 15183	0.0020	0.6 (210 ; 20.5)
C-15215	15195 – 15235	0.0026	–
C-15265	15245 – 15285	0.0026	1.6 (400 ; 19.8)
C-16000	15980 – 16020	0.0025	1.2 (320 ; 20.0)
C-16650(2)	16620 – 16680	0.0036	2.3 (380 ; 19.9)
C-16784	16770 – 16798	0.0017	0.5 (170 ; 20.7)
C-16822	16808 – 16836	0.0017	–
C-16934	16918 – 16950	0.0019	1.3 (390 ; 19.8)
C-16976	16962 – 16990	0.0016	1.0 (360 ; 19.9)
C-17152	17134 – 17170	0.0021	0.7 (190 ; 20.6)
C-17580	17555 – 17605	0.0028	2.2 (430 ; 19.7)

(1) First entry is the lines flux in photons/m^2/s/arcsec^2. Numbers in brackets are the equivalent continuum flux (i.e. the line flux averaged over the band-width) in photons/m^2/s/arcsec^2/μm and in AB-mag/arcsec^2.
(2) Region used by Maihara et al. (1993) to define the sky-continuum

Maihara et al. (1993) and correct them for the contribution of the sky-emission lines before computing the continuum level.

We attempted to measure the sky continuum emission using the extracted GIANO spectrum. This spectrum is shown in Figure B.4 and listed in Table 4 (available only in electronic format). The H-band has enough S/N ratio to show a faint continuum of about 300 photons/m^2/s/arcsec^2/μm (equivalent to 20.1 AB-mag/arcsec^2); this level is shown as a dashed line in the figure. It corresponds to 5 e$^-$/pixel/hr at the GIANO detector. A formal computation of noise (i.e. including read-out, dark-current and photon statistics) yields a convincing 5σ detection once the spectrum is re-sampled to a resolving power of R=5,000. The contribution by systematic errors is more difficult to estimate. On the one hand, the procedure used to subtract detector dark and persistency (see Section B.2) has correctly produced a zero continuum in the bands where the atmosphere is opaque (the uppermost order in the 2D frame of Figure B.3). On the other hand, however, we cannot exclude that second order effects have left some residual instrumental artifacts in the H-band. An analysis of the dark frames affected by persistency indicates that second order effects tend to increase the residuals, rather than over-subtracting the residual continuum level in the H-band. Therefore, we are reasonably confident that the true sky-continuum cannot be larger than the observed value.

In the Y and J bands our spectra have a lower S/N ratio because the efficiency of the GIANO detector drops at shorter wavelengths. The measured upper limits correspond to about 19 AB-mag/arcsec^2 and are compatible with the measurements by Sullivan & Simcoe (2012). In general, the Y and J bands are much less contaminated by line emission and the higher resolving power of GIANO is no longer needed to find spectral regions that properly sample the sky continuum.

B.4 Discussion and conclusions

We took advantage of the second commissioning of the GIANO high-resolution infrared spectrograph at La Palma Observatory to point the instrument directly to the sky. This yielded a sky spectrum much deeper than those collected through the fibre-interface to the TNG telescope and published in Oliva et al. (2013). The spectrum extends from 0.97 to 2.4 μm and includes the whole Y, J, and H-bands.

The spectrum shows about 1500 emission lines, a factor of two more than in previous works. Of these, 80% are identified as OH transitions while the others are attributable to O_2 or unidentified. Roughly half of the OH lines arise from highly excited rotational states, presumably associated with lower density clouds at higher altitudes. We derive physical parameters useful to model this hot-OH component that as yet has never been included in the airglow models used by astronomers.

Several of the faint lines are in spectral regions that were previously believed to be free of lines emission. The continuum in the H-band is marginally detected at a level of about 300 photons/m^2/s/arcsec^2/μm equivalent to 20.1 AB-mag/arcsec^2. In spite of the very low sky-continuum level, the myriad of airglow emission lines in the H-band severely limits the spectral ranges that can be properly exploited for deep observations of faint objects with low/medium resolution spectrographs. We have identified a few spectral bands that could still remain quite dark at the resolving power foreseen for the faint-object spectrograph VLT-MOONS (R=6,600).

The spectrum and the updated lists of observed infrared sky-lines are published in electronic format.

Bibliography

Abia, C., Cunha, K., Cristallo, S., et al. 2011, ApJL, 737, L8

Alessandrini, E., Lanzoni, B., Miocchi, P., Ciotti, L., & Ferraro, F. R. 2014, ApJ, 795, 169

Aller, L. H., & Greenstein, J. L. 1960, ApJS, 5, 139

Alonso, A., Arribas, S., & Martínez-Roger, C. 1999, A&AS, 140, 261

Alvarez, R., & Plez, B. 1998, A&A, 330, 1109

Alves-Brito, A., Barbuy, B., Ortolani, S., et al. 2005, A&A, 435, 657

Alves-Brito, A., Schiavon, R. P., Castilho, B., & Barbuy, B. 2008, A&A, 486, 941

Anderson, J., & van der Marel, R. P. 2010, ApJ, 710, 1032

Andrievsky, S. M., Spite, M., Korotin, S. A., et al. 2008, A&A, 481, 481

Andrievsky, S. M., Spite, M., Korotin, S. A., et al. 2010, A&A, 509, A88

Arlandini, C., Käppeler, F., Wisshak, K., et al. 1999, ApJ, 525, 886

Arnett, W. D. 1978, ApJ, 219, 1008

Arnould, M., Goriely, S., & Takahashi, K. 2007, Phys. Rep., 450, 97

Asplund, M. 2005, ARA&A, 43, 481

Bailyn, C. D., & Pinsonneault, M. H. 1995, ApJ, 439, 70

Barbuy, B., Bica, E., & Ortolani, S. 1998, A&A, 333, 117

Barklem, P. S., Piskunov, N., & O'Mara, B. J., 2000, A&AS, 142, 467

Barklem, P. S., Christlieb, N., Beers, T. C., et al. 2005, A&A, 439, 129

Bastian, N., Lamers, H. J. G. L. M., de Mink, S. E., et al. 2013, MNRAS, 436, 2398

Bastian, N., Cabrera-Ziri, I., & Salaris, M. 2015, MNRAS, 449, 3333

Bastian, N., & Lardo, C. 2015, MNRAS, 453, 357

Baumgardt H., Makino J., Hut P., 2005, ApJ, 620, 238

Beccari, G., Ferraro, F. R., Lanzoni, B., & Bellazzini, M. 2006, ApJL, 652, L121

Bedin, L. R., Piotto, G., Anderson, J., et al. 2004, ApJL, 605, L125

Bellazzini, M., Ferraro, F. R., & Buonanno, R. 1999, MNRAS, 307, 619

Bellazzini, M., Ibata, R. A., Chapman, S. C., et al. 2008, AJ, 136, 1147

Bellazzini, M., Bragaglia, A., Carretta, E., et al. 2012, A&A, 538, A18

Bensby, T., Feltzing, S., & Lundström, I. 2003, A&A, 410, 527

Bensby, T., Feltzing, S., Lundström, I., & Ilyin, I. 2005, A&A, 433, 185

Bergbusch, P. A., & Stetson, P. B., 2009, AJ, 138, 1455

Bergemann, M., Lind, K., Collet, R., Magic, Z. & Asplund, M., 2012, MNRAS, 427, 27

Bergemann, M., & Nordlander, T. 2014, arXiv:1403.3088

Bernath, P. F., & Colin, R. 2009, J. Mol. Spec., 257, 20

Bertaux, J. L., Lallement, R., Ferron, S., Boonne, C., & Bodichon, R. 2014, A&A, 564, 46

Bessell, M. S. 1979, PASP, 91, 589

Binney, J., & Tremaine, S. 1987, Princeton, NJ, Princeton University Press, 1987, 747 p.

Blackwell, D. E., Petford, A. D., Arribas, S., Haddock, D. J., & Selby, M. J., 1990, A&A, 232, 396

Bland-Hawthorn, J., Englund, M., & Edvell, G. 2004, Optics Express, 12, 5902

Bressan, A., Marigo, P., Girardi, L., et al. 2012, MNRAS, 427, 127

Briley, M. M., Smith, G. H., Hesser, J. E., & Bell, R. A., 1993, AJ, 106, 142

Brogaard, K., VandenBerg, D. A., Bruntt, H., et al. 2012, A&A, 543, 106

Buonanno, R., Buzzoni, A., Corsi, C. E., Fusi Pecci, F., & Sandage, A. R. 1986, Mem. Soc. Astron. Italiana, 57, 391

Busso, M., Lambert, D. L., Beglio, L., et al. 1995, ApJ, 446, 775

Busso, M., Gallino, R., & Wasserburg, G. J., 1999, ARA&A, 37, 239

Buzzoni, A., Patelli, L., Bellazzini, M., Pecci, F. F., & Oliva, E. 2010, MNRAS, 403, 1592

Caffau, E., Ludwig, H.-G., Steffen, M., Freytag, B., & Bonifacio, P. 2011, Sol. Phys., 268, 255

Cameron, A. G. W. 1955, ApJ, 121, 144

Cameron, A. G. W. 1960, AJ, 65, 485

Campbell, S. W., D'Orazi, V., Yong, D., Constatino, T., N., Lattanzio, J. C., Stancliffe, R. J., Angelou. G. C., Wylie-de Boer, E. C., & Grundahl, F., 2013, Nature, 498, 198

Caputo, F., Chieffi, A., Tornambe, A., Castellani, V., & Pulone, L. 1989, ApJ, 340, 241

Cardelli, J. A., Clayton, G. C., & Mathis, J. S., 1989, ApJ, 345, 245

Carretta, E., & Gratton, R. G. 1997, A&AS, 121, 95

Carretta, E., Bragaglia, A., & Cacciari, C. 2004, ApJL, 610, L25

Carretta, E., Gratton, R. G., Bragaglia, A., Bonifacio, P., & Pasquini, L. 2004, A&A, 416, 925

Carretta, E., Bragaglia, A., Gratton, R. G., et al. 2006, A&A, 450, 523

Carretta, E., Bragaglia, A., Gratton, R. G., Lucatello, S., & Momany, Y. 2007, A&A, 464, 927

Carretta, E., Bragaglia, A., Gratton, R., & Lucatello, S. 2009, A&A, 505, 139

Carretta, E., Bragaglia, A., Gratton, R., D'Orazi, V., & Lucatello, S. 2009, A&A, 508, 695

Carretta, E., Bragaglia, A., Gratton, R. G., et al. 2009, A&A, 505, 117

Carretta, E., Bragaglia, A., Gratton, R., et al. 2010, ApJL, 712, L21

Carretta, E., Bragaglia, A., Gratton, R. G., et al. 2010, ApJL, 714, L7

Carretta, E., Bragaglia, A., Gratton, R. G., et al. 2010, A&A, 516, A55

Carretta, E., Gratton, R. G., Bragaglia, A., D'Orazi, V., & Lucatello, S. 2013, A&A, 550, 34

Carretta, E. 2013, A&A, 557, A128

Carretta, E., Bragaglia, A., Gratton, R. G., et al. 2014, A&A, 564, A60

Cassisi, S., Castellani, V., Degl'Innocenti, S., Piotto, G., & Salaris, M. 2001, A&A, 366, 578

Cassisi, S., Salaris, M., Pietrinferni, A., Vink, J. S., & Monelli, M. 2014, A&A, 571, 81

Castelli, F., & Kurucz, R. L. 2004, arXiv:astro-ph/0405087

Castelli, F., 2005, MSAIS, 8, 44

Cavallo, R. M., Sweigart, A. V., & Bell, R. A. 1996, ApJL, 464, L79

Cayrel, R., Depagne, E., Spite, M., et al. 2004, A&A, 416, 1117

Cescutti, G., Matteucci, F., Caffau, E., & François, P. 2012, A&A, 540, 33

Charbonnel, C., Chantereau, W., Decressin, T., Meynet, G., & Schaerer, D. 2013, A&A, 557, LL17

Cioni, M.-R. L., & Habing, H. J. 2003, A&A, 402, 133

Cirasuolo, M., Afonso, J., Bender, et al. 2011, The Messenger, 145, 11

Cirasuolo, M., Afonso, J., Carollo, M., et al. 2014, SPIE, 9147E, 0N1

Cohen, J. G. 1981, ApJ, 247, 869

Colucci, J. E., Bernstein, R. A., Cameron, S., McWilliam, A., & Cohen, J. G. 2009, ApJ, 704, 385

Conroy, C., & Spergel, D. N. 2011, ApJ, 726, 36

Content, R. 1996, ApJ, 464, 412

Cordero, M. J., Pilachowski, C. A., Johnson, C. I., et al. 2014, ApJ, 780, 94

Corsaro, E., Stello, D., Huber, D., et al. 2012, ApJ, 757, 190

Cosby, P. C., & Slanger, T. G. 2007, Can. J. Phys., 85, 77

Cote, P., Welch, D. L., F, Fischer, P., Da Costa, G. S., Tamblyn, P., Seitezer, P., & Irwin, M. J., 1994, ApJS, 90, 83

Cottrell, P. L., & Da Costa, G. S. 1981, ApJL, 245, L79

Cowan, J. J., & Thielemann, F.-K. 2004, Physics Today, 57, 47

Cuby, J. G., Lidman, C., & Moutou, C. 2000, Messenger, 101, 2

Cudworth K.M., 1986, AJ, 92, 348

Cunha, K., Smith, V. V., Lambert, D. L., & Hinkle, K. H. 2003, AJ, 126, 1305

Da Costa, G. S. & Marino, A. F., 2011, PASA, 28, 28

Dalessandro, E., Lanzoni, B., Ferraro, F. R., et al. 2008, ApJ, 677, 1069

Dalessandro, E., Beccari, G., Lanzoni, B., et al. 2009, ApJS, 182, 509

Dalessandro, E., Salaris, M., Ferraro, F. R., Mucciarelli, A., & Cassisi, S. 2013, MNRAS, 430, 459

Decressin, T., Meynet, G., Charbonnel, C., Prantzos, N., & Ekström, S. 2007, A&A, 464, 1029

Decressin, T., Baumgardt, H., Charbonnel, C., & Kroupa, P. 2010, A&A, 516, A73

Dekker, H. et al., 2000, Proc. SPIE, 4008, 534

De Marco, O., Shara, M. M., Zurek, D., et al. 2005, ApJ, 632, 894

de Mink, S. E., Pols, O. R., Langer, N., & Izzard, R. G. 2009, A&A, 507, L1

Denisenkov, P. A., & Denisenkova, S. N. 1989, Astronomicheskij Tsirkulyar, 1538, 11

D'Ercole, A., Vesperini, E., D'Antona, F., McMillan, S. L. W., & Recchi, S. 2008, MNRAS, 391, 825

D'Ercole, A., D'Antona, F., & Vesperini, E. 2011, MNRAS, 415, 1304

D'Orazi, V., Bragaglia, A., Tosi, M., Di Fabrizio, L., & Held, E. V., 2006, MNRAS, 368, 471

D'Orazi, V., Gratton, R., Lucatello, S., et al. 2010, ApJL, 719, L213

D'Orazi, V., Lucatello, S., Lugaro, M., et al. 2013, ApJ, 763, 22

Dotter, A., Sarajedini, A., Anderson, J., et al. 2010, ApJ, 708, 698

Drawin, H. W. 1969, Zeitschrift fur Physik, 228, 99

Dubath, P., Meylan, G., & Mayor, M. 1997, A&A, 324, 505

Edvardsson, B., Andersen, J., Gustafsson, B., et al. 1993, A&AS, 102, 603

Einsel, C., & Spurzem, R. 1999, MNRAS, 302, 81

Ellis, S. C., Bland-Hawthorn, J., Lawrence, J., et al. 2012, MNRAS, 425, 1682

Ennico, K. A., Parry, I. R., Kenworthy, M. A., et al. 1998, SPIE, 3354, 668

Fabricius, M. H., Noyola, E., Rukdee, S., et al. 2014, ApJL, 787, L26

Fabrizio, M. et al., 2012, PASP, 124, 519

Fenner, Y., Campbell, S., Karakas, A. I., Lattanzio, J. C., & Gibson, B. K. 2004, MNRAS, 353, 789

Fenner, Y., Murphy, M. T., & Gibson, B. K. 2005, MNRAS, 358, 468

Ferraro, F. R., Fusi Pecci, F., Testa, V., et al. 1995, MNRAS, 272, 391

Ferraro, F. R., Paltrinieri, B., Fusi Pecci, F., et al. 1997, A&A, 324, 915

Ferraro, F. R., Paltrinieri, B., Fusi Pecci, F., et al. 1997, ApJL, 484, L145

Ferraro, F. R., Paltrinieri, B., Fusi Pecci, F., Rood, R. T., & Dorman, B. 1998, ApJ, 500, 311

Ferraro, F. R., Messineo, M., Fusi Pecci, F., et al. 1999a, AJ, 118, 1738

Ferraro, F. R., Paltrinieri, B., Rood, R. T., & Dorman, B. 1999b, ApJ, 522, 983

Ferraro, F. R., Montegriffo, P., Origlia, L., & Fusi Pecci, F. 2000, AJ, 119, 1282

Ferraro, F. R., D'Amico, N., Possenti, A., Mignani, R. P., & Paltrinieri, B. 2001, ApJ, 561, 337

Ferraro, F. R., Sills, A., Rood, R. T., Paltrinieri, B., & Buonanno, R. 2003, ApJ, 588, 464

Ferraro, F. R., Possenti, A., Sabbi, E., et al. 2003, ApJ, 595, 179

Ferraro, F. R., Sollima, A., Pancino, E., et al. 2004, ApJL, 603, L81

Ferraro, F. R., Beccari, G., Rood, R. T., et al. 2004, ApJ, 603, 127

Ferraro, F. R., Sabbi, E., Gratton, R., et al. 2006, ApJL, 647, L53

Ferraro, F. R., Dalessandro, E., Mucciarelli, A., et al. 2009, Nature, 462, 483

Ferraro, F. R., Beccari, G., Dalessandro, E., et al. 2009, Nature, 462, 1028

Ferraro, F. R., Lanzoni, B., Dalessandro, E., et al. 2012, Nature, 492, 393

Ferraro, F. R., Lanzoni, B., Dalessandro, E., Mucciarelli, A., & Lovisi, L. 2015, Astrophysics and Space Science Library, 413, 99

Fiestas, J., & Spurzem, R. 2010, MNRAS, 405, 194

Fiorentino, G., Lanzoni, B., Dalessandro, E., et al. 2014, ApJ, 783, 34

Forestini, M., Goriely, S., Jorissen, A., & Arnould, M. 1992, A&A, 261, 157

Freeman, K. C., & Norris, J. 1981, ARA&A, 19, 319

Freytag, B. & Hofner, S., 2008, A&A, 483, 571

Fuhr, J. R., Martin, G. A., & Wiese, W. L., 1988, JPCRD, 17S

Fuhr, J. R., & Wiese, W. L., 2006, JPCRD, 35, 1669

Fulbright, J. P. 2000, AJ, 120, 1841

Fulbright, J. P., McWilliam, A., & Rich, R. M. 2006, ApJ, 636, 821

Fusi Pecci, F., Ferraro, F. R., Crocker, D. A., Rood, R. T., & Buonanno, R. 1990, A&A, 238, 95

Fusi Pecci, F., Ferraro, F. R., Corsi, C. E., Cacciari, C., & Buonanno, R. 1992, ApJ, 104, 1831

Gallino, R., Bisterzo, S., Cristallo, S., & Straniero, O. 2010, Mem. Soc. Astron. Italiana, 81, 998

Gebhardt, K., Pryor, C., Williams, T. B., & Hesser, J. E. 1995, AJ, 110, 1699

Geller, A. M., & Mathieu, R. D. 2011, Nature, 478, 356

Gilliland R. L., Bono G., Edmonds P. D., Caputo F., Cassisi S., Petro L. D., Saha A., & Shara M. M. 1998, ApJ, 507, 818

Gonzalez, G., & Wallerstein, G. 1998, AJ, 116, 765

Gosnell, N. M., Mathieu, R. D., Geller, A. M., et al. 2014, ApJL, 783, LL8

Gratton, R. G. 1982, A&A, 115, 171

Gratton, R. G., & Sneden, C. 1991, A&A, 241, 501

Gratton, R. G., Carretta, E., Eriksson, K., & Gustafsson, B. 1999, A&A, 350, 955

Gratton, R. G., Sneden, C., Carretta, E., & Bragaglia, A. 2000, A&A, 354, 169

Gratton, R. G., Bonifacio, P., Bragaglia, A., et al. 2001, A&A, 369, 87

Gratton, R. G., Carretta, E., Desidera, S., et al. 2003, A&A, 406, 131

Gratton, R., Sneden, C., & Carretta, E. 2004, ARA&A, 42, 385

Gratton, R. G., & Carretta, E. 2010, A&A, 521, A54

Gratton, R. G., Carretta, E., Bragaglia, A., Lucatello, S. & D'Orazi, V., 2010, A&A, 517, 81

Gratton, R. G., Johnson, C. I., Lucatello, S., D'Orazi, V., & Pilachowski, C. 2011, A&A, 534, A72

Gratton, R. G., Carretta, E., & Bragaglia, A. 2012, A&A Rev., 20, 50

Gratton, R. G., Lucatello, S., Sollima, A., et al. 2013, A&A, 549, 41

Grevesse, N., & Sauval, A. J., 1998, Space Science Reviews, 85, 161

Gustafsson, B., Edvardsson, B., Eriksson, K., et al. 2008, A&A, 486, 951

Harris, W. E. 1996, AJ, 112, 1487

Heiter, U., & Eriksson, K. 2006, A&A, 452, 1039

Herbst, T. M. 1994, PASP, 106, 1298

Hill, V., Lecureur, A., Gómez, A., et al. 2011, A&A, 534, A80

Hills, J. G., & Day, C. A. 1976, Astrophys. Lett., 17, 87

Hoefner, S., Jorgensen, U. G., Loidl, R., & Aringer, B. 1998, A&A, 340, 497

Ibata, R. A., Gilmore, G., & Irwin, M. J. 1994, Nature, 370, 194

Iben, I., Jr. 1965, ApJ, 142, 1447

Immeli, A., Samland, M., Gerhard, O., & Westera, P. 2004, A&A, 413, 547

Ivans, I. I., Sneden, C., Kraft, R. P., Suntzeff, N. B., Smith, V. V., Langer, G. E., & Fulbright, J. P., 1999, AJ, 118, 1273

Ivans, I. I., Kraft, R. P., Sneden, C., et al. 2001, AJ, 122, 1438

Iwamuro, F., Motohara, K., Maihara, T., Hata, R., & Harashima, T. 2001, PASJ, 53, 355

Iwamuro, F., Maihara, T., Ohta, K., et al. 2006, SPIE, 6269, 1B1

Izotov, Y. I., Stasińska, G., & Guseva, N. G. 2013, A&A, 558, A57

James, G., François, P., Bonifacio, P., et al. 2004, A&A, 427, 825

Johnson, J. A., Ivans, I. I., & Stetson, P. B. 2006, ApJ, 640, 801

Johnson, C. I., & Pilachowski, C. A. 2010, ApJ, 722, 1373

Johnson, C. I., & Pilachowski, C. A. 2012, ApJL, 754, L38

Johnson, C. I., McWilliam, A., & Rich, R. M. 2013, ApJL, 775, L27

Johnson, C. I., McDonald, I., Pilachowski, C. A., et al. 2015, AJ, 149, 71

Jorissen, A., Smith, V. V., & Lambert, D. L. 1992, A&A, 261, 164

Kacharov, N., Bianchini, P., Koch, A., et al. 2014, A&A, 567, A69

Kamann, S., Wisotzki, L., & Roth, M. M. 2013, A&A, 549, A71

Kaufer, A., Stahl, O., Tubbesing, S., et al. 1999, The Messenger, 95, 8

King I.R., 1966, AJ, 71, 64

Kirby, E. N., Guhathakurta, P., Bolte, M., Sneden, C., & Geha, M. C., 2009, ApJ, 705, 328

Kobayashi, C., Umeda, H., Nomoto, K., Tominaga, N., & Ohkubo, T. 2006, ApJ, 653, 1145

Kobayashi, C., Izutani, N., Karakas, A. I., et al. 2011, ApJL, 739, L57

Koch, A., & McWilliam, A. 2008, AJ, 135, 1551

Koch, A., & McWilliam, A., 2010, AJ, 139, 2289

Kraft, R. P. 1979, ARA&A, 17, 309

Kraft, R. P. 1994, PASP, 106, 553

Kraft, R. P., Sneden, C., Smith, G. H., et al. 1997, AJ, 113, 279

Kraft, R. P., & Ivans, I. I. 2003, PASP, 115, 143

Kunder, A., et al., 2013, AJ, 146, 119

Lambert, D. L., Smith, V. V., Busso, M., Gallino, R., & Straniero, O. 1995, ApJ, 450, 302

Lane, R. R., Kiss, L. L., Lewis, G. F., et al. 2010, MNRAS, 401, 2521

Lane, R. R., Kiss, L. L., Lewis, G. F., et al. 2010, MNRAS, 406, 2732

Langer, G. E., Hoffman, R., & Sneden, C. 1993, PASP, 105, 30

Langer, G. E., Hoffman, R. E., & Zaidins, C. S. 1997, PASP, 109, 244

Lanzoni, B., Sanna, N., Ferraro, F. R., et al. 2007, ApJ, 663, 1040

Lanzoni, B., Dalessandro, E., Ferraro, F. R., et al. 2007, ApJL, 668, L139

Lanzoni, B., Ferraro, F. R., Dalessandro, E., et al. 2010, ApJ, 717, 653

Lanzoni, B., Mucciarelli, A., Origlia, L., et al. 2013, ApJ, 769, 107

Lapenna, E., Mucciarelli, A., Lanzoni, B., et al. 2014, ApJ, 797, 124

Lardo, C., Pancino, E., Mucciarelli, A., & Milone, A. P. 2012, A&A, 548, A107

Lardo, C., Pancino, E., Mucciarelli, A., et al. 2013, MNRAS, 433, 1941

Lawler, J.E., Bonvallet, G., & Sneden, C., 2001, ApJ, 556, 452

Lawler, J. E., Guzman, A., Wood, M. P., Sneden, C., & Cowan, J. J. 2013, ApJS, 205, 11

Lecureur, A., Hill, V., Zoccali, M., et al. 2007, A&A, 465, 799

Lee, Y.-W., Joo, J.-M., Sohn, Y.-J., et al. 1999, Nature, 402, 55

Leigh, N., Sills, A., & Knigge, C. 2007, ApJ, 661, 210

Letarte, B., Hill, V., Jablonka, P., et al. 2006, A&A, 453, 547

Li Causi, G., Cabral, A., Ferruzzi, D., et al. 2014 SPIE, 9147E, 641

Limongi, M., & Chieffi, A. 2003, ApJ, 592, 404

Lind, K., Primas, F., Charbonnel, C., Grundahl, F., & Asplund, M. 2009, A&A, 503, 545

Lind, K., Asplund, M., & Barklem, P. S. 2009, A&A, 503, 541

Lind, K., Asplund, M., Barklem, P. S., & Belyaev, A. K. 2011, A&A, 528, A103

Lind, K., Bergemann, M., & Asplund, M., 2012, MNRAS, 427, 50

Lützgendorf, N., Kissler-Patig, M., Noyola, E., et al. 2011, A&A, 533, A36

Lützgendorf, N., Kissler-Patig, M., Gebhardt, K., et al. 2013, A&A, 552, A49

Maccarone, T. J., & Zurek, D. R. 2012, MNRAS, 423, 2

Maihara, T., Iwamuro, F., Yamashita, T., et al. 1993, PASP, 105, 940

Mallia, E., A., 1978, ApJ, 104, 645

Mapelli, M., Sigurdsson, S., Ferraro, F. R., et al. 2006, MNRAS, 373, 361

Mapelli, M., Ripamonti, E., Battaglia, G., et al. 2009, MNRAS, 396, 1771

Maraston, C. 2005, MNRAS, 362, 799

Marcolini, A., Gibson, B. K., Karakas, A. I., & Sánchez-Blázquez, P. 2009, MNRAS, 395, 719

Marin-Franch, A., et al., 2009, ApJ, 694, 1498

Marino, A. F., Milone, A. P., Piotto, G., et al. 2009, A&A, 505, 1099

Marino, A. F., Milone, A. P., Piotto, G., et al. 2011, ApJ, 731, 64

Marino, A. F., Sneden, C., Kraft, R. P., et al. 2011, A&A, 532, A8

Marino, A. F., Milone, A. P., Piotto, G., et al. 2012, ApJ, 746, 14

Marino, A. F., Milone, A. P., Przybilla, N., et al. 2014, MNRAS, 437, 1609

Marino, A. F., Milone, A. P., Karakas, A. I., et al. 2015, MNRAS, 450, 815

Martell, S. L., Smith, G. H., & Briley, M. M. 2008, AJ, 136, 2522

Martin, G. A., Fuhr, J. R., & Wiese, W. L., 1988, JPCRD, 17S

Mashonkina, L., Gehren, T., Shi, J.-R., Korn, A. J., & Grupp, F. 2011, A&A, 528, A87

Massari, D., Mucciarelli, A., Dalessandro, E., et al. 2012, ApJL, 755, L32

Massari, D., Mucciarelli, A., Ferraro, F. R., et al. 2014, ApJ, 795, 22

Massari, D., Mucciarelli, A., Ferraro, F. R., et al. 2014, ApJ, 791, 101

Matteucci, F., Raiteri, C. M., Busson, M., Gallino, R., & Gratton, R. 1993, A&A, 272, 421

Mayor, M., Imbert, M., Andersen, J., et al. 1983, A&AS, 54, 495

McCall, M. L. 2004, AJ, 128, 2144

McCarthy, J. K., & Nemec, J. M. 1997, ApJ, 482, 203

McCrea, W. H. 1964, MNRAS, 128, 147

McLaughlin, D. E., & van der Marel, R. P. 2005, ApJS, 161, 304

McLaughlin, D. E., Anderson, J., Meylan, G., Gebhardt, K., Pryor, C., Minniti, D., & Phinney, S., 2006, ApJS, 166, 249

McNamara, B. J., Harrison, T. E., Baumgardt, H., & Khalaj, P. 2012, ApJ, 745, 175

McWilliam, A., Preston, G. W., Sneden, C., & Shectman, S. 1995, AJ, 109, 2736

McWilliam, A., Preston, G. W., Sneden, C., & Searle, L. 1995, AJ, 109, 2757

McWilliam, A., Rich, R. M., & Smecker-Hane, T. A. 2003, ApJL, 592, L21

Melendez, J., & Barbuy, B., 2009, A&A, 497, 611

Meylan, G., Dubath, P., & Mayor, M. 1991, ApJ, 383, 587

Meylan, G., & Heggie, D. C. 1997, A&A Rev., 8, 1

Meynet, G. 1993, Space Sci. Rev., 66, 417

Meynet, G., & Arnould, M. 1996, Liege International Astrophysical Colloquia, 33, 89

Meynet, G., & Arnould, M. 2000, A&A, 355, 176

Milone, A. P. et al., 2012, A&A, 540, 16

Milone, A. P., Marino, A. F., Piotto, G., et al. 2015, MNRAS, 447, 927

Miocchi, P. 2007, MNRAS, 381, 103

Miocchi, P., Lanzoni, B., Ferraro, F. R., et al. 2013, ApJ, 774, 151

Miocchi, P., Pasquato, M., Lanzoni, B., et al. 2015, ApJ, 799, 44

Monaco, L., Pancino, E., Ferraro, F. R., & Bellazzini, M. 2004, MNRAS, 349, 1278

Monaco, L., Villanova, S., Bonifacio, P., et al. 2012, A&A, 539, A157

Monelli, M., Cassisi, S., Mapelli, M., et al. 2012, ApJ, 744, 157

Mucciarelli, A., Origlia, L., Ferraro, F. R., & Pancino, E., 2009, ApJ, 659L, 134

Mucciarelli, A., Salaris, M., Lovisi, L., et al. 2011, MNRAS, 412, 81

Mucciarelli, A., Bellazzini, M., Ibata, R., et al. 2012, MNRAS, 426, 2889

Mucciarelli, A., Pancino, E., Lovisi, L., Ferraro, F. R., & Lapenna, E. 2013, ApJ, 766, 78

Mucciarelli, A. 2013, arXiv:1311.1403

Mucciarelli, A., Bellazzini, M., Catelan, M., Dalessandro, E., Amigo, P., Correnti, M., Cortés, C.& D'Orazi, V, 2013, MNRAS, 435, 3667

Mucciarelli, A., Salaris, M., Bonifacio, P., Monaco, L., & Villanova, S. 2014, MNRAS, 444, 1812

Mucciarelli, A., Lapenna, E., Massari, D., Ferraro, F. R., & Lanzoni, B. 2015, ApJ, 801, 69

Mucciarelli, A., Lapenna, E., Massari, D., et al. 2015, ApJ, 809, 128

Mucciarelli, A., Bellazzini, M., Merle, T., et al. 2015, ApJ, 801, 68

Muñoz, C., Geisler, D., & Villanova, S. 2013, MNRAS, 433, 2006

Neckel, H., & Labs, D. 1984, Sol. Phys., 90, 205

Ness, M., Freeman, K., Athanassoula, E., et al. 2013, MNRAS, 430, 836

Nidever, D. L., Marcy, G. W., Butler, R. P., Fischer, D. A., & Vogt, S. S. 2002, ApJS, 141, 503

Nissen, P. E., Akerman, C., Asplund, M., et al. 2007, A&A, 469, 319

Nomoto, K., Thielemann, F.-K., & Wheeler, J. C. 1984, ApJL, 279, L23

Norris, J. 1981, ApJ, 248, 177

Norris, J., Cottrell, P. L., Freeman, K. C., & Da Costa, G. S. 1981, ApJ, 244, 205

Norris, J., & Freeman, K. C. 1982, ApJ, 254, 143

Noyola, E., Gebhardt, K., Kissler-Patig, M., et al. 2010, ApJL, 719, L60

Oliva, E., & Origlia, L. 1992, A&A, 254, 466

Oliva, E., Origlia, L., Maiolino, R., et al. 2012a, SPIE, 8446, 3T1

Oliva, E., Biliotti, V., Baffa, C., et al. 2012b, SPIE, 8453, 2T1

Oliva, E., Origlia, L., Maiolino, R., et al. 2013, A&A, 555, A78

Origlia, L., Ferraro, F. R., Fusi Pecci, F., & Oliva, E. 1997, A&A, 321, 859

Origlia, L., Ferraro, F. R., Fusi Pecci, F. & Rood, R. T., 2002, ApJ, 571, 458

Origlia, L., Ferraro, F. R., Bellazzini, M., & Pancino, E. 2003, ApJ, 591, 916

Origlia, L., Rood, R. T., Fabbri, S., et al. 2007, ApJL, 667, L85

Origlia, L., Rood, R. T., Fabbri, S., et al. 2010, ApJ, 718, 522

Origlia, L., Rich, R. M., Ferraro, F. R., et al. 2011, ApJL, 726, L20

Origlia, L., Massari, D., Rich, R. M., Mucciarelli, A., Ferraro, F. R., Dalessandro, E., & Lanzoni, B., 2013, ApJ, 779L, 5

Origlia, L., Ferraro, F. R., Fabbri, S., et al. 2014, A&A, 564, A136

Pancino, E., Ferraro, F. R., Bellazzini, M., Piotto, G., & Zoccali, M. 2000, ApJL, 534, L83

Pancino, E., Rejkuba, M., Zoccali, M., & Carrera, R. 2010, A&A, 524, A44

Pancino, E., Mucciarelli, A., Sbordone, L., et al. 2011, A&A, 527, A18

Pancino, E., Mucciarelli, A., Bonifacio, P., Monaco, L., & Sbordone, L. 2011, A&A, 534, A53

Pandey, G. 2006, ApJL, 648, L143

Pandey, G., Lambert, D. L., & Rao, N. K. 2008, ApJ, 674, 1068

Pasquini, L., et al., 2000, Proc. SPIE, 4008, 129

Pasquini, L., Bonifacio, P., Randich, S., Galli, D., & Gratton, R. G. 2004, A&A, 426, 651

Pasquini, L., Mauas, P., Käufl, H. U., & Cacciari, C. 2011, A&A, 531, A35

Peterson, R. C., Kurucz, R. L., & Carney, B. W. 1990, ApJ, 350, 173

Pietrinferni, A., Cassisi, S., Salaris, M., & Castelli, F. 2006, ApJ, 642, 797

Pilachowski, C., Leep, E. M., Wallerstein, G., & Peterson, R. C. 1982, ApJ, 263, 187

Pilachowski, C. A., Sneden, C., & Wallerstein, G. 1983, ApJS, 52, 241

Pilachowski, C. A., Sneden, C., & Kraft, R. P. 1996, AJ, 111, 1689

Piotto, G., De Angeli, F., King, I. R., et al. 2004, ApJL, 604, L109

Piotto, G., Milone, A. P., Anderson, J., et al. 2012, ApJ, 760, 39

Plez, B. 2012, Astrophysics Source Code Library, 5004

Prantzos, N., Charbonnel, C., & Iliadis, C. 2007, A&A, 470, 179

Pryor, C., & Meylan, G. 1993, Structure and Dynamics of Globular Clusters, 50, 357

Pumo, M. L., D'Antona, F., & Ventura, P. 2008, ApJL, 672, L25

Ramírez, I., Meléndez, J., & Asplund, M. 2009, A&A, 508, L17

Ramírez, I., & Allende Prieto, C. 2011, ApJ, 743, 135

Reddy, B. E., Tomkin, J., Lambert, D. L., & Allende Prieto, C. 2003, MNRAS, 340, 304

Reddy, B. E., Lambert, D. L., & Allende Prieto, C. 2006, MNRAS, 367, 1329

Redman, S. L., Lawler, J. E., Nave, G., Ramsey, L. W., & Mahadevan, S. 2011, ApJS, 195, 24

Reeves, H. 1970, Nature, 226, 727

Renda, A., Fenner, Y., Gibson, B. K., et al. 2004, MNRAS, 354, 575

Renzini, A., & Buzzoni, A. 1986, Spectral Evolution of Galaxies, 122, 195

Renzini, A., & Fusi Pecci, F. 1988, ARA&A, 26, 199

Robin, A. C., Reylé, C., Derrière, S., & Picaud, S. 2003, A&A, 409, 523

Romano, D., Matteucci, F., Ventura, P., & D'Antona, F. 2001, A&A, 374, 646

Romano, D., & Matteucci, F. 2007, MNRAS, 378, L59

Rood, R. T., 1973, ApJ, 184, 815

Rothman, L. S., Gordon, I. E., Barbe, A., et al. 2009, JQS&RT, 110, 533

Rousselot, P., Lidman, C., Cuby, J.-G., Moreels , G., & Monnet, G. 2000, A&A, 354, 1134

Salaris, M., & Cassisi, S. 2006, Evolution of Stars and Stellar Populations by Maurizio Salaris and Santi Cassisi. Wiley, 2006. ISBN: 978-0-470-09219-4

Sandage, A. R. 1953, AJ, 58, 61

Sarajedini, A. et al., 2007, AJ, 133, 1658

Sbordone, L., 2005, MSAIS, 8, 61

Sestito, P., Bragaglia, A., Randich, S., Carretta, E., Prisinzano, L. & Tosi, M., 2006, A&A, 458, 121

Shara, M. M., Saffer, R. A., & Livio, M. 1997, Astrophys. Lett., 489, L59

Sharma, R. D. 1985, Handbook of Geophysics, chapter 13 (Air Force Geophysics Laboratory, USAF)

Sharples, R., Bender, R., Agudo Berbel, A., et al. 2010, The Messenger, 139, 24

Shetrone, M. D. 1996, AJ, 112, 1517

Shetrone, M. D. 1996, AJ, 112, 2639

Siegel, M. H., Dotter, A., Majewski, S. R., et al. 2007, ApJL, 667, L57

Sills, A., Karakas, A., & Lattanzio, J. 2009, ApJ, 692, 1411

Simmerer, J., Ivans, I. I., Filler, D., et al. 2013, ApJL, 764, L7

Sirianni, M., Jee, M. J., Benítez, N., et al. 2005, PASP, 117, 1049

Skrutskie, M. F. et al. 2006, AJ, 131, 1163

Smith, G. H., & Norris, J. 1982, ApJ, 254, 149

Smith, G. H., & Norris, J. 1984, AJ, 89, 263

Smith, G. H. 1987, PASP, 99, 67

Smith, G. H., & Mateo, M. 1990, ApJ, 353, 533

Smith, G. H., & Wirth, G. D. 1991, PASP, 103, 1158

Smith, G. H., & Kraft, R. P. 1996, PASP, 108, 344

Smith, V. V., Cunha, K., Ivans, I. I., et al. 2005, ApJ, 633, 392

Sneden, C., & Crocker, D. A. 1988, ApJ, 335, 406

Sneden, C., Gratton, R. G., & Crocker, D. A. 1991, A&A, 246, 354

Sneden, C., Kraft, R. P., Prosser, C. F., & Langer, G. E. 1992, AJ, 104, 2121

Sneden, C., Kraft, R. P., Shetrone, M. D., et al. 1997, AJ, 114, 1964

Sneden, C. 2000, Liege International Astrophysical Colloquia, 35, 159

Sneden, C., Ivans, I. I., & Kraft, R. P. 2000, Mem. Soc. Astron. Italiana, 71, 657

Sneden, C., & Cowan, J. J. 2003, Science, 299, 70

Sollima, A., Pancino, E., Ferraro, F. R., et al. 2005, ApJ, 634, 332

Spite, F., & Spite, M. 1982, A&A, 115, 357

Stetson, P. B., & Pancino, E., PASP, 120, 1332

Straniero, O., Imbriani, G., Strieder, F., et al. 2013, ApJ, 763, 100

Sullivan, P. W., & Simcoe, R. A. 2012, PASP, 124, 1336

Sweigart, A. V. 1997, ApJL, 474, L23

Takeda, Y., Ohkubo, M., Sato, B., Kambe, E., & Sadakane, K. 2005, PASJ, 57, 27

Thévenin, F., & Idiart, T. P. 1999, ApJ, 521, 753

Thielemann, F.-K., Nomoto, K., & Yokoi, K. 1986, A&A, 158, 17

Thygesen, A. O., Sbordone, L., Andrievsky, S., et al. 2014, A&A, 572, 108

Tian, B., Deng, L.-C., Han, Z.-W., & Zhang, X.-B. 2006, A&A, 455, 247

Tinsley, B. M. 1979, ApJ, 229, 1046

Tolstoy, E., Hill, V., & Tosi, M., 2009, ARA&A, 47, 371

Tozzi, A., Oliva, E., Origlia, L., et al. 2014, SPIE, 9147E, 9N1

Trenti, M., & van der Marel, R. 2013, MNRAS, 435, 3272

Trinh, C. Q., Ellis, S. C., Bland-Hawthorn, J., et al. 2013, MNRAS, 432, 3262

Umeda, H., & Nomoto, K. 2005, ApJ, 619, 427

Valcarce, A. A. R., & Catelan, M. 2011, A&A, 533, A120

Valenti, E., Ferraro, F. R., & Origlia, L. 2004, MNRAS, 354, 815

Valenti, E., Ferraro, F. R., & Origlia, L. 2007, AJ, 133, 1287

van der Loo, M. P. J., & Groenenboom, G. C. 2007, J. of Chemical Physics, 126, 114314

van Loon, J. T., Groenewegen, M. A. T., de Koter, A., et al. 1999, A&A, 351, 559

Venn, K. A., Irwin, M., Shetrone, M. D., Tout, C. A., Hill, V., & E. Tolstoy, 2004, AJ, 128, 1177

Ventura, P., D'Antona, F., Mazzitelli, I., & Gratton, R. 2001, ApJL, 550, L65

Ventura, P., & D'Antona, F. 2005, ApJL, 635, L149

Ventura, P., & D'Antona, F. 2009, A&A, 499, 835

Vesperini, E., Varri, A. L., McMillan, S. L. W., & Zepf, S. E. 2014, MNRAS, 443, L79

Villanova, S., Piotto, G., King, I. R., et al. 2007, ApJ, 663, 296

Villanova, S., Piotto, G., & Gratton, R. G. 2009, A&A, 499, 755

Villanova, S., Geisler, D., Piotto, G., & Gratton, R. G. 2012, ApJ, 748, 62

Villanova, S., Geisler, D., Gratton, R. G., & Cassisi, S. 2014, ApJ, 791, 107

Wallerstein, G. 1962, ApJS, 6, 407

Werner, K., Rauch, T., & Kruk, J. W. 2005, A&A, 433, 641

Willman, B., & Strader, J. 2012, AJ, 144, 76

Wilson C. P., 1975, AJ, 80, 175

Wood, M. P., Lawler, J. E., Sneden, C., & Cowan, J. J. 2013, ApJS, 208, 27

Woosley, S. E., & Haxton, W. C. 1988, Nature, 334, 45

Woosley, S. E., & Weaver, T. A. 1995, ApJS, 101, 181

Worley, C. C., Cottrell, P. L., Freeman, K. C., & Wylie-de Boer, E. C., 2009, MNRAS, 400, 1039

Wylie, E. C., Cottrell, P. L., Sneden, C. A., & Lattanzio, J. C. 2006, ApJ, 649, 248

Xin, Y., Ferraro, F. R., Lu, P., et al. 2015, ApJ, 801, 67

Yong, D., Grundahl, F., Nissen, P. E., Jensen, H. R., & Lambert, D. L., 2005, A&A, 438, 875

Yong, D., & Grundahl, F. 2008, ApJL, 672, L2

Yong, D., Meléndez, J., Cunha, K., et al. 2008, ApJ, 689, 1020

Yong, D., Grundahl, F., D'Antona, F., et al. 2009, ApJL, 695, L62

Yong, D., Melendez, J., Grundahl, F., Roederer, I. U., Norris, J. E., Milone, A. P., Marino, A. F., Coelho, P., McArthur, B. E., Lind K., Collet, R., & Asplund, M., 2013, MNRAS, 434, 3542

Yong, D., Roederer, I. U., Grundahl, F., et al. 2014, MNRAS, 441, 3396

Yong, D., Alves Brito, A., Da Costa, G. S., et al. 2014, MNRAS, 439, 2638

Zhang, H. W., Gehren, T., Butler, K., Shi, J. R., & Zhao, G. 2006, A&A, 457, 645

Zhao, G., & Magain, P. 1990, A&AS, 86, 85

Zhao, G., & Magain, P. 1990, A&A, 238, 242

Zinn, R., & King, C. R. 1982, ApJ, 262, 700

Zinn, R., & West, M. J. 1984, ApJS, 55, 45

Zoccali, M., Hill, V., Lecureur, A., et al. 2008, A&A, 486, 177

Acknowledgements

My PhD research project would not have been possible without the help of many people. I wish to thank in particular Davide Massari, Emanuele Dalessandro and Paolo Donati. I have also spent a wonderful and fruitful period at Royal Observatory of Edinburgh made possible by Michele Cirasuolo. I want to thank also my friends, in Bologna and in my hometown Potenza, for their support and encouragement. This work is dedicated to all my family, a special thought goes to the memory of my uncle and my cousin.